Angular and momentum distribution of vector mesons produced in proton-proton and heavy-ion collisions at LHC energies

By

Sourav Kundu

PHYS11201504005

National Institute of Science Education and Research, Bhubaneswar

A thesis submitted to the

Board of Studies in Physical Sciences

In partial fulfillment of requirements

for the Degree of

DOCTOR OF PHILOSOPHY

of

HOMI BHABHA NATIONAL INSTITUTE

October, 2020

Homi Bhaba National Institute

Recommendations of the Viva Voce Committee

As members of the Viva Voce Committee, we certify that we have read the dissertation prepared by **Sourav Kundu** entitled **Angular and momentum distribution of vector mesons produced in proton-proton and heavy-ion collisions at LHC energies** and recommend that it may be accepted as fulfilling the thesis requirement for the award of Degree of Doctor of Philosophy.

Chairman - Dr. Sanjay Kumar Swain   _Sanjay Swain_ 23/12/2020

Guide / Convener - Prof. Bedangadas Mohanty   _Bomdhanty_ 23/12/2020

Co-guide - NA

Examiner 1 - Dr. Chitrasen Jena   _Jena_ 28/12/2020

Examiner 2 -

Member 1 - Dr. Prolay Kumar Mal   _Prolay_ Dec 23, 2020

Member 2 - Dr. Victor Roy   _Victor Roy_ 28.12.2020

Member 3 - Dr. Aruna Kumar Nayak   _Aruna Kumar Nayak_ 23.12.2020

Final approval and acceptance of this thesis is contingent upon the candidates submission of the final copies of the thesis to HBNI.

I/We hereby certify that I/we have read this thesis prepared under my/our direction and recommend that it may be accepted as fulfilling the thesis requirement.

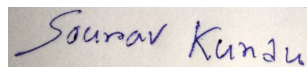Date : 23rd December, 2020

Place : NISER, Jatni

Bomdhanty

Prof. Bedangadas Mohanty

(Guide)

i

Statement by author

This dissertation has been submitted in partial fulfilment of requirements for an advanced degree at Homi Bhabha National Institute (HBNI) and is deposited in the Library to be made available to borrowers under rules of the HBNI.
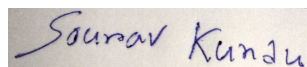
Brief quotations from this dissertation are allowable without special permission, provided that accurate acknowledgement of source is made. Requests for permission for extended quotation from or reproduction of this manuscript in whole or in part may be granted by the Competent Authority of HBNI when in his or her judgement the proposed use of the material is in the interests of scholarship. In all other instances, however, permission must be obtained from the author.

Sourav Kundu

Declaration

I hereby declare that I am the sole author of this thesis in partial fulfillment of the requirements for a postgraduate degree from National Institute of Science Education and Research (NISER). I authorize NISER to lend this thesis to other institutions or individuals for the purpose of scholarly research.

Sourav Kundu

List of publications and presentations

Experimental paper:

1. Evidence of spin-orbital angular momentum interactions in relativistic heavy-ion collisions, S. Acharya et al. (ALICE Collaboration), arXiv:1910.14408, Phys. Rev. Lett. 125, 012301 (2020). Editor's suggestion

2. Multiplicity dependence of $K^*(892)^0$ and $\phi(1020)$ production in pp collisions at 13 TeV, S. Acharya et al. (ALICE Collaboration), arXiv:1910.14397, Phys. Lett. B 807, 135501 (2020).

3. Production of light flavor hadrons in pp collisions at $\sqrt{s} = 7$ and $\sqrt{s} = 13$ TeV, S. Acharya et al. (ALICE Collaboration), arxiv:2005.11120, accepted for publication in Eur. Phys. J. C.

Phenomenological paper:

1. Study of charged particle multiplicity, average transverse momentum and azimuthal anisotropy in Xe+Xe collisions at $\sqrt{s_{NN}} = 5.44$ TeV using AMPT model, Sourav Kundu, Dukhishyam Mallick and Bedangadas Mohanty, Eur. Phys. J. A 55, 157 (2019).

2. Effect of color reconnection on forward-backward multiplicity and mean transverse momentum correlation, Sourav Kundu, Dukhishyam Mallick and Bedangadas Mohanty, arXiv:1912.05176.

Conference proceeding:

1. Spin alignment measurements of vector mesons with ALICE at the LHC, Sourav Kundu, Nucl. Phys. A 1005, 121912 (2021).

2. Spin alignment measurements of vector mesons in Pb-Pb collisions with ALICE at the LHC, Sourav Kundu, Springer Proc. Phys. 250, 423 (2020).

3. Spin alignment measurements of K^{*0} vector mesons with ALICE at the LHC, Sourav Kundu, PoS ICHEP2018, 671 (2019).

4. Identified Hadron Production in Proton-Proton Collisions at $\sqrt{s}$= 13TeV with ALICE at the LHC, Sourav Kundu, Springer Proc. Phys. 203, 497 (2018).

5. Multiplicity dependence of resonance production in pp collisions at $\sqrt{s} = 13$ TeV with ALICE, Sourav Kundu, DAE Symp. Nucl. Phys. 62, 830 (2017).

6. Resonance Production in pp Collisions at $\sqrt{s} = 13$ TeV with ALICE at LHC, Sourav Kundu, Nucl. Phys. 61, 752 (2016).

ALICE analysis note:
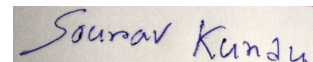
1. K^{*0} resonance production in pp collisions at $\sqrt{s} = 13$ TeV, Sourav Kundu, Bedangadas Mohanty and Ajay Kumar Dash, ID number: ANA-469, https://alice-notes.web.cern.ch/node/469.

2. K^{*0} production as a function of charged particle multiplicity in pp collisions at $\sqrt{s} = 13$ TeV with ALICE at the LHC, Sourav Kundu, Bedangadas Mohanty, Ajay Kumar Dash and Ranbir Singh, ID number: ANA-655, https://alice-notes.web.cern.ch/node/655.

3. Spin alignment measurements of K^{*0} vector meson at pp 13 TeV with ALICE at the LHC, Sourav Kundu, Bedangadas Mohanty, Ajay Kumar Dash and Ranbir Singh, ID number: ANA-633, https://alice-notes.web.cern.ch/node/633.

4. Spin alignment measurements of K^{*0} vector mesons produced in Pb-Pb collisions at $\sqrt{s_{\mathrm{NN}}} = 2.76$ TeV in ALICE at the LHC, Sourav Kundu, Bedangadas Mohanty, Ajay Kumar Dash and Ranbir Singh, ID number: ANA-635, https://alice-notes.web.cern.ch/node/635.

5. Spin alignment of K^{*0} vector meson w.r.t. Event plane in Pb-Pb collisions at $\sqrt{s_{\mathrm{NN}}} = 2.76$ TeV, Sourav Kundu, Bedangadas Mohanty, Ajay Kumar Dash and Ranbir Singh, ID number: ANA-768, https://alice-notes.web.cern.ch/node/768.

6. Spin alingment of K_S^0 in Pb-Pb collisions at $\sqrt{s_{\mathrm{NN}}} = 2.76$ and 5.02 TeV, Sourav Kundu, Bedangadas Mohanty, Ajay Kumar Dash and Ranbir Singh, ID number: ANA-636, https://alice-notes.web.cern.ch/node/636.

7. Spin alignment measurements of K^{*0} vector mesons produced in Pb-Pb collisions at $\sqrt{s_{\mathrm{NN}}} = 5.02$ TeV in ALICE at the LHC, Sourav Kundu, Bedangadas Mohanty, Ajay Kumar Dash and Ranbir Singh, ID number: ANA-750, https://alice-notes.web.cern.ch/node/750.

8. Spin alignment measurements of ϕ vector mesons w.r.t. event plane in Pb-Pb collisions at $\sqrt{s_{\mathrm{NN}}} = 2.76$ TeV with ALICE at the LHC, Sourav Kundu, Bedangadas Mohanty, Ajay Kumar Dash and Ranbir Singh, ID number: ANA-925, https://alice-notes.web.cern.ch/node/925.

9. Spin alignment measurements of ϕ vector mesons produced in Pb-Pb collisions at 2.76 TeV and in pp collisions at 13 TeV with ALICE at the LHC, Sourav Kundu, Bedangadas Mohanty, Ajay Kumar Dash and Ranbir Singh, ID number: ANA-898, https://alice-notes.web.cern.ch/node/898.

10. K^{*0} production in Xe-Xe collisions at $\sqrt{s_{\mathrm{NN}}} = 5.44$ TeV with ALICE at the LHC, Sourav Kundu, Bedangadas Mohanty, Ajay Kumar Dash and Ranbir Singh, ID number: ANA-779, https://alice-notes.web.cern.ch/node/779.

Conference and oral presentation:

1. Quark Matter (QM), 2019 Wuhan, China, Spin alignment measurements of vector mesons with ALICE at the LHC.

2. The 18th International Conference on Strangeness in Quark Matter (SQM), 2019 Bari, Italy, Spin alignment measurements of vector mesons in Pb-Pb collisions with ALICE at the LHC.

3. The 7th Asian Triangle Heavy-Ion Conference (ATHIC), 2018 Hefei, China, Light flavour hadron production in Xe–Xe collisions at $\sqrt{s_{\mathrm{NN}}} = 5.44$ TeV with ALICE at the LHC.

4. XXXIX International Conference on High Energy Physics (ICHEP), 2018 Seoul, South Korea, Spin alignment measurements of K^{*0} vector mesons in ALICE at the LHC.

5. Flavour Physics Conference, 2017 Quy Nhon, Vietnam, Strangeness enhancement and light flavor results at ALICE.

6. The 21st Particles & Nuclei International Conference (PANIC), 2017 Bejing, China, Polarization measurements of Λ hyperons and K^{*0} vector mesons with ALICE at the LHC.

7. International Nuclear Physics Conference (INPC), 2016 Adelaide, Australia, Light flavour hadron production in proton-proton collisions at 13 TeV with ALICE at the LHC.

8. XXIII DAE-BRNS High Energy Physics Symposium, 2018 Chennai, India, Spin alignment measurements of K^{*0} vector mesons in ALICE at the LHC.

9. 62nd DAE-BRNS Symposium on Nuclear Physics, 2017 Patiala, India, Multiplicity dependence of resonance production in pp collisions at $\sqrt{s} = 13$ TeV with ALICE.

10. XXII DAE-BRNS HIGH ENERGY PHYSICS SYMPOSIUM, 2016 Delhi, India, Identified hadron production in proton-proton collisions at $\sqrt{s} = 13$ TeV with ALICE at the LHC.

11. 61st DAE-BRNS Symposium on Nuclear Physics, 2016 Kolkata, India, Resonance Production in pp Collisions at $\sqrt{s} = 13$ TeV with ALICE at LHC.

Sourav Kundu

Dedicated to my family, teachers and friends

Acknowledgements

This thesis would not have seen the daylight unless there were many well-wishers who had shown me the path. I am thankful to all of them. PhD is a long road and on this road, I learnt many invaluable things from my teachers, collaborators and friends, which contributed to fulfilling this dream. Even though I tried to recall everyone's contribution during my PhD days, please accept my apologies if I missed someone who deserved to be mentioned.

First and foremost, I would like to express my deepest and sincere gratitude to my PhD supervisor Prof. Bedangadas Mohanty for his precious guidance throughout my PhD. This thesis would not have been possible without his guidance, continuous support and advice. His dedication, sincerity and generosity inspired me and gave me the strength to sail through this journey. His constructive criticism of my research work was very essential for the successful completion of this work. He was always available to provide help and I could recall, there were several instances where he was available for physics discussions even at late night. I am thankful to him for providing me with all the necessary resources for my research work and I appreciate all the opportunities that he gave me to attend several national and international conferences. I am sure, my words are not enough to describe his impact on me during my PhD. His inspiring advice will stay with me throughout my life. Thank you sir, for giving me the opportunity. I owe you all success ahead.

I would like to thank Prof. Sudhakar Panda (Director of NISER) for providing all the support required to complete my PhD. I am thankful to all my doctoral committee members Dr. Sanjay Kumar Swain, Dr. Prolay Kumar Mal, Dr. Victor Roy and Dr. Aruna Kumar Nayak for their support and motivation. I would like to thank all the faculty and staff members of NISER for their support. I am very grateful to the School of Physical Sciences, NISER for providing me with all the required resources.

I thank my fellow PhD students at the high energy physics group at NISER for constructive physics discussions, company and all the fun time we had throughout my PhD. It has been truly a privilege to work with Dr. Ranbir Singh, Dr. Varchaswi K S Kashyap, Dr. Ajay Dash, Dr. Chitrasen Jena, Dr. Kishora Nayak, Dr. Vipul

I was blessed with a bunch of positive-minded and helpful friends at NISER. My sincere thanks to Vijay, Ashutosh, Samir, Debashish, Anirban, Abhilash and Arjun for making my PhD life cheerful with their constant support, love, help and good wishes. The time that I have spent with you all are very special and will always remain close to my heart.

I am thankful to my school, college and university teachers for their guidance because of which I am able to reach this stage. Most importantly, I would like to express my respect, gratitude and humbleness to my parents for their blessings, constant support and encouragement throughout my life. Without the support, love and encouragement of my parents and sister, this would not have been possible. My sincere thanks to my wife for her patience and support during my PhD. I thank the almighty God for his blessings to complete my research successfully.

Contents

List of Figures

9

13

21

23

List of Tables

Chapter 6

Summary

The discovery of production of Quark-Gluon Plasma in heavy-ion collisions was announced at CERN about 20 years ago. The existence of the dense state of matter was further validated and confirmed in experiments at the Relativisitc Heavy Ion Collider (RHIC). Since then, the properties of this new phase of matter have been probed using the particles produced in relativistic heavy-ion collisions at centre of mass energies spanning a range of more than 3 orders of magnitude. The various kinds of particles that are produced have different intrinsic properties like charge, mass, lifetime, spin. This provides a rich opportunity to use different particles to probe various aspects of the dense matter created in the collision and its subsequent evolution. A systematic study of the dependence of the results on the system size and the colliding energy provides further insights.

Motivated by the above, in this thesis we studied features associated with the production of K^{*0} vector mesons. These resonant states have a spin 1 and a lifetime of the order of 10^{-23} s. The short lifetime is comparable to the time of evolution of dense matter to the hadronic final state, enabling probing the matter at different states of evolution. We have studied some features of the production of vector meson and investigated occurrence of its preferential spin state in Pb–Pb collisions, its transverse momentum distributions, its production in collisions of deformed nuclei, and in pp collisions at the highest available energies. In a subject of which the understanding is continuously evolving, a comparison with theoretical models or event generators help to understand the physics processes better and also contribute to a better design

of the future experiments. With this as the premise, our results were compared with models or theoretical framework wherever possible, providing a direction for further theoretical or phenomenological work towards a complete understanding of the physics of heavy-ion collisions.

The details of analysis and the results of the present thesis are summarised here. In addition to an introduction and details about the experiment, the other three chapters provide new results primarily on the following:

- Preferential alignment of spin of K^{*0} and ϕ vector mesons in Pb–Pb collisions. +++

- Production of K^{*0} in a system of deformed nuclei (Xe–Xe) collisions.

- Production of K^{*0} in pp collisions at the highest available energies.

While exploring the above, we encountered other aspects of interest and addressed them. These include conclusions based on m_{T} and x_{T} scaling and effects of deformation of Xe nucleus, and are included in this thesis. In the following, we summarise the motivation of the work and the results of this thesis, along with the inferences and an outlook.

Given the importance of spin-orbit interactions in several fields of physics (atomic physics, solid-state physics, nuclear physics), it is imperative to look for its possible effect on particles with spin in a system with high orbital angular momentum. Features in the production of K^{*0} and ϕ vector mesons in non-central (3–10 fm) collisions of heavy ions are ideally suited to look for the presence of this interaction, considering the large initial state angular momentum of the order of $\sim 10^{7}$ $\hbar$ in non-central collisions. The spin-orbit interaction may manifest itself in the polarization of the quarks, which may be retained in the final hadron produced in the collision.

We investigated the possible spin alignment of K^{*0} and ϕ vector mesons produced in non-central Pb–Pb collisions. The spin alignment of the vector mesons is established using the diagonal element ρ_{00} of the spin density matrix. The ρ_{00} corresponds to the probability of finding a vector meson in spin state 0 out of 3 possible spin states of -1, 0 and 1. In the absence of spin alignment all 3 states are equally probable, yielding $\rho_{00} = 1/3$; deviations from 1/3 indicate the presence of spin alignment. The ρ_{00} for vector mesons can be determined from the angular distribution of the decay daughter(s) of vector meson with respect to a quantization axis, which may be chosen as the direction perpendicular to either the reaction plane (in experiments, the event plane is chosen as the proxy of the reaction plane) or the production plane.

In this thesis, we report the first observations on preferential alignment of spin of vector mesons in heavy-ion collisions. The results are obtained using the measurements with the ALICE detector at the LHC energies. The results of spin alignment of K^{*0} and ϕ vector mesons are obtained in Pb–Pb collisions at $\sqrt{s_{\mathrm{NN}}} = 2.76$ TeV and in pp collisions at $\sqrt{s} = 13$ TeV. The alignment of spin of the vector mesons, at a 3σ level for K^{*0} and a 2σ level for ϕ, is observed in non-central heavy-ion collisions confirming the existence of a spin-orbital angular momentum interaction. The spin density matrix element ρ_{00} is determined to be lower than 1/3 in mid-central Pb–Pb collisions at low p_{T} ($p_{\mathrm{T}} < 2$ GeV/c), and consistent with 1/3 at high p_{T} [1]. These conclusions of alignment are substantiated with the observed value of $\rho_{00} = 1/3$ [1] for many other cases including those for vector mesons produced in pp collisions, for K_S^0 in non-central heavy-ion collisions and by determining ρ_{00} for vector mesons by choosing a random direction to define the event plane.

The deviation of ρ_{00} values from 1/3 for vector mesons produced at low p_{T} in mid-central Pb–Pb collisions can be attributed to the presence of a large initial angular momentum in non-central heavy-ion collisions. This is also supported by the similar-

ity of the centrality dependence of the spin alignment effect and of the initial angular momentum in the collision. The spin-orbit coupling polarizes the quark, which subsequently carries its polarization to the hadron formed via recombination [2, 3]. The p_{T} dependence of ρ_{00} observed for vector mesons in non-central collisions is qualitatively explained by a model describing the recombination phenomena [3]. Further, the deviation of ρ_{00} from 1/3 is greater when the quantisation axis is chosen perpendicular to the event plane, as compared to when chosen perpendicular to the production plane. This suggests that the alignment occurs along the direction of initial orbital angular momentum and the signal is carried to the other quantisation axis (perpendicular to production plane) due to the elliptic flow in the system. The extent of quark polarization obtained using models from the measured value of Λ hyperon is much less than the extent of quark polarization estimated from the measured spin alignment of vector mesons. Any differences in the retention of quark polarisation in the hadrons may be due to many possible reasons primarily rooted in the difference of how a polarized quark retains its polarization in a meson or a baryon during the process of hadronization. The extent of spin alignment of the vector mesons and its determination are affected by the regeneration and re-scattering of the decay products in the hadronic phase; the possibility of decay products in the hadronic phase being affected by the lifetime of the hadron. Moreover, while most of the vector mesons are directly produced, hyperons are often the decay products of resonances. Considering the absence of a quantitative theory to explain ρ_{00} values, the results of this thesis provide a motivation to formulate the fundamental interactions and evolution in heavy-ion collisions and thereby explain these observations.

In the second part of the thesis, we report results obtained by probing the hadronic phase, the final state of the evolution, by investigating possible re-scattering effects. The short lifetime of K^{*0} resonance ($\sim$4 fm/c) is comparable to the time taken by

the dense nuclear matter to evolve to its final state. This allows the possibility of its decay products to re-scatter due to elastic and pseudo-elastic interactions with other particles in the hadronic phase. Like for all short lived resonances, the yield of K^{*0} is determined from its reconstruction using the energy and momentum of the decay products. The change in energy and momentum due to re-scattering in the hadronic phase affects the yield of the resonance. The final measured yield is affected by the combined effect of interplay between the re-scattering and any regeneration effects. The results on the yield of K^{*0} and on its ratio with the yield of stable particles are presented.

We also report the results on K^{*0} production in a system of deformed nuclei (Xe–Xe) collisions at $\sqrt{s_{NN}} = 5.44$ TeV. Considering that most experimental results are obtained in collisions of spherical nuclei, it is imperative to make some systematic studies due to deformation of Xe nuclei before reporting the results on K^{*0} production. The effect of deformation of the Xe nucleus was determined within the framework of A Multiphase Transport (AMPT) model. We observe from the results of simulations that the deformation does not affect the multiplicity, transverse momentum distribution and $\langle p_T \rangle$ of produced charged particle significantly. The different initial conditions of spatial anisotropy in collisions of deformed Xe nuclei as compared to those in collisions of spherical Pb nuclei, provide an opportunity to study the effect of deformation on observable sensitive to the initial conditions, such as the elliptic flow. An enhancement of $\sim15\%$ in elliptic flow in in central Xe–Xe as compared to those in central Pb–Pb collisions is observed due to the deformation of the Xe nucleus [4].

The dependence of the production of K^{*0} and of the re-scattering and regeneration effects of decay products in the hadronic phase can be investigated by comparing the results in Xe–Xe collision at $\sqrt{s_{NN}} = 5.44$ TeV reported in this thesis to the results obtained from different collision systems (pp, p–Pb and Pb–Pb) at similar

189

collision energies. The thesis includes results on the p_T spectra, p_T integrated yield, mean transverse momentum ($\langle p_\mathrm{T} \rangle$), ratio of yield of neutral K^{*0} to charged kaon and nuclear modification factor in Xe–Xe collisions at $\sqrt{s_\mathrm{NN}} = 5.44$ TeV. The measured $\mathrm{d}N/\mathrm{d}y$ values for K^{*0} in Xe–Xe collisions are observed to be consistent with those obtained from the measurements of pp, p–Pb and Pb–Pb collisions at similar charged particle multiplicity. This suggests that K^{*0} production is independent of collision system and mainly driven by the charged particle multiplicity which is a proxy of system volume. The two samples of events of similar charged particle multiplicity from collisions of Xe–Xe and Pb–Pb collisions yield comparable values of $\langle p_\mathrm{T} \rangle$ of K^{*0}, independent of the collision system, suggesting similar radial flow of K^{*0} for similar volumes of matter. The $\langle p_\mathrm{T} \rangle$ of K^{*0} was compared across pp, p–Pb, Xe–Xe and Pb–Pb collisions at the same final state charged particle multiplicity. A lower $\langle p_\mathrm{T} \rangle$ is observed in heavy-ion collisions as compared to the other collision systems that included a proton. Although the yield of K^{*0} in all systems at the same charged particle multiplicity is the same, the differences in $\langle p_\mathrm{T} \rangle$ indicate different dynamical evolution of the system in A–A collision as compared to the system produced in p–Pb and pp collisions. The measured K^{*0}/K yield ratios in central Xe-Xe collisions are observed to be suppressed as compared to corresponding ratios in pp collisions and peripheral Xe–Xe collisions. Comparable suppression was also reported earlier in Pb–Pb collisions indicating the presence of similar re-scattering effects across different systems. The yield of K^{*0} is used to determine the nuclear modification factor in Xe–Xe collisions, which is observed to be consistent with the measurement in Pb–Pb collisions at similar charged particle multiplicity. The nuclear modification factor indicated a suppression by a factor of about four at high p_T ($p_\mathrm{T} > 6$ GeV/c). This suppression is now known to be a consequence of parton energy loss in the medium [5].

Collisions of small systems such as proton-proton form a necessary benchmark

to compare results from heavy-ion collisions. Recent measurements of long range correlations, collective flow, strangeness enhancement and others in high multiplicity pp collisions have shown striking similarities with results obtained in heavy-ion collisions. Attempts to explain the observed, though unexpected, phenomena in pp collisions were made using ideas of multipartonic interaction (MPI) and color reconnection (CR). Results from pp collisions provide a necessary impetus to phenomenological models and help to tune the event generators. In the third part of this thesis, we reports the results on K^{*0} production and its spectra in different multiplicity intervals in pp collisions at highest available collision energy at $\sqrt{s} = 13$ TeV. Several conclusions based on comparison of these results with MC event generators, and with the corresponding spectra at $\sqrt{s} = 7$ TeV are included here.

The measured spectrum of K^{*0} in pp collisions at $\sqrt{s} = 13$ TeV have higher inverse slope parameter compared to the corresponding spectrum in pp collisions at $\sqrt{s} = 7$ TeV from earlier measurements. The ratio of p_{T} spectra of K^{*0} produced at 13 TeV and at 7 TeV is observed to be nearly unity at low p_{T}. This ratio is observed to increase with p_{T} indicating increase in hard processes with the increase of collision energy [6]. Monte-Carlo event generators such as PYTHIA, DIPSY and EPOS could reproduce the spectra only in the intermediate p_{T} range, overestimating at low and high p_{T}, and yet these generators were in good agreement with the experimentally measured ratio of the p_{T} spectra of K^{*0} in pp collisions at $\sqrt{s} = 13$ TeV and at 7 TeV. While the increase in $\langle p_{\mathrm{T}} \rangle$ with increasing $\langle \mathrm{d}N_{\mathrm{ch}}/\mathrm{d}\eta \rangle$ in A–A collisions is attributed to collective radial expansion, increase of $\langle p_{\mathrm{T}} \rangle$ with increasing multiplicity in pp collisions is qualitatively explained by both hydrodynamical model such as EPOS and color reconnection based model such as PYTHIA and DIPSY [7]. The $\langle p_{\mathrm{T}} \rangle$ of K^{*0} and ϕ mesons are compared with the $\langle p_{\mathrm{T}} \rangle$ of hadrons of comparable mass, namely proton and Λ, as hydrodynamical collective expansion results in same

$\langle p_\mathrm{T} \rangle$ for such hadrons. A mass ordering of $\langle p_\mathrm{T} \rangle$ is observed in central A–A collisions and is attributed to hydrodynamical radial flow. Absence of such an ordering in pp collisions supports [7] the color reconnection mechanism. Further, on investigating the empirical m_T and x_T scaling for identified hadrons in pp collisions at $\sqrt{s} = 13$ TeV, it is observed that the meson and baryon scaling does not uphold for $m_\mathrm{T} > 2$ GeV/c [6]. Also, the deviation in the m_T spectrum of pions from universal scaling of mesons [6] is often understood due to feed-down from resonance decays. The empirical x_T scaling for identified hadrons produced at the LHC energies [6] yield the value of exponent parameter $\langle n \rangle$ which is slightly higher for baryons than for mesons, and is also predicted by NLO pQCD [8].

The ratio of yields of K^{*0}/K showed a decrease with increasing charged particle multiplicity in pp collisions at $\sqrt{s} = 13$ TeV [7], similar to that observed in the A–A collisions, giving credence to the possible presence of re-scattering in the hadronic phase in small collision system, also explained by EPOS. Features of the current data on spectra support both EPOS and colour reconnection mechanism.

The observation of polarization of vector mesons, and the evidence of rescattering in the hadronic phase, as demonstrated in this thesis, augment the methods for probing the different stages of evolution of the matter produced in heavy-ion collisions. In non-central collisions, a large transient magnetic field of the order of $\sim 10^{14}$ Tesla is produced due to the spectator nuclei. Such a large magnetic field may affect $K^{*\pm}$ and K^{*0} differently because of the difference in their magnetic moments. On the basis of inferences drawn in this thesis and with increased statistics, the possible polarisation of vector mesons due to the magnetic field provides an opportunity for precision measurements demonstrating sensitivity to the effects of the transient magnetic field.

References

[1] S. Acharya et al. [ALICE Collaboration], Phys. Rev. Lett. 125, 012301 (2020).

[2] Z. -T. Liang et al., Phys. Rev. Lett. 94, 102301 (2005).

[3] Z. -T. Liang et al., Phys. Lett. B 629, 20 (2005).

[4] S. Kundu et al., Eur. Phys. J. A 55, 157 (2019).

[5] J. D. Bjorken, FERMILAB-PUB-82-59-THY (1982).

[6] S. Acharya et al. [ALICE Collaboration], arxiv:2005.11120.

[7] S. Acharya et al. [ALICE Collaboration], Phys. Lett. B 807, 135501 (2020).

[8] F. Arleo et al., Phys. Rev. Lett. 105, 062002 (2010).

Summary

Quantum chromodynamics (QCD) is the theory that describes the strong interactions observed in nature. QCD predicts that at a high temperature and/or density, the nuclear matter will make a transition to a strongly interacting matter in which quarks and gluons are free to move, and not confined as in hadrons. Such an extreme state of matter is known as quark-gluon plasma (QGP) which existed in the early stages of the Universe after the Big Bang. QGP can be created in laboratory by colliding heavy ions at relativistic energies. The properties of QGP can be investigated by determining the angular and momentum distribution of vector mesons produced in heavy-ion collisions. In a non-central heavy-ion collision, there is a large orbital angular momentum in the initial state. In the presence of large initial angular momentum, the vector mesons (spin = 1) can be polarized due to spin-orbit interaction or during the hadronization from polarized quarks. The polarization of vector mesons can be determined by measuring the angular distribution of the decay daughters of the vector meson with respect to the quantization axis in the rest frame of the vector meson. The quantization axis is considered along the direction perpendicular to either the production plane (defined by the momentum of vector meson and the beam axis), or perpendicular to the reaction plane (defined by the impact parameter and the beam axis) of the colliding system. The measured angular distribution can be used to estimate the elements of the spin density matrix, in particular the element ρ_{00} which is the probability of finding the vector meson in the spin 0 state out of the three possible spin states 1, 0 and -1. Deviation of ρ_{00} from the value 1/3 indicates the presence of spin alignment. We report the first evidence of significant spin alignment effect for vector mesons (K^{*0} and ϕ) in heavy-ion collisions. The measurements are carried out as a function of transverse momentum (p_{T}) and collision centrality with the ALICE detector using the particles produced at mid-rapidity ($|y| < 0.5$) in Pb–Pb collisions at a center-of-mass energy ($\sqrt{s_{\mathrm{NN}}}$) of 2.76 TeV. The initial angular momentum due to the extended size of the nuclei and the finite impact parameter in non-central heavy-ion collisions is missing in proton-proton collisions. Determination

of ρ_{00} for vector mesons produced in pp collisions and for spin zero K_S^0 produced in heavy-ion collisions provide a null test for spin alignment of vector mesons measured in the present work.

Short lifetimes of hadronic resonances compared to other stable hadrons are comparable to the time taken by the dense nuclear matter to evolve to its final state. This can be exploited to investigate the properties of the hadronic phase produced in heavy-ion collisions. K^{*0} yields are expected to be modified due to the interaction of their decay daughters within the hadronic medium. We present K^{*0} production in mid-rapidity for different collision centrality classes in Xe–Xe collisions at $\sqrt{s_{NN}} = 5.44$ TeV. The p_T spectra, p_T integrated yield, mean transverse momentum ($\langle p_T \rangle$), resonance to stable particle yield ratio (K^{*0}/K) and nuclear modification factor are presented. Recent measurements in high multiplicity pp collisions show striking similarities between small system and heavy-ion collisions. In order to find the possible presence of hadronic phase effect in small collisions system, K^{*0} production as a function of charged particle multiplicity in pp collisions at $\sqrt{s} = 13$ TeV are also presented. Measured K^{*0}/K yield ratio decreases with increasing charged particle multiplicity in both heavy-ion (Xe–Xe and Pb–Pb) and pp collisions. Since K^{*0} has a short lifetime, its decay products scatter in their passage through the hadronic medium changing their momenta and hence affecting the reconstruction of the parent particle, thereby decreasing the measured yield.

In addition to measuring the K^{*0} production in Xe–Xe collisions at $\sqrt{s_{NN}} = 5.44$ TeV, we have also compared the measured bulk properties for Xe–Xe collisions to those from A Multiphase Transport (AMPT) model. The shape of the Xe nucleus is non-spherical and is therefore generally referred to as a deformed nucleus. In this work, we have studied the effect of deformation of Xe nucleus on the bulk properties such as charged particle yield, mean transverse momentum, elliptic flow and triangular flow. The results of AMPT model calculations are also obtained for a spherical shape of the Xe nucleus to determine the effect of deformation. The measured charged particle multiplicity and $\langle p_T \rangle$ do not show any effect due to deformation; the elliptic flow is enhanced by ∼15% due to the deformation of the Xe nucleus in central Xe–Xe collisions.

Chapter 1

Introduction

The foundations of high energy nuclear and particle physics as a modern science were laid in the early 20th century. The year 1911 saw the discovery of the atomic nucleus in an experiment on scattering of alpha particles against a thin gold foil, thereby changing the then world view of the atom [1]. Subsequently the discovery of the proton [2] and the neutron [3] as constituents of the nucleus could explain many nuclear properties. Experimental investigations of the scattering of electrons from protons, often termed as Deep Inelastic Scattering (DIS), confirmed the composite nature of the proton and the existence of partons, which were later identified as the fractionally charged quarks [4, 5]. In 1979, experiments at the DESY laboratory in Germany provided the first direct proof of the existence of gluon [6] in e^+e^- annihilation.

As per current understanding of the subatomic structure, all matter is made up of fundamental particles called quarks and leptons. The Standard Model (SM) of particle physics is the accepted theoretical framework which describes the interactions between the quarks and leptons. The model describes these interactions as exchange of bosons, namely photons, W and Z bosons and gluons. Some of these bosons including W,Z and gluons were predicted by the SM, and later their existence was confirmed in experiments. The discovery of the Higgs boson has confirmed one of the major predictions of the Standard Model [7, 9, 10]. The coupling of the various particles with the Higgs boson provided mass to the particles. The experimental verification of the SM has been confirmed to high precision.

Each of the particles in the SM is characterized by a set of quantum numbers such

as spin, electric charge and more characteristic numbers such as baryon and lepton numbers, charm and others. The SM describes the interactions between the spin 1/2 fermions and their antiparticles with the spin 1 gauge bosons. The fermions are the six spin 1/2 leptons (electron, muon, tau, electron neutrino, muon neutrino and tau neutrino), six spin 1/2 quarks (up, down, charm, strange, top and bottom), with equal number of antiparticles. The model also has four spin 1 gauge bosons (gluon, photon, $W^{\pm}$ and Z, with eight states of gluons and two states of W boson) and the spin 0 Higgs boson. Elementary particles interact with each other through exchange of bosons, a mechanism described by the SM. The SM describes three different kinds of interactions: strong, electromagnetic and weak, each characterised by their strength and the different mediators namely gluons, photons and W and Z bosons respectively. A schematic representation of the particles in the SM is shown in Fig. 1.1.
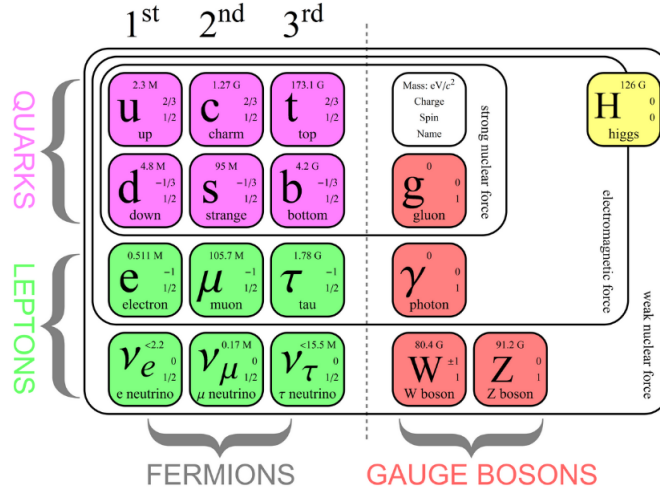
Figure 1.1: The schematic representation of standard model. This figure has been taken from [8].

The theoretical framework that describes the interactions are based on gauge invariance and are known as gauge theories. Amongst the three interactions mentioned above, the theoretical framework that describes the strong interactions is also

a gauge theory and is known as Quantum chromodynamics (QCD). In this thesis, we describe the study of properties of strongly interacting QCD matter created at high temperature and/or density in heavy-ion collisions. This chapter contains a brief introduction to the QCD and to Quark-Gluon Plasma (QGP), followed by an introduction to heavy-ion collisions and signatures of Quark-Gluon Plasma (QGP) formation in heavy-ion collisions. The chapter also includes a description of the importance of the production of resonance particles to understand the dynamics of the system. The physics motivations behind this thesis are briefly discussed in the last section.

1.1   Quantum chromodynamics

The QCD, a gauge field theory of the strong interaction, describes the interaction between quarks and gluons, which are characterised by a color quantum number. Colorless hadrons (mesons and baryons) are composed of quarks and gluons. The meson contains a quark and an anti-quark pair whereas the baryon consists of three valance quarks. The potential for the QCD interaction can be described as,

$$V_{\mathrm{QCD}}(r) \;=\; -\frac{4}{3}\,\frac{\alpha_{\mathrm{s}}}{r} \;+\; kr. \tag{1.1}$$

Where "α_{s}" is the running coupling constant of the QCD, k is a constant known as the color string tension and "r" denotes the distance between two interacting partons (quarks and gluons). The QCD coupling constant depends on momentum transfer Q^2 between partons as

$$\alpha_{\mathrm{s}}(Q^2) \;=\; \frac{12\pi}{(11N_{\mathrm{c}} \;-\; 2N_{\mathrm{f}})ln(Q^2/\lambda_{\mathrm{QCD}}^2)}. \tag{1.2}$$

Here N_{f} is the number of quark flavors, N_{c} is the number of color charges and λ_{QCD} is the non-perturbative QCD scale parameter. The perturbative QCD is applicable

for small values of α_s. Figure 1.2 shows α_s as a function of Q. Equation 1.2 ensures two novel properties of QCD: the quark confinement and the asymptotic freedom. According to Eq. 1.2, at small momentum transfer or large distance scales, the QCD
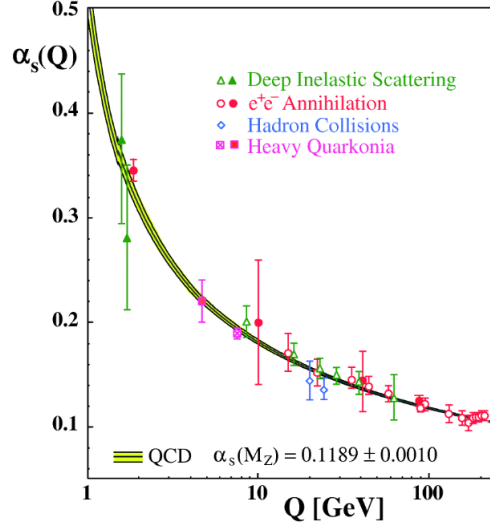
Figure 1.2: The QCD running coupling constant as a function of momentum transfer, compared with various experimental measurements, covering a wide range of momentum transfer. This figure has been taken from [16].

coupling constant between quarks and gluons becomes large. As a result quarks and gluons are no longer free, instead they are confined inside hadrons. This is known as the quark confinement [11]. On the other hand, at large momentum transfer ($Q^2 >> \lambda^2_{\mathrm{QCD}}$) or small distance scales, the QCD coupling constant becomes small resulting into a free state of quarks and gluons inside the QCD vacuum. This property of the QCD matter is known as the asymptotic freedom. Figure 1.2 shows a good agreement between the QCD based theoretical calculations and experimental results for the QCD coupling constant over a wide range of momentum transfer. In 2004, David Gross [12, 13], Frank Wilczek [12, 13], and David Politzer [14] were awarded the Nobel prize for their theoretical contributions towards the discovery of the asymptotic freedom.

1.2   QCD phase transition and quark-gluon plasma

The transition from a state of hadrons to a deconfined state of quarks and gluons is known as the deconfinement phase transition of the QCD. The asymptotic freedom suggests that at large momentum transfer, or small distance, force between quarks and gluons becomes weak. As a result, quarks and gluons behave as free particles. In 1974, T.D. Lee [15] proposed the possibility of creating a dense nuclear matter of asymptotically free quarks and gluons by having a very high nucleon density over a relatively large volume. Such a dense nuclear state of asymptotically free partons is known as the Quark-Gluon Plasma (QGP). Experimentally QGP is defined as, **"a (locally) thermally equilibrated state of matter in which quarks and gluons are deconfined from hadrons, so that color degrees of freedom become manifest over nuclear, rather than merely nucleonic volume [17]."** Lattice QCD (LQCD) calculations [18, 19, 20, 21] also predict the existence of QGP state at high temperature. Figure 1.3 shows normalized energy density as a function of temperature from LQCD calculations for different quark flavors. Normalized energy density shows a rapid increase at $T = T_c \geq 154 \pm 9$ MeV. This can be understood as an increase in number of degrees of freedom, hence a transition from the hadronic matter to a state of free quarks and gluons.

Figure 1.4 shows a schematic diagram for various phases of the QCD matter. Different phases of nuclear matter can be achieved by varying temperature (T) and baryon chemical potential (μ_B: the amount of energy required to add or remove a baryon from the system). Normal nuclear matter is represented by $T \simeq 0$ and $\mu_B \sim 1$ GeV. Deconfined state of quarks and gluons is expected to exist at high T and low μ_B whereas, at low T and low μ_B, quarks and gluons are confined inside the hadron. LQCD calculations predict a smooth crossover [23] from hadronic phase to
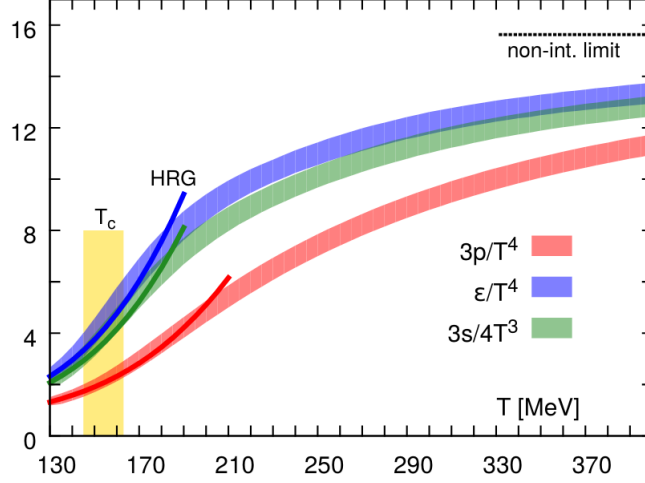
Figure 1.3: The normalized (normalized to quadratic power of temperature) energy density, pressure density and entropy density as a function of temperature from LQCD calculation with zero baryon chemical potential. Results are for (2+1) quark flavor. Solid lines at low temperature are correspond to hadron resonance gas (HRG) model calculations. The dashed line at high temperature shows the result for non-interacting quark gluon gas. This figure has been taken from [22].

QGP phase at high T and low μ_B whereas, at high μ_B, several model calculations have shown the transition to be a first-order phase transition [24]. At very high μ_B and low T, the matter may show a phenomena like the color superconductivity [25], which may occur when quarks may form cooper pairs.

1.3 Heavy-ion collisions

As per the current understanding, the QGP existed a few microseconds after the Big-Bang. The QGP can be formed at very high temperature and/or energy density as described above. Experimentally, the only known way to create such a deconfined state of the QCD matter in laboratory is by colliding heavy ions at relativistic energies. Heavy-ion collision experiments at the Relativistic Heavy Ion Collider (RHIC), the Large Hadron collider (LHC), and future experiments at the Facility for Anti-proton
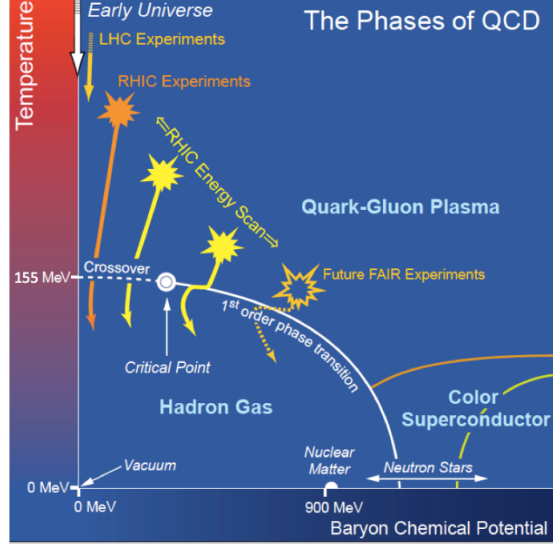
Figure 1.4: A schematic illustration of the QCD phase diagram [26].

and Ion Research (FAIR) and the Nuclotron based Ion Collider fAcility (NICA) are designed to search for the signature of the QGP phase and study its properties. The QCD phase diagram described in Sec. 1.2 can be explored experimentally by varying collision energy since both T and μ_{B} depend on the collision energy. In this section, a brief history of heavy-ion experimental facilities, space-time evolution of the QCD matter produced in heavy-ion collisions and an introduction to the kinematics of heavy-ion collisions are presented.

1.3.1 Experimental facilities for heavy-ion collisions

The first heavy-ion collision experiment with a collision energy of 1–2 A GeV/c was carried out in 1970 at the Bevalac, Lawrence Berkeley National Laboratory, USA. After the success at the Bevalac, other heavy-ion collision experiments started operating at various accelerator facilities across the globe. These are shown in Tab. 1.1.

Table 1.1: Heavy-ion collision experiments at various accelerator facilities

Year	Facility	Type	Collision energy ($\sqrt{s_{\text{NN}}}$)
1987–1994	AGS (Alternating Gradient Synchrotron) at BNL (Brookhaven National Laboratory)	Fixed target	< 14.2 GeV
1994–now	SPS (Super Proton Synchrotron) at CERN (European Organization for Nuclear Research)	Fixed target	5.0–17.3 GeV
2002–2014	SIS18 (Schwer Ionen Synchrotron) at GSI Helmholtz Centre for Heavy Ion Research	Fixed target	< 2.4 GeV
2000–now	RHIC (Relativistic Heavy Ion Collider) at BNL	Collider	7.7–200 GeV
2009–now	LHC (Large Hadron Collider) at CERN	Collider	2.76, 5.02 and 5.44 TeV

1.3.2 Space-time evolution

Hot and dense QCD matter produced in relativistic heavy-ion collisions evolves through different stages. Figure 1.5 illustrates a diagram for the space-time evolution of a heavy-ion collision, as per the present understanding. Two large nuclei moving at relativistic speeds are Lorentz contracted. The time t = 0 is defined as the time of their collision. During the collision, the overlapping region between the two nuclei is compressed and the large kinetic energy carried by the two incoming nuclei is deposited within a small volume of space in a short duration of time. If the energy density after the collision is sufficiently high, then a deconfined state of quarks and gluons is expected to be formed. Initially, the deconfined state so produced may not be in thermal equilibrium. After a short time of about 1 fm/c (known as the pre-equilibrium state), the matter reaches a state of local thermal equilibrium and is called the QGP. The evolution of the state is described by assuming the plasma to behave as a hydrodynamical fluid. The QGP matter starts expanding due to the pressure gradient and as a consequence it cools down with time. At T = T_c, the crit-
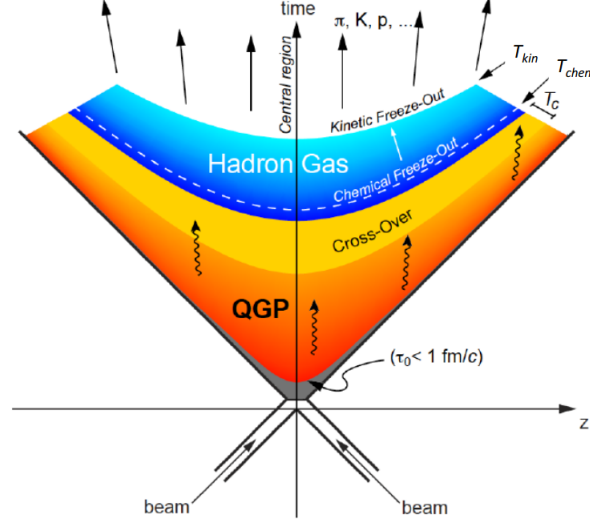
Figure 1.5: A schematic diagram for space-time evolution of heavy-ion collision [27].

ical temperature, quarks and gluons hadronize and a state of hadron gas is created. The hadron gas expands further and inelastic interactions between hadrons cease at $T = T_{ch}$, known as the chemical freeze-out temperature. At this point the chemical composition of the system is fixed; the relative abundance of different kinds of particles does not change after the system cools to T_{ch}. As it cools below T_{ch}, elastic interactions between hadrons continue till the kinetic freeze-out temperature T_{fo}. At the T_{fo}, the mean free path of hadrons becomes large compared to the dynamical size of the system. After T_{fo}, hadrons stream freely.

1.3.3 Kinematics in heavy-ion experiments

The coordinate system in the colliding beam experiment ALICE at the LHC is chosen such that the z-direction is parallel to the beam direction. The positive z direction is from the point of origin toward the V0A detector 2.2.4. The nominal interaction point where the two beams collide is at the center of the Time Projection Chamber (TPC) detector 2.2.2, and is denoted as origin (0,0,0) of the coordinate system. The

collisions are generally spread around the interaction point and the primary vertex of the collision is determined from data. For most analyses that use the reconstructed tracks, information of the primary vertex is a necessity.

1.3.3.1 Transverse momentum

The momentum of a produced particle can be decomposed into two parts. One is the longitudinal momentum along the beam direction (p_z) and the other is the transverse momentum (p_T) which is the projection of the particle momentum in the transverse plane (xy). The p_T is defined as

$$p_T = \sqrt{p_x^2 + p_y^2}, \qquad (1.3)$$

where p_x and p_y are the momentum components along the x and the y-axes. The p_T is invariant under Lorentz transformation.

1.3.3.2 Rapidity

In heavy-ion collisions, rapidity (y) is used as a measure for the relativistic velocity of a produced particle. In the relativistic limit, velocity is not an additive quantity. Advantage of using rapidity is that it is additive under Lorentz transformation. The rapidity of a particle is defined as,

$$y = \frac{1}{2} ln \frac{E + p_z}{E - p_z}, \qquad (1.4)$$

where E is its energy. The rapidity is equivalent to the velocity of the particle in the non-relativistic limit where the momentum (p) of a particle is comparable or smaller than its mass (m_0).

1.3.3.3 pseudorapidity

In the experiment, we generally measure the momentum of a particle. In order to know the energy of a particle, we need the mass of the particle and hence we need to

identify the particle. For situations where the identification of particle is difficult, a convenient approximation to the rapidity is the pseudorapidity (η), defined as,

$$\eta = \frac{1}{2}ln\frac{p + p_z}{p - p_z} = -ln[tan(\frac{\theta}{2})], \tag{1.5}$$

where θ is the angle between the momentum of the produced particle and the beam direction. The pseudorapidity can also be expressed in terms of the rapidity and the transverse mass ($m_T = \sqrt{m_0^2 + p_T^2}$) as [31],

$$\eta = \frac{1}{2}ln\frac{\sqrt{m_T^2 cosh^2 y - m^2} + m_T sinh y}{\sqrt{m_T^2 cosh^2 y - m^2} - m_T sinh y}. \tag{1.6}$$

1.3.3.4 Natural units

In experimental high energy physics, measurements are generally expressed in terms of natural units, where the Planck's constant ($\hbar$) and the speed of light (c) are considered as unity. In this system of units, mass, length and time are given in Tab. 1.2.

Table 1.2: Natural units for mass, length and time along with the conversion from SI units

Quantity	Natural units ($\hbar = c = 1$)	conversion
Mass	GeV	1 kg = 5.61×10^{26} GeV
Length	GeV^{-1}	1 m = 5.07×10^{15} GeV^{-1}
Time	GeV^{-1}	1 s = 1.52×10^{24} GeV^{-1}

1.3.4 Variables used often for particle production

In heavy-ion collision experiment, charged particle multiplicity and invariant yield are two basic variables which are often used to quantify the production of final state particles.

1.3.4.1 Multiplicity

In the heavy-ion experiment charged particle multiplicity refers to the total number of produced charged particles in the final state of an event (a single collision).

1.3.4.2 Invariant yield

One of the fundamental variables in heavy-ion collisions corresponds to the number of particles produced and is expressed as an yield which is invariant under Lorentz transformations. The invariant yield, integrated over azimuthal angle, is defined as

$$E\frac{\mathrm{d}^3 N}{\mathrm{d}p^3} \quad = \quad \frac{1}{2\pi}\frac{\mathrm{d}^2 N}{p_\mathrm{T}\mathrm{d}p_\mathrm{T}\mathrm{d}y}, \tag{1.7}$$

where N is the number of particles produced.

1.3.4.3 Centrality: Collision geometry of heavy-ion collision

Figure 1.6 shows a geometrical representation of a heavy-ion collision in the xz plane. Two nuclei collide with a non-zero impact parameter, defined as perpendicular distance between the centeres of the two nuclei. The impact parameter (b) varies from 0 fm for a head-on collision to about twice the radius of the nucleus for the most peripheral collisions. Events in heavy-ion collisions are classified into various centrality classes according to the value of the impact parameter. The central collisions correspond to small values of b (less than about 3 fm for heavy nuclei such as Au or Pb) and peripheral collisions correspond to large values of b value (larger than about 10 fm for Au or Pb nuclei). Since the impact parameter cannot be measured in the experiment, a Glauber model fits to the charged particle multiplicity distribution is used to classify the minimum bias sample of events in different centrality classes [32, 33]. Central collisions are characterized by events with large charged particle multiplicity, whereas peripheral collisions correspond to low-multiplicity events.
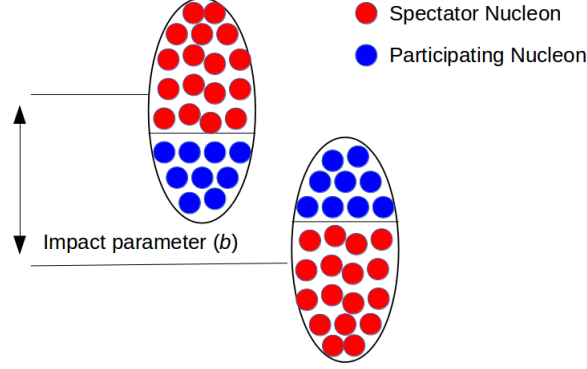
Figure 1.6: A schematic figure of heavy-ion collision.

1.4 Experimental signature of QGP formation

In this section, we discuss few experimental signatures which indicate creation of the QGP phase in heavy-ion collisions.

1.4.1 Jet quenching

In high energy heavy-ion collisions, high momentum partons are produced from the initial hard scattering. These high momentum partons fragment into a collimated shower of particles, known as the jet. When a parton propagates through the hot and dense QGP medium, it loses energy due to interactions with other partons inside the medium. In these interactions, parton looses its energy through collisions and medium-induced gluon radiation [28]. Energy loss of high-p_{T} partons leads to suppression of yiled of high-p_{T} hadrons. This phenomenon is known as jet quenching and was first proposed by Bjorken [29]. An experimental measure of jet quenching is the nuclear modification factor (R_{AA}), defined as

$$R_{\mathrm{AA}}(p_{\mathrm{T}}) \;=\; \frac{1}{<N_{\mathrm{coll}}>} \frac{\sigma_{\mathrm{inel}}^{\mathrm{AA}} \frac{\mathrm{d}^2 N^{\mathrm{AA}}}{\mathrm{d}p_{\mathrm{T}}\mathrm{d}y}}{\sigma_{\mathrm{inel}}^{\mathrm{pp}} \frac{\mathrm{d}^2 N^{\mathrm{pp}}}{\mathrm{d}p_{\mathrm{T}}\mathrm{d}y}}, \tag{1.8}$$

where $\langle N_{\text{coll}} \rangle$ is the mean number of binary (nucleon-nucleon) collisions in nucleus nucleus collisions and σ_{inel} is the inelastic cross section, respectively. Heavy-ion collisions are denoted by the superscript/subscript "AA", and proton-proton collisions are denoted by "pp". If AA collision is a simple superposition of pp collisions, then the R_{AA} is expected to be one and any deviation from the value one implies the presence of the effects caused by the medium. Figure 1.7 shows the nuclear modification factor
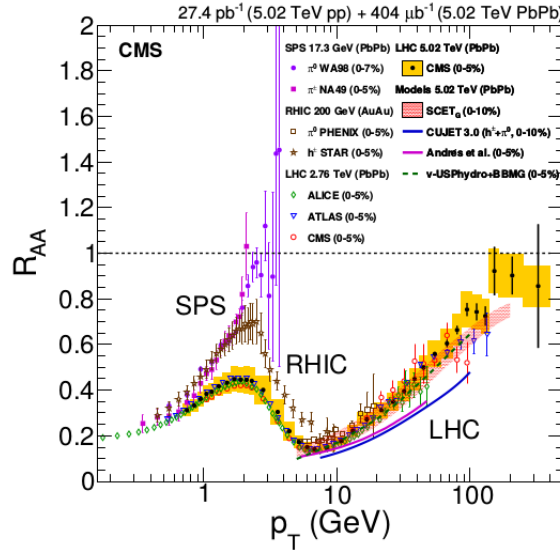
Figure 1.7: R_{AA} as a function of p_{T} for inclusive charged particles and π^0 in central heavy-ion collision at the SPS, RHIC, and LHC energies. This figure has been taken from [30].

of inclusive charged hadron and π^0 in central A–A collisions at $\sqrt{s_{\text{NN}}} = 0.017$, 0.2, 2.76 and 5.02 TeV. Jet quenching effect is observed both at RHIC and LHC energies. Di-jets are always produced back to back from hard scattering due to momentum conservation. It may happen that a jet is produced at the edge of the medium, known as the near-side jet and due to momentum conservation another jet is produced inside the medium, known as the away-side jet. The away-side jet propagates more through the medium, compared to the near-side jet. As a result, the away-side jet would be

more quenched compared to the near-side jet. Experimentally, this can be observed by looking at the azimuthal correlation between a high-p_{T} trigger particle and associated particles. Figure 1.8 shows the di-hadron correlation of trigger hadrons ($p_{\mathrm{T}} > 4$ GeV/c) with the associated hadrons ($p_{\mathrm{T}} > 2$ GeV/c) for pp, d–Au and Au–Au collisions. The away side peak (at around 3.14 radians) in Au–Au collisions is suppressed compared to the near side peak (at around 0 radians) as the away side jet is more quenched compared to the near side jet. However, in pp and d–Au collisions no such suppression of the away side jet is observed, suggesting the absence of jet quenching effect in small collision systems.
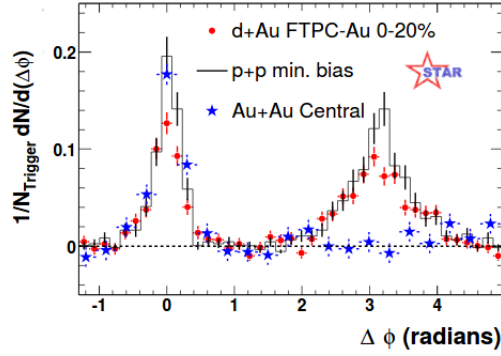
Figure 1.8: Di-hadron azimuthal correlation of high-p_{T} charged hadrons in pp, d–Au and Au–Au collisions [17].

1.4.2 J/ψ suppression

In a medium of electromagnetic plasma, the potential of a charged particle is screened due to the presence of surrounding charges. This effect is known as the Debye screening or shielding. This effect can also be extended in the QGP, which can be treated as a plasma of color charges. J/ψ is a bound state of c$\bar{\mathrm{c}}$ pair and produced at the initial stage of heavy-ion collisions. In the QCD vacuum, the potential between c$\bar{\mathrm{c}}$

pair can be expressed as,

$$V(r) \;=\; \frac{a}{r} \;+\; kr, \tag{1.9}$$

where a and k are constants representing the coupling and the string tension, respectively, and "r" corresponds to the distance between the c and the $\bar{\text{c}}$. In the QGP medium, the string tension k becomes zero as T approaches T_c and the only interaction remains at high temperature ($T > T_c$) is the long-range Coulomb like potential. The $\frac{a}{r}$ term of Eq. 1.9 gets modified in the presence of surrounding color charges inside the QGP medium. The modified potential between c$\bar{\text{c}}$ in the QGP medium can be expressed as,

$$V(r) \;=\; \frac{a}{r} e^{-r/\lambda_{\mathrm{D}}}, \tag{1.10}$$

where λ_{D} is the Debye length and depends on T. In the year 1986, Matsui and Satz [34] showed that the Debye length in the QGP medium would become smaller than the size of the J/ψ radius. As a result bound state of c$\bar{\text{c}}$ would not occur. This leads to a suppression of J/ψ production in the QGP medium. The suppression of J/ψ is considered as one of the signatures of QGP production in heavy-ion collisions and was first observed at the SPS [35] and subsequently confirmed by the RHIC [36, 37] and the LHC in later years.

Figure 1.9 shows the nuclear modification factor (R_{AA}) of J/ψ at mid-rapidity as a function of average number of participants ($\langle N_{\mathrm{part}} \rangle$) in Pb–Pb collisions at $\sqrt{s_{\mathrm{NN}}}$ = 2.76 TeV. Results are also compared with the lower energy measurements from PHENIX collaboration at the RHIC. Large $\langle N_{\mathrm{part}} \rangle$ values correspond to central collisions and small $\langle N_{\mathrm{part}} \rangle$ values correspond to peripheral collisions. The R_{AA} of J/ψ is significantly lower than 1 at both LHC and RHIC energies, indicating a clear suppression of J/ψ production. The R_{AA} of J/ψ in Pb–Pb collisions at $\sqrt{s_{\mathrm{NN}}}$ = 2.76
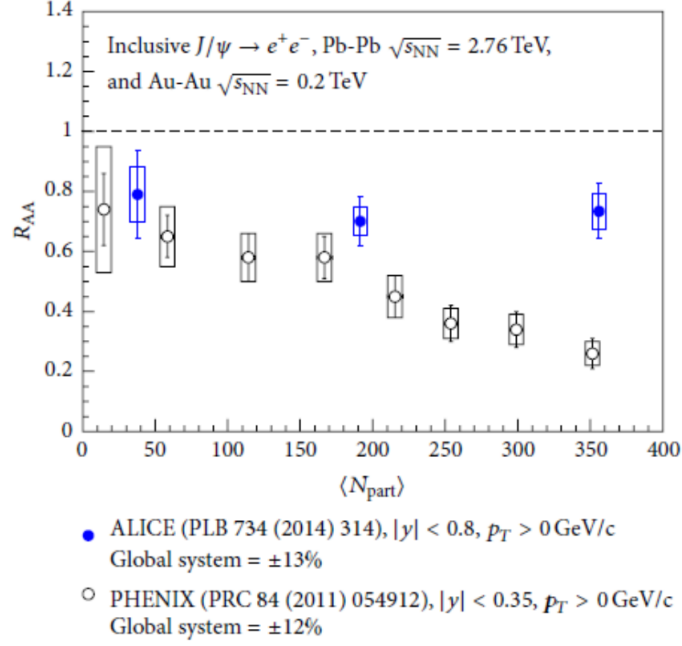
Figure 1.9: R_{AA} for J/ψ as a function of $\langle N_{\mathrm{part}} \rangle$ in Pb–Pb collisions at $\sqrt{s_{\mathrm{NN}}}$ =2.76 TeV, along with the measurements from PHENIX collaboration at $\sqrt{s_{\mathrm{NN}}} = 200$ GeV. This figure is taken from [38].

TeV does not show any significant centrality dependence. The meaured value of R_{AA} of J/ψ in Pb–Pb collisions at $\sqrt{s_{\mathrm{NN}}} = 2.76$ TeV is larger than the value measured in Au–Au collisions at $\sqrt{s_{\mathrm{NN}}} = 200$ GeV, implying a decreased suppression at LHC energy as compared to RHIC energy. These observations at LHC energy are compatible with the formation of QGP medium that suppress the production of J/ψ, followed by the recombination process in which a fraction of $c\bar{c}$ pairs coalesce and enhance the production of J/ψ at LHC energy.

1.4.3 Strangeness enhancement

Enhancement of the strange particle production in heavy-ion collisions is considered as one of the primary signatures of QGP production [39]. The net strangeness is zero both before and after the collsions in pp as well as in AA collisions. Strange quarks

are mainly produced from two types of process, gg $\rightarrow$ s$\bar{\text{s}}$ and q$\bar{\text{q}}$ $\rightarrow$ s$\bar{\text{s}}$. In the gluon rich QGP medium, production of s$\bar{\text{s}}$ pairs from the gluon–gluon collision dominates over the light quark annihilation. It leads to enhanced production of strange hadrons for the QGP medium compared to pp collisions, where light quark annihilation is the main channel of strangeness production. Observable for the strangeness enhancement is expressed as,

$$\epsilon \;=\; \frac{2}{<N_{\text{part}}>}\frac{\frac{dN^{\text{AA}}}{dy}}{\frac{dN^{\text{PP}}}{dy}}. \tag{1.11}$$

If the value of ϵ is larger than unity, then it can be attributed as an enhancement in the strangeness production. The numerator of Eq. 1.11 corresponds to the enhancement in strange quark production. However, the value of ϵ also depends on the yield of strange particle in pp collisions. In canonical suppression picture [40], production of strange particle in pp collisions can be suppressed and leads to $\epsilon > 1$. The ϕ $(s\bar{s})$ meson has no net strangeness. Its production in pp collisions should not be canonically suppressed, while the production of hadrons with open strangeness (e.g. K, Λ, Ξ and Ω) may be canonically suppressed. Therefore, the measurement of ϕ meson is essential to understand and quantify the extent of the strangeness enhancement.

Figure 1.10 shows the strangeness enhancement factor (ϵ) as a function of $\langle N_{\text{part}} \rangle$ in Au–Au and Cu–Cu collisions at $\sqrt{s_{\text{NN}}} = 200$ and 62.4 GeV for K, ϕ, Λ and Ξ. Enhancement for ϕ meson production in Au–Au and Cu–Cu collisions clearly indicates the enhanced production of strange quarks indicating the presence of a hot and dense partonic medium formed in heavy-ion collisions. This also suggests that the observed enhancements of open strange hadrons are likely to be due to the similar effects, not limited to canonical suppression of strangeness production in pp collisions.
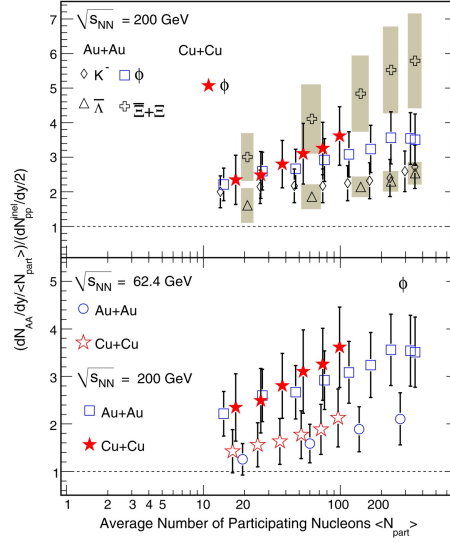
Figure 1.10: ϵ as a function of $\langle N_{\text{part}} \rangle$ for K (s = 1), ϕ (s = 0), Λ (s = 1) and Ξ (s = 2) in Au–Au and Cu–Cu collisions at $\sqrt{s_{\text{NN}}}$ = 200 and 62.4 GeV [41].

1.4.4 Elliptic flow

The elliptic flow of produced particles in heavy-ion collisions is one of the most important observables to understand the initial condition and collectivity of the produced medium. In non-central heavy-ion collisions, the overlapping region between the two colliding nuclei has an almond-like shape. This initial spatial anisotropy is transformed into the momentum anisotropy as interactions between constituents develop a pressure gradient. This momentum anisotropy leads to an azimuthal anisotropy of produced particles. The azimuthal distribution of produced particles can be expressed as,

$$\frac{d\text{N}}{d\phi} \propto 1 + 2v_1 cos(\phi - \psi) + 2v_2 cos(2(\phi - \psi)) + \ldots\ldots, \quad (1.12)$$

where ϕ is the azimuthal angle of produced particle and ψ is the reaction plane angle (angle made by the reaction plane with the x-axis). The reaction plane is defined by the impact parameter vector and the beam direction. The elliptic flow v_2 is the second Fourier coefficient of the azimuthal distribution and can be expressed as $v_2 = $

$\langle cos2(\phi - \psi)\rangle$, where $\langle\rangle$ corresponds to the average over all particles in all events. Figure 1.11 shows the v_2 of π, K and p in Pb–Pb collisions at $\sqrt{s_{NN}} = 2.76$ TeV [42]. Measurements are also compared with the results from STAR [43] and PHENIX [44] experiments at lower $\sqrt{s_{NN}}$. The measured values of v_2 at low p_T is observed to be comparable at LHC and RHIC energies. This observation is consistent with the predictions from the hydrodynamic models. The p_T integrated v_2 at the LHC is about 30% higher [45] compared to RHIC and is generally understood to be due to the larger radial flow at LHC energies compared to the RHIC energies. Hydrodynamical models [46] with QGP in the initial stage are able to explain the large values of the measured v_2.
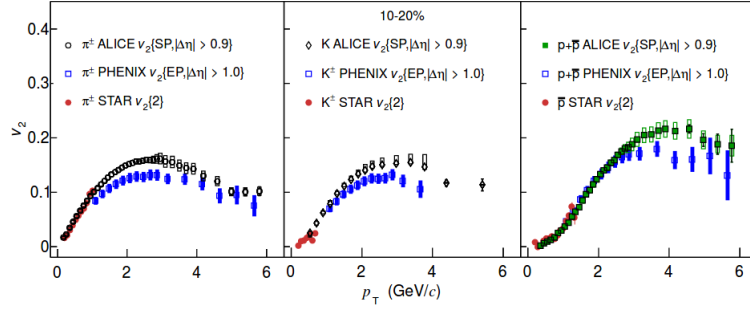
Figure 1.11: The comparison of the p_T differential v_2 for identified hadrons for 10–20% centrality class of Pb–Pb and Au–Au collisions at the LHC and RHIC energies.

1.5 Resonance production in heavy-ion collisions

Resonances are short-lived particles of lifetime of $O\left(10^{-23}\right)$ sec (or a few fm/c) and decay through strong interactions. The lifetime (τ) and width (Γ) of a resonance is related through $\Gamma\ \tau = \hbar$. Table 1.3 shows the lifetime of some experimentally measured resonances. The short lifetimes of the resonance particles are comparable to the time taken by the dense nuclear matter to evolve to its final state. This makes resonance particles a sensitive probe of the hadronic phase created in heavy-ion

Table 1.3: Experimentally measured resonances in high energy hadron collisions along with their lifetime.

Resonance	$\rho^0(770)$	$\Delta^0(1232)$	$f^0(980)$	$K^{*0}(892)$	$\Sigma^*(1385)$	$\Lambda^*(1520)$	$\phi(1020)$
Lifetime (fm/c)	1.1	1.6	2.6	4	5.5	12.6	45

collisions. Due to their short lifetimes, they often decay within the hadronic phase. The decay daughters of the resonances can elastically scatter with particles in the hadronic phase, thereby changing their momenta. The yields of resonances estimated through invariant mass spectra get affected by the change in momenta, leading to a suppression of the measured yield. This process is known as re-scattering effect.
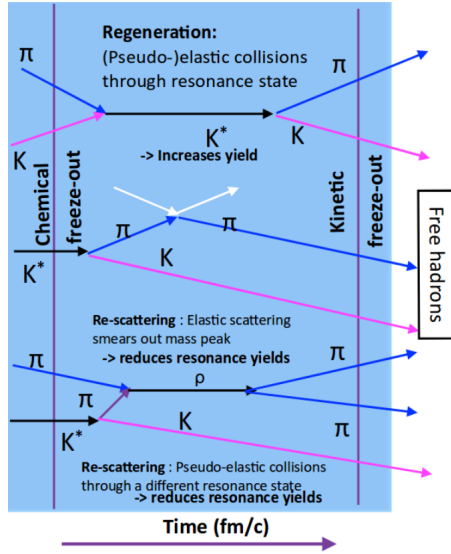
Figure 1.12: Schematic diagram for the re-scattering and regeneration effect.

Inside the hadronic phase resonances can also be regenerated via pseudo-elastic interaction (for example $K\pi \rightarrow K^{*0} \rightarrow \pi K$) and this effect, called regeneration, causes enhancement of reconstructed resonance yield. Figure 1.12 shows a schematic diagram for the re-scattering and regeneration effect. The combined effect of both re-scattering and regeneration contributes to the final measured resonance yield. Therefore the study of resonance production can shed light on the re-scattering and regeneration effects. These effects can be understood by looking at the resonance to stable particle ratios (K^{*0}/K ratio) and comparing it to the measurement in pp collisions. Results from the STAR [47, 48] and ALICE [49, 50, 51] experiments show a decrease in measured K^{*0}/K ratio in heavy-ion collisions, compared to pp collisions. This observation suggests the dominance of re-scattering effect over regeneration effect. Figure 1.13

shows K^{*0}/K ratio and ϕ/K ratio as a function of $\langle \mathrm{d}N_{\mathrm{ch}}/\mathrm{d}\eta\rangle^{1/3}$ in Pb–Pb collisions at $\sqrt{s_{\mathrm{NN}}} = 2.76$ TeV and in pp collisions at $\sqrt{s} = 7$ TeV. The results are also compared to the thermal model prediction. The values of K^{*0}/K ratio are observed to decrease with increasing centrality in Pb–Pb collisions. In central Pb–Pb collisions K^{*0}/K ratio is significantly lower compared to the measurement in pp collisions and the thermal model prediction. Suppression of K^{*0}/K ratio in Pb–Pb collisions can be understood as a re-scattering effect of K^{*0} decay daughter in the hadronic phase. On the other hand, ϕ/K ratio remains same in pp and Pb–Pb collisions which is expected due to the large lifetime of ϕ mesons ($\sim$46 fm) compared to K^{*0} mesons ($\sim$4 fm). Due to the large lifetime, ϕ mesons might decay predominantly outside the hadronic medium.
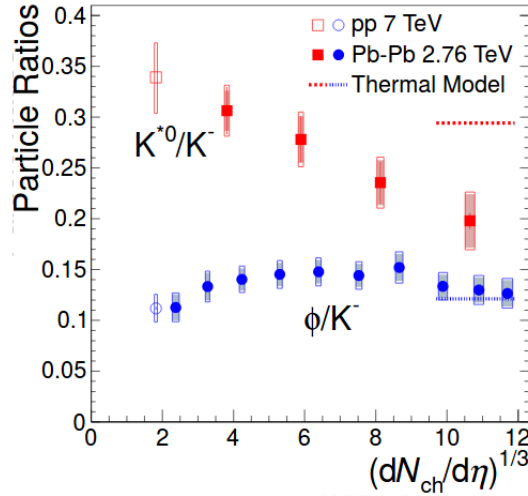
Figure 1.13: K^{*0}/K ratio and ϕ/K ratio as a function of $\langle \mathrm{d}N_{\mathrm{ch}}/\mathrm{d}\eta\rangle^{1/3}$ in pp and Pb–Pb collisions at $\sqrt{s_{\mathrm{NN}}} = 2.76$ TeV and $\sqrt{s} = 7$ TeV, respectively [49].

Due to different masses and quark content, hadronic resonances also carry a wealth of information on different aspects of hadron collisions, including the processes that determine the shapes of particle momentum spectra, strangeness production, and collective effects. Short-lived resonances with finite spin (eg. vector mesons: K^{*0},

ϕ) are sensitive to probe the initial stage of heavy-ion collisions. The system created in non-central relativistic nucleus-nucleus collisions possesses large orbital angular momentum. Due to spin-orbit coupling, particles produced in such a system could become globally polarized along the direction of the angular momentum of the system. Measurements of the spin alignment for the K^{*0} vector meson, produced in relativistic heavy-ion collisions, may provide new insights into the initial conditions and evolution of the dense matter produced in the collisions [52].

1.6 Thesis motivation

The time evolution of heavy-ion collision mainly has three stages: i) initial state, ii) QGP formation and hydrodynamic expansion of the medium and iii) final state: hadronization, hadronic phase, and freeze out. Vector mesons (spin = 1), especially short-lived resonances (K^{*0} and ϕ) produced in heavy-ion collisions can be used to probe each of the stages. In this thesis, angular and momentum distributions of vector mesons produced in proton-proton and heavy-ion collisions at LHC energies are used to probe the initial and final state properties of the medium formed in the heavy-ion collisions.

1.6.1 Spin alignment of vector mesons in heavy-ion and proton proton collisions

In non-central (impact parameter ∼3–10 fm) heavy-ion collisions, there exists a large orbital angular momentum about the centroid of the participant matter. In addition, a large magnetic field is also generated by the protons in the nuclear spectator which remains from the non-overlapping part of the nuclei in the collision. The spectators pass by the collision zone with relativistic speed. Both the angular momentum and the magnetic field are perpendicular to the reaction plane (the plane defined

by the beam axis and impact parameter direction), shown in left panel of Fig. 1.14. The angular momentum estimated in non-central collisions is $\sim 10^7 \, \hbar$ [53] and estimated magnetic field is $\sim 10^{14}$ T [54]. While the magnetic field is expected to be short-lived (a few fm/c), the angular momentum is conserved, and its effect could manifest throughout the evolution of the system formed in the collision. Right panel of Fig. 1.14 shows a model calculation [53] for the impact parameter dependence of the angular momentum in Au–Au collisions at $\sqrt{s_{\mathrm{NN}}} = 200$ GeV. In the presence of a
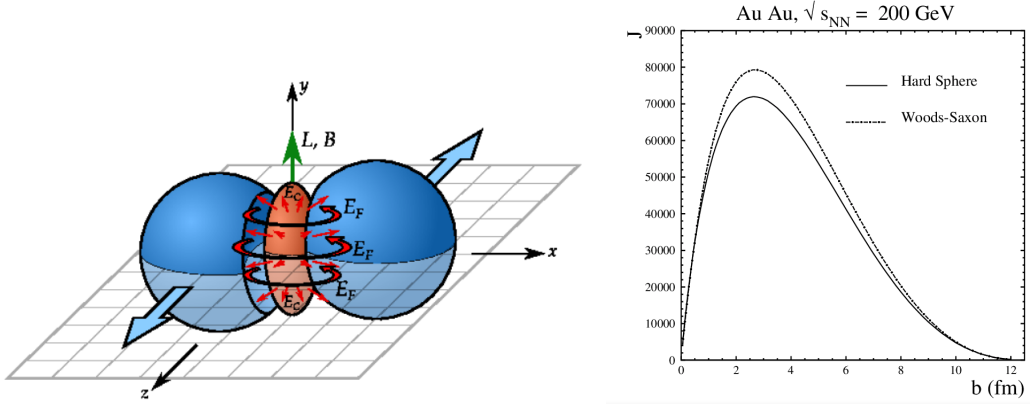
Figure 1.14: Left panel: An illustration of non-central heavy-ion collisions. The global angular momentum and the magnetic field are perpendicular to the reaction plane. Right panel: Angular momentum as a function impact parameter for two different nucleon distributions, hard sphere and Woods-Saxon. This calculation is for Au–Au collisions at $\sqrt{s_{\mathrm{NN}}} = 200$ GeV [53].

large initial angular momentum, the quarks and anti-quarks can be polarized due to the spin-orbital angular momentum interaction of QCD, which further leads to the net polarization of vector mesons (K^{*0} and ϕ) [57, 58, 59, 60, 61]. Spin alignment measurement of vector meson provides a unique opportunity to probe these initial conditions of heavy-ion collisions and can shed light on the presence of spin-orbital angular momentum interaction in heavy-ion collisions.

Spin alignment of vector mesons is quantified by the diagonal element ρ_{00} of a 3×3 hermitian spin density matrix [55]; ρ_{00} is the probability of finding a vector meson in

spin state 0 out of 3 possible spin states of -1, 0 and 1. In the absence of spin alignment all 3 states are equally probable which makes $\rho_{00} = 1/3$ and in the presence of spin alignment ρ_{00} will deviate from 1/3. The spin density matrix element ρ_{00} for vector mesons can be measured in the experiment by looking at the angular distribution of the decay daughter of vector meson with respect to a quantization axis. Quantization axis is chosen as the direction perpendicular to the reaction plane or is chosen as perpendicular to the production plane (defined by the momentum of the vector meson and beam axis). In the experiment, event plane [56] is used as a proxy for reaction plane (as impact parameter direction can not be directly measured) and the results are further corrected for the event plane resolution. The angular distribution is expressed as [55],

$$\frac{\mathrm{d}N}{\mathrm{d}cos\theta^*} \propto [1 - \rho_{00} + (3\rho_{00} - 1)cos^2\theta^*], \quad\quad (1.13)$$

where θ^* is the angle made by the decay daughters of vector meson with the quantization axis in the rest frame of vector meson. The derivation of Eq. 1.13 is given in Appendix A.1. In the absence of spin alignment, a uniform angular distribution is expected yielding $\rho_{00} = 1/3$. Whereas if the spins of the mesons are aligned, then the angular distribution of the decay products is non-uniform and the value of the spin density matrix element ρ_{00} deviates from 1/3.

In theory there are some specific predictions from quark model for vector meson spin alignment. In the the presence of a large angular momentum, the spin-orbit coupling of QCD could lead to a polarization of quarks followed by a net-polarization of vector mesons along the direction of the angular momentum [58, 59, 60, 61]. In quark polarization model, polarization of quarks is inversely proportional to square of its mass. Quark model predicts [58, 59, 60, 61] $\rho_{00} < 1/3$ if the vector meson is produced from the recombination of two polarized quarks, and $\rho_{00} > 1/3$ if the

hadronization of a polarized parton proceeds via the fragmentation process. In the recombination hadronization scenario, ρ_{00} is expected to have maximum deviation from $1/3$ at low-p_T, whereas at high-p_T the value of ρ_{00} reaches $1/3$. Quark model also predicts that the spin alignment effect is larger for K^{*0} than ϕ due to their respective constituent quark composition. The initial large magnetic field may also affect the ρ_{00} [61]. For electrically neutral vector mesons the magnetic field leads to $\rho_{00} > 1/3$, and for electrically charged vector mesons it leads to $\rho_{00} < 1/3$. In addition, recent theory development in Ref. [62] predicts $\rho_{00} > 1/3$ for the ϕ meson due to the coherent ϕ meson field. All these predictions are tested in this thesis by measuring the spin alignment of K^{*0} and ϕ vector mesons in Pb–Pb collisions at LHC energy.

In this thesis the first measurement of spin alignment of vector mesons (K^{*0} and ϕ) in heavy-ion collisions (Pb–Pb) at the LHC is reported. ρ_{00} measurements are carried out at mid-rapidity ($|y| < 0.5$) as a function of p_T and collision centrality with the ALICE detector in Pb–Pb collisions at $\sqrt{s_{NN}} = 2.76$ TeV. The ρ_{00} values are extracted from the angular distribution of the vector mesons decay daughter with respect to the direction perpendicular to the reaction plane and also with respect to direction perpendicular to the production plane. Measurements are also compared with the results from the following cases which correspond to the null hypothesis:

i) ρ_{00} for K^{*0} and ϕ in pp collisions where we do not expect the presence of a large initial angular momentum.

ii) ρ_{00} for spin 0 hadron K_S^0 in Pb–Pb collisions for which spin alignment is not expected.

iii) Measurements with respect to the random event plane, where the random plane is constructed by randomizing the event plane vector in azimuthal plane.

1.6.2 System size dependence of K^{*0} production with the ALICE detector at the LHC

The ALICE collaboration has recorded the data for small collision systems (pp, p–Pb) as well as for heavy-ion collision systems(Pb–Pb and Xe–Xe). This data sets allow us to investigate the system size dependence of particle production at LHC energies. Study of K^{*0} resonance production as a function of charged particle multiplicity can shed light on the system size dependence of hadronic re-scattering of K^{*0} decay daughter inside the hadronic phase.

1.6.2.1 K^{*0} production in Xe–Xe collisions

The ALICE experiment in the years 2017 and 2015 recorded ^{129}Xe–^{129}Xe and ^{208}Pb–^{208}Pb collisions at $\sqrt{s_{\mathrm{NN}}} = 5.44$ and 5.02 TeV, respectively. This unique data set allows investigating bulk properties of particle production such as particle yield, mean transverse momentum, azimuthal anisotropies etc. for very different systems at similar collision energies. In particular, the charged particle multiplicities in Xe–Xe collisions are comparable to those in high multiplicity proton-proton (pp) and proton-lead (p–Pb) collisions. Therefore, measurements in Xe–Xe collisions can be used to understand the evolution of the system from small (pp and p–Pb) to large (Pb–Pb) system. Study of K^{*0} production in Xe–Xe collisions and comparison with pp, p–Pb and Pb–Pb collisions allows us to understand the system size dependence of re-scattering and regeneration effect.

In this thesis, we have presented K^{*0} production at mid-rapidity for different collision centrality classes in Xe–Xe collisions at $\sqrt{s_{\mathrm{NN}}} = 5.44$ TeV. The p_{T} spectra, p_{T} integrated yield, mean transverse momentum ($\langle p_{\mathrm{T}} \rangle$) and ratio of yield of neutral K^{*0} to charged kaon are reported. In addition, we have also measured the R_{AA} for K^{*0} to understand initial partonic energy loss inside the dense medium created in the

collisions. Measurements of above observables for K^{*0} in Xe–Xe collisions are also compared with the corresponding results from pp, p–Pb and Pb-Pb collisions [51] to understand the system size dependence of particle production.

Further, we have also studied the bulk properties of produced particles in Xe–Xe collisions, using A Multiphase Transport Model (AMPT) model [63]. Xe is a non-spherical nucleus and referred to as a deformed shape nucleus [64]. In this work, the deformation of Xe nucleus in AMPT model is introduced by using a deformed Woods-Saxon profile [65] of nucleon distribution inside the nucleus. We have studied the effect of deformation of Xe nucleus on the bulk properties such as charged particle yield, elliptic flow and triangular flow. Results from AMPT model are also compared with the ALICE measurements [66, 67].

1.6.2.2 K^{*0} production in pp collisions

Recent measurements in high multiplicity pp collisions show striking similarities with results from heavy-ion collisions. Observation of near side long-range two particle correlation [68] (shown in 1.15), elliptic flow [69] (shown in the left panel of 1.16), enhancement in strangeness production [70] (shown in the right panel of 1.16) in high multiplicity pp collisions are similar to the corresponding observations in heavy-ion collisions. These observations have generated a huge interest among experimental and theoretical physicists to understand the underlying physics behind the high multiplicity pp collisions.

New physics phenomenon like multipartonic interactions (MPI) [71], color reconnection (CR) [72] are introduced to understand the results from high multiplicity pp collisions. These observations encourage us to look at the K^{*0} resonance production as a function of $dN_{ch}/d\eta$ in pp collisions in order to find the possible presence of the hadronic phase effect in small systems.
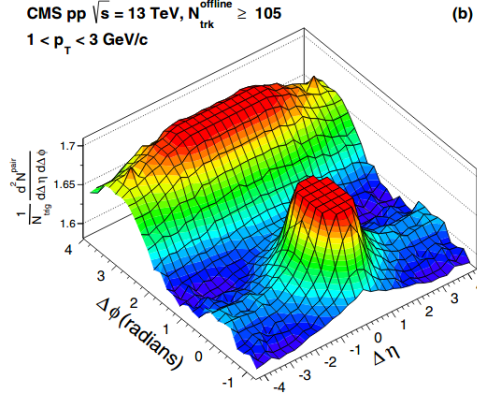
Figure 1.15: 2-D two-particle correlation functions in pp collisions at $\sqrt{s} = 7$ TeV for high multiplicity events over an intermediate p_T range ($1 < p_T < 3$ GeV/c). A clear and significant "ridge" like structure is observed at $\Delta\phi = 0$ and is extended upto $\Delta\eta = 4$. This figure is taken from [68].

In this thesis, we have studied K^{*0} production as a function of charged particle multiplicity in pp collisions at $\sqrt{s} = 13$ TeV, the highest center of mass energy currently reached at LHC. The p_T spectra, $< p_T >$ integrated yield, $< p_T >$ and K^{*0}/K yield ratio as a function of charged particle multiplicity as well as in minimum bias pp collisions are reported. Measurements from pp collisions at 13 TeV are compared with the results from pp collisions at 7 TeV [73] and p-Pb collisions at 5.02 TeV [74] to understand energy and system size dependence of particle production. The results from various Monte Carlo (MC) event generators such as, PYTHIA [75], EPOS [76] and DIPSY [77] are also compared to ALICE measurements.
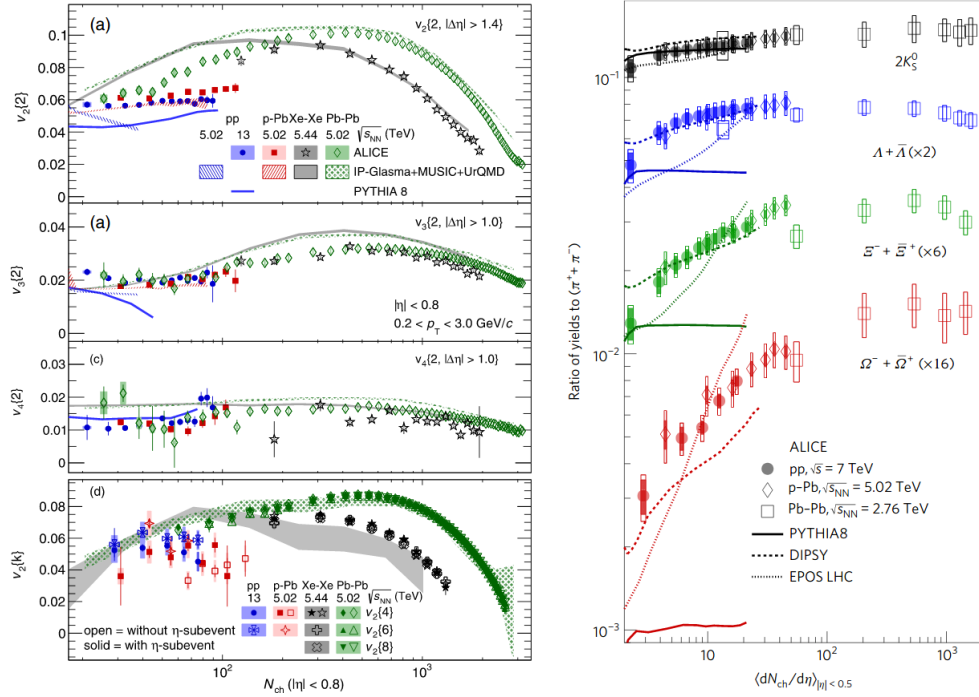
Figure 1.16: Left panel: Multiplicity dependence of the azimuthal anisotropies $v_n k$, obtained from multi-particle cumulants method with pseudorapidity separation 1.4 1.0 in pp, p–Pb, Xe–Xe and Pb–Pb collisions. Non zero v_2, v_3 and v_4 are observed in pp and p–Pb collisions. This figure is taken from [69]. Right panel: The p_T integrated yield ratio of strange hadrons to charged pion as a function of charged particle multiplicity in pp, p–Pb and Pb–Pb collisions. The ratio increases significantly with increasing charged particle multiplicity. The observed enhancement increases with strangeness content of hadrons. This figure is taken from [70].

References

[1] E. Rutherford, Phil. Mag. 21, 669 (1911).

[2] E. Rutherford, Phil. Mag. 37, 581 (1919).

[3] J. Chadwick, Nature 129, 312 (1932).

[4] E. D. Bloom et al., Phys. Rev. Lett. 23, 930 (1969).

[5] M. Breidenbach et al., Phys. Rev. Lett. 23, 935 (1969).

[6] R. Brandelik [TASSO Collaboration] et al., Phys. Lett. B 86, 243 (1979).

[7] Julia Woithe et al., Phys. Educ. 52, 034001 (2017).

[8] https://www.physik.uzh.ch/groups/serra/StandardModel.html

[9] G. Aad et al. [ATLAS collaboration], Phys. Lett. B 716, 1 (2012).

[10] W. Adam et al. [CMS collaboration], Phys. Lett. B 716, 30 (2012).

[11] H. Perkins, Introduction to High Energy Physics.

[12] D. J. Gross et al., Phys. Rev. Lett. 30, 1343 (1973).

[13] D. J. Gross et al.,Phys. Rev. D 8, 3633 (1973).

[14] H. D. Politzer, Phys. Rev. Lett. 30, 1346 (1973).

[15] T. D. Lee et al., Phys. ReV. D 9, 2291 (1974).

[16] S. Bethke, Prog. Part. Nucl. Phys. 58, 351 (2007).

[17] J. Adams et al. [STAR collaboration], Nucl.Phys.A 757,102 (2005).

[18] F. Karsch, Nucl. Phys. A 698, 199 (2002).

[19] F. Karsch, Prog. Theor. Phys. Suppl. 153, 106 (2004).

[20] R. C. Hwa et al., vol. 3, World Scientific (2004).

[21] R. V. Gavai et al., Phys. Rev. D 71, 114014 (2005).

[22] H. Ding et al., Int. J. Mod. Phys. E 24, 1530007 (2015).

[23] Y. Aoki et al., Nature 443, 675 (2006).

[24] S. Ejiri, Phys. Rev. D 78, 074507 (2008).

[25] K. Rajagopal, arXiv:0011333[hep-ph].

[26] U. Heinz et al., arXiv:1501.06477 [nucl-th].

[27] J. D. Bjorken, Phys. Rev. D 27, 140 (1983).

[28] D. H. Perkins, Introduction to High Energy Physics [Cambridge University Pres], 2000.

[29] J. D. Bjorken, FERMILAB-PUB-82-59-THY (1982).

[30] R. Pasechnik et al., Universe 3, 7 (2017).

[31] C-Y. Wong, Introduction to High-Energy Heavy-Ion Collisions [World Scientific Publishing Co. Pte. Ltd.], 1994.

[32] B. Abelev et al. [STAR Collaboration], Phys. Rev. C 81, 024911 (2010).

[33] B. Abelev et al. [ALICE Collaboration], Phys. Rev. C 88, 044909 (2013).

[34] T. Matsui et al., Phys. Lett. B 178, 416 (1986).

[35] R. Arnaldi et al. [NA60 Collaboration], Nucl. Phys. A 783, 261 (2007).

[36] A. Adare et al. [PHENIX Collaboration], Phys. Rev. Lett. 98, 232301 (2007).

[37] A. Adare et al. [PHENIX Collaboration], Phys. Rev. C 84, 054912 (2011).

[38] A. Kurepin et al., Eur. Phys. J. A 52, 260 (2016).

[39] P. Koch et al., Phys. Rep. 142, 167 (1986).

[40] K. Redlich et al., Eur. Phys. J. C 24, 589 (2002).

[41] B. I. Abelev et al. [STAR Collaboration], Phys. Lett. B 673, 183 (2009).

[42] B. Abelev et al. [ALICE Collaboration], JHEP 06, 190 (2015).

[43] J. Adams et al. [STAR Collaboration], Phys. Rev. C 72, 014904 (2005).

[44] S. S. Adler et al. [PHENIX Collaboration], Phys. Rev. Lett. 91, 182301 (2003).

[45] K. Aamodt et al. [ALICE Collaboration], Phys. Rev. Lett. 105, 252302 (2010).

[46] B. Schenke et al., Phys. Lett.B 702, 59 (2011).

[47] B. I. Abelev et al.[STAR Collaboration], Phys. Rev. C 78, 044906 (2008).

[48] M. M. Aggarwal et al.[STAR Collaboration], Phys. Rev. C 84, 034909 (2011).

[49] B. Abelev et al. [ALICE Collaboration], Phys. Rev. C 91, 024609 (2015).

[50] J. Adam et al. [ALICE Collaboration], Phys. Rev. C 95, 064606 (2017).

[51] S. Acharya et al. [ALICE Collaboration], Phys. Lett. B 802, 135225 (2020).

[52] S. Acharya et al. [ALICE Collaboration], Phys. Rev. Lett. 125, 012301 (2020).

[53] F. Becattini et al., Phys. Rev. C 77, 024906 (2008).

[54] D. E. Kharzeev et al., Nucl. Phys. A 803, 227 (2008).

[55] K. Schilling et al., Nucl. Phys. B 15, 397 (1970).

[56] A. M. Poskanzer et al., Phys. Rev. C 58, 1671 (1998).

[57] S. A. Voloshin, arXiv:0410089[nucl-th].

[58] Z.-T. Liang et al., Phys. Rev. Lett. 94, 102301 (2005).

[59] Z.-T. Liang et al., Phys. Lett. B 629, 20 (2005).

[60] Z.-T. Liang, J. Phys. G 34, S323 (2007).

[61] Y. -G. Yang et al., Phys. Rev. C 97, 034917 (2018).

[62] X. -L. Sheng et al., arXiv:1910.13684[nucl-th].

[63] Z. W. Lin et al., Phys. Rev. C 72, 064901 (2005).

[64] P. M'aller et al., At. Data Nucl. Data, Tabl. 1, 109 (2006).

[65] K. Hagino et al., Phys. Rev. C 74, 017310 (2006).

[66] S. Acharya et al. [ALICE Collaboration], Phys. Lett. B 784, 82 (2018).

[67] S. Acharya et al. [ALICE Collaboration], Phys. Lett. B 788, 166 (2019).

[68] V. Khachatryan et al. [CMS Collaboration], Phys. Rev. Lett. 116, 172302 (2016).

[69] S. Acharya et al. [ALICE Collaboration], Phys. Rev. Lett. 123, 142301 (2019).

[70] J. Adam et al. [ALICE Collaboration], Nat. Phys. 13, 535 (2017).

[71] T. Sjöstrand et al., Phys. Rev. D 36, 2019 (1987).

[72] T. Sjöstrand et al., JHEP 0605, 026 (2006).

[73] S. Acharya et al.ALICE Collaboration], Phys. Rev. C 99, 024906 (2019).

[74] J. Adam et al. [ALICE Collaboration], Eur. Phys. J. C 76, 245 (2016).

[75] P. Z. Skands et al., Eur. Phys. J. C 74, 3024 (2014).

[76] K.Werner et al., Phys. Rev. C 89, 064903 (2014).

[77] C. Bierlichet al., J. High Energy Phys. 3, 148 (2015).

[78] M. E. Rose, Elementary theory of angular momentum [John Wiley & Sons, Inc.], 1957.

Chapter 2

A Large Ion Collider Experiment (AL-ICE)

The "Large Hadron Collider (LHC)", a scientific wonder of 21st century was built at CERN, Geneva to explore the nature of the universe. Presently, the LHC accelerator is the largest and most powerful particle accelerator in the world. A Large Ion Collider Experiment (ALICE) is one of the major experiment at LHC. ALICE is a dedicated heavy-ion collisions detector, taking data of hadronic and nuclear collisions from 2009. In this chapter, an overview of the LHC and its major experiments are discussed. This followed by a brief description of the ALICE sub-detectors, and online and offline computing system.

2.1   The Large Hadron Collider (LHC) at CERN

The LHC accelerator is situated in Switzerland and France border in a 26.7 km long underground tunnel at a depth about 50–150 m. The LHC is made of two rings of superconducting magnets with a number of accelerating structures to boost the energy of the particles along the way. Figure 2.1 shows CERN accelerator complex which consists of different accelerator systems such as the Linear Accelerator 2 (LINAC 2), the Proton Synchrotron Booster (PSB), the Proton Synchrotron (PS), the Super Proton Synchrotron (SPS) etc. Each of this accelerator systems sequentially boost the energy of a beam of particles before being injected into the main LHC ring. The accelerating process for protons starts from a simple bottle of hydrogen gas as a proton source. Hydrogen gas break down into its constituent protons and electrons
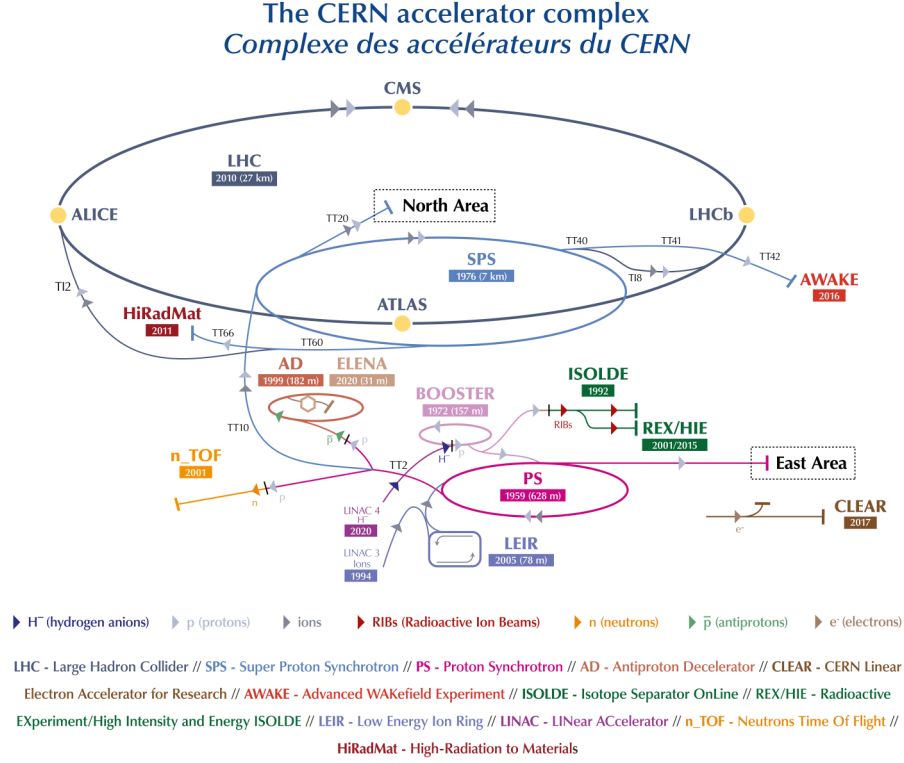
Figure 2.1: CERN accelerator complex and the locations of the four major LHC experiments: ALICE, ATLAS, CMS and LHCb along the LHC ring [1]

by applying an electrical field. Protons are then accelerated up to 100 kV and sent to a Radio Frequency Quadrupole (QRF) that speeds up and focuses the particle beam. QRF accelerates the proton beam upto 750 keV. After this proton beam is sent to the linear accelerator (LINAC 2) which accelerate protons up to the energy of 50 MeV. In next stage protons are subsequently passed to the PSB, the PS, and the SPS where the energy of proton is accelerated up to 450 GeV. After that protons are injected in two directions into the main LHC ring where the energy is ramped up to the desired energy of collisions. On the other hand, the lead (Pb) ion beam starts from a vapour of lead atoms obtained by heating a 2 cm long, 500 mg pure lead sample to 500°C. An electric field is used to remove few electrons from Pb atom

and the newly created Pb ions are first accelerated by a LINAC 3 up to the energy of 4.2 MeV per nucleon. In LINAC 3 further electrons are removed from the Pb ions. In next step, the ions are accelerated to 72 MeV per nucleon in the Low Energy Ion Ring (LIER). These first three stages are unique for heavy ions. After that Pb ions are accelerated subsequently in the PS and SPS. In the PS, energy of Pb ions are boosted up to 5.9 GeV per nucleon and the remaining electrons from the Pb ion are stripped away. In the SPS, the Pb beam is accelerated upto 177 GeV per nucleon and finally injected in two directions into the LHC.
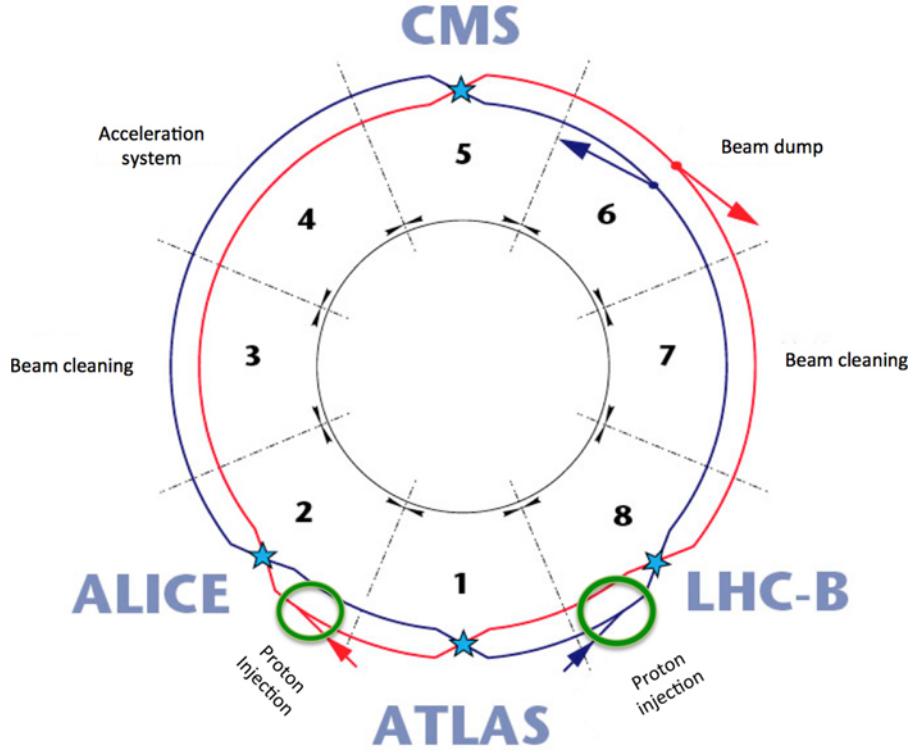
Figure 2.2: Schematic layout of the LHC [2].

Particles are injected into the LHC ring from the point 2 and point 8 in two opposite directions. The Radio Frequency (RF) system accelerates the beam at the point 4. Two beams cross each other at four points 1, 2, 5 and 8, where the four main experiments A Toroidal LHC ApparatuS (ATLAS), ALICE, Compact Muon Solenoid

(CMS) and Large Hadron Collider beauty (LHCb) are located. The beam dumps at point 6, and the collimation system cleans the beam at point 3 and 7 by removing the beam bunches which have large spatial spread from the bunch center. Figure 2.2 shows a schematic layout of the LHC operation points. With the present accelerator facilities at LHC, the maximum center of mass energy that can be reached in the LHC is 14 TeV and 5.5 TeV per nucleon for proton proton collisions and heavy-ion collisions, respectively.

2.2   The ALICE experiment at LHC

The ALICE detector at the LHC is dedicated to the heavy-ion collisions experiment to understand the formation and evolution of the nuclear matter, formed in heavy-ion collisions. The ALICE detector is 26 m long, 16 m wide, 16 m high and has weight of 10,000 tones, situated about 56 m under the ground in the village of St Genis-Pouilly in Switzerland-France border. In ALICE, the coordinate system is chosen as right handed Cartesian coordinate system where z axis is along the beam direction and origin (0, 0, 0) is at the center of the TPC detector. The muon arm side of the ALICE detector system is chosen as negative z axis. The x and y axes are orthogonal to z axis where the x axis is pointing towards the LHC center and y axis is vertically upward. The ALICE detector systems are categorized into three groups: central-barrel detectors, forward detectors, and the muon spectrometer. The ALICE detector consists of 19 detector subsystems as shown in Fig. 2.3. The positions, η and ϕ acceptances, and purposes of ALICE detector subsystems are summarized in Tab. 2.1.

In this thesis ITS, TPC, TOF and V0 detectors are extensively used for the analysis of ALICE data. These detectors are briefly discussed in the following sub-

Table 2.1: Summary of the positions, η and ϕ acceptances and purposes of ALICE detector subsystems [10].

Detector	Position (in cm)	η acceptance	ϕ acceptance (in °)	Purpose
Central barrel detector:				
SPD	$r = 3.9$	$|\eta| < 2.0$	$0° < \phi < 360°$	tracking, vertex
	$r = 7.6$	$|\eta| < 1.4$	$0° < \phi < 360°$	tracking, vertex
SDD	$r = 15.0$	$|\eta| < 0.9$	$0° < \phi < 360°$	tracking, particle identification
	$r = 23.9$	$|\eta| < 0.9$	$0° < \phi < 360°$	tracking, particle identification
SSD	$r = 38.0$	$|\eta| < 1.0$	$0° < \phi < 360°$	tracking, particle identification
	$r = 43.0$	$|\eta| < 1.0$	$0° < \phi < 360°$	tracking, particle identification
TPC	$85 < r < 247$	$|\eta| < 0.9$	$0° < \phi < 360°$	tracking, particle identification
TRD	$290 < r < 368$	$|\eta| < 0.8$	$0° < \phi < 360°$	tracking, $e^{\pm}$ identification
TOF	$370 < r < 399$	$|\eta| < 0.9$	$0° < \phi < 360°$	particle identification
PHOS	$460 < r < 478$	$|\eta| < 0.12$	$220° < \phi < 320°$	photons
EMCAL	$430 < r < 455$	$|\eta| < 0.7$	$80° < \phi < 187°$	photons
HMPID	$r = 490$	$|\eta| < 0.6$	$1° < \phi < 59°$	particle identification
ACORDE	$r = 850$	$|\eta| < 1.3$	$30° < \phi < 150°$	cosmics
Forward detector:				
PMD	$z = 367$	$2.3 < \eta < 3.9$	$0° < \phi < 360°$	photons
FMD	$z = 320$	$3.6 < \eta < 5.0$	$0° < \phi < 360°$	charged particles
	$z = 80$	$1.7 < \eta < 3.7$	$0° < \phi < 360°$	charged particles
	$z = -70$	$-3.4 < \eta < -1.7$	$0° < \phi < 360°$	charged particles
V0	$z = 329$	$2.8 < \eta < 5.1$	$0° < \phi < 360°$	charged particles
	$z = -88$	$-3.7 < \eta < -1.7$	$0° < \phi < 360°$	charged particles
T0	$z = 370$	$4.6 < \eta < 4.9$	$0° < \phi < 360°$	time, vertex
	$z = -70$	$-3.3 < \eta < -3.0$	$0° < \phi < 360°$	time, vertex
ZDC	$z = \pm 11300$	$|\eta| > 8.8$	$0° < \phi < 360°$	forward neutrons
ZDC	$z = \pm 11300$	$6.5 < |\eta| < 7.5$	$|\phi| < 10°$	forward protons
ZDC	$z = \pm 730$	$4.8 < \eta < 5.7$	$|2\phi| < 32°$	photons
Muon spectrometer:				
MCH	$-1420 < z < -540$	$-4.0 < \eta < -2.5$	$0° < \phi < 360°$	muon tracking
MTR	$-1710 < z < -1610$	$-4.0 < \eta < -2.5$	$0° < \phi < 360°$	muon trigger

66
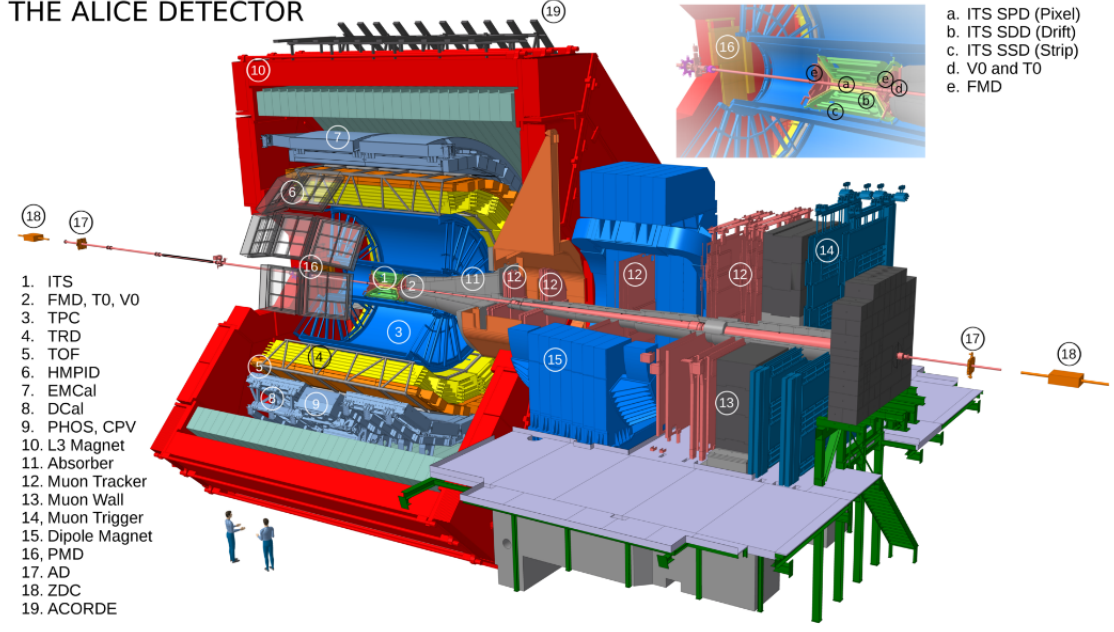
Figure 2.3: Schematic diagram for the ALICE detector systems [3].

sections.

2.2.1 The Inner Tracking System (ITS)

The Inner Tracking System (ITS) is a six layer of cylindrical silicon detector located at radii between 3.9 and 43 cm and surrounds the beam pipe which is a 800 μm thick beryllium cylinder with 2.9 cm radius. A geometrical view of silicon detector has been shown in Fig. 2.4. The η and ϕ acceptance for different layers of the ITS detector is shown in Tab. 2.1. The main purposes of ITS are the determination of the primary vertex with a resolution better than 100 μm and to reconstruct secondary vertices, particle identification and tracking upto a very low-momentum (< 200 MeV/c). AL-ICE ITS allows to reconstruct the tracks traversing the dead TPC region or very low p_{T} tracks that do not reach the TPC. Therefore the momentum and angular resolution of tracks reconstructed by TPC can be improved by ITS.

67
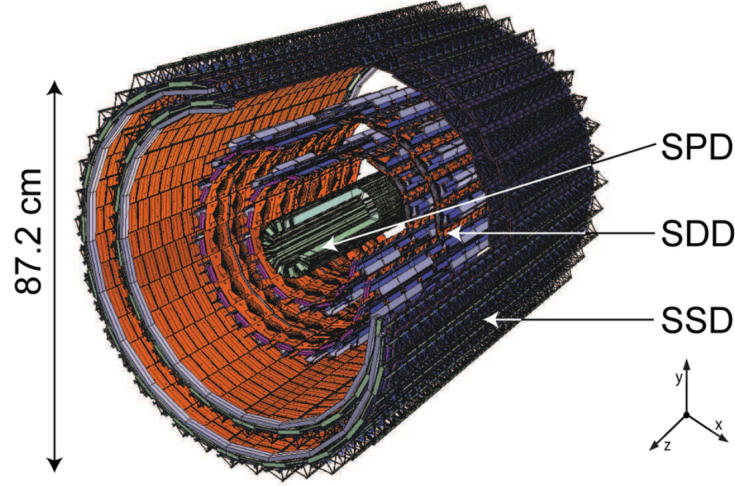
Figure 2.4: Schematic diagram for the ALICE ITS [3].

The innermost 2 layers of ITS are the Silicon Pixel Detectors (SPD). It has a full azimuthal coverage and pseudo-rapidity acceptance of $|\eta| < 2.0$. SPD is mainly used for the determination of primary and secondary vertices and can operate at very high track densities about 50 tracks/cm^3 and in a high radiation environment. The main component of SPD modules are the hybrid silicon pixels in the form of a two dimensional matrix of reverse-biased silicon based p-n junction diodes. For large acceptance coverage and high granularity, there are almost 9.8 million pixel cells. Each cell on the detector matrix is connected to a cell of the same size on a front-end CMOS chip through a conductive solder ball. CMOS chip contains most of the readout electronics. Each of the pixel chips provide a Fast-OR digital pulse when it detects a particle signal above the threshold. This makes SPD capable of generating a prompt trigger. Therefore, SPD is also used as level-2 (L2) trigger [5].

The 3$^{\text{rd}}$ and 4$^{\text{th}}$ layers of the ITS are Silicon Drift Detector (SDD). SDD modules are assembled on linear structures known as ladders. SDD is divided into two drift regions where the electrons are moved in two opposite directions under a drift field

of 500 V/cm. Charges are collected in each drift region with anodes which are kept independent of the drift voltage by using a second bias supply. The z-position of a track is reconstructed from the charge collected along anode, whereas the x and y coordinates of a track are reconstructed from the drift time of the charges. The signal measured by the SDD is proportional to the energy loss by the particles inside the detectors which is useful for the particle identification in low p_T region.

Silicon Strip Detectors (SSD) are the two outermost ITS. Each of the SSD modules is composed of double sided strip sensor. The innermost SSD layer consists of 34 ladders, each of them having 22 modules along the beam direction whereas other SSD layers are made up of 38 ladders, each of them having 25 modules. Each SSD module is composed of a 1536-strip double-sided silicon sensor. It also provides the measurement of the track position and particle identification via energy loss measurements. SSD and SDD have analogous readouts which has a large dynamic range that allows the particle identification via energy loss for low momentum particles down to $p_T = 100$ MeV/c. The average energy loss of charged particles inside ITS as a function of transverse momentum is shown in Fig. 2.5.

2.2.2 The Time Projection Chamber (TPC)

Main tracking detector of the ALICE experiment is the Time Projection Chamber (TPC) detector. The TPC is optimized to measure the momentum of charged particles with very good position resolution of tracks (800–1100 μm in the transverse plane and 1100–1250 μm along the z-direction). Figure 2.6 shows a schematic layout of the ALICE TPC. The TPC has a full azimuthal angle coverage and it covers pseudo-rapidity range of $|\eta| < 0.9$. The TPC is a cylindrical shaped gas detector having an inner and outer radius of 80 cm and 250 cm, respectively. It covers a length of 500 cm along the beam axis and occupying an active volume of 92 m^3. The TPC is filled
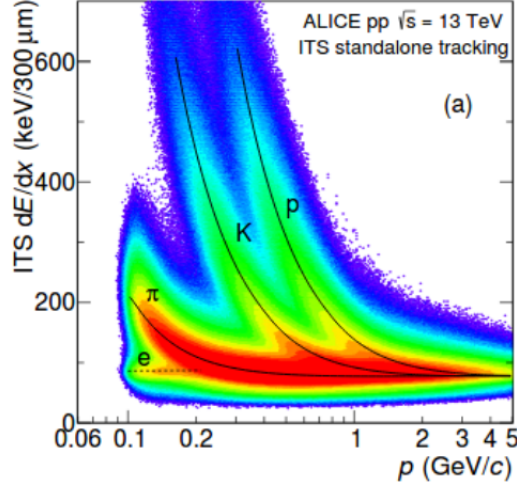
Figure 2.5: Average energy loss as a function of transverse momentum in pp collisions at $\sqrt{s} = 13$ TeV [6]. The lines are a parametrization of the detector response based on a hybrid parametrization with a polynomial function at low p/m and a Bethe-Bloch formula.

with a mixture of Ne and CO_2 gas with the proportion of 90:10.

The TPC drift volume is divided into two segments by a cylindrical conducting electrode which is placed at the center of the TPC. The central electrode maintains a uniform axial electrostatic field of 400 V/cm, parallel to the beam line directed towards the membrane. Figure 2.7 shows the working principle of the TPC. When a charged particle passes through the active gas volume, it excites and ionizes gas atoms along the trajectory of the track. As a result, the charged particle loses an amount of energy per unit track length (dE/dx) depending on the mass of the particle. Ionized free electrons are drifted towards the end plates of the cylinder due to the electric field and the ions are drifted towards the high voltage cathode placed at the center of the TPC. The drifting of electrons are not affected by the external magnetic field as it is oriented parallel to the electric field. Drifted electrons are amplified by an avalanche process at the end of drift path around the anode wires. The x, y positions of the tracks are reconstructed from the hits on the anode pads at the end plates. The
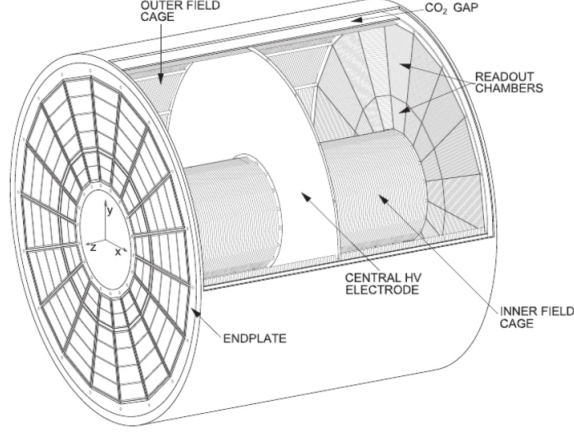
Figure 2.6: A schematic layout for the ALICE TPC [7].

z-coordinates of the tracks are reconstructed based on the information of drift velocity and arrival time of the drift electrons at the anode plane. Multi-Wire Proportional Chambers (MWPCs) at the end plates are used for the readout of the signal. There are two end plates in the TPC and each of the end plate has 36 readout chambers which are arranged in 18 sectors. Each of the readout sectors consists of an an Outer Readout Chamber (OROC) and an Inner Readout Chamber (IROC). The tracks are reconstructed from the 3D space points and the p_{T} is calculated from the curvature of the track.

The TPC is one of the major detector in ALICE used for the particle identification. The particle is identified inside the TPC from the simultaneous measurements of charge, momentum and specific energy loss of each track that traverse through the TPC volume. Average energy loss inside the TPC is parametrized by a modified Bethe-Bloch function, originally proposed by ALEPH collaboration [9].

$$f(\beta\gamma) \; = \; \frac{p_1}{\beta^{p_4}} \; \left(p_2 \; - \; \beta^{p_4} \; - \; ln(p_3 \; + \; \frac{1}{(\beta\gamma)^{p_5}}) \right). \qquad (2.1)$$

Here β and γ are the velocity and lorentz factor for the track, respectively. The parameters p_1 to p_5 are extracted from the fit during each data taking period. The

71
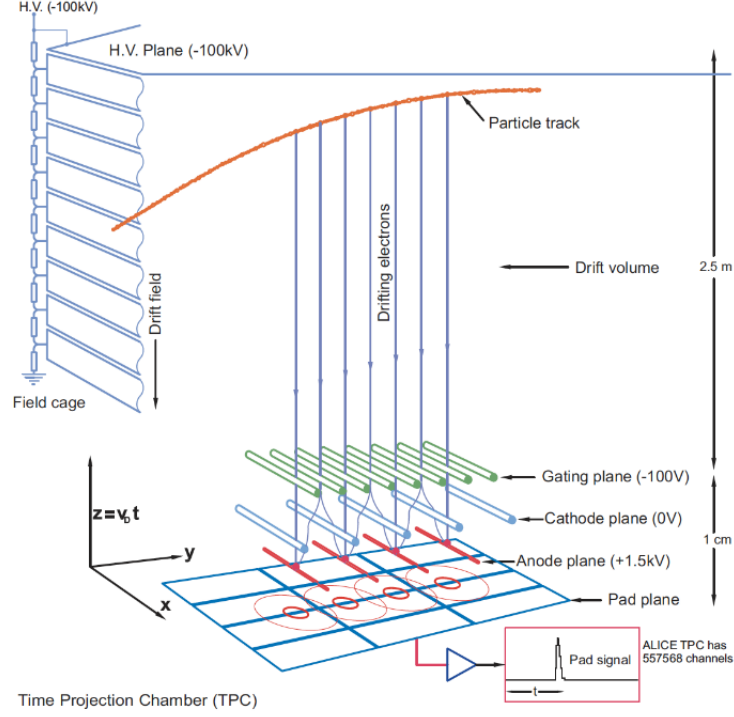
Figure 2.7: A schematic illustration of the working principle of the TPC [8].

dE/dx distribution as a function of momentum has different bands corresponding to different masses, hence the different particles. dE/dx of tracks as a function of momentum using the TPC detector in PbPb collisions at $\sqrt{s_{\mathrm{NN}}} = 2.76$ TeV has been shown in Fig. 2.8. The solid line corresponds to the expectations from Bethe-Bloch formula.

2.2.3 The Time Of Flight (TOF) detector

The TOF detector in ALICE is placed around the Transition Radiation Detector (TRD) having inner radius of 3.7 m and outer radius of 3.99 m with η and ϕ acceptance of $|\eta| < 0.9$ and 2π, respectively. It is a cylindrical gas detector comprising of Multi-gap Resistive Plate Chamber (MRPC). Whenever a charged particle traverses through the TOF detector, it ionizes the gas and the avalanche electrons move towards the
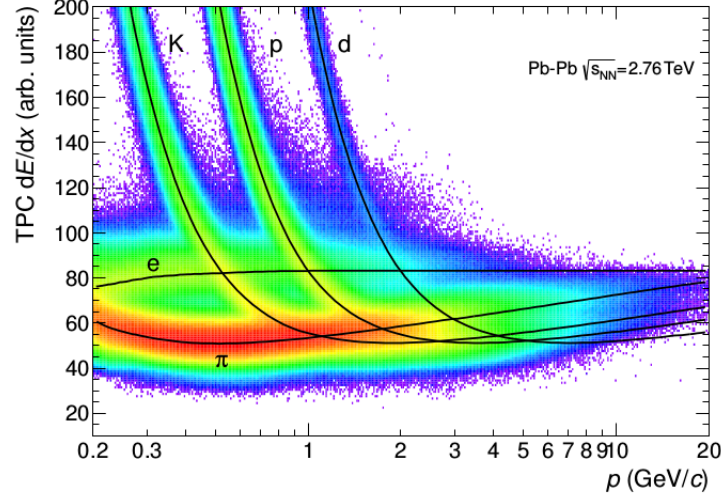
Figure 2.8: Average energy loss of tracks as a function of momentum using TPC in Pb–Pb collisions at $\sqrt{s_{\text{NN}}} = 2.76$ TeV [10].

electrode. Resistive plates in each gap stop the avalanche electrons. A very fast signal with a time resolution about 80 ps is provided by the induced charge. In ALICE, TOF is used to identify particles up to intermediate momentum where the separation between pions and protons with momentum up to 4 GeV/c and the separation between pions and kaons with momentum up to 2.5 GeV/c is good.

Particle identification in the TOF detector is based on the measurement of flight time (τ_{TOF}) of a particle inside the TOF detector. Flight time of a charged particle is measured as difference between the reconstructed times of the hits in the TOF and T0 detectors (provides the collision time). The time of flight is related to the particle velocity as, $\beta = \frac{L}{c\tau_{\text{TOF}}}$, where L is the path length traversed by the particle. The mass (m_0) of the particle is related to its momentum by,

$$m_0 = \frac{p}{\gamma\beta}. \tag{2.2}$$

Here p is the momentum of the particle, obtained from the TPC and γ is the lorentz factor. Figure 2.9 shows measured β for tracks using the TOF detector as a function

of their momenta in Pb–Pb collisions at $\sqrt{s_{\mathrm{NN}}} = 2.76$ TeV.
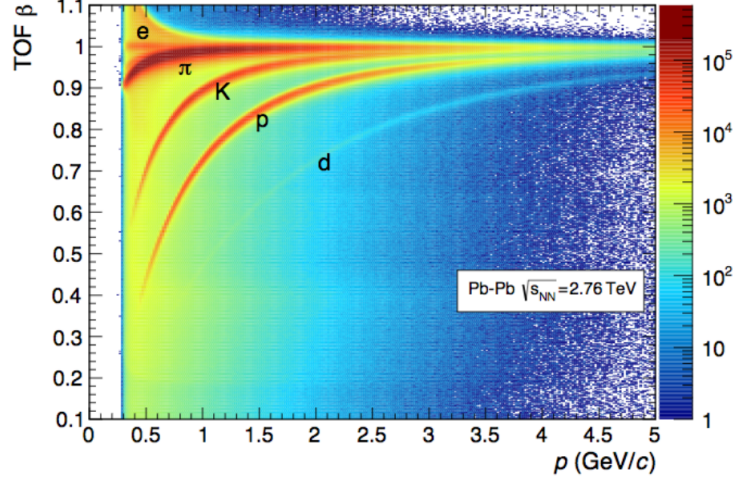
Figure 2.9: Distribution of β, measured by using TOF detector as a function of momentum of particles which reach the TOF detector in Pb–Pb collisions at $\sqrt{s_{\mathrm{NN}}} = 2.76$ TeV [10].

2.2.4 The VZERO (V0) detector

The V0A and V0C detectors are small-angle plastic scintillator detectors situated in the forward directions on both sides of the ALICE collision vertex. They cover full azimuthal angle and the pseudo-rapidity ranges of $2.8 < \eta < 5.1$ for the V0A detector and $-3.7 < \eta < -1.7$ for the V0C detector. Both of the V0 detectors consist of two arrays of 32 scintillator counters. The scintillating light is collected by photomultipliers (PMTs) through Wave-Length Shifting (WLS) fibres. Figure 2.10 shows the position of two V0 detectors in ALICE layout. The V0 detectors are dedicated to provide a minimum bias trigger during the data taking of pp and heavy-ion collisions. They are also used to discriminate the beam-gas interactions by correlating V0A and V0C timing. In addition, V0 detectors are also used to determine the collision centrality in heavy-ion collisions, multiplicity classes in pp collisions and the event plane by measuring the V0A and V0C amplitudes. Details about the centrality and the
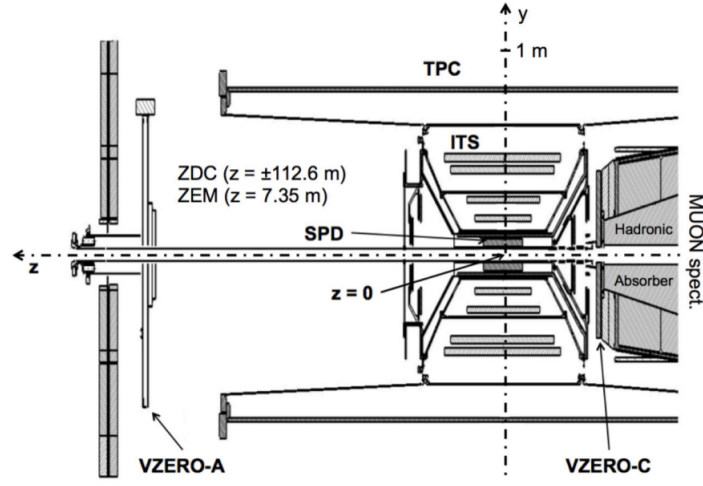
Figure 2.10: Position of the V0A and V0C detectors within the layout of the ALICE experiment [11].

event plane estimation are given in 3.1.13.1.4, and estimation of multiplicity classes is discussed in 5.0.1.

References

[1] C. De Melis, http://cds.cern.ch/record/2119882.

[2] Castillo et al., The Search and Discovery of the Higgs Boson [Morgan & Claypool Publishers], (2015).

[3] ALICE Collaboration figure repository, https://alice-figure.web.cern.ch/node/11218.

[4] K. Aamodt et al. [ALICE Collaboration], J. Instrum. 5, 3003 (2010).

[5] ALICE Inner Tracking System (ITS): Technical Design Report, CERN-LHCC-99-012, http://edms.cern.ch/file/398932/1.

[6] S. Acharya et al. [ALICE Collaboration], arXiv:2005.11120 [nucl-ex].

[7] ALICE Time Projection Chamber: Technical Design Report, CERN-LHCC-2000-001, http://cdsweb.cern.ch/record/451098.

[8] A. Kalweit, https://cds.cern.ch/record/2119440.

[9] W. Blum et al., https://cds.cern.ch/record/1105920.

[10] B. Abelev et al. [ALICE Collaboration], Int. J. Mod. Phys. A 29, 1430044 (2014).

[11] E. Abbas et al. [ALICE Collaboration], J. Instrum. 8, P10016 (2013).

Chapter 3

Spin alignment of vector mesons in heavy-ion and proton proton collisions

In non-central heavy-ion collisions a large initial angular momentum is expected to be created. A theoretical study predicts the magnitude of the angular momentum to be $\sim 10^7 \hbar$ [1]. In presence of large initial angular momentum, vector mesons (spin = 1) can be polarized due to the spin-orbital interaction of QCD. Spin alignment measurements of vector mesons provide a unique opportunity to probe this initial condition in heavy-ion collisions. Spin alignment can be studied by measuring the angular distributions of the decay daughters of vector mesons with respect to the quantization axis. The quantization axis can be perpendicular to the production plane, defined by the momentum of the vector meson and the beam axis or it can be perpendicular to the reaction plane, subtended by the impact parameter and the beam axis. The angular distribution is expressed as [2],

$$\frac{\mathrm{d}N}{\mathrm{d}\cos\theta^*} = \mathrm{N}_0 \left[1 - \rho_{00} + \cos^2\theta^*(3\rho_{00} - 1)\right]. \tag{3.1}$$

Here θ^* is the angle made by the decay daughter of vector meson with the quantization axis in the rest frame of the vector meson. N_0 is the normalization constant. ρ_{00} is the second diagonal element of the 3×3 hermitian spin density matrix. In the experiment the event plane is used as a proxy of the reaction plane as the impact parameter direction is not directly measured in the experiment. Observed ρ_{00} w.r.t. the event plane is corrected with the event plane resolution to get the ρ_{00} w.r.t. the reaction

plane. Resolution correction is carried out by applying following equation [3](see Appendix B.1 for the derivation)

$$\rho_{00}^{\text{corrected}} = \frac{1}{3} + (\rho_{00}^{\text{obs}} - \frac{1}{3}) \times \frac{4}{1 + 3R}, \tag{3.2}$$

where R is the 2nd order event plane resolution for vector mesons. R value is extracted by weighting the event plane resolution in small centrality bin with the yield of vector mesons in those centrality. ρ_{00} corresponds to the probability of finding a vector meson in spin state 0, where vector mesons can occupy 3 spin states –1, 0 and 1. In absence of spin alignment all spin states are equally probable which makes $\rho_{00} = 1/3$ and leads to a flat angular distribution. Deviation of ρ_{00} from 1/3 would lead to a non-uniform angular distribution which is the experimental evidence of the presence of large initial angular momentum, leading to the spin alignment of vector mesons.

In this chapter, we present the first ALICE measurements of the transverse momentum (p_{T}) and centrality dependence of ρ_{00} for K^{*0} and ϕ vector mesons in Pb–Pb collisions at $\sqrt{s_{\text{NN}}} = 2.76$ TeV and in pp collisions at $\sqrt{s} = 13$ TeV. Measurements are carried out with respect to the perpendicular direction to the production plane (PP) and the event plane (EP). Measurements are also compared with several control measurements such as ρ_{00} for vector mesons in pp collisions where presence of angular momentum is not expected, ρ_{00} for the spin zero hadron K_S^0 in Pb–Pb collisions and ρ_{00} for vector mesons w.r.t. the perpendicular direction of a random event plane (RndEP).

3.1 Analysis details

3.1.1 Event selection

The analysis is carried out on 14 million and 43 million minimum bias Pb–Pb collisions at $\sqrt{s_{\text{NN}}} = 2.76$ TeV and in pp collisions at $\sqrt{s} = 13$ TeV, respectively. Minimum bias

Pb–Pb and pp collision events were collected at a solenoidal magnetic field of B = 0.5 T. Pb–Pb collisions data were collected with a Minimum Bias (MB) trigger which requires at least one hit in any of V0A, V0C, and Silicon Pixel Detectors (SPD). Whereas, minimum bias event in pp collisions required at least one hit in both V0A and V0C, in coincidence with proton bunches arriving from opposite directions of the experiment along the beam line. In addition to the trigger conditions in Pb–Pb and pp collisions, beam induced background events were removed by using the timing information in the V0 detectors and taking into account the correlation between tracklets and clusters in the SPD detector. Pile-up events are removed for the analysis by excluding events with multiple vertices reconstructed in the SPD. For the analysis only those events are selected which have a primary collision vertex reconstructed with the SPD detector and the z position of primary vertex (v_z) is within ± 10 cm along the beam axis from the center of the TPC detector to ensure uniform detector acceptance.

For centrality selection the V0 detector is used. The centrality estimation is based on the sum of the V0A and V0C amplitudes, which are proportional to the ionisation energy deposited in detectors in the $2.8 < \eta < 5.1$ and $-3.7 < \eta < -1.7$ ranges, respectively. The amplitudes are classified in percentiles of selected events and results are reported in classes defined with this sum of amplitudes, henceforth denoted as the V0M centrality classes. For example, 0–10% corresponds to the top 10% of the V0M amplitude distribution. The V0M amplitude distribution is further fitted with the two component Glauber Monte Carlo model to get impact parameter (b), average number of binary collisions ($\langle N_{coll} \rangle$), and $\langle N_{part} \rangle$ for any given range of V0M amplitude. Figure 3.1 shows the V0M amplitude distribution and the Glauber Monte Carlo fit in Pb–Pb collisions at $\sqrt{s_{NN}} = 2.76$ TeV [4].

Table 3.1 shows collision centrality classes and their corresponding $\langle N_{part} \rangle$ values,
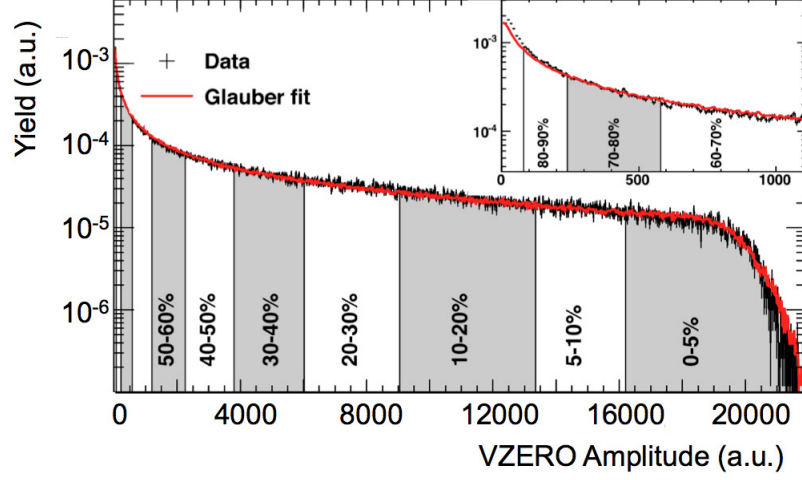
Figure 3.1: Centrality selection using V0M amplitude distribution in Pb–Pb collisions at $\sqrt{s_{\mathrm{NN}}} = 2.76$ TeV [4]. The red line shows the fit with a Glauber model. The shaded areas define the different centrality classes of hadronic collisions

used in this analysis [1].

3.1.2 Track selection

Invariant mass reconstruction of K^{*0} and ϕ signals are carried out with the charged K and π tracks which are coming from the primary vertex of the collision, also known as primary tracks. Track selection criteria are applied to limit the contamination due to secondary particles, to maximize tracking efficiency and improve the $\mathrm{d}E/\mathrm{d}x$ and momentum resolution for primary charged particles, and to guarantee an optimal particle identification (PID) quality. Primary tracks are selected within kinematic acceptance $p_{\mathrm{T}} > 0.15$ GeV/c to maintain a good momentum resolution and track reconstruction efficiency [6], and $|\eta| < 0.8$ to avoid edge effects in the TPC acceptance [6]. The selection of primary tracks require to satisfy good quality track criteria. Primary tracks are reconstructed using the TPC and ITS detectors with a Kalman

---

[1]For K^{*0} measurements with respect to the production plane, 2–10% centrality class is used instead of 0–10% centrality class to reduce combinatorial background contribution and to get smooth residual background shape.

Table 3.1: $\langle N_{\mathrm{part}} \rangle$ values and their corresponding systematic errors along with the number of analyzed events for various centrality classes in Pb–Pb collisions at $\sqrt{s_{\mathrm{NN}}}$ = 2.76 TeV [4, 5].

Analysis	Centrality (%)	$\langle N_{\mathrm{part}} \rangle$	Number of events (in Million)
K^{*0} (EP) and ϕ (EP)	0–10%	356.2 ± 3.8	1.44
	10–30%	225.5 ± 3.5	2.88
	30–50%	108.6 ± 1.8	2.88
	50–80%	32.9 ± 1.3	4.32
K^{*0} (PP)	2–10%	345.3 ± 4.0	1.15
	10–30%	225.5 ± 3.5	2.88
	30–50%	108.6 ± 1.8	2.88
	50–80%	32.9 ± 1.3	2.88
	50–70%	41.0 ± 1.3	2.88
	70–90%	11.4 ± 0.3	2.88
ϕ (PP)	0–20%	308.1 ± 3.7	2.88
	20–40%	157.2 ± 3.1	2.88
	40–60%	68.6 ± 2.0	2.88
	60–80%	16.9 ± 0.5	2.88

filter algorithm for the tracking. Tracks which pass the TPC and ITS refit (refitting of primary tracks from the outermost layers of TPC to the innermost layers of the ITS with a prolongation to the primary vertex and vice-versa) are used for this analysis. Good quality tracks also require to have a signal in at least one of the SPD layers with a maximum χ^2 per cluster value of 36, obtained from the fit of ITS clusters. To reduce the contribution from the weak decay particles and the interaction with the detector material, a selection criteria on the distance of closest approach (DCA) of the primary track to the primary vertex is also applied. The good quality tracks require to have DCA $< 7\sigma_{\mathrm{DCA_{xy}}}$ in the transverse plane and DCA < 2 cm along the longitudinal or beam direction. $\sigma_{\mathrm{DCA_{xy}}}$ depends on the p_{T} of the track and can be expressed as $0.0026 + 0.005p_{\mathrm{T}}{}^{-1.1}$ cm ($0.0015 + 0.005p_{\mathrm{T}}{}^{-1.1}$ cm in pp collisions). Accepted tracks require to cross at least 70 horizontal segments ("rows") out of maximum available 159 along the transverse readout plane of the TPC with a maximum χ^2 per cluster value of 4, obtained from the fit of TPC clusters. In addition, the value for the ratio of the number of crossed rows to the number of findable clusters in the

TPC is larger than 0.8 and rejection of track with kink decay (a track which decays to muon and neutrino) is also applied to ensure the good quality tracks.

3.1.3 Particle identification

The daughter particles of K^{*0} and ϕ are kaons and pions, and they can be identified by using Time Projection Chamber (TPC) [6] and Time Of Flight (TOF) [6]. In TPC, particles are identified by their specific energy loss ($\mathrm{d}E/\mathrm{d}x$) and in TOF particles are identified by their time of flight. Both pions and kaons are selected by a criterion of $|\mathrm{n}\sigma_{\mathrm{TPC}}| < 2.0$ with a TOF veto of $|\mathrm{n}\sigma_{\mathrm{TOF}}| < 3.0$ (shown in Fig. B.2 and Fig. B.3 of Appendix B.2). "TOF veto" means that the TOF criterion is applied only for cases where the reconstructed track matches a hit in the TOF; for tracks without a match in TOF, no TOF criterion is applied. $\mathrm{n}\sigma_{\mathrm{TPC}}$ is defined as,

$$\mathrm{n}\sigma_{\mathrm{TPC}} \;=\; \frac{\mathrm{d}E/\mathrm{d}x_{\mathrm{measured}} \;-\; \mathrm{d}E/\mathrm{d}x_{\mathrm{expected}}}{\sigma_{\mathrm{TPC}}}, \tag{3.3}$$

where $\mathrm{d}E/\mathrm{d}x_{\mathrm{measured}}$ is the measured average energy loss of a track inside the TPC, $\mathrm{d}E/\mathrm{d}x_{\mathrm{expected}}$ is the expected average energy loss of a pion (corresponds to $\mathrm{n}\sigma_{\mathrm{TPC}}$ for pion) or kaon (corresponds to $\mathrm{n}\sigma_{\mathrm{TPC}}$ for kaon) track, obtained from the parametrization of modified Bethe-Bloch function. The $\mathrm{d}E/\mathrm{d}x$ value of a track is measured by taking the truncated mean of lowest 60% of the measured clusters to avoid ionization fluctuation and TPC edge effect. σ_{TPC} is the PID resolution of the TPC and the typical resolution value is $\sim$5.2% for pp collisions and $\sim$6.5% for 0–5% most central A–A collisions.

In the TOF detector mass or the identity of a particle is obtained by combining the information of the flight time of a particle measured in the TOF detector and its momentum information from the ITS and the TPC detectors. The start time of the flight is assumed to be the collision time and is obtained for each event from the T0

detector. nσ_{TOF} is defined as,

$$\text{n}\sigma_{\text{TOF}} \;=\; \frac{t_{\text{measured}} \;-\; t_{\text{expected}}}{\sigma_{\text{TOF}}}, \tag{3.4}$$

where t_{measured} is the flight time of a particle measured in the TOF detector and t_{expected} is the expected time calculated from the track length and momentum assuming that the track is a pion (corresponds to nσ_{TOF} for pion) or kaon (corresponds to nσ_{TOF} for kaon) track. σ_{TOF} is the PID resolution of the TOF and the value is ~ 56 ps.

It should be noted that in pp collisions the above quoted value for the TPC PID criteria are only applied for momentum (p) > 0.4 GeV/c for both $K^{\pm}$ and $\pi^{\pm}$. Wider TPC PID selection criteria are used at low momentum. Specifically, for $p < 0.3$ GeV/c, a selection criterion of $|\text{n}\sigma_{\text{TPC}}| < 6.0$ and for $0.3 < p < 0.4$, $|\text{n}\sigma_{\text{TPC}}| < 4.0$ is applied for both pions and kaons.

3.1.4 Event plane estimation

The event plane is determined from the azimuthal distribution of the final state particles. The procedure to extract the event plane angle Ψ from the produced particles starts with the reconstruction of the flow vector for each event. Flow vector is calculated for each harmonic, n, of the Fourier expansion of the azimuthal distribution. The event flow vector Q_{n} in the transverse plane is defined as :

$$Q_{\text{n,x}} = \sum_{\text{n=i}} w_{\text{i}} cos(\text{n}\phi_{\text{i}}) = Q_{\text{n}} cos(\text{n}\Psi_{\text{n}}); \quad Q_{\text{n,y}} = \sum_{\text{n=i}} w_{\text{i}} sin(\text{n}\phi_{\text{i}}) = Q_{\text{n}} sin(\text{n}\Psi_{\text{n}}), \tag{3.5}$$

where sum goes over all particles i used to calculate the event plane. The quantities ϕ_{i} and w_{i} are the lab azimuthal angle and weight for particle i, where for odd harmonics $w_{\text{i}}(-\text{y}) = -w_{\text{i}}(\text{y})$. The weights are introduced, since not all the particles have the same flow. The weight coefficients are there to enhance the contribution of particles

with larger flow and hence make the Q vector a better defined observable. Experimentally it is observed that flow increases with the transverse momentum, therefore a good choice of the weights for the calculation of flow vector Q_n can be p_T itself or some monotonic function $w_i(p_T) \propto p_T$. In this analysis we are calculating the event plane from V0 and inverse of multiplicity is used as the weight factor. The observed event plane angle of the nth harmonic is the azimuthal angle of Q_n calculated as

$$\Psi_n = \frac{1}{n} \arctan\left(\frac{Q_{n,y}}{Q_{n,x}}\right). \tag{3.6}$$

By construction $\Psi_n \in \left[\frac{-\pi}{n}, \frac{\pi}{n}\right]$. As long as the colliding nuclei are not polarized, any ensemble of events should have randomly distributed azimuthal angles of the reaction planes. The finite acceptance of the detector induces bias which cause the particles to be azimuthally anisotropic in the laboratory system. This anisotropy can be removed by making the distribution of event planes isotropic in the laboratory.

3.1.5 Event plane flattening method

Collision of two nuclei in the laboratory frame is random, therefore the event plane angle distribution should be isotropic in the laboratory frame for an ideal detector acceptance. However, in experiments, the detectors have a finite acceptance or non-uniform acceptance which makes an anisotropic event plane angle distribution. A number of methods [7, 8] are used to make the event plane angle distribution uniform. These methods sometimes used in a combination with each other. Three methods have been used to make the V0 event plane azimuthal angle distribution flat:

Gain equalization

The gain equalization is performed on individual detector channels and is given by

$$M'_c = \frac{M_c}{\langle M \rangle}, \tag{3.7}$$

where M_c is the multiplicity and $\langle M \rangle$ is the average multiplicity of the detector channel.

Recentering

It is observed that for non-flat distribution of the event plane angle, the flow vector Q_n distributions over a large number of events are not centered around zero. In this method the Q_n-vector distributions are made to be centered around zero by subtracting the average Q_n vectors; i.e.

$$X'_n = X_n - \langle X_n \rangle; \qquad Y'_n = Y_n - \langle Y_n \rangle, \tag{3.8}$$

where $X_n = \sum_i w_i cos(n\phi_i)$ and $Y_n = \sum_i w_i sin(n\phi_i)$ and X'_n & Y'_n are the new corrected position of Q_n vector. The averages $\langle X_n \rangle$ and $\langle Y_n \rangle$ are made over many events. The green solid lines in Figure 3.2 shows the Ψ_2 distribution from V0A after recentering for centrality class 30-40%.

Shift correction

After recentering corrections the event plane is flat with small modulations. Further corrections are applied after recentering using the shift correction method [9]. The equation for shift correction is given by:

$$n\Delta\Psi_n = \sum_{i=1}^{i_{max}} \frac{2}{i}(-\langle sin(in\Psi_n)\rangle cos(in\Psi_n) + \langle cos(in\Psi_n)\rangle sin(in\Psi_n)). \tag{3.9}$$

The corrected event plane angle after shift correction is given as:

$$\Psi'_n = \Psi_n + \sum_{i=1} \frac{2}{in}(-\langle sin(in\Psi_n)\rangle cos(in\Psi_n) + \langle cos(in\Psi_n)\rangle sin(in\Psi_n)). \tag{3.10}$$

In this analysis, the correction is done upto 20th harmonic i.e. summation runs over i=1 to 20. Larger value of 'i' is chosen to reduce the contribution from higher order harmonics. The event plane distribution after shift correction in a centrality class 30–40% from V0A is shown in Fig. 3.2 by black solid line. To have a quantitative
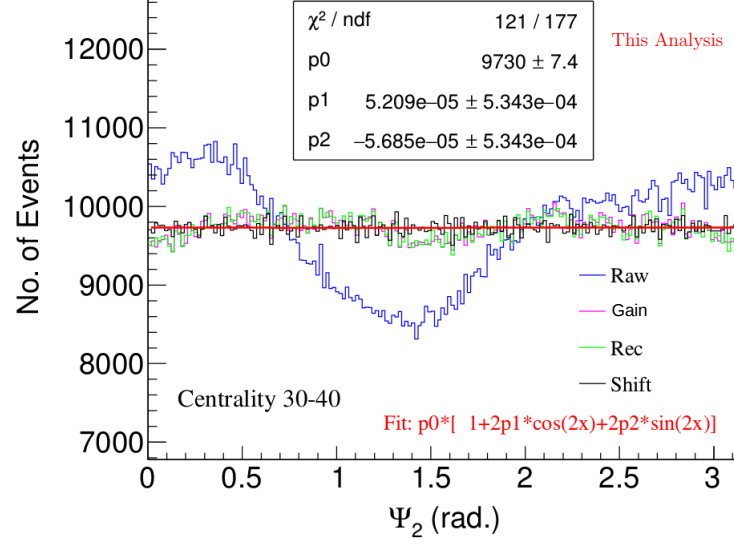
Figure 3.2: Event plane angle (Ψ_2) distribution before correction (blue line), after gain equalization (magenta line), recentering (green line) and shift correction (black line) in Pb–Pb collisions at $\sqrt{s_{NN}}$ = 2.76 TeV. The red line shows the fit to Ψ_2 distribution after shift correction.

approach for the flatness of Ψ_2 distribution, we have fitted the event plane angle distribution with a function

$$f(\Psi) = p0[1 + 2 \times p1 \times cos(2\Psi) + 2 \times p2 \times sin(2\Psi)]. \tag{3.11}$$

The coefficient $p1$ gives the flow contribution from the event plane itself. One can see that after shift correction $p1$ is very small ($\sim 0.005\%$). The event plane distributions for various centralities are shown in Appendix B.3.

3.1.6 Event plane resolution

The event plane is an estimation of the reaction plane and is affected by the finite resolution. Among the various methods to calculate the event plane resolution, we have used three sub-event method [10]. In this method we need three η-windows with charged particle information to determine the event plane resolution. The resolution
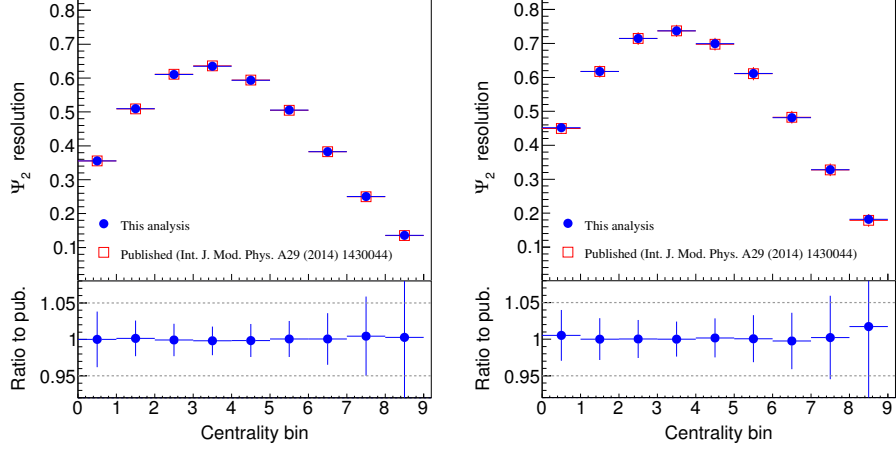
Figure 3.3: Ψ_2 resolution in different centrality classes from V0A (top left) and V0C (top right) using three event method. For comparison, the published results are plotted. The bottom panels show the ratio of the Ψ_2 resolution from this analysis to the published results. The centrality bin number 0 and 9 corresponds to most central and most peripheral collisions, respectively.

of a particular η-window is given by :

$$\langle cos[(\Psi_n^A - \Psi_R)]\rangle = \sqrt{\frac{\langle cos[n(\Psi_n^A - \Psi_n^B)]\rangle \langle cos[n(\Psi_n^A - \Psi_n^C)]\rangle}{\langle cos[n(\Psi_n^B - \Psi_n^C)]\rangle}}, \qquad (3.12)$$

where Ψ_A, Ψ_B and Ψ_C are the event plane angle calculated from three different η-windows. For this analysis we are making use of event plane from TPC ($-0.8 < \eta < 0.8$), V0A ($2.8 < \eta < 5.1$) and V0C ($-3.7 < \eta < -1.7$). The Ψ_2 resolution are shown in the Fig. 3.3 for V0A (top left) and V0C (top right). For comparison the published results are also plotted and are in good agreement with the current analysis results. The ratios of Ψ_2 resolution from this analysis to the published values are also shown in the bottom panels of Fig. 3.3.

3.2   Signal extraction

K^{*0} [2] and ϕ signals in a given $\cos\theta^*$, centrality and p_{T} bin are extracted by invariant mass technique through the hadronic decay channel (K^{*0} ($\overline{K}^{*0}$) $\to \pi^-(\pi^+)K^+(K^-)$ and $\phi \to K^+K^-$ with branching ratio 66.6% and 49.2%, respectively) at mid-rapidity (-0.5 < y < 0.5). Invariant mass distribution of unlike charged πK (KK) pairs is described as,

$$M_{\pi K(KK)} \;=\; \sqrt{(E_{\pi K(KK)} \;+\; E_{\pi K(KK)})^2 \;-\; |p_{\pi K\vec{(KK)}} \;+\; p_{\pi K\vec{(KK)}}|^2}, \qquad (3.13)$$

where E and $\vec{p}$ are the energy and momentum of decay daughters, respectively. K^{*0} and ϕ meson signals are extracted from the invariant mass distribution of un-like charged πK and KK pairs from same events, respectively. The invariant mass distribution of unlike charged πK (KK) pairs from same events in 10–50% Pb–Pb collisions for $1.2 < p_{\mathrm{T}} < 1.6$ GeV/c ($0.5 < p_{\mathrm{T}} < 0.8$ GeV/c) and $0.6 < \cos\theta^* < 0.8$ is shown in the left panel (right panel) of Fig. 3.4. Invariant mass distributions of unlike charged πK and KK pairs K^{*0} and ϕ signals along with large combinatorial backgrounds, respectively. Combinatorial backgrounds are estimated by the invariant mass distribution of unlike charged daughter pairs from mixed events. For this anal-ysis we have mixed five events which have z-vertex difference within 1 cm, centrality difference within 5% (in case of pp collisions we use multiplicity difference within 5) and the event plane angle difference within 20° (only used for analysis in Pb–Pb collisions) in order to keep the event characteristics as similar as possible during the mixing of events. The mixed event distribution statistics is about five times higher compared to that of the same event distribution. The mixed event combinatorial background distribution is then normalized to the same event invariant mass distri-bution in the invariant mass region more than 5Γ (Γ corresponds to the full width at

---

[2] K^{*0} corresponds to average of K^{*0} and $\overline{K}^{*0}$, through out the analysis.
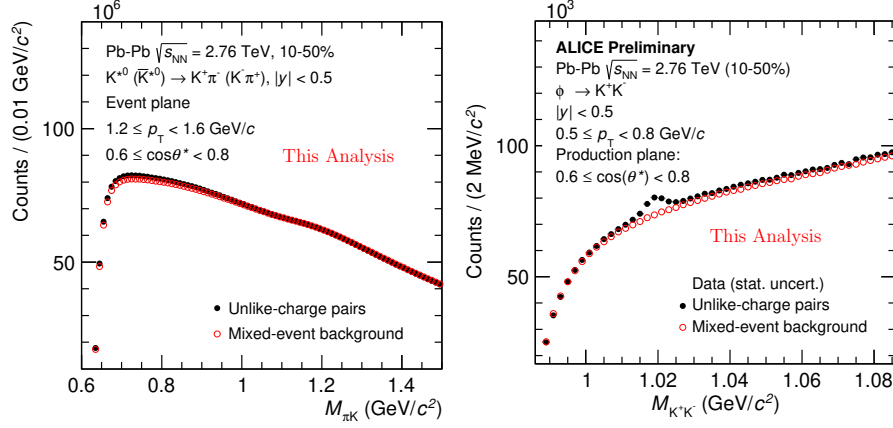
Figure 3.4: Left panel: Invariant mass distribution of unlike charged πK pairs from same events (black marker) and normalized mixed event background (red marker) for $1.2 < p_T < 1.6$ GeV/c and $0.6 < \cos\theta^* < 0.8$ in 10–50% Pb–Pb collisions at $\sqrt{s_{NN}} = 2.76$ TeV. Quantization axis is normal to the EP. Right panel: Invariant mass distribution of unlike charged KK pairs from same events and normalized mixed event background for $0.5 < p_T < 0.8$ GeV/c and $0.6 < \cos\theta^* < 0.8$ in 10–50% Pb–Pb collisions at $\sqrt{s_{NN}} = 2.76$ TeV. Quantization axis is normal to the PP.

half maximum of the resonance signal) away from the signal peak. Normalized mixed event backgrounds for πK and KK pairs are shown in the Fig. 3.4. The normalized mixed event background is subtracted from the same event invariant mass distribution to get the K^{*0} and ϕ signal. After subtraction of the combinatorial background, a certain amount of background still present, known as residual background. The residual background mainly originates due to the production of correlated daughter pairs from the decays of other hadrons and jets. Misidentification of K and π also contributes to the residual background. The combinatorial background subtracted πK invariant mass distribution is fitted with a combination of the Breit-Wigner and a 2nd order polynomial function to obtain the K^{*0} meson signal and combinatorial background subtracted KK invariant mass distribution is fitted with a combination of the Voigtian and a 2nd order polynomial function to obtain the ϕ meson signal. The Breit-Wigner and Voigtian distribution functions along with a 2nd polynomial

function are described in Eq. 3.14 and Eq. 3.15

$$\frac{Y}{2\pi} \frac{\Gamma}{(M_{\pi K} - M_0)^2 + \frac{\Gamma^2}{4}} + AM_{\pi K}^2 + BM_{\pi K} + C, \qquad (3.14)$$

$$\frac{Y\Gamma}{2\pi^{3/2}\sigma} \int_{-\infty}^{\infty} exp(\frac{(m_{KK} - m')^2}{2\sigma^2}) \frac{dM_{KK}}{(M_{KK} - M_0)^2 + \frac{\Gamma^2}{4}} + AM_{KK}^2 + BM_{KK} + C.$$
(3.15)

Here M_0 and Γ are the mass and width of K^{*0} and ϕ mesons. σ is the mass resolution of the ϕ meson. The parameter Y is the area under the Breit-Wigner and Voigtian distributions and give the raw yield of K^{*0} and ϕ respectively. Figure 3.5 shows K^{*0} and ϕ signal after mixed event background subtraction in 10–50% Pb–Pb collisions for the same p_T and $\cos\theta^*$ ranges as shown in Fig. 3.4. During the fitting of K^{*0} meson signal, width of the Breit-Wigner distribution is kept fixed to PDG value, whereas for the fitting of ϕ meson signal Voigtian width is left free and mass resolution is fixed from Monte-Carlo (MC) simulation. Resonance peak position and width from invariant mass fitting, and mass resolution from MC simulation are shown in the Appendix B.4. In order to obtain $\cos\theta^*$ distributions, K^{*0} and ϕ signals are extracted for various p_T and $\cos\theta^*$ intervals in different centrality classes of Pb–Pb collisions and in minimum bias pp collisions. The K^{*0} and ϕ signals for selected p_T intervals and centrality classes are shown in the Appendix B.5.

In addition, as a control measurement K_S^0 analysis is performed for the 20–40% Pb–Pb collisions. The K_S^0 meson is reconstructed from the invariant mass distribution of unlike charged pion pairs, where daughter pions are selected by using V-shaped decay topology [11]. Topological selection criteria for selection of daughter pions are same as used in [11]. The combinatorial background for K_S^0 candidate is significantly reduced by using topological criteria to select the distinctive V-shaped decay topology. Details about the K_S^0 signal extraction are given in the Appendix B.6.
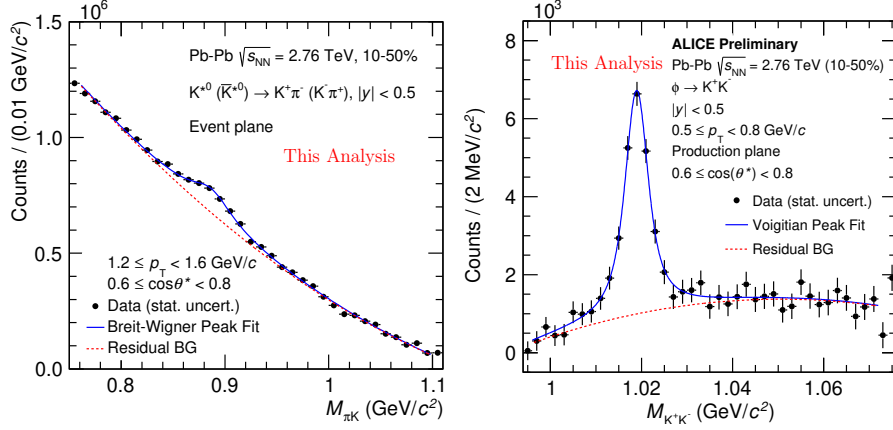
Figure 3.5: Left panel: Mixed event background subtracted πK invariant mass distribution for $1.2 < p_T < 1.6$ GeV/c and $0.6 < \cos\theta^* < 0.8$ in 10–50% Pb–Pb collisions at $\sqrt{s_{NN}} = 2.76$ TeV. Invariant mass distribution is fitted with the Breit-Wigner + 2nd order polynomial of $M_{\pi K}$ function. The Breit-Wigner function describes the K^{*0} signal and the residual background is described by the 2nd order polynomial function. Quantization axis is normal to the EP. The typical significance ($\frac{S}{\sqrt{S+B}}$; S = signal, B = combinatorial background) value for the signal is 14.7. Right panel: Mixed event background subtracted KK invariant mass distribution for $0.5 < p_T < 0.8$ GeV/c and $0.6 < \cos\theta^* < 0.8$ in 10–50% Pb–Pb collisions at $\sqrt{s_{NN}} = 2.76$ TeV. Mixed event background subtracted invariant mass distribution is fitted with the Voigtian + 2nd order polynomial of M_{KK} function. The Voigtian function describes the ϕ signal and the residual background is described by the 2nd order polynomial function. Quantization axis is normal to the PP. Uncertainties on data points are statistical only. The typical significance value for the signal is 21.1.

3.2.1 Raw yield extraction

The raw yield of K^{*0} and ϕ mesons are calculated by using two different methods: bin counting and function integration method, where function integration is used as default and bin counting is used for systematic study. In bin counting method, the raw yield (N_{bincount}) is calculated from the mixed event background subtracted histogram of invariant mass distribution in a limited mass range: $M(\text{PDG}) - 2\,\Gamma$ to $M(\text{PDG}) + 2\Gamma$, where $M(\text{PDG}) = 896$ MeV/c^2 for the K^{*0} meson and 1020 MeV/c^2 for the ϕ meson, and $\Gamma = 48.7$ MeV/c^2 for the K^{*0} meson and 4.2 MeV/c^2 for the ϕ meson. Amount of residual background in the limited mas range is estimated from

the integral of the residual background fit function and subtracted from the total entries of the invariant mass histogram in same mass range to get N_{bincount}. The N_{bincount} is then added with two tail correction terms. The tail correction terms are

$$N_{\mathrm{low}} \;=\; \int_{M_K + M_\pi \ (2M_k \ \mathrm{for} \ \phi)}^{M_{\mathrm{PDG}} - 2\Gamma} fit(m_{\mathrm{inv}}) \mathrm{d}m_{\mathrm{inv}} \qquad (3.16)$$

$$N_{\mathrm{high}} \;=\; \int_{M_{\mathrm{PDG}} + 2\Gamma}^{\infty} fit(m_{\mathrm{inv}}) \mathrm{d}m_{\mathrm{inv}}, \qquad (3.17)$$

where $fit(m_{\mathrm{inv}})$ is Breit-Wigner distribution for the K^{*0} and Voigtian distribution for the ϕ. Final yield from bin counting method is

$$Y_{\mathrm{BC}} \;=\; N_{\mathrm{low}} \;+\; N_{\mathrm{bincount}} \;+\; N_{\mathrm{high}}. \qquad (3.18)$$

The yield in function integration method is extracted by integrating the peak fitting function (Breit-Wigner distribution for the K^{*0} and Voigtian distribution for the ϕ) over the mass region $M_K + M_\pi < m_{\mathrm{inv}} < \infty$ for the K^{*0} and $2M_K < m_{\mathrm{inv}} < \infty$ for the ϕ. Extracted K^{*0} and ϕ yields as a function of p_{T} for various $\cos\theta^*$ ranges in 10–50% Pb–Pb collisions and minimum bias pp collisions are shown in Fig. 3.6 and in Fig. 3.7. Raw p_{T} spectrum is normalized to the total number of accepted events.

3.2.2 Acceptance × Efficiency

Acceptance × Efficiency for K^{*0} and ϕ mesons in various p_{T} and $\cos\theta^*$ bins are obtained from Monte Carlo (MC) simulation. Particle production and resonance decays for Pb–Pb collisions data set are simulated by using HIJING [12] model, whereas for pp collisions PYTHIA8 [13] event generator is used. Particle interactions with the ALICE detector are simulated by using GEANT3 [14]. The same event selection and track selection criteria as data are used to analyze the simulated data. Particles produced by the event generator (without any detector effects) are referred as "generated" particles. These particles are the input for the GEANT3 detector simulation
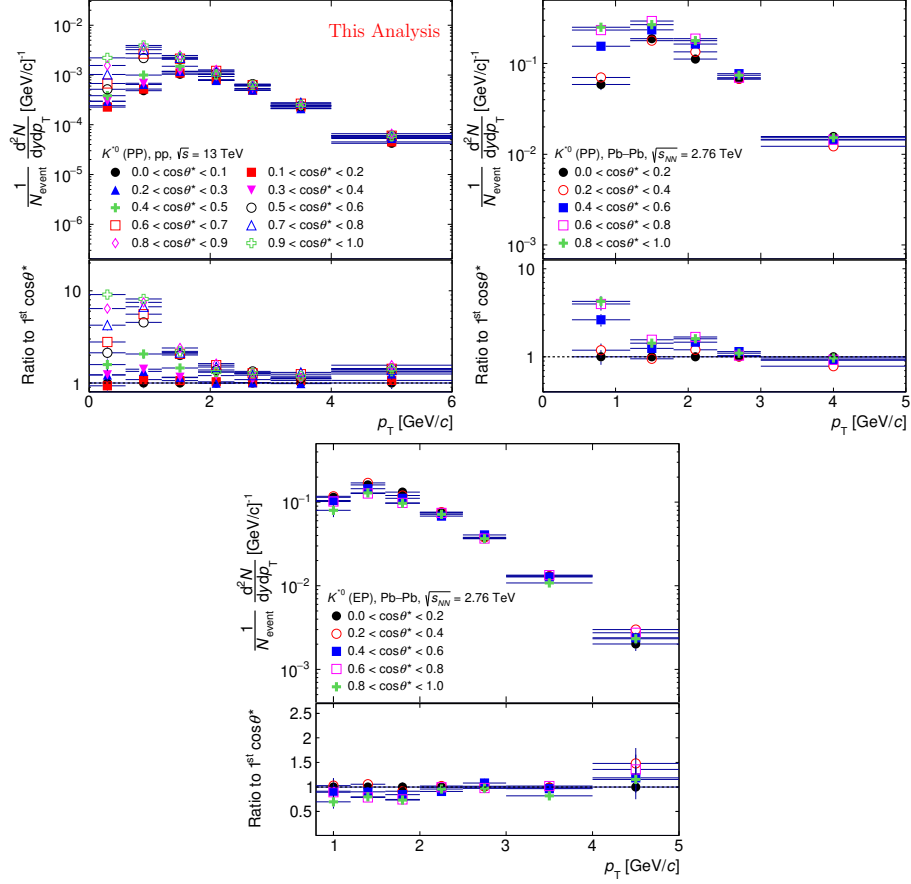
Figure 3.6: Raw K^{*0} meson yields as a function of p_{T} at $|y| < 0.5$ for different $\cos\theta^*$ bins in 10–50% Pb–Pb collisions at $\sqrt{s_{\mathrm{NN}}} = 2.76$ TeV and in minimum bias pp collisions at $\sqrt{s} = 13$ TeV. Lower panels show the ratio of raw yields with respect to those in lowest $\cos\theta^*$ bin. Vertical bars correspond statistical uncertainties on raw yields.
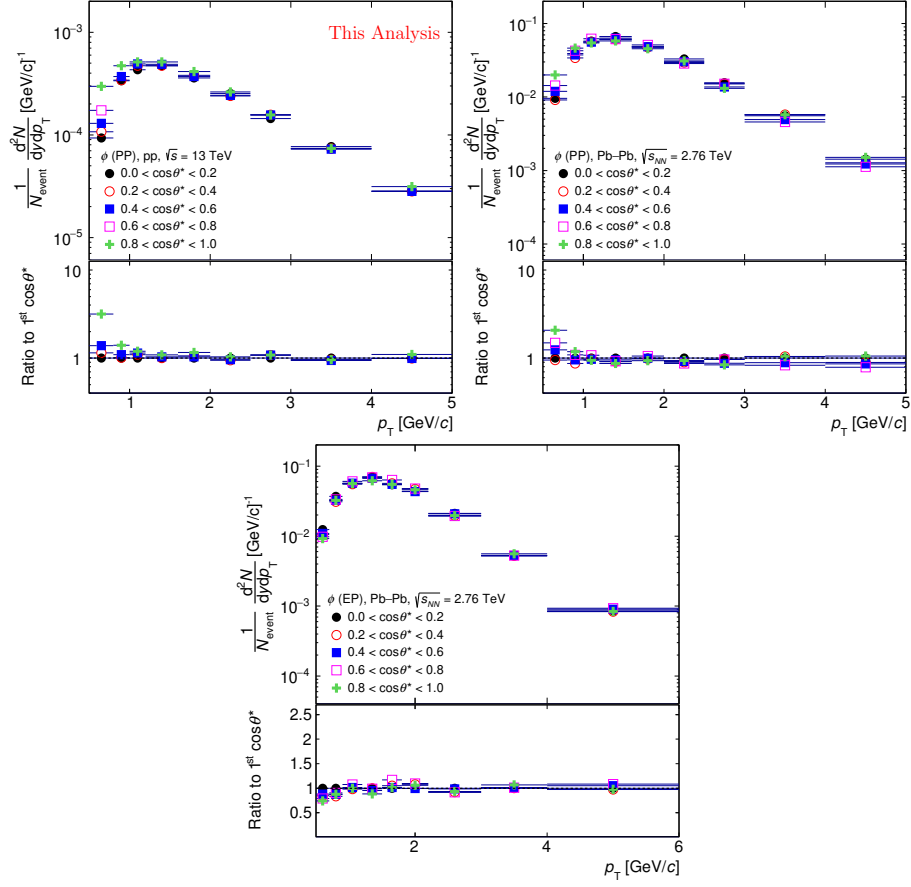
Figure 3.7: Raw ϕ meson yields as a function of p_T at $|y| < 0.5$ for different $\cos\theta^*$ bins in 10–50% Pb–Pb collisions at $\sqrt{s_{NN}} = 2.76$ TeV and in minimum bias pp collisions at $\sqrt{s} = 13$ TeV. Lower panels show the ratio of raw yields with respect to those in lowest $\cos\theta^*$ bin. Vertical bars correspond statistical uncertainties on raw yields.

and the track reconstruction algorithm. Tracks which are identified by the reconstruction algorithm and which pass the track and PID selection criteria are referred as "reconstructed" tracks. The K^{*0} is said to be reconstructed if both the daughter tracks of K^{*0} have been reconstructed.

Acceptance $\times$ Efficiency ($A \times \epsilon_{\rm rec}$) is the ratio of the number of reconstructed K^{*0} (ϕ) mesons having decay daughters $K^{\pm}$, $\pi^{\mp}$ (K^{+}, K^{-}) to the number of generated K^{*0} (ϕ). Both generated and reconstructed K^{*0} and ϕ mesons are counted in rapidity interval $|y| < 0.5$. The uncertainty on $A \times \epsilon_{\rm rec}$ is calculated using the Bayesian approach described in [15]. The statistical uncertainty on $A \times \epsilon_{\rm rec}$ can be expressed as,

$$\sigma_{\epsilon} = \sqrt{\frac{k+1}{n+2}\left(\frac{k+2}{n+3} - \frac{k+1}{n+2}\right)}, \tag{3.19}$$

where k and n are number of reconstructed and generated vector mesons, respectively. The statistical uncertainty on $A \times \epsilon_{\rm rec}$ is added in quadrature with the statistical uncertainty on the uncorrected vector meson yield to get the total statistical uncertainty on the corrected vector meson yield for each $p_{\rm T}$ and $\cos\theta^{*}$ bin.

The $A \times \epsilon_{\rm rec}$ as a function of $p_{\rm T}$ for various $\cos\theta^{*}$ ranges in 10–50% Pb–Pb collisions and minimum bias pp collisions are shown in Fig. 3.8 and in Fig. 3.9. A strong dependence of $A \times \epsilon_{\rm rec}$ on $\cos\theta^{*}$ is observed at low $p_{\rm T}$ for the production plane analysis in both Pb–Pb and pp collisions. This dependence is mainly due to the acceptance of daughter tracks as discussed in the Appendix B.10.

A MC closure test has been carried out to verify that the corrected yields and $\cos\theta^{*}$ distribution is not affected by this dependency. Details about MC closure test is given in the Appendix B.10. In order to verify the measurements, several consistency checks related to $A \times \epsilon_{\rm rec}$ correction are carried out. Two different event generators (PYTHIA and HIJING) are used to determine the reconstruction efficiency
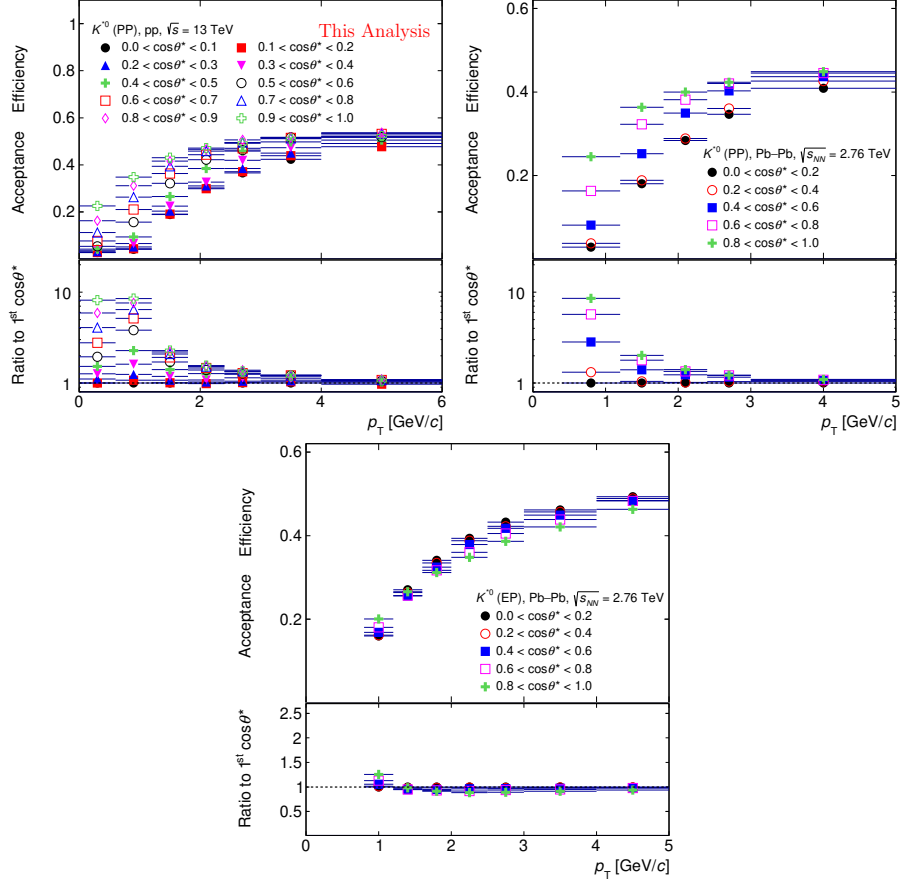
Figure 3.8: Acceptance × Efficiency for the K^{*0} as a function of p_T at $|y| < 0.5$ for different $\cos\theta^*$ bins in 10–50% Pb–Pb collisions at $\sqrt{s_{NN}} = 2.76$ TeV and in minimum bias pp collisions at $\sqrt{s} = 13$ TeV. Lower panels show the ratio of Acceptance × Efficiency with respect to those in lowest (1st) $\cos\theta^*$ bin. Vertical bars correspond statistical uncertainties on raw yields.
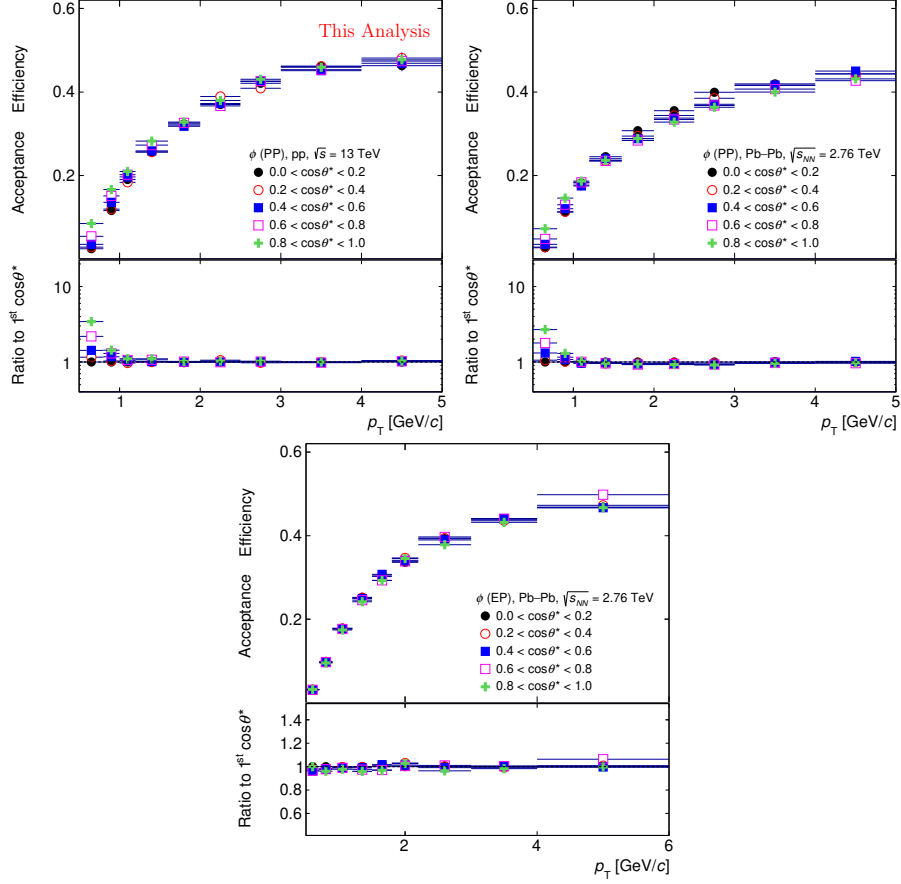
Figure 3.9: Acceptance × Efficiency for the ϕ as a function of p_T at $|y| < 0.5$ for different $\cos\theta^*$ bins in 10–50% Pb–Pb collisions at $\sqrt{s_{NN}} = 2.76$ TeV and in minimum bias pp collisions at $\sqrt{s} = 13$ TeV. Lower panels show the ratio of Acceptance × Efficiency with respect to those in lowest $\cos\theta^*$ bin. Vertical bars correspond statistical uncertainties on raw yields.

and the results are consistent. The dependence of the reconstruction efficiency for a $\cos\theta^*$ range on the azimuthal angle of vector meson (ϕ_V) relative to the event plane angle (ψ) is also studied. The reconstruction efficiencies obtained in a $\cos\theta^*$ range by integrating over ϕ_V - ψ are similar to the efficiency obtained by averaging over the ϕ_V - ψ bins. Efficiency calculation using the event plane from reconstructed MC tracks and generated MC tracks are calculated and results are consistent. In calculation of $A \times \epsilon_{\rm rec}$, $\cos\theta^*$ are obtained by using the momentum information from both the generated track and reconstructed track. In both cases $A \times \epsilon_{\rm rec}$ are consistent. All these checks are discussed in the Appendix B.10.

3.2.3   Re-weighted Acceptance $\times$ Efficiency

The simulated resonance spectra used in the $A \times \epsilon_{\rm rec}$ calculation may have different shapes than the measured resonance spectra and $A \times \epsilon_{\rm rec}$ may vary significantly over the width of a $p_{\rm T}$ bin in the measured spectrum at low $p_{\rm T}$. Therefore, a re-weighting procedure of simulated $p_{\rm T}$ spectra is carried out to consider the shape of the simulated $p_{\rm T}$ distribution as well as the change in $A \times \epsilon_{\rm rec}$ over the width of a $p_{\rm T}$ bin at low $p_{\rm T}$. The left panel of Fig. 3.10 shows the generated and reconstructed K^{*0} spectrum plotted along with the measured ($A \times \epsilon_{\rm rec}$ corrected) K^{*0} spectrum and the Levy-Tsallis [16] fit of the measured spectrum for $0.6 < \cos\theta^* < 0.8$ in 10–50% Pb–Pb collisions with respect to the PP. An iterative procedure is performed to determine the correct weighting and therefore the correct $A \times \epsilon_{\rm rec}$.

- $A \times \epsilon_{\rm rec}$ is calculated from MC generated and reconstructed $p_{\rm T}$ spectrum in similar $p_{\rm T}$ binning as used in data.

- $A \times \epsilon_{\rm rec}$ is used to correct the measured $p_{\rm T}$ spectrum.

- $A \times \epsilon_{\rm rec}$ corrected $p_{\rm T}$ spectrum is fitted with Levy-Tsallis [16] function.

- MC simulated spectra are again extracted in smaller p_T bins. Levy-Tsallis fit of measured spectrum is used to weight the MC generated spectrum. A p_T dependent weight is applied to the generated spectrum so that it follows the fit (the right panel of Fig. 3.10). The same weight is also applied to the reconstructed spectrum.

- Now this weighted simulated spectra are used to calculate the $A \times \epsilon_\mathrm{rec}$ in a similar p_T binning as used in data.

- Above mention procedure is repeated until the change between $A \times \epsilon_\mathrm{rec}$ in two successive iteration becomes < 0.1 %. It is observed that two iterations are usually sufficient for this procedure to converge.

The ratio between original $A \times \epsilon_\mathrm{rec}$ and weighted $A \times \epsilon_\mathrm{rec}$ is the re-weighted factor. The re-weighted factor is maximum at low p_T, whereas at intermediate and high p_T the correction factor is negligible. Final corrected yield is obtained with weighted $A \times \epsilon_\mathrm{rec}$. The re-weighted factor as a function of p_T for various $\cos\theta^*$ ranges in 10–50% Pb–Pb collisions and minimum bias pp collisions are shown in Fig. 3.11 and in Fig. 3.12 for K^{*0} and ϕ mesons, respectively. The re-weighted factor is larger in the PP analysis compared to the EP analysis. This is due to the effect of acceptance on the shape of MC reconstructed spectra as shown in the Appendix B.11.

3.3 Corrected p_T spectra

Raw spectra are corrected for the $A \times \epsilon_\mathrm{rec}$ and branching ratio. The normalized corrected spectra is obtained by using the following formula:

$$\frac{d^2N}{dp_\mathrm{T}dy} = \frac{\text{Raw Counts}}{2 \times N_\mathrm{evt} \times \text{BR} \times dp_\mathrm{T} \times dy \times A \times \epsilon_\mathrm{rec}}, \qquad (3.20)$$
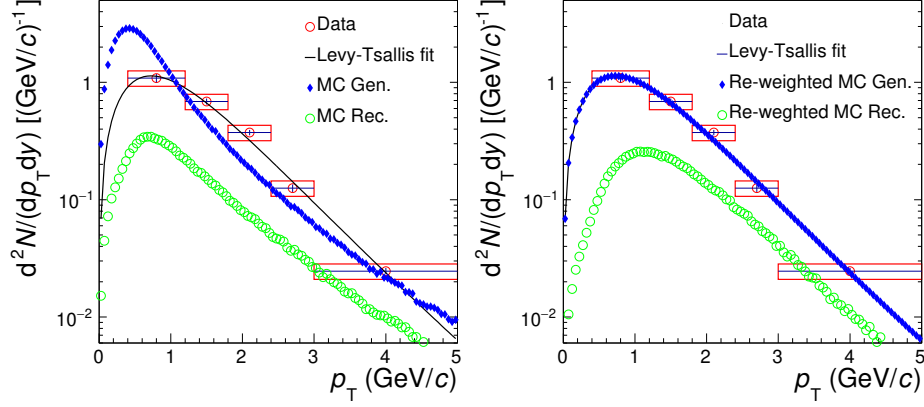
Figure 3.10: Left panel: Measured K^{*0} spectrum (red) along with Levy-Tsallis fit (black curve) and un-weighted MC simulated spectra in 10–50% Pb–Pb collisions at $\sqrt{s_{NN}} = 2.76$ TeV for $0.6 < \cos\theta^* < 0.8$. Right panel: Weighted MC simulated K^{*0} spectra along with measured K^{*0} spectrum and Levy-Tsallis fit.
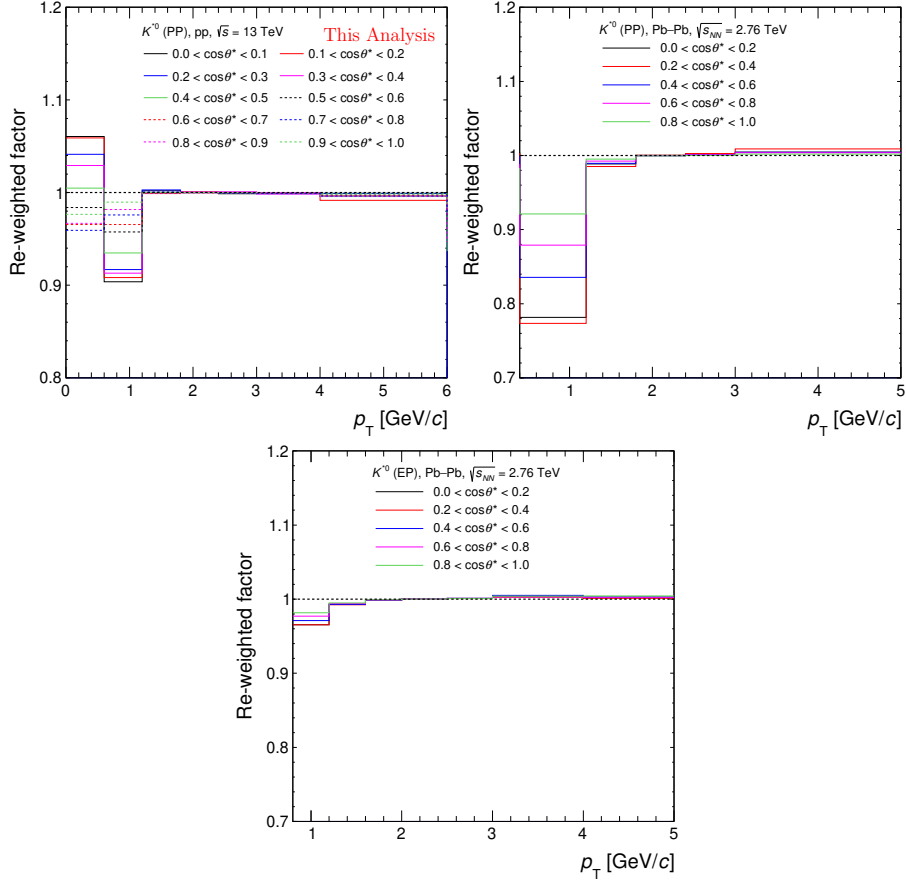
Figure 3.11: The re-weighted factor for the K^{*0} as a function of p_T for different $\cos\theta^*$ bins in 10–50% Pb–Pb collisions at $\sqrt{s_{NN}} = 2.76$ TeV and in minimum bias pp collisions at $\sqrt{s} = 13$ TeV.
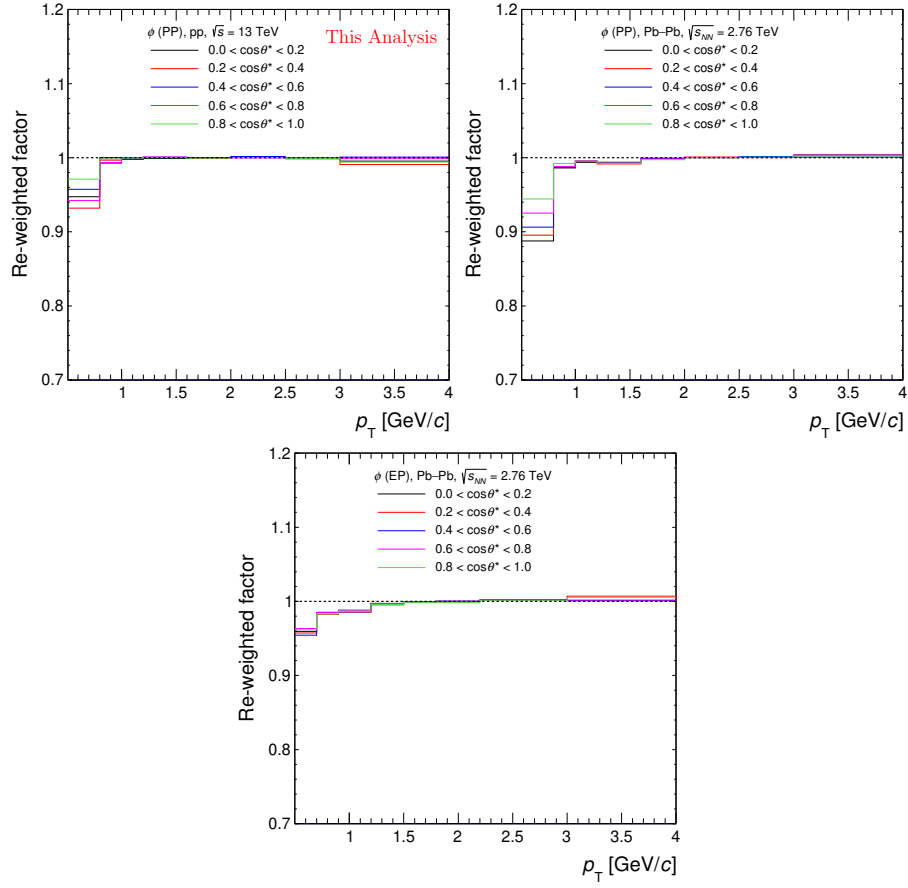
Figure 3.12: The re-weighted factor for the ϕ as a function of p_T for different $\cos\theta^*$ bins in 10–50% Pb–Pb collisions at $\sqrt{s_{NN}} = 2.76$ TeV and in minimum bias pp collisions at $\sqrt{s} = 13$ TeV.
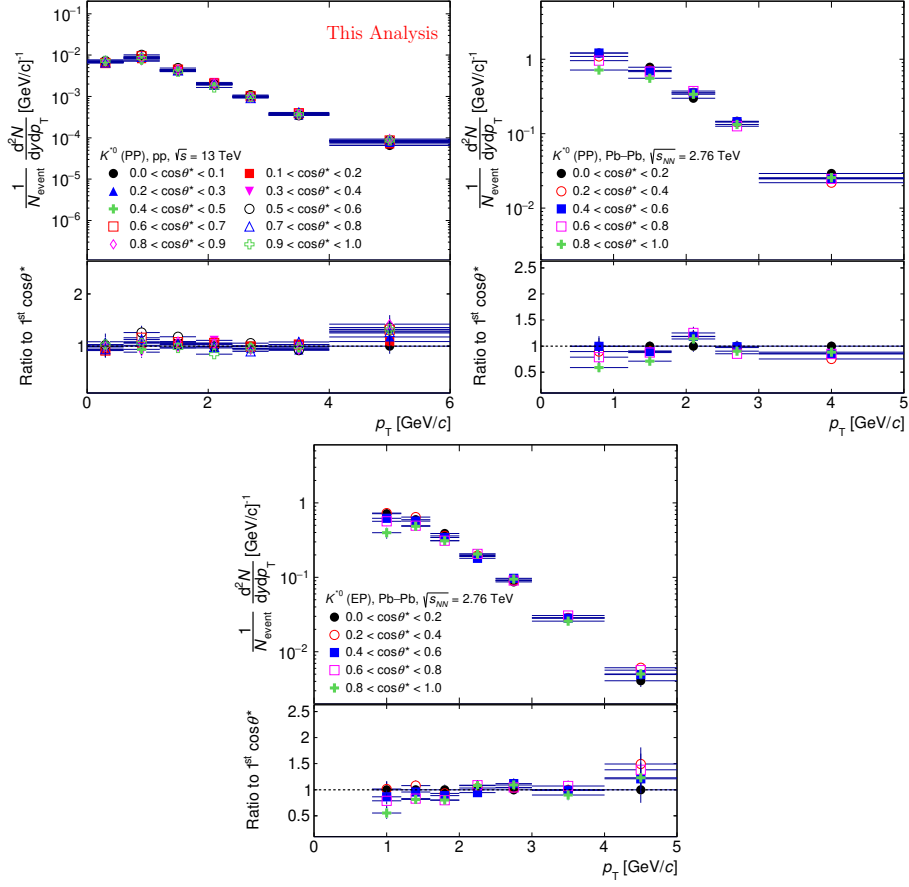
Figure 3.13: The efficiency and acceptance corrected K^{*0} meson yields as a function of p_T for different $\cos\theta^*$ bins in 10–50% Pb–Pb collisions at $\sqrt{s_{NN}} = 2.76$ TeV and in minimum bias pp collisions at $\sqrt{s} = 13$ TeV. Lower panels show the ratio of corrected yields with respect to those in lowest $\cos\theta^*$ bin. Vertical bars correspond statistical uncertainties on raw yields.

where factor 2 is used to average over K^{*0} and $\overline{K}^{*0}$ and BR is the branching ratio (0.66 for K^{*0} and 0.49 for ϕ). Corrected K^{*0} and ϕ yields as a function of p_T for various $\cos\theta^*$ ranges in 10–50% Pb–Pb collisions and minimum bias pp collisions are shown in Fig. 3.13 and in Fig. 3.14.

The yields of vector mesons are summed over $\cos\theta^*$ bins for each p_T interval to obtain the p_T distributions. These p_T distributions are found to be consistent within the uncertainties with the published [17] p_T distributions in Pb–Pb collisions. Figure 3.15 shows few example of comparison of corrected yield between this analysis
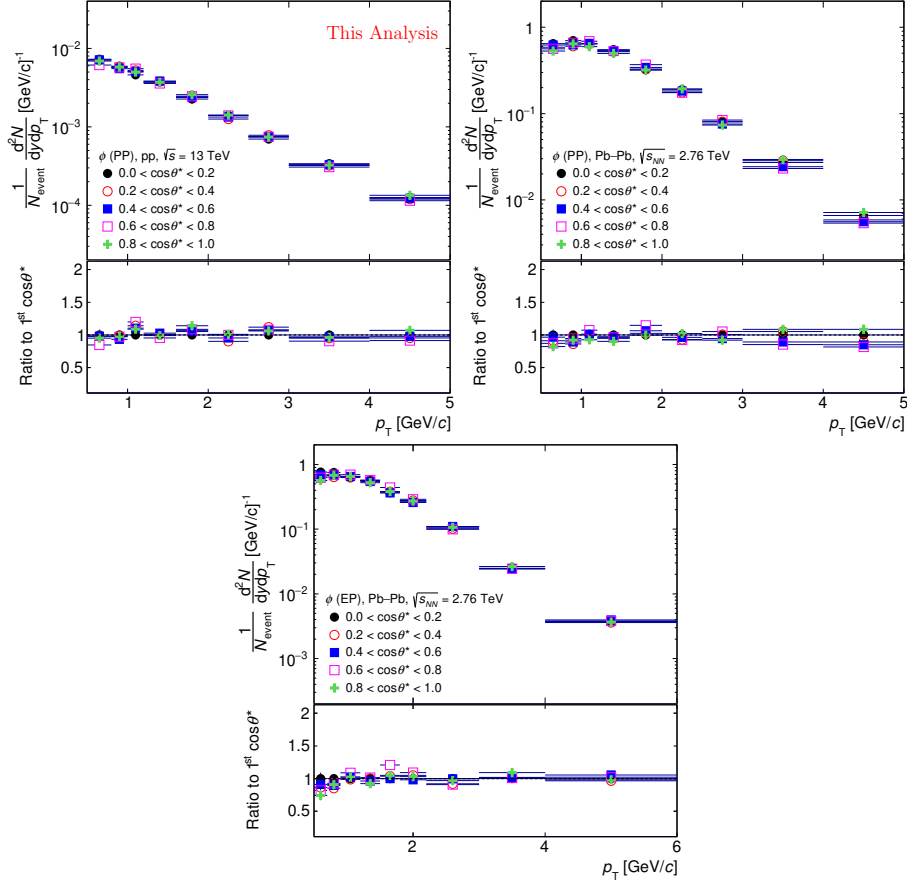
Figure 3.14: The efficiency and acceptance corrected ϕ meson yields as a function of p_{T} for different $\cos\theta^*$ bins in 10–50% Pb–Pb collisions at $\sqrt{s_{\mathrm{NN}}} = 2.76$ TeV and in minimum bias pp collisions at $\sqrt{s} = 13$ TeV. Lower panels show the ratio of corrected yields with respect to those in lowest $\cos\theta^*$ bin. Vertical bars correspond statistical uncertainties on raw yields.

and published result.

3.4   Corrected $\cos\theta^*$ distributions

The efficiency and acceptance corrected $dN/d\cos\theta^*$ distributions at mid-rapidity for selected p_{T} ranges in minimum bias pp collisions and 10–50% central Pb–Pb collisions are shown in Fig 3.16 along with those for K_S^0 in 20–40% central Pb–Pb collisions. These distributions are fitted with the functional form given in Eq. 3.1 to extract the ρ_{00} values for each p_{T} range in pp and Pb–Pb collisions. The angular distributions
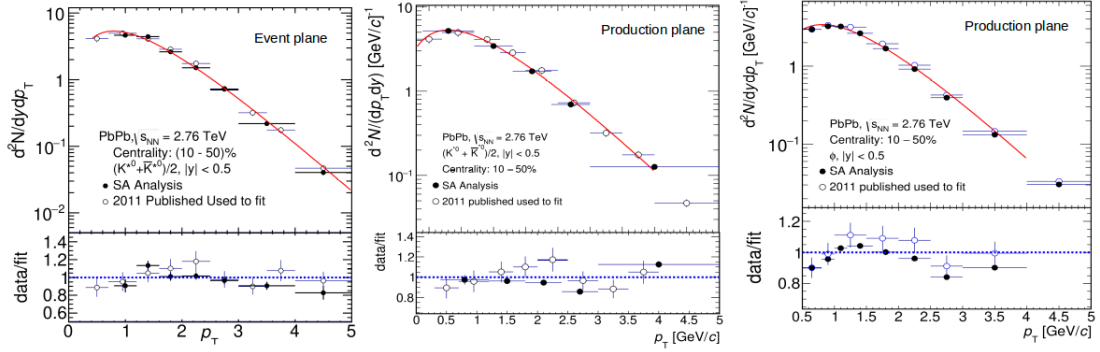
Figure 3.15: Comparison of the efficiency and acceptance corrected vector meson yield between this analysis and published result. Uncertainties on the published [17] data points are $\sqrt{(\text{statistical uncertainties})^2 + (\text{systematic uncertainties})^2}$ and uncertainties on the corrected yields obtained from this analysis are statistical only.

for vector mesons in Pb–Pb collisions with respect to the normal to both PP and EP show a strong $\cos\theta^*$ dependence, whereas for vector mesons in pp collisions and for K_S^0 in Pb–Pb collisions the distributions are nearly uniform with $\cos\theta^*$. The efficiency and acceptance corrected $\cos\theta^*$ distributions for vector mesons and K_S^0 in selected p_T ranges and centrality classes are given in the Appendix B.7.

3.5 Systematic uncertainties

Systematic uncertainties on ρ_{00} have three major contributions: 1) uncertainties due to signal extraction, 2) uncertainties due to particle identification criteria and 3) uncertainties due to track selection criteria.

A particular variation is considered as a source of systematic uncertainty if it fails the Barlow check [18]. Barlow check is carried out as follows: let us consider two cases, where one measurement is due to the default selection criteria and another is due to a systematic variation of a default selection criteria (e.g. normalization range variation). Let the yield in the default case be denoted as y_{def} with statistical error σ_{def} and yield in the systematic case be denoted as y_{sys} with statistical error σ_{sys}. Then the difference between yields be denoted as $\Delta = y_{\text{def}} - y_{\text{sys}}$ and the quadrature
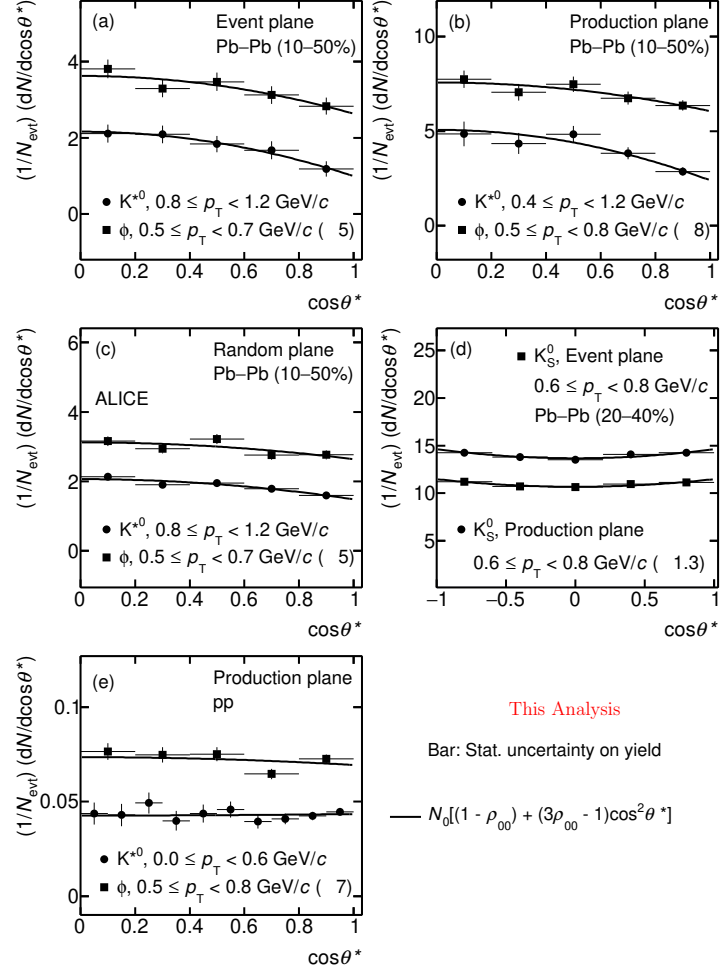
Figure 3.16: Angular distribution of the vector meson decay daughter in the rest frame of the vector meson with respect to the quantization axis at $|y| < 0.5$ in pp collisions at $\sqrt{s} = 13$ TeV and Pb–Pb collisions at $\sqrt{s_{NN}} = 2.76$ TeV. Panels (a) - (c) show results for K^{*0} and ϕ with respect to the EP, PP, and random event plane. Panels (d) and (e) are the results for K_S^0 with respect to both the PP and EP, and for vector mesons in pp collisions with respect to PP, respectively.

105

difference of their statistical error as $\sigma = \sqrt{\sigma_{\text{def}}^2 - \sigma_{\text{sys}}^2}$. Barlow number "n" is defined as $n = \Delta/\sigma$. If $n < 1$ then the variation passes Barlow check and consistent with the default measurement with the corresponding statistical uncertainties, hence excluded from the calculation of systematic uncertainties. We consider following steps to do Barlow check:

- For a systematic variation we calculate the factor n for each p_{T} bin in a given $\cos\theta^*$ range.

- Plot the histogram or frequency distribution of n.

- If two measurements are statistically consistent then the n distribution should have following criteria: 1) Mean at 0, 2) Rms < 1.0, 3) In $|n| < 1$ there will be > 68% of counts, 4) In $|n| < 2$ there will be > 95% of counts.

- As the entries are less so a modified criteria is proposed for passing the Barlow check. 1) $|Mean| < 0.3$, 2) Rms < 1.3, 3) In $|n| < 1$ there will be > 55% of counts, 4) In $|n| < 2$ there will be > 75% of counts.

- If any 3 of these above mention criteria are passed for a given source then we consider that the source pass barlow check. If a source passes the Barlow check, we exclude it from systematic uncertainties as the variation is governed by statistical uncertainty.

After selecting the true sources for systematic uncertainties, we fit the corrected $\cos\theta^*$ distribution of each variation to get ρ_{00} values for those variations. Let for a given source we have k number of variations. Then the systematic uncertainty on ρ_{00} due to this source is $\sqrt{\frac{1}{k} \sum_{i=1}^{k} (\rho_{00}^{\text{def}} - \rho_{00}^{i})^2}$. From the previous analysis on resonance production measurements in Pb–Pb collisions, it is found that the systematic
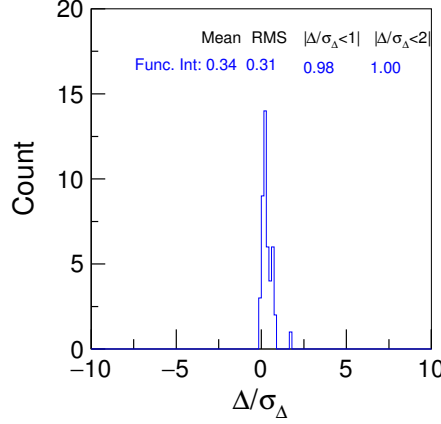
Figure 3.17: Barlow check due to bin counting in 10–50% Pb–Pb collisions for K^{*0}. The quantization axis is perpendicular to the event plane.

uncertainties are independent of centralities. We have estimated the systematic uncertainties for centrality class 10–50% and the same % uncertainties are propagated in other centrality classes. An example of the Barlow check for yield extraction method is shown in Fig. 3.17.

3.5.1 Systematic uncertainty due to signal extraction

Systematic uncertainty due to signal extraction includes variations of normalization range for mixed event background normalization during signal extraction of vector mesons, variations of fitting range during the fitting of mixed background subtracted invariant mass distribution of unlike charged πK and KK pairs, variation of residual background fit function (3rd order polynomial function instead of default 2nd order polynomial function for K^{*0} and 1st order polynomial function instead of default 2nd order polynomial function for ϕ), and by leaving the width of the K^{*0} resonance peak free, and keeping the width of ϕ resonance peak fixed to the PDG value while the mass resolution is free.

3.5.2 Systematic uncertainty due to particle identification

Systematic uncertainty due to PID includes variations of TPC nσ and TOF nσ for π and K selection. For default measurements TPC 2 σ with TOF VETO 3 σ is used for both π and K selection, whereas TPC 3σ with TOF VETO 4σ and TPC 2σ with TOF VETO 2σ are used for systematic study.

3.5.3 Systematic uncertainty due to track and event selection

Systematic uncertainty due to track selection is estimated by varying the default track selection criteria of the analysis as discussed in 3.1.2. This includes variations of distance of closest approach from the primary vertex along the beam direction and in the transverse plane, number of the TPC crossed rows variations, variations of χ^2 per cluster value obtained from the fitting of the TPC clusters and the ITS clusters during track reconstruction and variations of the ratio of the number of crossed rows to the number of findable clusters in the TPC.

Systematic uncertainties exhibit a small fluctuations as a function of p_{T}, while one might expect the "true systematic uncertainties to be more smoothly varying. The dips and spikes in the systematic uncertainties have been smoothed by averaging over nearest bin to achieve a more uniform set of systematic uncertainties. Each of the PID selection criteria, track selection criteria and signal extraction criteria are varied independently and contribution from each of the sources are added in quadrature to get the total systematic uncertainties, considering them uncorrelated to each other. Figure 3.18 and Fig. 3.19 shows contributions from various sources along with the total systematic uncertainties on observed ρ_{00} (Y_{sys}) and the event plane resolution corrected ρ_{00} ($Y_{\mathrm{sys}}^{\mathrm{rescor}}$) after Barlow check and smoothening for K^{*0} and ϕ, respectively. $Y_{\mathrm{sys}}^{\mathrm{rescor}}$ are related to Y_{sys} by $Y_{\mathrm{sys}}^{\mathrm{rescor}} = \frac{\rho_{00}^{\mathrm{obs}}}{\rho_{00}^{\mathrm{rescor}}} \times Y_{\mathrm{sys}} \times \frac{4}{1+3R}$.

An alternative method of systematic uncertainty estimation on ρ_{00} value from the
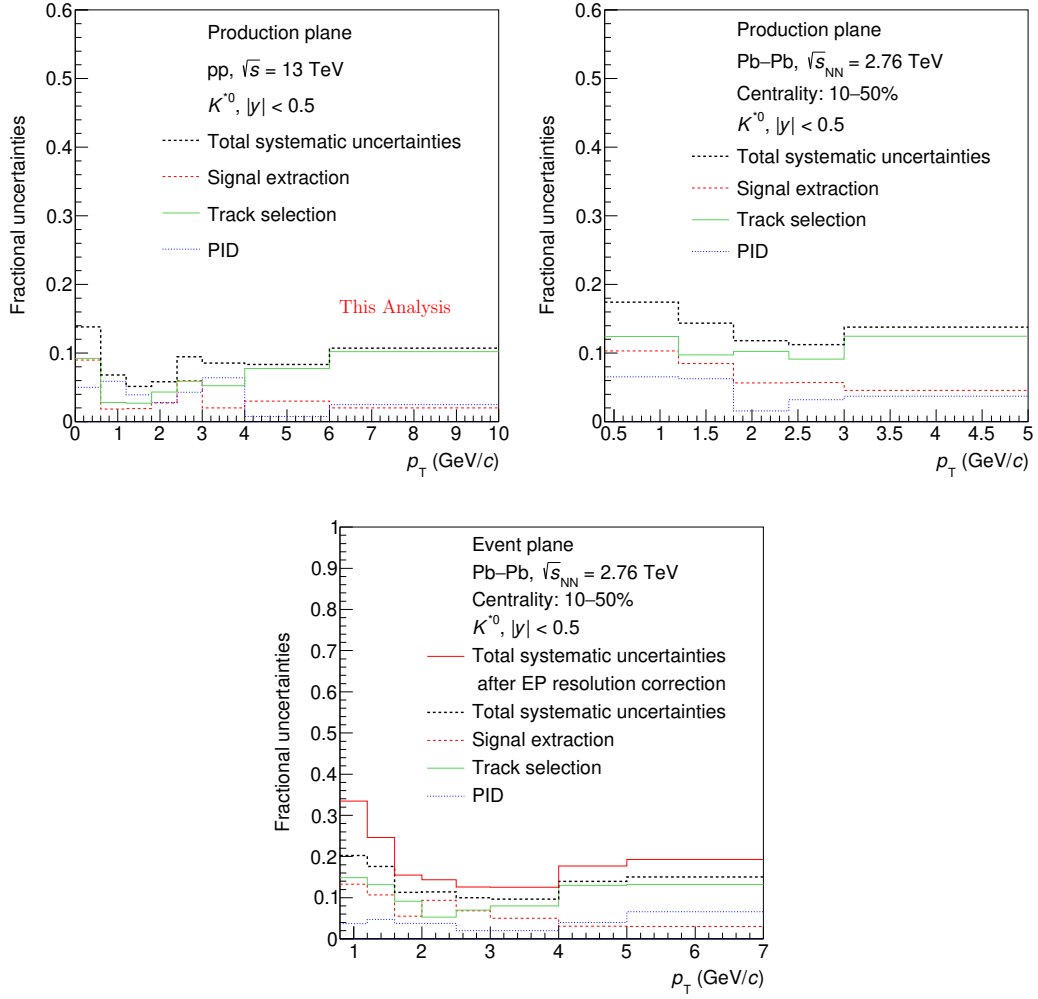
Figure 3.18: Fractional systematic uncertainties on ρ_{00} for the K^{*0} meson in pp and Pb–Pb collisions.
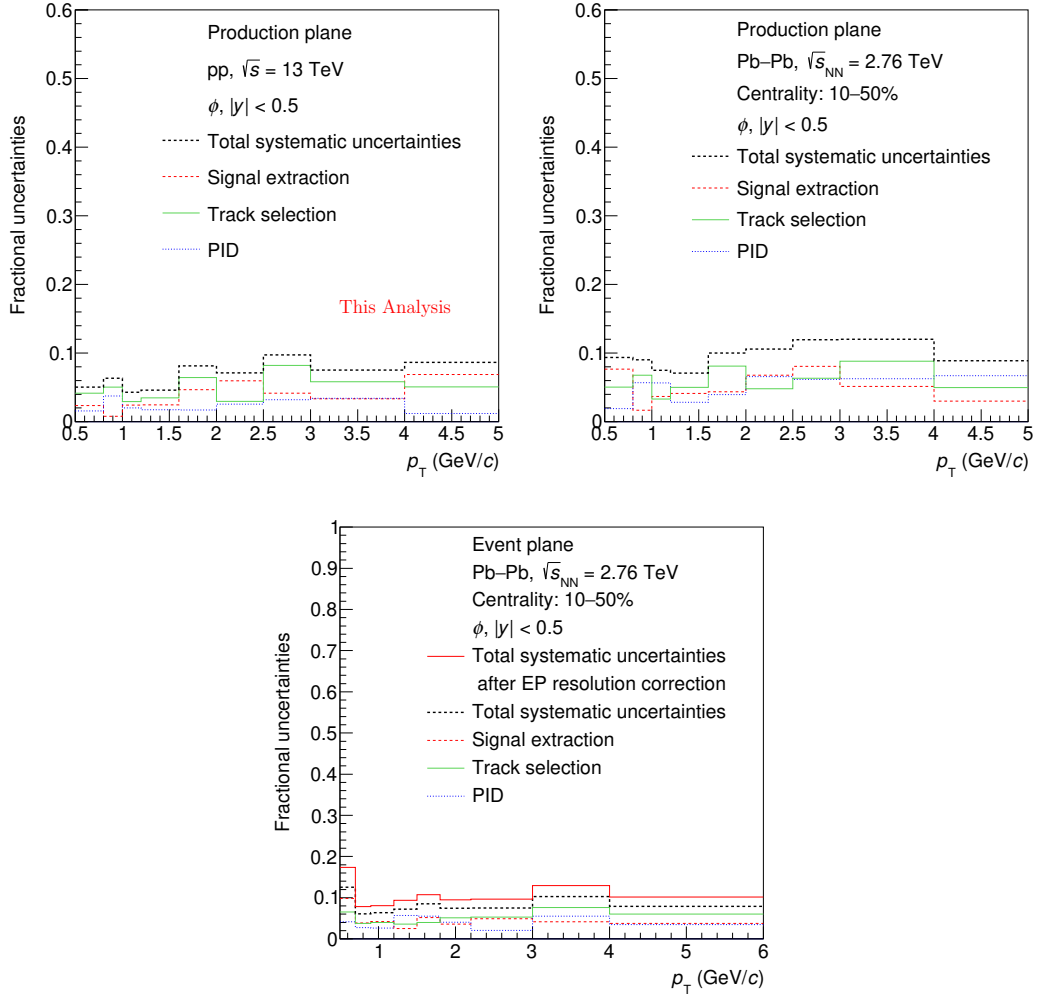
Figure 3.19: Fractional systematic uncertainties on ρ_{00} for the ϕ meson in pp and Pb–Pb collisions.

Table 3.2: Summary of systematic uncertainties on observed ρ_{00} values for K^{*0} and ϕ vector mesons

Particle	Signal extraction		Track selection		Particle identification	
	low p_{T}	highp_{T}	low p_{T}	highp_{T}	low p_{T}	highp_{T}
K^{*0}	12%	4%	14%	11%	5%	4%
ϕ	8%	3%	6%	5%	3%	4.5%

systematic uncertainty on measured vector meson yield is also performed as a cross check. We have found that the systematic uncertainty used for this analysis is compatible with those obtained from the alternative method. Detail about the alternative method of systematic uncertainty estimation on ρ_{00} is given in Appendix B.12.

A summary of systematic uncertainties on observed ρ_{00} for K^{*0} and ϕ meson averaging over different frame of refference and collision system is given in Table 3.2.

3.6 Results

3.6.1 Transverse momentum dependence of ρ_{00}

Figure 3.20 shows ρ_{00} values as a function of p_{T} for vector mesons and K_S^0 at $|y| < 0.5$ in Pb–Pb collisions at $\sqrt{s_{\mathrm{NN}}} = 2.76$ TeV and in pp collisions at $\sqrt{s} = 13$ TeV [19]. Panels (a) and (b) show measurements with respect to normal to the EP, panels (c) and (d) show results with respect to perpendicular direction of the PP, and panels (e) and (f) show measurements with respect to the normal to the RndEP. The left column of Fig. 3.20 shows results for K^{*0} and the right column of Fig. 3.20 shows results for the ϕ. Measured ρ_{00} values for the K^{*0} and ϕ with respect to the EP and the PP in 10–50% Pb–Pb collisions at $\sqrt{s_{\mathrm{NN}}} = 2.76$ TeV deviate from 1/3 at low p_{T}, whereas at high p_{T}, measurements are consistent with 1/3. Control measurements such as ρ_{00} values for vector mesons in pp collisions at $\sqrt{s} = 13$ TeV and ρ_{00} values
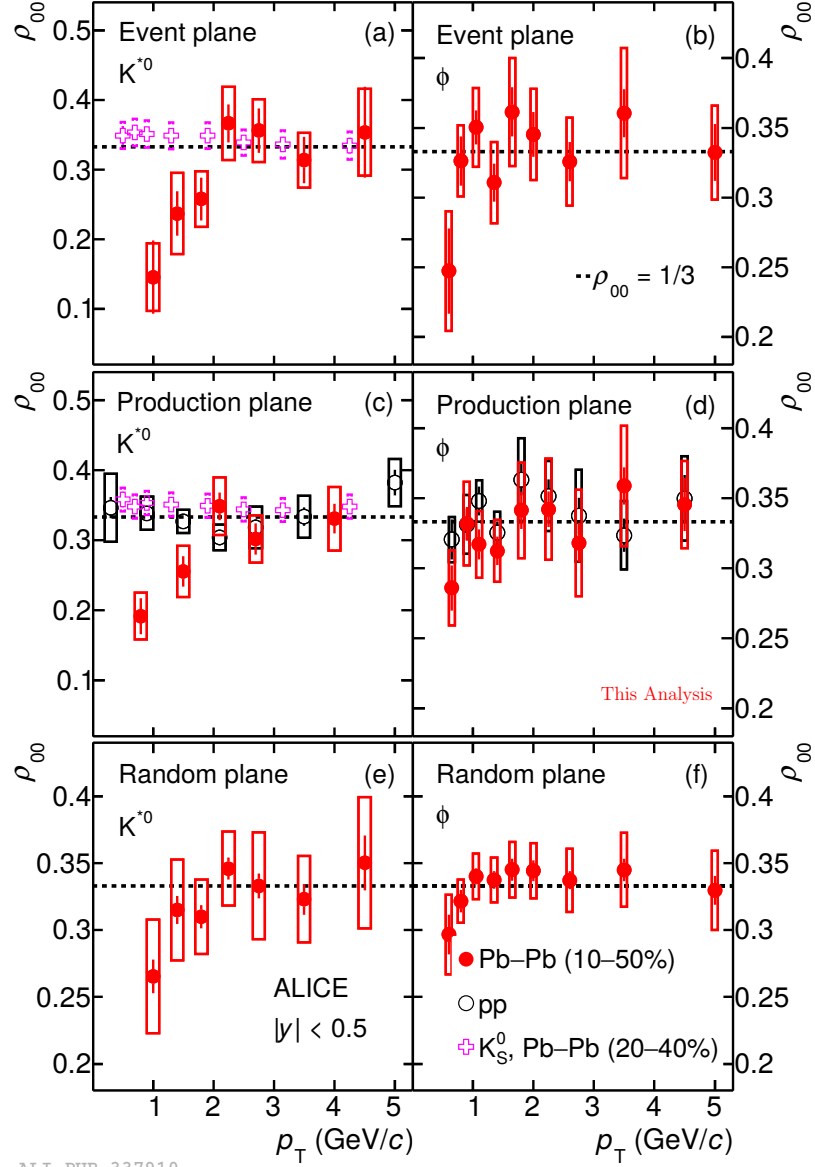
Figure 3.20: The p_T dependence of ρ_{00} corresponding to K^{*0}, ϕ, and K_S^0 mesons at $|y| < 0.5$ in Pb–Pb collisions at $\sqrt{s_{NN}} = 2.76$ TeV and in minimum bias pp collisions at $\sqrt{s} = 13$ TeV [19]. The statistical and systematic uncertainties are shown as bars and boxes, respectively.

for K_S^0 in 20–40% Pb–Pb collisions are consistent with 1/3 throughout the whole measured p_T interval. The extracted ρ_{00} values for vector mesons with respect to the RndEP are also consistent with 1/3 except in the lowest p_T bin where a small deviation from 1/3 is observed. At low p_T we observe the hierarchy, ρ_{00} (EP) < ρ_{00} (PP) < ρ_{00} (RndEP).

This hierarchy between different frames of reference can be understood from the analytical relations between different frames. The relation between measured ρ_{00} with respect to two different frames of references is

$$\rho_{00} \text{ (A)} - \frac{1}{3} = \left(\rho_{00} \text{ (B)} - \frac{1}{3} \right) \left(\frac{1}{4} + \frac{3}{4} \cos 2\psi \right), \tag{3.21}$$

where frame A is obtained by rotating frame B by angle ψ. Averaging over angle ψ gives,

$$\rho_{00} \text{ (A)} - \frac{1}{3} = \left(\rho_{00} \text{ (B)} - \frac{1}{3} \right) \left(\frac{1}{4} + \frac{3}{4} \langle \cos 2\psi \rangle \right). \tag{3.22}$$

The transformation from the EP to PP is obtained by taking into account the elliptic flow of the vector meson which leads to

$$\langle \cos 2\psi \rangle = \frac{1}{2\pi} \int_{-\pi}^{\pi} \cos(2\psi)[1 + 2v_2 \cos(2\psi)] d\psi = v_2. \tag{3.23}$$

Using Eq. 3.22 and Eq. 3.23, analytical relation between EP and PP can be expressed as,

$$\rho_{00} \text{ (PP)} - \frac{1}{3} = \left(\rho_{00} \text{ (EP)} - \frac{1}{3} \right) \left(\frac{1 + 3v_2}{4} \right). \tag{3.24}$$

In order to verify 3.24 a toy model simulation with PYTHIA (version 8.2) event generator [32] is carried out. PYTHIA does not have any azimuthal anisotropy and spin alignment. For this study we have taken the event plane angle as zero, which corresponds impact parameter along x-axis. In order to find the relations between different frames, v_2 (0.15 ± 0.06, value expected for hadrons with mass similar to K^{*0} in Pb–Pb collisions at $\sqrt{s_{NN}} = 2.76$ TeV [33]) is introduced to K^{*0} by appropriate
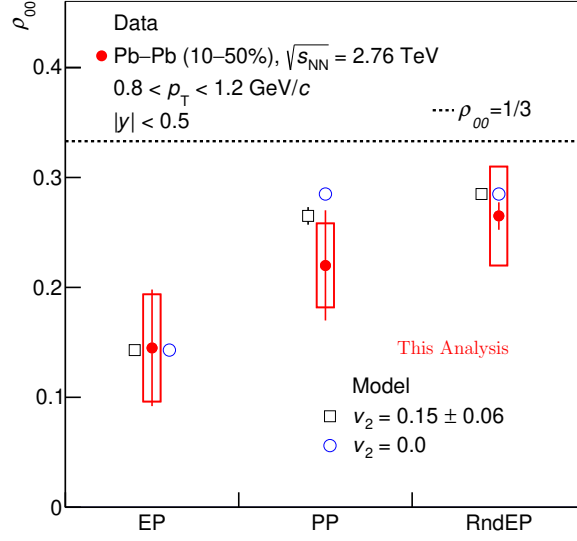
Figure 3.21: ρ_{00} values from data in 10–50% Pb–Pb collisions at $0.8 < p_T < 1.2$ GeV/c with respect to various planes [19] compared with expectations from model simulations with and without added elliptic flow (v_2). The statistical and systematic uncertainties are shown as bars and boxes, respectively.

rotation of its momentum in the azimuthal plane. The modified angle in the azimuthal plane is calculated by solving the following equation

$$\phi_0 = \phi + v_2 \sin 2\phi, \tag{3.25}$$

where ϕ_0 is azimuthal angle of a K^{*0} in absence of v_2 and for a given value of v_2, ϕ_0 transforms to ϕ. Then spin alignment through ρ_{00} same as measured in data is introduced with respect to the event plane by rotating the momentum of decay daughters in K^{*0} rest frame by solving

$$\cos \theta_0^* = 3/2 \times [(1 - \rho_{00}) \cos \theta^* + 1/3(3\rho_{00} - 1) \cos^3 \theta^*]. \tag{3.26}$$

Here θ_0^* is the angle made by the decay daughter of K^{*0} with the quantization axis in absence of spin alignment. θ_0^* transforms to θ^* to introduce a given input value of ρ_{00}. In this study we assume that the ϕ^* (azimuthal angle of vector meson decay daughter in vector meson rest frame, see Fig. B.1) is remain fixed during the rotation.

114

With these modifications, calculations as in the experimental data are carried out. The results are shown in Fig. 3.21 for two cases, with and without v_2 [19]. The result corresponding to the event plane is correctly retrieved in the model. The model results for $v_2 = 0$, are same for the production plane and random event plane. However with $v_2 = 0.15$, the ρ_{00} (PP) value is lower and closer to data for PP. The toy model reproduces the hierarchy observed in the ρ_{00} values for various planes as observed in data.

The RndEP is defined by randomizing the event plane angle in the azimuthal plane (xy plane). The quantization axis is obtained by taking cross product of the event plane vector and z-axis (beam axis). Hence, the quantization axis is always in the xy plane, and a residual effect is present due to use of a common z-axis. Decay daughters of polarized vector mesons could have angular correlation with respect to the z-axis. This residual effect is due to the angular distribution of decay daughters, which follow a oblate or prolate shape, which is rotationally symmetric around the quantization axis (when the off-diagonal terms in the spin density matrix are zero). Rotating such a shape around the z-axis does not lead to a uniform decay angular distribution. This effect results in small deviation of ρ_{00} values from 1/3 for RndEP. This deviation of ρ_{00} from 1/3 for RndEP has been also discussed in Ref [3]. The physical picture is that spin alignment with respect to the event plane is coupled to that in the production plane through the elliptic flow of the system. The ρ_{00} (RndEP) is lower than 1/3 as the quantization axis is always perpendicular to the beam axis, resulting in a residual effect. This residual effect can be removed by choosing the quantisation axis in a random direction in 3 dimensions for each event. If the quantization axis is random in 3 dimension, then the residual effect is not present and the ρ_{00} value is consistent with 1/3 (shown in the Appendix B.9).
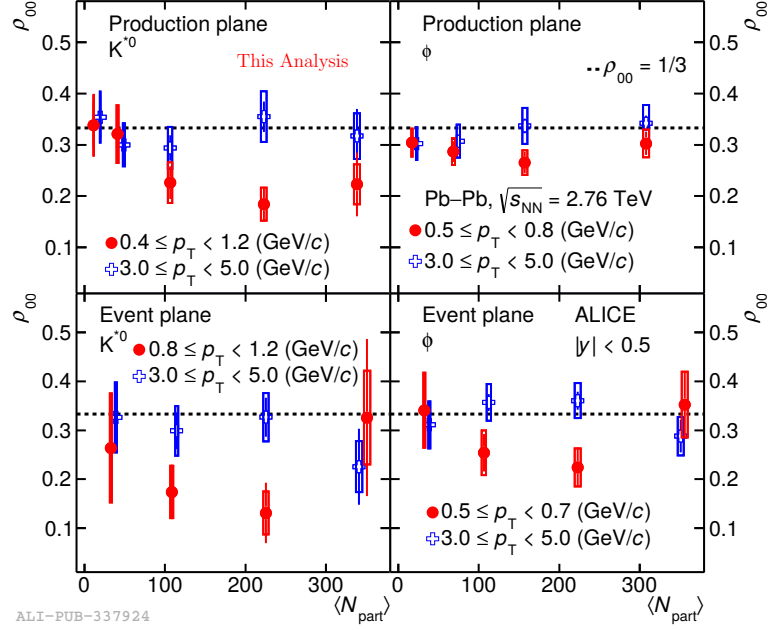
Figure 3.22: ρ_{00} vs. $\langle N_{\mathrm{part}} \rangle$ for vector mesons at low p_{T} and high p_{T} in Pb–Pb collisions at $\sqrt{s_{\mathrm{NN}}} = 2.76$ TeV [19]. Bars and boxes represent statistical and systematic uncertainties, respectively.

3.6.2 Centrality dependence of ρ_{00}

Figure 3.22 shows ρ_{00} as a function of the average number of participant nucleons ($\langle N_{\mathrm{part}} \rangle$) for K^{*0} and ϕ w.r.t. both the PP and EP for two different p_{T} region [19]. Measured ρ_{00} values for vector mesons at high p_{T} do not show any centrality dependence and are consistent with 1/3 for all studied centrality classes. However, at low p_{T} a clear centrality dependence of the measured ρ_{00} value is observed. At low p_{T} maximum deviation of ρ_{00} from 1/3 occurs in mid-central collisions whereas in central and peripheral collisions, the measurements are consistent with 1/3.

3.7 Discussion

3.7.1 Theory expectation

In theory there are some specific predictions for vector meson spin alignment. In the the presence of a large angular momentum, the spin-orbit coupling of quantum chromodynamics (QCD) could lead to a polarization of quarks followed by a net-polarization of vector mesons along the direction of the angular momentum [20, 37, 21, 22]. In quark polarization model [20, 37, 21, 22] $\rho_{00} < 1/3$ if the vector meson is produced from the recombination of two polarized quarks, and $\rho_{00} > 1/3$ if the hadronization of a polarized parton proceeds via the fragmentation process. In the quark recombination hadronization scenario, ρ_{00} is expected to have maximum deviation from $1/3$ at low-p_{T}, whereas at high-p_{T} and ρ_{00} reach the value of $1/3$. ρ_{00} is expected to have a smaller deviation from $1/3$ for both central and peripheral heavy-ion collisions, and a maximum deviation for mid-central collisions, where the angular momentum is also maximal [1].

The observed p_{T} dependence of ρ_{00} is qualitatively consistent with the prediction from the quark recombination model of polarized quarks [20, 37, 21, 22] which attributes the spin alignment to polarization of quarks in the presence of large initial angular momentum in non-central heavy-ion collisions and a subsequent hadronization by the process of recombination. The centrality or $\langle N_{\mathrm{part}} \rangle$ dependence of ρ_{00} is consistent with the variation of initial angular momentum with impact parameter in heavy-ion collisions [1].

3.7.2 Comparison to other experiments

Spin alignment measurements have been performed in various collision systems in the past. Several measurements in $\mathrm{e^+e^-}$ [23, 24, 25], hadron–proton [26] and nucleon–

nucleus collisions [27] were carried out to understand the role of spin in the dynamics of particle production. These measurements in small collision systems with respect to the production plane have $\rho_{00} > 1/3$ and off-diagonal elements close to zero. For pp collisions at $\sqrt{s} = 13$ TeV the $\rho_{00} \sim 1/3$ for the p_{T} range studied. Initial measurements at RHIC[3] with a relatively small sample of Au–Au collisions at $\sqrt{s_{\mathrm{NN}}} = 200$ GeV did not find significant spin alignment for the vector mesons [28]. Recent preliminary results from the STAR collaboration [29] have also found similar p_{T} dependency of ρ_{00} for K^{*0} mesons at lower $\sqrt{s_{\mathrm{NN}}}$. However, ρ_{00} for ϕ mesons are larger than $1/3$ in mid-central Au–Au collisions at $\sqrt{s_{\mathrm{NN}}} = 200$ GeV [30]. The $\rho_{00} > 1/3$ for ϕ mesons do not explained by naive quark recombination and fragmentation model [20] but can be interpreted as an effect of coherent ϕ meson field [31].

3.7.3 Extraction of quark and vector meson polarization

In recombination hadronization scenario of polarized quarks, the ρ_{00} of vector mesons are related to quark polarization as $\rho_{00} = \frac{1 - P_{\mathrm{q}} P_{\bar{\mathrm{q}}}}{3 + P_{\mathrm{q}} P_{\bar{\mathrm{q}}}}$ where P_{q} and $P_{\bar{\mathrm{q}}}$ are the polarization of quark and anti-quark in presence of the initial angular momentum [20]. Assuming $P_{\mathrm{u}} = P_{\bar{\mathrm{u}}} = P_{\mathrm{d}} = P_{\bar{\mathrm{d}}}$ and $P_{\mathrm{s}} = P_{\bar{\mathrm{s}}}$, the measured p_{T} integrated ρ_{00} values for K^{*0} and ϕ mesons in 10–50% Pb–Pb collisions could translate to light quark polarization of $\sim$0.8 and strange quark polarization of $\sim$0.2. Using a thermal and non-relativistic approach as discussed in [38], vorticity (ω) and temperature (T) are related to ρ_{00} and vector meson polarization (P_{V}) as $\rho_{00} \simeq \frac{1}{3}\left(1 - \frac{(\omega/T)^2}{3}\right)$ and $P_{\mathrm{V}} \simeq (2\omega/3T)$, respectively. Also in this approach, the measured ρ_{00} for K^{*0} would correspond to K^{*0} polarization of $\sim$0.6 and the ρ_{00} for ϕ mesons would give ϕ meson polarization of $\sim$0.3.

---

[3]STAR experiment results have a different event plane resolution correction.

3.7.4 Comparison to hyperon polarization

The polarization of Λ baryons (spin = 1/2) is found to decrease with increasing $\sqrt{s_{NN}}$ [34, 35]. The measured global polarization for Λ baryon at LHC energies are compatible with zero within uncertainties (P_Λ (%) = 0.01 ± 0.06 ± 0.03) [36]. For spin-1/2 particle measurements are done w.r.t. 1st order event plane as one need to know the orientation (sign) of the angular momentum vector. However, for spin 1 particles the effect of "spin up" and "spin down" are the same, so one need only the second order event plane. The spin alignment for vector mesons in heavy ion collisions could have contributions from angular momentum [37, 20], electromagnetic fields [22] and mesonic fields [31]. While no quantitative theoretical calculation for vector meson polarization at LHC energies exists, the expected order of magnitude can be estimated and the measurements for vector mesons and hyperons can be related in a model dependent way.

In the quark recombination model, Λ polarization linearly depends on quark polarization (p_q) [37] whereas ρ_{00} depends on the square of quark polarization [20]. With these assumptions and taking the input of p_q from Λ polarization measurements at LHC energies [36], one would expect ρ_{00} is closed to 1/3. Therefore, the observed deviation of ρ_{00} from 1/3 is surprisingly large. However, for spin 1/2 particles the angular distribution of the decay daughters is an odd function and hence depends on the sign of the angular momentum direction. For spin 1 particles the angular distribution of the decay daughters is an even function and only depends on the strength of the angular momentum not on the sign. Unlike vector mesons, hyperons also have a large decay contribution. The ρ_{00} value may also depend on the details of the transfer of the quark polarization to the hadrons during hadronization. In addition, re-scattering, regeneration, lifetime and mass of the hadron, and interaction of the hadron with

the medium may also affect the magnitude of ρ_{00}. Till now, no quantitative theory expectation for vector meson spin alignment at LHC energies exists, therefore these measurements will trigger further theoretical works to understand the results.

3.8   Summary

We report for the first time a significant spin alignment effect (3σ level for K^{*0} and 2σ level for ϕ) for vector mesons in heavy-ion collisions. A deviation of ρ_{00} from $1/3$ at low p_{T} and in mid-central Pb–Pb collisions, supports the presence of a large initial angular momentum in non-central heavy-ion collisions, which leads to quark polarization via spin-orbit coupling, subsequently transferred to hadronic degrees of freedom by hadronization via recombination. However, the measured spin alignment is surprisingly large compared to the polarization measured for Λ hyperons where, in addition, a strong decrease in polarization with $\sqrt{s_{\mathrm{NN}}}$ is observed. In future measurements, the difference in the polarization of $K^{*\pm}$ and K^{*0}, due to their difference in magnetic moment, would be directly sensitive to the effect of the large initial magnetic field produced in heavy-ion collisions.

References

[1] F. Becattini et al., Phys. Rev. C 77, 024906 (2008).

[2] K. Schilling et al., Nucl. Phys. B 15, 397 (1970).

[3] A. H. Tang et al., Phys. Rev. C 98, 044907 (2018).

[4] B. Abelev et al. [ALICE Collaboration], Phys. Rev. C 88, 044909 (2013).

[5] K. Aamodt et al. [ALICE Collaboration], Phys. Rev. Lett. 106, 032301 (2011).

[6] B. B. Abelev et al. [ALICE Collaboration], Int. J. Mod. Phys. A 29, 1430044 (2014).

[7] A. M. Poskanzer et al., Phys. Rev. C 58, 1671 (1998).

[8] C. Alt et al., Phys. Rev. C 68, 034903 (2003).

[9] J. Barrette et al. [E877 Collaboration], Phys. Rev. C 56, 3254 (1997).

[10] A. M. Poskanzer et al., Phys. Rev. C 58, 1671 (1998).

[11] B. B. Abelev et al. [ALICE Collaboration], Phys. Rev. Lett. 111, 222301 (2013).

[12] X. N. Wang et al., Phys. Rev. D 44, 3501 (1991).

[13] P. Z. Skands et al., Eur. Phys. J. C 74, 3024 (2014).

[14] R. Brun et al., Report No.CERN-W5013, 1994

[15] T. Ullrich et al., arxiv:0701199 [physics.data-an].

[16] C. Tsallis, J. Stat. Phys 52, 479 (1988).

[17] J. Adam et al. [ALICE Collaboration], Phys. Rev. C 95, 064606 (2017).

[18] R. Barlow, arXiv:0207026[hep-ex].

[19] S. Acharya et al. [ALICE Collaboration], Phys. Rev. Lett. 125, 012301 (2020).

[20] Z. -T. Liang et al., Phys. Lett. B 629, 20 (2005).

[21] Z.-T. Liang, J. Phys. G 34, S323 (2007).

[22] Y. -G. Yang et al., Phys. Rev. C 97, 034917 (2018).

[23] K. Ackerstaff et al. [OPAL Collaboration], Phys. Lett. B 412, 210 (1997).

[24] K. Ackerstaff et al. [OPAL Collaboration], Z. Phys. C 74, 437 (1997).

[25] P. Abreu et al. [OPAL Collaboration], Phys. Lett. B 406, 271 (1997).

[26] M. Barth et al. [Brussels-Genoa-Mons-Nijmegen-Serpukhov-CERN Collaboration], Nucl. Phys. B 223, 296 (1983).

[27] A. N. Aleev et al. [EXCHARM Collaboration], Phys. Lett. B 485, 334 (2000).

[28] B. I. Abelev et al. [STAR Collaboration], Phys. Rev. C 77, 061902 (2008).

[29] S. Singha [STAR collaboration], arXiv:2002.07427[nucl-ex].

[30] C. Zhou [STAR collaboration], Nucl. Phys. A 982, 559 (2019).

[31] X.-L. Sheng et al., arXiv:1910.13684[nucl-th].

[32] T. Sj´ostrand et al., Comput. Phys. Commun. 191, 159 (2015).

[33] B. B. Abelev et al. [ALICE Collaboration], JHEP 06, 190 (2015).

[34] L. Adamczyk et al. [STAR Collaboration], Nature 548, 62 (2017).

[35] J. Adam et al. [STAR Collaboration], Phys. Rev. C 98, 014910 (2018).

[36] S. Acharya et al. [ALICE Collaboration], arXiv:1909.01281[nucl-ex].

[37] Z. -T. Liang et al., Phys. Rev. Lett. 94, 102301 (2005).

[38] F. Becattini et al., Phys. Rev.C 95, 054902 (2017).

[39] B. Abelev et al. [ALICE Collaboration], Phys. Rev. C 91, 024609 (2015).

Chapter 4

K^{*0} production in Xe–Xe collisions at $\sqrt{s_{\mathrm{NN}}} = 5.44$ TeV with the ALICE detector at the LHC

Resonances are short-lived particles having a lifetime of the order of few fm$/c$ and can be used to study the properties of the hadronic phase, produced in heavy-ion collisions. In fact, in central A–A (Pb–Pb, Xe–Xe) collisions, where the lifetime of the hadronic phase is similar to short-lived resonances, regeneration and re-scattering effects become important. Study of K^{*0} (lifetime ~ 4 fm$/c$) production in A–A collisions is important to understand the properties of the hadronic phase. The ALICE experiment has recently recorded Xe–Xe as well as Pb–Pb collisions at $\sqrt{s_{\mathrm{NN}}} = 5.44$ and 5.02 TeV, respectively. This unique data set allows investigating bulk particle production for two different systems at similar collision energies. In particular, the charged particle multiplicities in Xe–Xe collisions are comparable to those in peripheral and mid-central Pb–Pb collisions and high multiplicity proton–lead (p–Pb) collisions.

In this chapter, we present K^{*0} production as a function of transverse momentum (p_{T}) in various collision centralities of Xe–Xe collisions. The p_{T} integrated yield, average transverse momentum ($\langle p_{\mathrm{T}} \rangle$), and K^{*0}/K yield ratio as a function of average charged particle multiplicity ($\langle \mathrm{d}N_{\mathrm{ch}}/\mathrm{d}\eta \rangle$) are reported. Measurements from Xe–Xe collisions are compared with the measurements from Pb–Pb and p–Pb collisions to understand the system size dependence of K^{*0} production. In addition, the nuclear modification factor (R_{AA}) of K^{*0} in Xe–Xe collisions and comparison with the measurement from

Pb–Pb collisions is also shown.

Before going to the K^{*0} production, in the next section, we discuss about another important aspect about Xe–Xe collisions. The Xe nucleus has a moderate prolate deformation [1] compared to spherical Pb nucleus. Deformation of the Xe nucleus allows us to probe different initial condition compared to collisions between spherical shape Pb nuclei. In the next section, we report the effect of deformation of the Xe nucleus on measured bulk observables in Xe–Xe collisions at $\sqrt{s_{\mathrm{NN}}} = 5.44$ TeV based on a transport model calculation.

4.1   Study of bulk observables in Xe–Xe collisions at $\sqrt{s_{\mathrm{NN}}} = 5.44$ TeV using the AMPT model

In this section, we have studied the $\langle \mathrm{d}N_{\mathrm{ch}}/\mathrm{d}\eta \rangle$ and the elliptic flow of inclusive charged particles produced in Xe–Xe collisions at $\sqrt{s_{\mathrm{NN}}} = 5.44$ TeV, using A Multiphase Transport (AMPT) Model [2, 3]. We have used string melting (SM) version of AMPT (version 2.25t7) with a partonic cross section of 3mb. String fragmentation parameters a and b are 0.3 and 0.15 GeV^{-2}, respectively. This set of parameter values are chosen as they were successfully described ALICE experiment data of $\langle \mathrm{d}N_{\mathrm{ch}}/\mathrm{d}\eta \rangle$, particle ratios, v_2 etc. at $\sqrt{s_{\mathrm{NN}}} = 2.76$ TeV [4] and 5.02 TeV [5].

AMPT is a hybrid transport model and consists of four primary stages.

- Initial condition: Initial condition in AMPT is taken from HIJING [6] model.

- Partonic scattering: Scattering among partons are introduced by using Zhang's parton cascade model [7]. Two body scattering cross sections from the pQCD with screening masses are used to calculate parton scattering.

- Hadronization: In SM version of AMPT, a quark coalescence model is used to combine partons into hadrons.

- Hadronic interaction: A Relativistic Transport (ART) [8] model is used for the evaluation of the hadronic matter, which includes interactions between hadrons.

AMPT model is further modified by implementing the deformation information of the Xe nucleus in the model framework. In AMPT model, the deformation of the Xe nucleus is introduced by using a deformed Woods-Saxon [9] profile,

$$\rho = \frac{\rho_0}{1 + \exp(|r - R|/d)}, \tag{4.1}$$

where

$$R = R_0[1 + \beta_2 Y_2^0(\theta) + \beta_4 Y_4^0(\theta)], \tag{4.2}$$

ρ_0 is the normal nuclear density, R_0 is the radius of the Xe nucleus, d is the diffuseness parameter and β_2, β_4 are the deformed parameters of the Xe nucleus. We have used $R_0 = 5.4$ fm, $d = 0.59$ fm, $\beta_2 = 0.162$ and $\beta_4 = $ -0.003 [1]. $Y_l^m(\theta)$ is the spherical harmonics.

In this study, the collision configuration of Xe nucleus is chosen by the random orientation of the semi-major axis and the semi-minor axis of the colliding deformed Xe nucleus. In order to see the effect of deformation on bulk observables, results for Xe–Xe collisions with spherically symmetric Xe nucleus are also presented. 50 K minimum bias events for each of the configuration at $\sqrt{s_{\mathrm{NN}}} = 5.44$ TeV are used for this study.

4.1.1   Results

In order to compare the model result with the ALICE experiment, analysis for AMPT simulation is performed with similar event and centrality selection criteria as used in ALICE experiment. Events which have at least 1 charged particle present in $|\eta| < 1$, are selected for the analysis. This condition is similar to INEL>0 trigger, used in the ALICE experiment [10, 11]. Centrality is estimated from the multiplicity distribution

of charged particle in the η range $2.8 < \eta < 5.1$ and $-3.7 < \eta < -1.7$. This centrality selection mimics the centrality estimation with V0M amplitude (amplitude in V0A detector + amplitude in V0C detector), used in the ALICE experiment.

4.1.1.1   Charged particle multiplicity
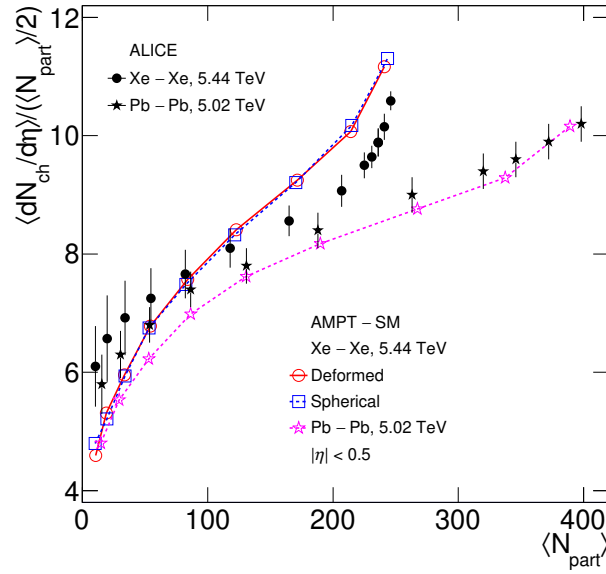
Figure 4.1: $\langle \mathrm{d}N_{\mathrm{ch}}/\mathrm{d}\eta \rangle$ per participating nucleons as a function of $\langle \mathrm{N}_{\mathrm{part}} \rangle$ from the AMPT model calculations for Xe–Xe and Pb–Pb collisions at $\sqrt{s_{\mathrm{NN}}}$ = 5.44 and 5.02 TeV, respectively. The model results are compared with the corresponding ALICE measurements [13, 14].

Figure 4.1 shows the $\langle \mathrm{d}N_{\mathrm{ch}}/\mathrm{d}\eta \rangle$ per participating nucleons ($\mathrm{N}_{\mathrm{part}}$) as a function of $\langle \mathrm{N}_{\mathrm{part}} \rangle$ in Xe–Xe and Pb–Pb collisions at $\sqrt{s_{\mathrm{NN}}}$ = 5.44 and 5.02 TeV, respectively [12]. Results from AMPT model are compared with the ALICE measurements [13, 14]. In Xe–Xe collisions, AMPT model calculation is consistent with the ALICE measurements in mid-central collisions but overestimates and underestimates the scaled $\langle \mathrm{d}N_{\mathrm{ch}}/\mathrm{d}\eta \rangle$ in central and peripheral collisions, respectively. However, in Pb–Pb collisions, experimental measurements are well described by the AMPT model, except in

the peripheral collisions where the model underestimates the ALICE measurements. We find that $\langle \mathrm{d}N_{\mathrm{ch}}/\mathrm{d}\eta \rangle$ /$(\langle \mathrm{N_{part}} \rangle$ /2) at a given $\langle \mathrm{N_{part}} \rangle$ is similar for collisions of spherical and deformed shape Xe nuclei. This observation suggests that the deformation of the Xe nucleus does not have any significant effect on the final state charged particle multiplicity.

4.1.1.2   Eccentricity and elliptic flow

Figure 4.2 shows the average participant eccentricity ($\langle \epsilon_2 \rangle$) as a function of collision centrality in Xe–Xe collisions at $\sqrt{s_{\mathrm{NN}}}$ = 5.44 TeV for two different collision configurations (deformed: collision with deformed shape Xe nucleus and spherical: collision with spherical shape Xe nucleus) in the AMPT model [12]. The participant eccentricity is defined as [15],

$$\epsilon_2 \;=\; \frac{\sqrt{\langle r^2 cos(2\phi_{\mathrm{part}}) \rangle^2 + \langle r^2 sin(2\phi_{\mathrm{part}}) \rangle^2}}{\langle r^2 \rangle}, \tag{4.3}$$

where r and ϕ_{part} are the polar coordinates of the participating nucleons in the transverse plane. We have found that the $\langle \epsilon_2 \rangle$ depends on the initial collision configurations of Xe nucleus. In central Xe–Xe collisions, $\langle \epsilon_2 \rangle$ for the deformed collision configuration is larger compared to the spherical nuclei collision configuration.

The elliptic flow (v_2) is the second order Fourier coefficient of the azimuthal angle distribution [16] of produced particles. The v_2 is calculated by the scalar product method. In the scalar product method, the v_2 is defined as [17],

$$v_{\mathrm{n}}\{2, |\Delta\eta|\rangle 2\} \;=\; \frac{\langle\langle u_{\mathrm{n,k}} Q_{\mathrm{n}}^* \rangle\rangle}{\sqrt{\frac{\langle Q_{\mathrm{n}} Q_{\mathrm{n}}^{\mathrm{A}*} \rangle \langle Q_{\mathrm{n}} Q_{\mathrm{n}}^{\mathrm{B}*} \rangle}{\langle Q_{\mathrm{n}}^{\mathrm{A}} Q_{\mathrm{n}}^{\mathrm{B}*} \rangle}}}, \tag{4.4}$$

where flow vector Q_{n} and $u_{\mathrm{n,k}}$ are $\sum_{\mathrm{j}} e^{\mathrm{in}\phi_{\mathrm{j}}}$ and $e^{\mathrm{in}\phi_{\mathrm{k}}}$, respectively. The azimuthal angle of the j$^{\mathrm{th}}$ particle is denoted by ϕ_{j} and k corresponds to the particle of interest. $u_{\mathrm{n,k}}$ is estimated in $|\eta| < 0.8$. Double bracket ($\langle\langle\rangle\rangle$) corresponds to an average over all particles, in all events and single bracket ($\langle\rangle$) corresponds to an average over all events. The
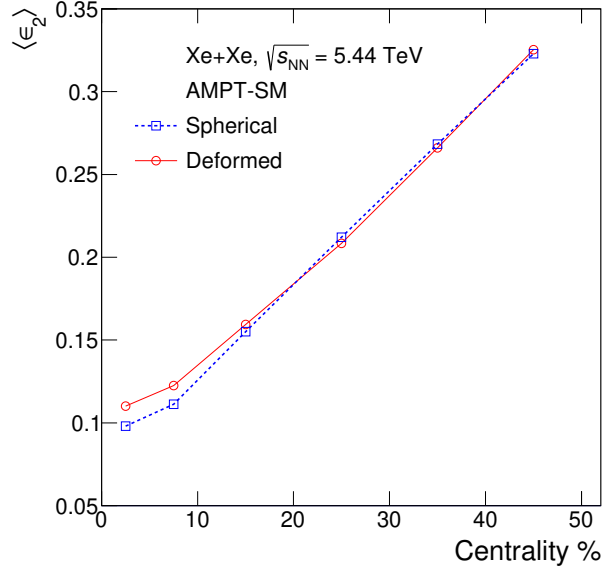
Figure 4.2: $\langle \epsilon_2 \rangle$ vs. collision centrality for two different Xe–Xe collision configurations in AMPT model.

symbol $*$ refers to the complex conjugate. Flow vectors Q_{n}, $Q_{\mathrm{n}}^{\mathrm{A}}$ and $Q_{\mathrm{n}}^{\mathrm{B}}$ are calculated in $2.8 < \eta < 5.1$, $-3.7 < \eta < 1.7$ and $|\eta| < 0.8$, respectively. $u_{\mathrm{n,k}}$ and Q_{n} are calculated in two different η regions with a large η gap $|\Delta\eta| > 2$. The upper panel of Fig. 4.3 shows the p_{T} integrated $\langle v_2 \rangle$ as a function of collision centrality from AMPT model calculation for Xe–Xe and Pb–Pb collisions [12]. The lower panel of Fig. 4.3 shows the ratios of elliptic flow between Xe–Xe and Pb–Pb collisions. We find that in central Xe–Xe collisions, the $\langle v_2 \rangle$ for the deformed collision configuration is larger compared to the spherical collision configuration and above 10% collision centrality, they are consistent with each other. The $\langle v_2 \rangle$ in central Xe–Xe collisions with the deformed shape of Xe nucleus is significantly higher compared to Pb–Pb collisions. Although, above 10% collision centrality $\langle v_2 \rangle$ values in Pb–Pb collisions are higher compared to the values obtained from the Xe–Xe collisions. In 0–5% centrality, the $\langle v_2 \rangle$ for deformed shape Xe–Xe collisions is $\sim$20% higher compared to Pb–Pb collisions and above 20% collision centrality the $\langle v_2 \rangle$ in Xe–Xe collisions is $\sim$12% lower compared to
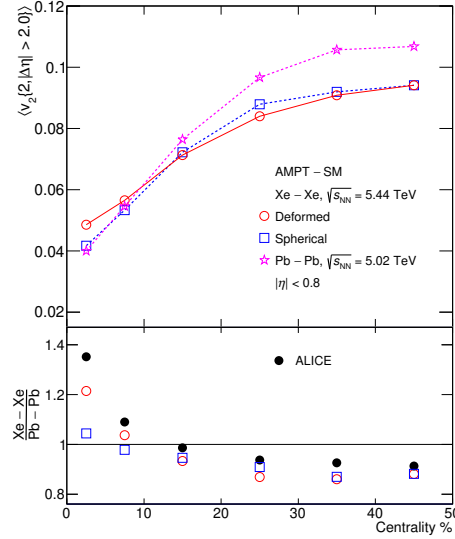
Figure 4.3: Upper panel: $\langle v_2 \rangle$ as a function of collision centrality from AMPT model study for two different configurations of Xe–Xe collisions at $\sqrt{s_{\mathrm{NN}}}$ = 5.44 TeV and Pb–Pb collisions at $\sqrt{s_{\mathrm{NN}}}$ = 5.02 TeV. Lower panel: Ratios of $\langle v_2 \rangle$ between Xe–Xe and Pb–Pb collisions. Results from AMPT are compared with the ALICE measurements [10].

Pb–Pb collisions. Similar centrality dependence of the $\langle v_2 \rangle$ ratio between Xe–Xe and Pb–Pb collisions are also observed for the ALICE measurements [10]. Experimental measurement shows a significant increase of measured $\langle v_2 \rangle$ in central Xe–Xe collisions compared to central Pb–Pb collisions and this can be understood as an effect of the deformation of the Xe nucleus. This is due to the difference of initial eccentricities between Xe–Xe collisions with spherical and deformed shape Xe nuclei.

4.2 Study of K^{*0} production in Xe–Xe collisions at $\sqrt{s_{\mathrm{NN}}}$ = 5.44 TeV with the ALICE detector

The measurement of K^{*0} resonance production in high-energy heavy-ion collisions provides information on the properties of the medium and its evolution at different stages. We have studied the K^{*0} resonance production in Xe–Xe collisions at $\sqrt{s_{\mathrm{NN}}}$ = 5.44 TeV with the ALICE detector at the LHC. K^{*0} signals have been reconstructed

through their hadronic decays (K^{*0} ($\overline{K}^{*0}$) $\rightarrow K^{+}(K^{-})\ \pi^{-}(\pi^{+})$) with branching ratio of 66.6% at mid-rapidity ($|y| < 0.5$) in p_{T} ranges over 0.4 to 12.0 GeV/c, for four different centrality classes.

4.2.1 Analysis details

4.2.1.1 Event selection

For the first time on 12th and 13th of October 2017, LHC produced collisions of Xe nuclei with 6 hours of stable Xe beam. Minimum bias Xe–Xe collisions at $\sqrt{s_{\mathrm{NN}}} = $ 5.44 TeV were collected at a reduced solenoidal magnetic field of B = 0.2 T in the ALICE detector. Xe–Xe collisions data were collected with a online Minimum Bias (MB) trigger which requires a hit in both the V0 detectors, in coincidence with a signal in each of the two neutron ZDCs. Beam induced background events and pile-up events were removed for the analysis. For the analysis only those events are selected which have a primary collision vertex reconstructed with the SPD detector and the z position of primary vertex (v_{z}) within ± 10 cm along the beam axis from the center of the TPC detector to ensure uniform detector acceptance.

Total number of accepted events after all event selection criteria are 1.44 M. For centrality selection the V0 detector is used as discussed in Sec. 3.1.1. The upper panel of Fig. 4.4 shows the V0M amplitude distribution and the Glauber Monte Carlo fit in Xe–Xe collisions at $\sqrt{s_{\mathrm{NN}}} = 5.44$ TeV. The lower panel of Fig. 4.4 shows data to fit ratio. The centrality classes used for this analysis are: V0M percentiles (0–30, 30–50, 50–70, and 70–90 %). Table 4.1 shows the number of analyzed events, $\langle \mathrm{d}N_{\mathrm{ch}}/\mathrm{d}\eta \rangle$, $\langle N_{\mathrm{part}} \rangle$ and $\langle N_{\mathrm{coll}} \rangle$ for various centrality classes [19] in Xe–Xe collisions at $\sqrt{s_{\mathrm{NN}}} = $ 5.44 TeV. Efficiency corrected $\langle \mathrm{d}N_{\mathrm{ch}}/\mathrm{d}\eta \rangle$ values [13] are estimated from charged tracks which are reconstructed by using the information of the ITS and the TPC detectors.
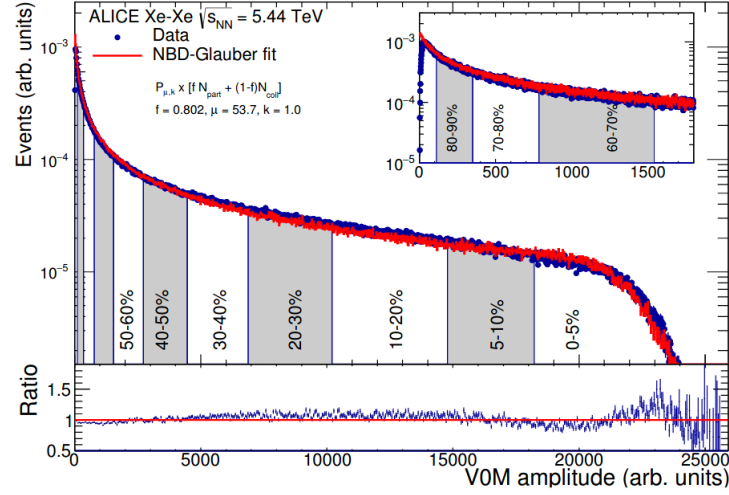
Figure 4.4: Centrality selection using V0M amplitude distribution in Xe–Xe collisions at $\sqrt{s_{\mathrm{NN}}}$ = 5.44 TeV [19].

Table 4.1: List of number of analyzed events, $\langle \mathrm{d}N_{\mathrm{ch}}/\mathrm{d}\eta \rangle$, $\langle \mathrm{N}_{\mathrm{part}} \rangle$ and $\langle \mathrm{N}_{\mathrm{coll}} \rangle$ in Xe–Xe collisions at $\sqrt{s_{\mathrm{NN}}}$ = 5.44 TeV [19].

Centrality (%)	Number of events (M)	$\langle \mathrm{d}N_{\mathrm{ch}}/\mathrm{d}\eta \rangle$	$\langle \mathrm{N}_{\mathrm{part}} \rangle$	$\langle \mathrm{N}_{\mathrm{coll}} \rangle$
0–30	0.48	645.7 ± 17.67	168.1 ± 3.17	552.2 ± 34.33
30–50	0.32	256.5 ± 6.5	68.4 ±3.75	131.5 ± 15.0
50–70	0.32	91.5 ± 2.5	26.9 ±2.55	33.8 ± 4.55
70–90	0.32	23 ± 1.1	7.8 ±0.78	6.6 ± 0.72

4.2.1.2   Track selection and particle identification

Invariant mass reconstruction of K^{*0} signals are carried out with the charged K and π tracks which are coming from the primary vertex of the collision, also known as primary tracks. Primary tracks are selected within kinematic acceptance $p_{\mathrm{T}} > 0.15$ GeV/c and $|\eta| < 0.8$. The selection of primary tracks require to satisfy good quality track criteria. Track selection criteria are same as used for K^{*0} spin alignment study in pp collisions at $\sqrt{s} = 13$ TeV and are discussed in 3.1.2. The daughter particles of K^{*0} are kaons and pions, and they can be identified by using Time Projection Chamber (TPC) [18] and Time Of Flight (TOF) [18]. In TPC, particles are identified by their specific energy loss (dE/dx) and in TOF particles are identified by their time of flight. Particle identification criteria are same as used for K^{*0} spin alignment study in pp collisions at $\sqrt{s} = 13$ TeV and are discussed in 3.1.3.

4.2.2   Signal extraction

The K^{*0} signal in a given centrality and p_{T} bin is extracted from the invariant mass distribution of its hadronic decay daughters. In this chapter, the K^{*0} and $\overline{K}^{*0}$ are averaged i.e $(K^{*0} + \overline{K}^{*0})/2$ and denoted as K^{*0}. Invariant mass distribution of unlike charged πK pair is described as,

$$M_{\pi K} = \sqrt{(E_\pi + E_K)^2 - |\vec{p_\pi} + \vec{p_K}|^2}, \qquad (4.5)$$

where E and $\vec{p}$ are the energy and momentum of decay daughters, respectively. The invariant mass distribution of unlike charged πK pairs from the same events over a range $1.6 < p_{\mathrm{T}} < 2.0$ GeV/c in 0–30% Xe–Xe collisions is shown in the left panel of Fig. 4.5. This distribution contains K^{*0} signals along with large combinatorial backgrounds. Combinatorial backgrounds are estimated by the invariant mass distribution of unlike charged πK pairs from mixed events (details are given in Sec. 3.2).
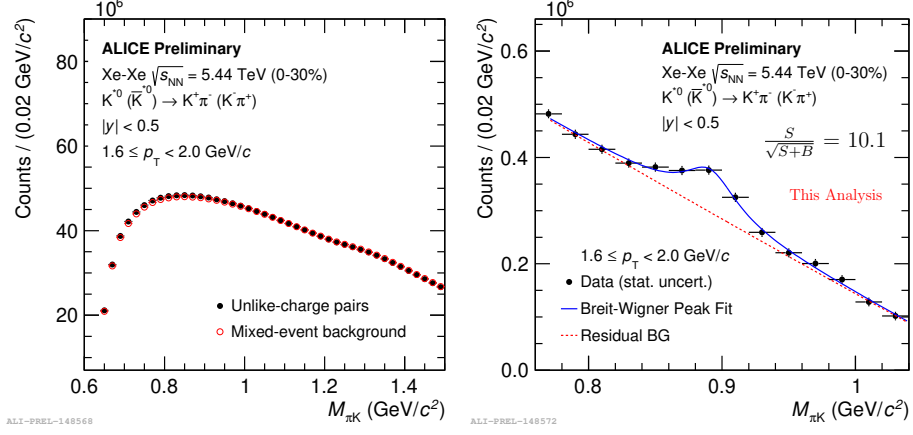
Figure 4.5: Left panel: Invariant mass distribution of unlike charged πK pairs from the same event (black marker) and normalized mixed event background (red marker). Right panel: Mixed event background subtracted πK invariant mass distribution, fitted with a Breit-Wigner + 2nd order polynomial of $M_{\pi K}$ function. The Breit-Wigner function describes the K^{*0} signal and the residual background is described by the 2nd order polynomial function. Uncertainties on data points are statistical only. The typical significance ($\frac{S}{\sqrt{S+B}}$; S = signal, B = combinatorial background) value for the signal is also given.

The mixed event combinatorial background distribution is then normalized to the same event invariant mass distribution (shown in the left panel of Fig. 4.5) in the invariant mass region 1.1 to 1.15 GeV/c^2 (for p_T bin 0.4-0.8 GeV/c normalization is done in invariant mass region 0.66 to 0.7 GeV/c^2 as it reproduces the residual background shape better). The normalized mixed event background is subtracted from the same event invariant mass distribution to get the K^{*0} signal. After subtraction of the combinatorial background, a certain amount of background is still present, known as residual background. The residual background mainly originates due to the production of correlated πK pair from the decays of other hadrons and jets. Misidentification of K and π also contributes in the residual background. The combinatorial background subtracted πK invariant mass distribution is fitted with the Breit-Wigner distribution plus a residual background function. Total fit function

(BW + Res. bkg.) is,

$$\frac{Y}{2\pi} \frac{\Gamma}{(M_{\pi K} - M_0)^2 + \frac{\Gamma^2}{4}} + AM_{\pi K}^2 + BM_{\pi K} + C. \qquad (4.6)$$

Here M_0 and Γ are the mass and width of the K^{*0}. During the fitting width parameter is kept fixed to PDG value, whereas the mass parameter is left free. For systematic uncertainty, the width parameter is kept free. The parameter Y is the area under the Breit-Wigner distribution and gives the raw yield or number of K^{*0}. The right panel of Fig. 4.5 shows K^{*0} signal after mixed event background subtraction for $0.8 < p_{\mathrm{T}} < 1.2$ GeV/c in 0-30% Xe–Xe collisions.

4.2.3   Raw p_{T} spectra

Raw p_{T} spectra for the K^{*0} are extracted in 4 different centrality bins. K^{*0} yields are extracted for 10 different p_{T} bins : 0.4-0.8, 0.8-01.2, 1.2-1.6, 1.6-2.0, 2.0-2.5, 2.5-3.0, 3.0-4.0, 4.0-6.0, 6.0-8.0 and 8.0-12.0 GeV/c in centrality classes 0–30%, 30–50%, 50–70% and 70–90%. In order to get the K^{*0} raw yield, mixed event background subtracted πK invariant mass distribution is fitted with BW + 2nd order polynomial for each p_{T} bin. We kept the width of the K^{*0} meson fixed to the PDG value (48.7 MeV/c^2) during fitting. πK invariant mass distributions for various p_{T} intervals in selected centrality classes are given in the Appendix C.

The yield of K^{*0} is calculated by using two different methods : bin counting and function integration, where function integration is used as default and bin counting is used for systematic study. Details about yield extraction methods are discussed in Sec. 3.2.1.

4.2.4   Acceptance $\times$ Efficiency for K^{*0} in Xe–Xe collisions

Acceptance $\times$ Efficiency ($A \times \epsilon_{\mathrm{rec}}$) as a function of p_{T} for K^{*0} in Xe–Xe collisions are obtained from Monte Carlo (MC) simulation. For simulation 0.7 million events

are used. Particle productions and decays for this data set are simulated by using HIJING model [6], while particle interactions with the ALICE detector are simulated by using GEANT3. Details about $A \times \epsilon_{\mathrm{rec}}$ correction are discussed in Sec. 3.2.2. The $A \times \epsilon_{\mathrm{rec}}$ as a function of p_{T} for K^{*0} in different centrality classes are shown in the left panel of Fig. 4.6. The right panel of Fig. 4.6 shows the ratios of $A \times \epsilon_{\mathrm{rec}}$ in each centrality class to the minimum bias events.

From the figure we observed a small centrality dependence in $A \times \epsilon_{\mathrm{rec}}$. We used the
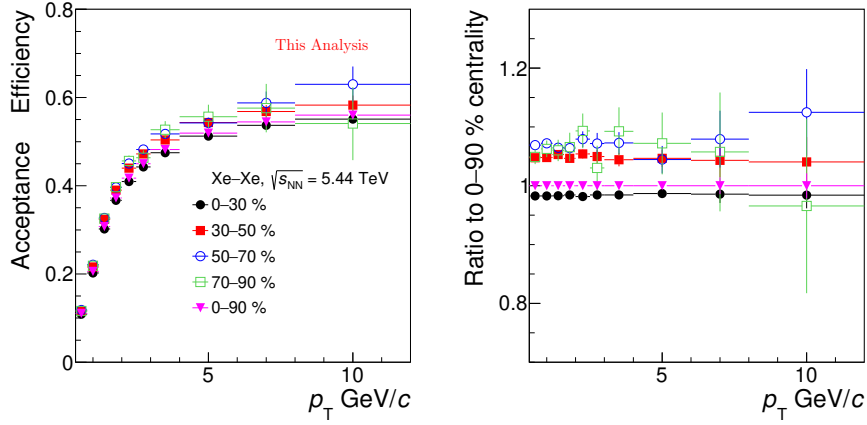
Figure 4.6: Left panel shows Acceptance × Efficiency as a function of p_{T} in different centrality classes. Right panel shows the ratio of Acceptance × Efficiency in different centrality classes to 0–90 % centrality class. Results are for Xe–Xe collisions at $\sqrt{s_{\mathrm{NN}}} = 5.44$ TeV and $|y| < 0.5$.

$A \times \epsilon_{\mathrm{rec}}$ of individual centrality separately, to correct the p_{T} spectra. The $A \times \epsilon_{\mathrm{rec}}$ is further corrected through a re-weighting procedure to account shape of simulated spectra, as discussed in Sec. 3.2.3. Figure 4.7 shows re-weighted factor (ratio between original $A \times \epsilon_{\mathrm{rec}}$ and weighted $A \times \epsilon_{\mathrm{rec}}$) for the K^{*0} meson in 0–30% Xe–Xe collisions at $\sqrt{s_{\mathrm{NN}}} = 5.44$ TeV. The correction factor is maximum at low p_{T} and about 3%, whereas at intermediate and high p_{T} the correction factor is negligible.
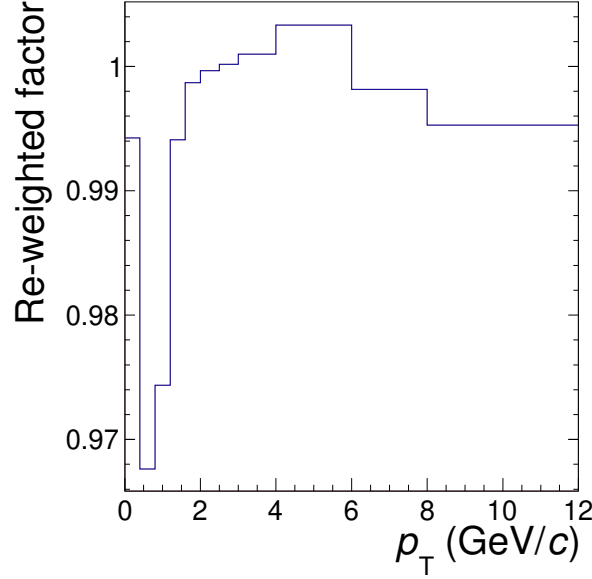
Figure 4.7: Ratio between original $A \times \epsilon_{\mathrm{rec}}$ and weighted $A \times \epsilon_{\mathrm{rec}}$ for the K^{*0} meson in 0–30% Xe–Xe collisions at $\sqrt{s_{\mathrm{NN}}}$ = 5.44 TeV.

4.3 Corrected p_{T} spectra

Raw spectra are corrected for the $A \times \epsilon_{\mathrm{rec}}$ and branching ratio. The normalized corrected spectra is obtained by using the following formula:

$$\frac{\mathrm{d}^2 N}{\mathrm{d}p_{\mathrm{T}}\mathrm{d}y} = \frac{\text{Raw Counts}}{2 \ \times \ N_{\mathrm{evt}} \ \times \ \mathrm{BR} \ \times \ \mathrm{d}p_{\mathrm{T}} \ \times \ \mathrm{d}y \times \ A \ \times \ \epsilon_{\mathrm{rec}}}, \tag{4.7}$$

where factor 2 is used to average over K^{*0} and $\overline{K}^{*0}$ and BR is the branching ratio. Other correction factors such as signal loss correction (see 5.0.5 for details) and correction due to vertex reconstruction (see 5.0.5 for details) are negligible for the measurements in heavy-ion collisions. Figure 4.8 shows corrected p_{T} spectra for K^{*0} in different centrality classes in Xe–Xe collisions at $\sqrt{s_{NN}}$ = 5.44 TeV.
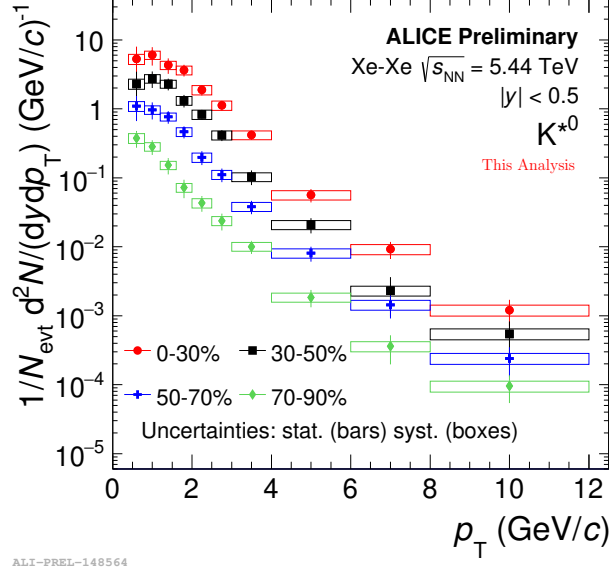
Figure 4.8: Corrected p_{T} spectra for K^{*0} for different centrality classes in Xe–Xe collisions at $\sqrt{s_{\mathrm{NN}}} = 5.44$ TeV. Statistical and systematic uncertainties are represented by bar and boxes, respectively. Width of systematic boxes represent the range of p_{T} bins, used in this analysis.

4.4 Systematic uncertainties

Systematic uncertainties on K^{*0} yields are calculated by varying the default analysis selection criteria. A particular variation is considered as a source of systematic uncertainty if it fails the Barlow check [22]. Barlow check is carried out in a similar way as discussed in Sec. 3.5.

Systematic uncertainties on K^{*0} yield extraction have three major contributions: 1) uncertainties due to signal extraction, 2) uncertainties due to particle identification and 3) uncertainties due to track and event selection.

4.4.1 Systematic uncertainty due to signal extraction

Systematic uncertainty due to signal extraction includes variations of normalization range for mixed event background normalization during K^{*0} signal extraction, varia-

tions of fitting range during the BW + 2$^{\text{nd}}$ order Polynomial function fitting of mixed background subtracted invariant mass distribution of unlike charged πK pairs, variation of residual background fit function (3$^{\text{rd}}$ order polynomial function instead of default 2$^{\text{nd}}$ order Polynomial function), and variation of K^{*0} width by leaving the width of the K^{*0} peak free instead of keeping it fixed to the PDG value during the fitting of invariant mass distributions.

4.4.2   Systematic uncertainty due to particle identification

Systematic uncertainty due to PID includes variations of TPC nσ and TOF nσ for π and K selection. For default measurements TPC 2 σ with TOF VETO 3 σ is used for both π and kaon selection, whereas TPC 2 σ and TPC 3 σ with TOF VETO 3 σ are used for the systematic study.

4.4.3   Systematic uncertainty due to track and event selection

Systematic uncertainty due to track selection and event selection criteria is estimated by varying the default selection criteria as discussed in 4.2.1.2, 4.2.1.1. This includes variations of distance of closest approach from the primary vertex along the beam direction and in the transverse plane, number of the TPC crossed rows variations, variations of χ^2 per cluster value obtained from the fitting of the TPC clusters and the ITS clusters during track reconstruction and variations of the ratio of the number of crossed rows to the number of findable clusters in the TPC. This source also includes variations of the z position of primary vertex during the event selection.

4.4.4   Uncertainty due to tracking efficiency

Uncertainty due to the K^{*0} tracking efficiency is estimated from the uncertainty on the single particle tracking efficiency, using the momentum information of K^{*0} decay

daughters.

4.4.5   Uncertainties due to material budget and hadronic interaction

The tracking of a particle also depends on the detector material as the energy loss of the particles depends on the detector material. Therefore the uncertainty due to implementation of detector material in the simulations have to be taken into account. Uncertainty associated with the hadronic interactions with detector material is studied by GEANT4 simulation. Systematic uncertainties due to the material budget and hadronic interaction are taken from the analysis of K^{*0} meson in p–Pb collisions [23] as the detector material and composition during Xe–Xe run was same as during the data taking for p–Pb collisions.

Systematic uncertainties exhibit a small fluctuations as a function of p_{T}, while one might expect the true systematic uncertainties to be more smoothly varying. The dips and spikes in the systematic uncertainties have been smoothed by averaging over nearest bin to achieve a more uniform set of systematic uncertainties. Figure 4.9 shows systematic uncertainties for K^{*0} in 0–30% Xe–Xe collisions at $\sqrt{s_{\mathrm{NN}}}$ = 5.44 TeV. For systematic study each of the event selection criteria, PID selection criteria, track selection criteria and signal extraction criteria are varied independently and contribution from each of the sources are added in quadrature to get the total systematic uncertainties, considering them uncorrelated to each other. Total systematic uncertainty for K^{*0} in Xe–Xe collisions varies between 13–18% with p_{T}.
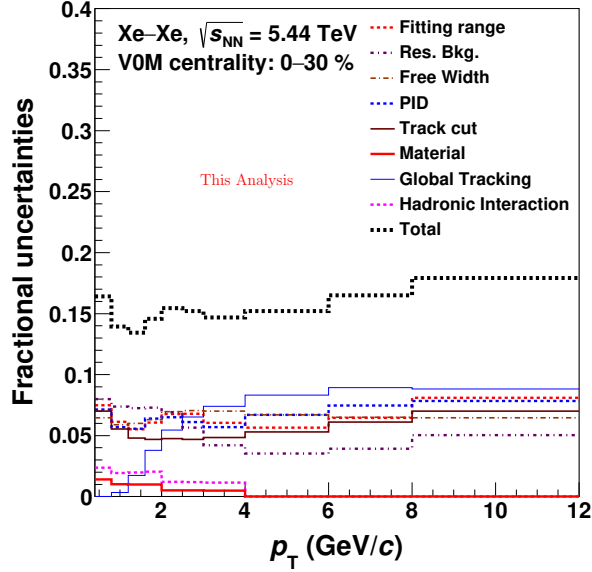
Figure 4.9: Fractional systematic uncertainties from various sources of systematic uncertainties in 0–30% Xe–Xe collisions at $\sqrt{s_{\mathrm{NN}}}$ = 5.44 TeV.

4.5 Results

4.5.1 Transverse momentum integrated yield and mean transverse momentum

The $\mathrm{d}N/\mathrm{d}y$ and $\langle p_{\mathrm{T}} \rangle$ values are obtained by integrating the spectrum in the measured p_{T} range and by extrapolating the spectrum in the unmeasured p_{T} range. Levy-Tsallis fit function [21] as shown in Eq. 4.8, is used to extrapolate the spectrum to zero p_{T}. Contribution in $\mathrm{d}N/dy$ and $\langle p_{\mathrm{T}} \rangle$ from the high p_{T} extrapolation is negligible. The Levy-Tsallis distribution is described as,

$$\frac{\mathrm{d}^2 N}{\mathrm{d}y\mathrm{d}p_{\mathrm{T}}} = p_{\mathrm{T}} \frac{\mathrm{d}N}{\mathrm{d}y} \frac{(n-1)(n-2)}{nC[nC + m_0(n-2)]} \times \left[1 + \frac{\sqrt{p_{\mathrm{T}}^2 + m_0^2} - m_0}{nC} \right]^{-n}, \quad (4.8)$$

where m_0 is the mass of the particle, n, C and the integrated yields $\mathrm{d}N/\mathrm{d}y$ are the free parameters. Table 4.2 shows the Levy-Tsallis fit parameters in different centrality classes.

Table 4.2: Levy-Tsallis fit parameters obtained from the fitting of K^{*0} spectra for different centrality classes in Xe–Xe collisions at $\sqrt{s_{\mathrm{NN}}} = 5.44$ TeV.

Centrality (%)	n	C (MeV)	dN/dy	χ^2/NDF	extrapolation
0–30	19.3 ±11.7	0.47 ±0.07	11.3 ±1.6	0.45	11%
30–50	20.7 ±15.6	0.44 ±0.07	5.0 ±0.7	0.42	12%
50–70	9.3 ±2.7	0.34 ±0.06	1.8 ±0.3	0.20	14%
70–90	7.0 ±1.6	0.27 ±0.06	0.5 ±0.1	0.12	17%

The dN/dy is defined as,

$$\frac{\mathrm{d}N}{\mathrm{d}y} = I_{\mathrm{hist}} + I_{\mathrm{extrapolated}}, \tag{4.9}$$

where $I_{\mathrm{hist}} = \sum \mathrm{f}(p_{\mathrm{T}}, y)\mathrm{d}p_{\mathrm{T}}$ in the measured range and $I_{\mathrm{extrapolated}} = \int \mathrm{f}(p_{\mathrm{T}}, y)p_{\mathrm{T}}\mathrm{d}p_{\mathrm{T}}$ in the extrapolated region. Similarly, the mean transverse momentum ($\langle p_{\mathrm{T}} \rangle$) is defined as:

$\langle p_{\mathrm{T}} \rangle = (\sum p_{\mathrm{T}}\mathrm{f}(p_{\mathrm{T}}, y)\mathrm{d}p_{\mathrm{T}} + \int p_{\mathrm{T}}\mathrm{f}(p_{\mathrm{T}}, y)\mathrm{d}p_{\mathrm{T}})/(I_{\mathrm{hist}} + I_{\mathrm{extrapolated}})$. Here $\mathrm{f}(p_{\mathrm{T}}, y)$ is the invariant yield. The statistical and systematic uncertainties are estimated from the fit function in unmeasured region and from the data points in the measured region. The statistical and systematic uncertainties are calculated from the re-fit of the spectrum, obtained by moving the data points up and down randomly (with a Gaussian random number) within the statistical and systematic uncertainties, respectively, assuming that the uncertainties are fully uncorrelated in the p_{T} bins.

dN/dy as a function of $\langle \mathrm{d}N_{\mathrm{ch}}/\mathrm{d}\eta \rangle$ for the K^{*0} in Xe–Xe collisions at $\sqrt{s_{\mathrm{NN}}} = 5.44$ TeV is shown in Fig. 4.10. Results are also compared with the measurements in pp, p–Pb and Pb–Pb collisions at $\sqrt{s_{\mathrm{NN}}} = 5.02$ TeV [23, 24] to understand the system size dependence of resonance production. The dN/dy increases from peripheral to central Xe–Xe collisions. We have observed that at similar charged particle multiplicity, the K^{*0} yield in Xe–Xe collisions is consistent with those in p–Pb and Pb–Pb collisions. Measured K^{*0} yield as a function of $\langle \mathrm{d}N_{\mathrm{ch}}/\mathrm{d}\eta \rangle$ fall in a single line suggests that the

K^{*0} production is similar for events with similar charged particle multiplicity and does not depend on collision system. Similar behaviour is also observed for other identified hadrons [25]. This indicates that hadrochemistry at LHC energies scales with charged particle multiplicity density which is a proxy of initial energy density or system volume.
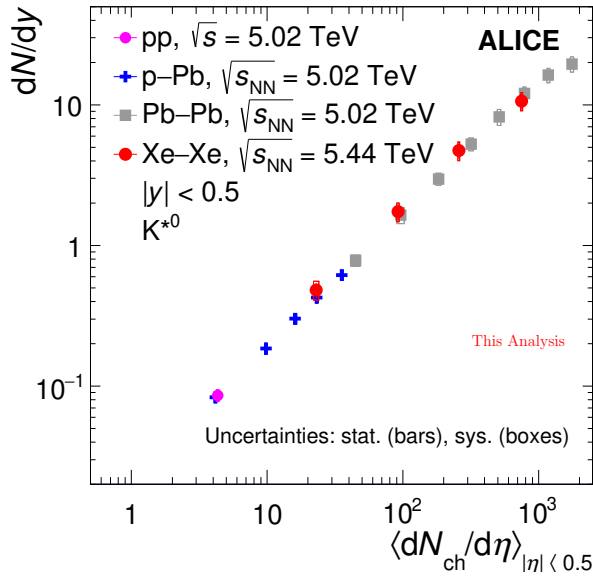
Figure 4.10: $\mathrm{d}N/\mathrm{d}y$ vs. $\langle \mathrm{d}N_{\mathrm{ch}}/\mathrm{d}\eta \rangle$ for K^{*0} in Xe–Xe collisions at $\sqrt{s_{\mathrm{NN}}} = 5.44$ TeV and in pp, p–Pb and Pb–Pb collisions at $\sqrt{s_{\mathrm{NN}}} = 5.02$ TeV [23, 24]. Box represents total systematic uncertainty and bar represents statistical uncertainty.

Figure 4.11 shows $\langle p_{\mathrm{T}} \rangle$ as a function of $\langle \mathrm{d}N_{\mathrm{ch}}/\mathrm{d}\eta \rangle$ for the K^{*0} in Xe–Xe collisions. Results are compared with the measurements in pp, p–Pb and Pb–Pb collisions [23, 24]. $\langle p_{\mathrm{T}} \rangle$ increases from peripheral to central Xe–Xe collisions as the collective flow velocity increases from peripheral to central Xe–Xe collisions. Measurements in Xe–Xe collisions are consistent with those in Pb–Pb collisions at similar $\langle \mathrm{d}N_{\mathrm{ch}}/\mathrm{d}\eta \rangle$. Unlike $\mathrm{d}N/\mathrm{d}y$, measured $\langle p_{\mathrm{T}} \rangle$ values in small collision systems (pp, p–Pb) are not consistent with A–A collisions at similar $\langle \mathrm{d}N_{\mathrm{ch}}/\mathrm{d}\eta \rangle$. Similar behaviour is also observed for other identified hadrons [26]. In small collision system, increment

of $\langle p_{\rm T} \rangle$ with $\langle {\rm d}N_{\rm ch}/{\rm d}\eta \rangle$ is much stronger compared to the A–A collisions, suggesting different dynamical evolution in small collision systems and A–A collisions. Study based on the Blast-wave model fit of π, K and p spectra [25] shows that the transverse radial flow velocity in small collision system (pp, p–Pb) is significantly larger compared to the heavy-ion collisions (Pb–Pb) at similar charged particle multiplicity. Larger $\langle p_{\rm T} \rangle$ in small collision system compared to the heavy-ion collisions is probably due to the larger radial flow velocity in small collision sytem.
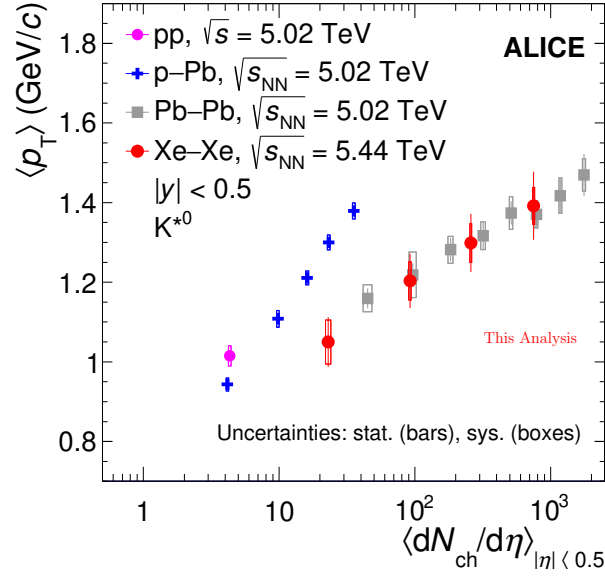
Figure 4.11: $\langle p_{\rm T} \rangle$ vs. $\langle {\rm d}N_{\rm ch}/{\rm d}\eta \rangle$ for K^{*0} in Xe–Xe collisions at $\sqrt{s_{\rm NN}} = 5.44$ TeV and in pp, p–Pb and Pb–Pb collisions at $\sqrt{s_{\rm NN}} = 5.02$ TeV [23, 24]. Box represents total systematic uncertainty and bar represents statistical uncertainty.

4.5.2 Resonance to stable particle ratio

The $p_{\rm T}$ integrated K^{*0}/K and ϕ/K ratios as a function of $\langle {\rm d}N_{\rm ch}/{\rm d}\eta \rangle^{1/3}$ in pp, p–Pb, Xe–Xe and Pb–Pb collisions [23, 24, 27] are shown in Fig. 4.12. $\langle {\rm d}N_{\rm ch}/{\rm d}\eta \rangle^{1/3}$ is used as a proxy for system volume and mimics the radius of the produced medium [28]. A smooth evolution is observed for these ratios as a function of $\langle {\rm d}N_{\rm ch}/{\rm d}\eta \rangle^{1/3}$, from

low multiplicity pp to central A–A collisions. We have observed that the K^{*0}/K ratio decreases with increasing $\langle \mathrm{d}N_{\mathrm{ch}}/\mathrm{d}\eta \rangle^{1/3}$ from low multiplicity pp to central A–A collisions. Decreasing K^{*0}/K ratio with increase in $\langle \mathrm{d}N_{\mathrm{ch}}/\mathrm{d}\eta \rangle^{1/3}$ in A–A collisions can be understood as due to a re-scattering effect of K^{*0} decay daughters inside the hadronic phase. This observation also suggests that the re-scattering effect is dominant over regeneration effect. The K^{*0}/K yield ratio in Xe–Xe collisions at $\sqrt{s_{\mathrm{NN}}}$ = 5.44 TeV and Pb–Pb collisions at $\sqrt{s_{\mathrm{NN}}}$ = 2.76 and 5.02 TeV are consistent with each other for similar values of $\langle \mathrm{d}N_{\mathrm{ch}}/\mathrm{d}\eta \rangle^{1/3}$. This suggests that the strength of re-scattering effect depends on $\langle \mathrm{d}N_{\mathrm{ch}}/\mathrm{d}\eta \rangle^{1/3}$ which is a proxy for the system volume. On the other hand, measured ϕ/K ratio is nearly flat across all collision systems and multiplicities. The ϕ is a long lived resonance having lifetime 10 times more compared to the K^{*0}. Therefore, the ϕ meson yield is insensitive to re-scattering effect in the hadronic phase.
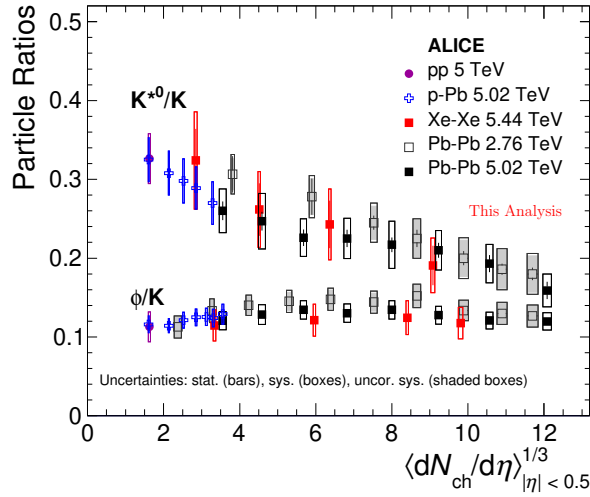
Figure 4.12: K^{*0}/K and ϕ/K ratios as a function of $\langle \mathrm{d}N_{\mathrm{ch}}/\mathrm{d}\eta \rangle^{1/3}$ in pp, p–Pb, Xe–Xe and Pb–Pb collisions [23, 24, 27].

4.5.3   Nuclear modification factor (R_{AA})

R_{AA} has proven to be a powerful observable for the study of parton propagation in the dense QCD medium. We have calculated the R_{AA} of K^{*0} in Xe–Xe collisions and compared the result with the measurement from Pb–Pb collisions and p–Pb collisions at $\sqrt{s_{\mathrm{NN}}}$ = 5.02 TeV. R_{AA} is defined as

$$R_{\mathrm{AA}} = \frac{\frac{\mathrm{d}^2 N^{\mathrm{AA}}}{\mathrm{d}y \mathrm{d}p_{\mathrm{T}}}}{\langle T_{\mathrm{AA}} \rangle \frac{\mathrm{d}^2 \sigma_{\mathrm{inel}}^{\mathrm{PP}}}{\mathrm{d}y \mathrm{d}p_{\mathrm{T}}}}, \tag{4.10}$$

where $\langle N_{\mathrm{coll}} \rangle$ is the average number of binary collisions, σ_{inel} is the inelastic cross section in pp collisions and $\langle T_{\mathrm{AA}} \rangle$ is the thickness function, defined by $\langle N_{\mathrm{coll}} \rangle / \sigma_{\mathrm{inel}}^{\mathrm{pp}}$. $\langle N_{\mathrm{coll}} \rangle$ and $\langle T_{\mathrm{AA}} \rangle$ values are taken from [19].

In order to calculate the nuclear modification factor, the K^{*0} p_{T} spectrum in pp collisions and the inelastic pp cross section are needed. In the ALICE experiment, pp collisions data at $\sqrt{s}$ = 5.44 TeV does not exist. Therefore, we have used an interpolation method to extract the K^{*0} p_{T} spectrum and the inelastic pp cross section at $\sqrt{s}$ = 5.02 TeV. The K^{*0} p_{T} spectrum is calculated by using the PYTHIA simulation and the experimentally measured K^{*0} spectrum at $\sqrt{s}$ = 5.02 TeV, as shown in Eq. 5.0.5.

$$\mathrm{f}(p_{\mathrm{T}}) \text{ at 5.44 TeV} = \frac{\mathrm{f}(p_{\mathrm{T}}) \text{ at 5.44 TeV from MC simulation}}{\mathrm{f}(p_{\mathrm{T}}) \text{ at 5.02 TeV from MC simulation}} \times$$
$$\mathrm{f}(p_{\mathrm{T}}) \text{ at 5.02 TeV from experiment.} \tag{4.11}$$

Here $\mathrm{f}(p_{\mathrm{T}})$ corresponds to the K^{*0} p_{T} spectrum. Figure 4.13 shows the interpolated p_{T} spectrum of K^{*0} in pp collisions at $\sqrt{s}$ = 5.44 TeV, along with the p_{T} spectrum of K^{*0} in pp collisions at $\sqrt{s}$ = 5.02 TeV. For statistical and systematic uncertainties on the data points, we have used the same % of uncertainties as used for K^{*0} p_{T} spectrum in pp collisions at $\sqrt{s}$ = 5.02 TeV.

The inelastic cross section (σ_{inel}) in pp collisions at $\sqrt{s}$ = 5.44 TeV is calculated by interpolating the existing data. We fitted σ_{inel} vs. $\sqrt{s}$ with a functional form
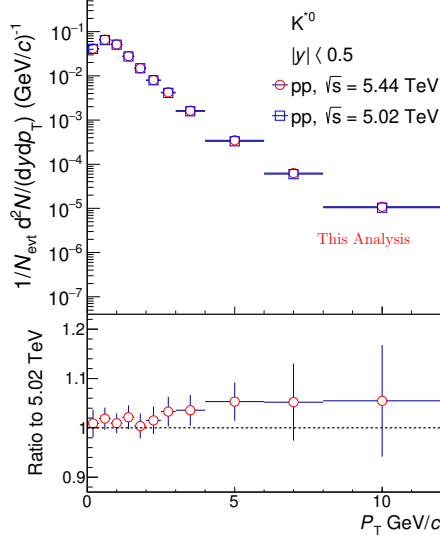
Figure 4.13: Upper panel shows interpolated K^{*0} p_{T} spectrum in pp collisions at $\sqrt{s}$ = 5.44 TeV. Lower panel shows the ratio between K^{*0} p_{T} spectrum in pp collisions at $\sqrt{s}$ = 5.02 and 5.44 TeV.

a$(\sqrt{s})^n$. Figure 4.14 shows the σ_{inel} vs. $\sqrt{s}$. Parametrized fit function is further used to calculate the inelastic cross section (σ_{inel}) in pp collisions at $\sqrt{s}$ = 5.44 TeV. Extracted inelastic cross section at $\sqrt{s}$ = 5.44 TeV is 68.4 ± 0.5 mb.

Figure 4.15 shows the R_{AA} of K^{*0} in Xe–Xe collisions at $\sqrt{s_{\mathrm{NN}}}$ = 5.44 TeV along with the measurement in Pb–Pb collisions at $\sqrt{s_{\mathrm{NN}}}$ = 5.02 TeV [24] at similar $\langle \mathrm{d}N_{\mathrm{ch}}/\mathrm{d}\eta \rangle$. The R_{AA} of K^{*0} in Xe–Xe and Pb–Pb collisions are consistent with each other when they are compared at similar charged particle multiplicity. Measured R_{AA} values for K^{*0} are found to be suppressed by a factor of 4 to 5 with respect to unity at high p_{T} ($p_{\mathrm{T}} > 6$ GeV/c). This can be interpreted as a consequence of the partonic energy loss inside the medium [29].

4.6 Summary

We have presented the measurements of K^{*0} production in Xe–Xe collisions at
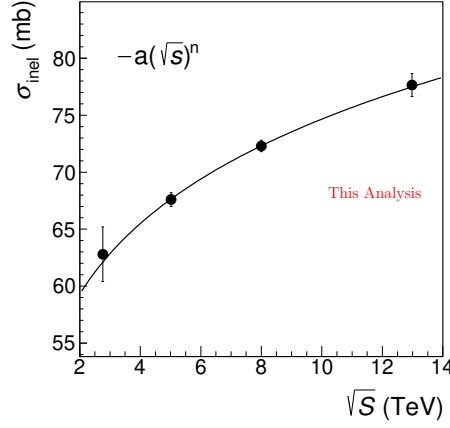
Figure 4.14: σ_{inel} as a function of $\sqrt{s}$.
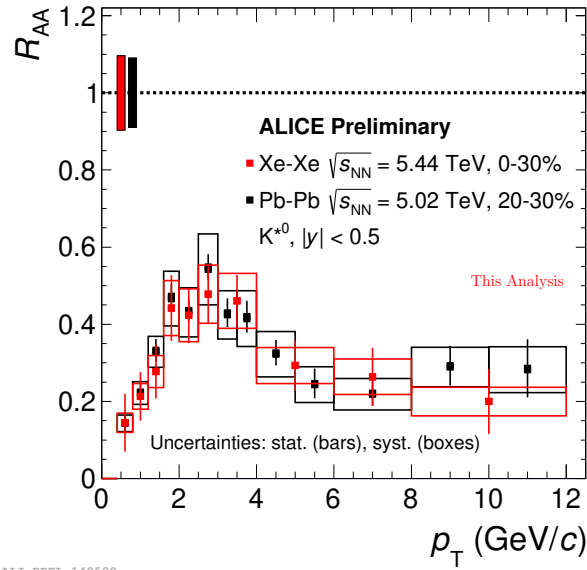
Figure 4.15: R_{AA} of K^{*0} in Xe–Xe collisions at $\sqrt{s_{\mathrm{NN}}} = 5.44$ TeV and in Pb–Pb collisions at $\sqrt{s_{\mathrm{NN}}} = 5.02$ TeV. Statistical and systematic uncertainties are represented by bars and boxes, respectively. The boxes around unity indicate the uncertainty on the normalization of R_{AA} which include the uncertainty on the $\langle T_{\mathrm{AA}} \rangle$ and the normalization uncertainty due to the normalization of pp measurements to the INEL events.

$\sqrt{s_{\mathrm{NN}}} = 5.44$ TeV. K^{*0} signals are extracted in four different centrality classes over p_{T} range 0.4–12.0 GeV/c. Measured dN/dy and $\langle p_{\mathrm{T}} \rangle$ values for K^{*0} in Xe–Xe collisions at $\sqrt{s_{\mathrm{NN}}} = 5.44$ TeV are consistent with the measurements from Pb–Pb collisions at $\sqrt{s_{\mathrm{NN}}} = 5.02$ TeV at similar $\langle \mathrm{d}N_{\mathrm{ch}}/\mathrm{d}\eta \rangle$. Suppression of K^{*0}/K yield ratios in central Xe–Xe collisions compared to pp collisions and peripheral Xe–Xe collisions can be understood as a re-scattering effect of K^{*0} decay daughters in the hadronic phase. In addition we also calculate the R_{AA} of K^{*0} in Xe–Xe collisions and compare the results with the measurements from Pb–Pb collisions at $\sqrt{s_{\mathrm{NN}}} = 5.02$ TeV. Measured R_{AA} values of K^{*0} in Xe–Xe collisions are consistent with those obtained in Pb–Pb collisions for similar charged particle multiplicity. R_{AA} values are found to be suppressed by a factor of 4-5 with respect to unity at high p_{T} ($p_{\mathrm{T}} > 6$ GeV/c), which can be interpreted as a consequence of parton energy loss in the medium.

In addition, we have also studied the effect of deformation of the Xe nucleus on measured bulk observables, using A Multiphase Transport Model. We have found that the measured charged particle multiplicity in collisions of deformed shape Xe nucleus and spherical shape Xe nucleus are similar. However, elliptic flow in the central collision is enhanced by $\sim 15\%$ due to the deformation of Xe nucleus compared to the measurements obtained from the collision of the spherical shape Xe nucleus. This observation suggests that the deformation of Xe nucleus is responsible for the higher v_2 measured by the ALICE experiment in central Xe–Xe collisions compared to the central Pb–Pb collisions.

References

[1] P. Mäller et al., Atom. Data Nucl. Data Tabl. 109, 1 (2016).

[2] Z. W. Lin et al., Phys. Rev. C 72, 064901 (2005).

[3] J. Xu et al., Phys. Rev. C 83, 034904 (2011).

[4] Z. W. Lin et al., Phys. Rev. C 90, 014904 (2014).

[5] G. L. Ma et al., Phys. Rev. C 93, 054911 (2016).

[6] X. N. Wang et al., Phys. Rev. D 44, 3501 (1991).

[7] B. Zhang, Comput. Phys. Commun. 109, 193 (1998).

[8] B. A. Li et al., Phys. Rev. C 52, 2037 (1995).

[9] K. Hagino et al., Phys. Rev. C 74, 017310 (2006).

[10] S. Acharya et al. [ALICE Collaboration], Phys. Lett. B 784, 82 (2018).

[11] S. Acharya et al. [ALICE Collaboration], Phys. Lett. B 788, 166 (2019).

[12] S. Kundu et al, Eur. Phys. J. A 55, 157 (2019).

[13] S. Acharya et al. [ALICE Collaboration], Phys. Lett. B 790, 35 (2019).

[14] J. Adam et al, [ALICE Collaboration], Phys. Rev. Lett. 116, 222302 (2016).

[15] B. Alver et al., Phys. Rev. C 81, 054905 (2010).

[16] S. Voloshin et al., Z. Phys. C 70, 665 (1996).

[17] C. Adler et al. [STAR Collaboration], Phys. Rev. C 66, 034904 (2002).

[18] B. Abelev et al. [ALICE Collaboration], Int. J. Mod. Phys. A 29, 1430044 (2014).

[19] S. Acharya et al. [ALICE Collaboration], ALICE Public Note: https://cds.cern.ch/record/2315401.

[20] T Ullrich et al., arxiv:0701199 [physics.data-an].

[21] C. Tsallis, J. Stat. Phys 52, 479 (1988).

[22] R. Barlow, arXiv:0207026[hep-ex].

[23] J. Adam et al. [ALICE Collaboration], Eur. Phys. J. C 76, 245 (2016).

[24] S. Acharya et al. [ALICE Collaboration], Phys. Lett. B 802, 135225 (2020).

[25] S. Acharya et al. [ALICE Collaboration], Eur. Phys. J. C 80, 693 (2020).

[26] S. Acharya et al. [ALICE Collaboration], Phys. Rev. C 99, 024906 (2019).

[27] J. Adam et al. [ALICE Collaboration], Phys. Rev. C 95, 064606 (2017).

[28] J. Adam et al. [ALICE Collaboration], Phys. Rev. C 91, 034906 (2015).

[29] J. D. Bjorken, FERMILAB-PUB-82-59-THY (1982).

Chapter 5

K^{*0} production in pp collisions at $\sqrt{s} = 13$ TeV with the ALICE detector at the LHC

In the previous chapter we have seen the importance of K^{*0} resonance for understanding various medium properties like re-scattering, regeneration and partonic energy loss in the medium formed in heavy-ion collisions (Xe–Xe and Pb–Pb). The study of K^{*0} in pp collisions can be used as a baseline to corresponding studies in Pb-Pb collisions at the LHC energies. Measurements of identified particles in pp collisions also serve as an input to tune the modeling of several Monte Carlo (MC) event generators such as PYTHIA [1] EPOS-LHC [2].

Recent measurements in high-multiplicity pp and p–Pb collisions show some characteristics which has so far been solely attributed to A–A collisions. The systems, created in pp, p–Pb and A–A collisions are classified based on the final state charged particle multiplicity, referred as "activity" of the event in different collision systems. Observation of the near side long range two particle correlation [3], the elliptic flow [4], the enhancement in strangeness production [5] in high multiplicity pp collisions have brought an immense interest among experimental and theoretical physicists to understand the underlying physics behind the high multiplicity pp collisions. All these observations are could be related to existence of a QGP phase seen in Pb–Pb collisions. This encourages us to look at the K^{*0} resonance production as a function of $\langle \mathrm{d}N_{\mathrm{ch}}/\mathrm{d}\eta \rangle$ in pp collisions in small systems.

Collectivity: In A–A collisions, elliptic and radial flow manifests the hydrody-

namical evolution of the produced QGP medium. Observation of elliptic flow [4] in small system suggests the possibility of presence of collective motion in small system. In addition, other observations in small systems such as increase of the inverse slope of p_T spectra with increasing multiplicity (known as hardening of p_T spectra) [6, 7, 8], enhancement in the baryon to meson ratio at intermediate p_T ($2 < p_T < 7$ GeV/c) [6, 7, 8] are qualitatively similar to the behaviour observed in Pb–Pb collisions [9, 10, 11], where these effects are understood as an effect of collective expansion of the system. Due to the collective motion of the produced medium, particles get a momentum boost in the transverse direction respect to the beam direction, leading to hardening of spectra and enhancement in the baryon to meson ratio. Momentum boost due to the collective motion increases from peripheral to central collisions and is larger for higher mass particles. Measurements of $\langle p_T \rangle$ of K^{*0}, and comparison with other identified hadrons will provide a better understanding of the collectivity in small system.

In addition, multiplicity dependent study of identified hadrons provide an important input to tune various phenomenological model such as color reconnection (CR), rope hadronization and core-corona effect. It has been shown in Ref. [12] that the collective flow-like behaviour in small systems, similar to those observed in heavy-ion collisions, is explained by QCD based MC generator like PYTHIA [1]. It attributes the collectivity in the small systems to CR [13] mechanism. CR in PYTHIA provides an alternate mechanism for flow-like effect in small systems compared to hydrodynamical processes attributed to flow in heavy-ion collisions. CR allows for the interaction between strings and creates a flow-like effect in the final observable. Rope hadronization is modelled in DIPSY event generator [14]. In the rope hadronization picture, the larger and denser collision systems form color ropes [15, 16], groups of overlapping strings that hadronize with a larger effective string tension leads to an increase in the

production of strange hadrons with increasing charged-particle multiplicity.

Strangeness enhancement: Regarding strangeness enhancement, EPOS model [2] qualitatively reproduces features seen in the data. Core-corona model is implemented in EPOS. In this model, the collision is divided into "core and "corona regions, with the division determined by the string or parton density. Regions with a density greater than the threshold density become the core, which evolve as a QGP. This is surrounded by a more dilute corona, for which fragmentation occurs as in the vacuum. Strangeness production is higher in the core region, which makes up a greater fraction of the volume of the larger collision systems. This also results in strangeness enhancement with increasing multiplicity. The core region also undergoes hadronic re-scattering.

m_T scaling: Particle productions at low p_T (p_T < 2 GeV/c) are mainly dominated by soft scattering processes, which involve small momentum transfer. In low momentum regime, particle production can't be calculated from the first principle of QCD calculation and QCD inspired phenomenological models are generally used to describe the particle production at low p_T. Therefore, measurements of identified hadrons at low p_T provide important information to constraint such models. The transverse mass (m_T) spectra scaling was first proposed by R. Hagedorn [17]. The m_T spectra in pp collisions, seem to be sampled in an approximately universal curve after scaling with some arbitrary normalization factors. This effect is known as the m_T scaling. The m_T scaling was first observed at the ISR energies [18]. Later on, the STAR collaboration observed m_T scale breaking in pp collisions at $\sqrt{s}$ = 200 GeV [19]. They found a clear separation between baryon and meson spectra at $p_\mathrm{T} \geq$ 2.0 GeV/c. In pp collisions at $\sqrt{s}$ = 200 GeV, the separation between the baryon and meson spectra seems to be increased over the measured m_T range. Measurements with ALICE detector in pp collisions at $\sqrt{s}$ = 13 TeV provides the opportunity to

extend the spectra upto a very high p_T or m_T. This data with higher kinematic reach in p_T and at higher collision energy can be used to study the above features. Moreover, recent studies, based on identified particle spectra measured in pp collisions at $\sqrt{s}$ =7 TeV by ALICE, indicate that m_T scaling between mesons breaks in the low-p_T region. These observations motivate us test the empirical transverse mass (m_T) scaling at low p_T for identified hadrons pp collisions at $\sqrt{s} = 13$ TeV.

x_T scaling: Invariant cross section of particle production near mid-rapidity have been found to follow a universal scaling at high x_T ($x_T = 2p_T /\sqrt{s}$), which is known as the x_T scaling. The x_T scaling has been observed by the CDF Collaboration in p$\bar{\text{p}}$ collisions at the Tevatron [20, 21], by the UA1 Collaboration at the CERN SPS [22], by the STAR Collaboration in pp collisions at RHIC [23], and by the CMS Collaboration [24] at the CERN LHC. At high p_T invariant cross section of particle production can be calculated in a pQCD framework by convoluting the leading-twist (LT) $2 \rightarrow 2$ hard sub-process cross section along with the parton distribution function and the fragmentation function [25]. The high p_T cross section of particle production can be expressed as

$$E\frac{d^3\sigma}{dp^3} = \frac{1}{\sqrt{s}^n}\text{g}(x_T),$$

(5.1)

where g(x_T) is a universal function. The parameter n provide information about the scattering processes. pQCD based calculation with LT processes predicts $n = 4$, whereas NLO pQCD calculation including higher twist (HT) processes leads to n > 4 [26]. In addition, HT processes also predicts a larger value of the exponent (n) for baryons than for mesons. In this chapter, all these predictions are investigated for identified hadrons produced in pp collisions at $\sqrt{s} = 13$ TeV.

In the first part of this chapter, we report the K^{*0} production as a function of p_T in inelastic (INEL) pp collisions at $\sqrt{s} = 13$ TeV. K^{*0} are reconstructed at mid-

rapidity ($|y| < 0.5$) with their hadronic decays (K^{*0} ($\overline{K}^{*0}$) $\rightarrow K^+(K^-)\,\pi^-(\pi^+)$). The p_{T} integrated yield ($\mathrm{d}N/\mathrm{d}y$) and mean transverse momentum ($\langle p_{\mathrm{T}} \rangle$) as a function of $\sqrt{s}$ are presented. In addition, empirical m_{T} and x_{T} scaling for identified hadrons in pp collisions at $\sqrt{s} = 13$ TeV are also shown. In the second part of this chapter, we present the measurements of K^{*0} mesons production as a function of $\langle \mathrm{d}N_{\mathrm{ch}}/\mathrm{d}\eta \rangle$ in pp collisions at $\sqrt{s} = 13$ TeV. $\mathrm{d}N/\mathrm{d}y$, $\langle p_{\mathrm{T}} \rangle$ and particle ratios are shown as a function of $\langle \mathrm{d}N_{\mathrm{ch}}/\mathrm{d}\eta \rangle$ and are compared with the measurements from pp, p–Pb and Pb–Pb collisions. Results are also compared with the calculations from various MC event generators.

5.0.1 Analysis details

The data from pp collisions at center of mass energy $\sqrt{s} = 13$ TeV, collected in the year 2015 are analyzed here. This analysis is based on a data sample of $\sim$43 million minimum bias triggered events. Event selection criteria and trigger condition is same as used in the spin alignment analysis of K^{*0} in pp collisions Sec. 3.1.1. For the multiplicity dependent K^{*0} production we have selected a subset of INEL events, which are also known as INEL > 0 events. INEL > 0 events correspond to those events, which have atleast one charged particle in the range $|\eta| < 1$. For K^{*0} production in inelastic pp collision this condition is not used and all the analyzed events are INEL events. INEL > 0 sample is divided into various multiplicity classes based on the V0M amplitude. Figure. 5.1 shows the normalized V0M amplitude (V0M/$\langle$V0M$\rangle$) distribution in pp collisions at $\sqrt{s} = 13$ TeV. Table 5.1 shows the $\langle \mathrm{d}N_{\mathrm{ch}}/\mathrm{d}\eta \rangle$ at midrapidity ($|y| < 0.5$) for various multiplicity classes [27] in pp collisions at $\sqrt{s} = 13$ TeV. $\langle \mathrm{d}N_{\mathrm{ch}}/\mathrm{d}\eta \rangle$ values are estimated from the combined informations of the ITS and the TPC detectors.

ALI-PERF-131164
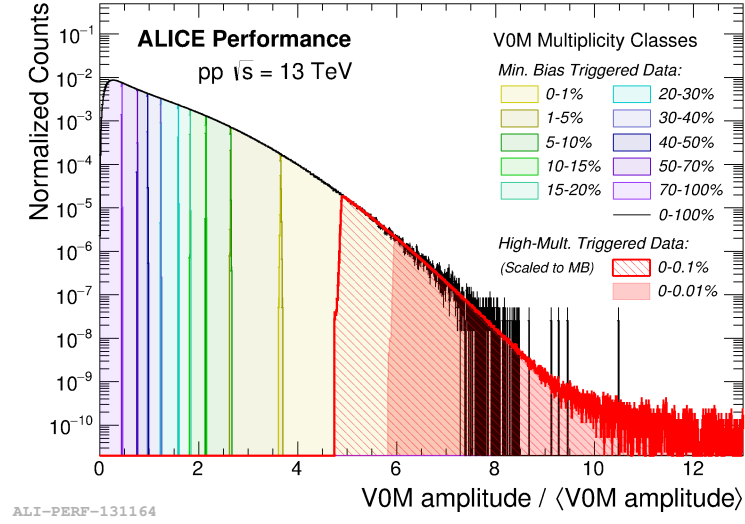
Figure 5.1: Selection of multiplicity classes using normalized V0M amplitude distribution in pp collisions at $\sqrt{s} = 13$ TeV.

Table 5.1: $\langle \mathrm{d}N_{\mathrm{ch}}/\mathrm{d}\eta \rangle$ for various multiplicity classes [27] in pp collisions at $\sqrt{s} = 13$ TeV.

V0M multiplicity class (%)	$\langle \mathrm{d}N_{\mathrm{ch}}/\mathrm{d}\eta \rangle$
INEL > 0	6.89±0.11
I (0–1%)	25.75±0.40
II (1–5%)	19.83±0.30
III (5–10%)	16.12±0.24
IV (10–15%)	13.76±0.21
V (15–20%)	12.06±0.18
VI (20–30%)	10.11±0.15
VII (30–40%)	8.07±0.12
VIII (40–50%)	6.48±0.10
IX (50–70%)	4.64±0.07
X (70–100%)	2.52±0.04

Invariant mass reconstruction of K^{*0} signals are carried out with the charged K and π tracks. Tracks are selected after satisfying track selection criteria. Selected tracks are then identified by using Time Projection Chamber (TPC) and Time Of Flight (TOF) detectors. Track selection and particle identification criteria are same as used for K^{*0} production in Xe–Xe collisions. Details are given in Sec. 3.1.2 and in Sec. 3.1.3, respectively.

5.0.2 K^{*0} signal extraction in pp collisions at $\sqrt{s} = 13$ TeV

K^{*0} mesons are reconstructed using an invariant mass analysis of their hadronic decays in a given multiplicity class and p_{T} bin. Branching ratios for K^{*0} ($\overline{K}^{*0}$) $\rightarrow$ $K^+\pi^-$ ($K^-\pi^+$) are 66.66% at mid-rapidity ($|y| < 0.5$). In this thesis chapter, the K^{*0} and $\overline{K}^{*0}$ are averaged i.e ($K^{*0} + \overline{K}^{*0}$)/2 and denoted as K^{*0}. First the invariant mass distribution of unlike charged daughter particle pairs is computed in same event. This invariant mass distribution gives a peak at the mass position of the mother, but the peak is obtained over a combinatorial background. The signal for K^{*0} is extracted by subtracting the combinatorial backgrounds from the unlike charge distributions. The combinatorial background is estimated using event mixing technique (details are given in Sec. 3.2). Like sign background is used for the lowest p_{T} bin in most central multiplicity class as it reproduces the residual background shape better. In the "like sign" method, tracks of identical charge from the same event are combined to form pairs. The like sign background is normalized by $2\sqrt{N_{++}N_{--}}$, where N_{++} and N_{--} are the number of negative-negative and positive-positive pairs in each invariant mass bin, respectively. After combinatorial background subtraction the K^{*0} signal along with the residual background are fitted with the Breit-Wigner (BW) + 2$^{\mathrm{nd}}$ order polynomial fit function. The BW function describes the K^{*0} signal, whereas residual backgrounds are described by second-order polynomial. Area under the BW

distribution is the K^{*0} yield. The invariant mass distribution of unlike charged πK pairs of both same event and mixed event are shown in the left panel of Fig. 5.2. Signal after mixed event background subtraction in the p_T range 1.2–1.4 GeV/c is shown in the right panel of Fig. 5.2. Extracted mass peak position from BW fit is consistent with the PDG value above $p_T > 4$ GeV/c, whereas at low p_T extracted mass peak positions are lower compared to the PDG value [28]. This mass shift at low p_T is also observed in pp collisions measurements at other collision energies [29, 30, 31].
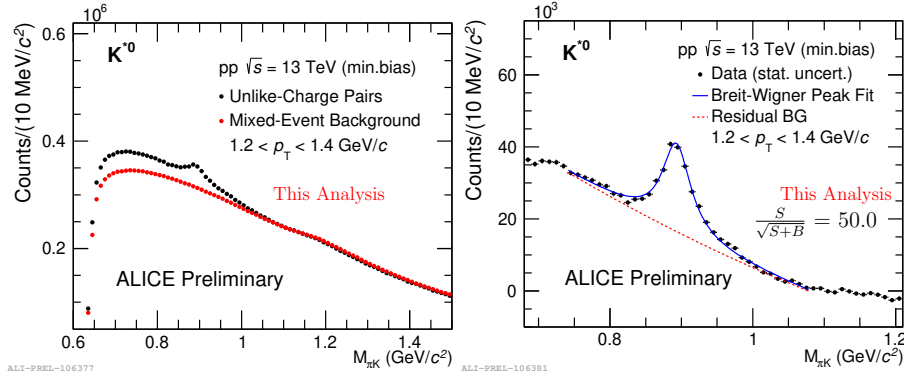
Figure 5.2: Left Panel: Unlike charged πK invariant mass ($M_{\pi K}$) distribution from the same event along with normalized mixed event background for p_T range $1.2 \leq p_T < 1.4$ GeV/c at mid-rapidity in minimum bias INEL pp collisions at $\sqrt{s} = 13$ TeV. Right Panel: $M_{\pi K}$ distribution after mixed event background subtraction in minimum bias pp collisions at $\sqrt{s} = 13$ TeV. Errors are statistical only. The typical significance ($\frac{S}{\sqrt{S+B}}$; S = signal, B = combinatorial background) value for the signal is also given.

5.0.3   Raw p_T spectra

Raw p_T spectra for the K^{*0} meson are extracted in minimum bias INEL pp collisions as well as in 10 different V0M multiplicity classes: INEL > 0, I, II, III + IV, V, VI, VII, VIII, IX and X. In each multiplicity classes K^{*0} signals are extracted over a p_T range 0 to 10 GeV/c, whereas for minimum bias pp collisions, signals are extracted over p_T range 0 to 15 GeV/c due to larger statistics. In order to get the K^{*0} raw

yield, combinatorial background subtracted πK invariant mass distribution is fitted with BW + 2$^{\text{nd}}$ order polynomial function for each p_T bin. During the fitting width parameter in BW function is kept fixed to the PDG value (48.7 MeV/c^2). Mixed event background subtracted πK invariant mass distribution in various multiplicity classes are shown in the Appendix D.1. The yield of K^{*0} is calculated with bin counting and function integration method (see Sec. 3.2.1 for details). Function integration is used as default and bin counting is used for systematic study. K^{*0} yields are plotted as a function of p_T to get the raw p_T spectra for K^{*0}. Raw p_T spectrum in a given multiplicity class is normalized to the total number of accepted events in that multiplicity class.

5.0.4 Acceptance $\times$ Efficiency for K^{*0} in pp collisions

Acceptance $\times$ Efficiency ($A \times \epsilon_{\text{rec}}$) as a function of p_T for K^{*0} in pp collisions are obtained from 43 million Monte Carlo (MC) simulated events. Particle productions and decays for this data set are simulated by using PYTHIA (the Monash 2013 tune of PYTHIA 8 [1]) at $\sqrt{s} = 13$ TeV, while particle interactions with the ALICE detector are simulated by using GEANT3. $A \times \epsilon_{\text{rec}}$ as a function of p_T for K^{*0} in INEL pp collisions at $\sqrt{s} =$13 TeV is shown in Fig. 5.3. The left panel of Fig. 5.4 shows $A \times \epsilon_{\text{rec}}$ as a function of p_T for K^{*0} in various V0M multiplicity classes and the right panel of Fig. 5.4 shows ratios of $A \times \epsilon_{\text{rec}}$ in each multiplicity classes to the $A \times \epsilon_{\text{rec}}$ in INEL > 0 events. A small multiplicity dependence (5% at lowest p_T bin) of $A \times \epsilon_{\text{rec}}$ is observed. Therefore, the raw spectrum in each multiplicity class is corrected with the corresponding $A \times \epsilon_{\text{rec}}$ from the same multiplicity class.

In addition a re-weighting procedure is also performed to encounter the shape of the generated p_T spectra in MC. This procedure is similar as used for the spin alignment analysis (discussed in Sec. 3.2.3). Re-weighting factors are within 3% at low
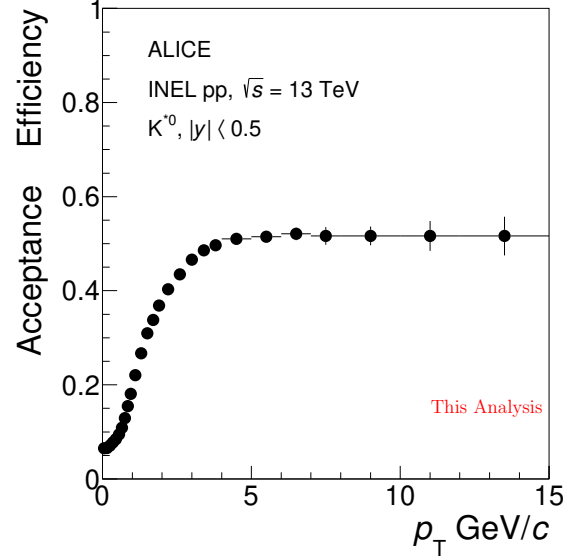
Figure 5.3: Left panel: Acceptance × Efficiency as a function of p_T in INEL pp collisions at $\sqrt{s}$ =13 TeV. Errors are statistical only and calculated using Bayesian approach (see 3.2.2).
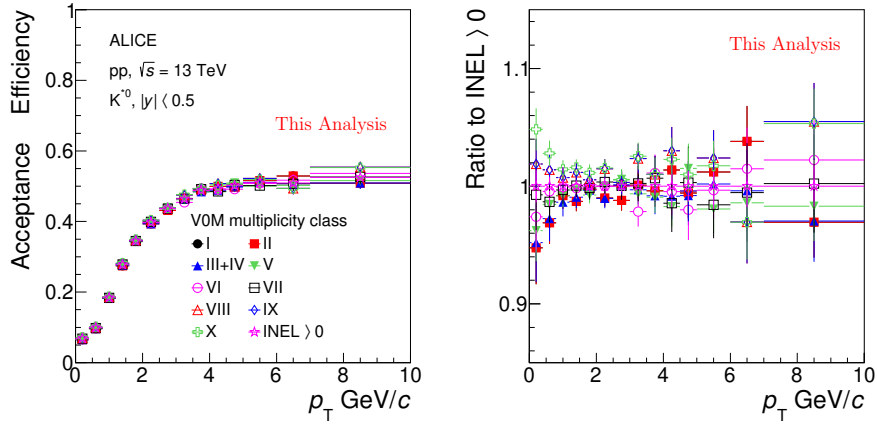
Figure 5.4: Left panel: Acceptance × Efficiency as a function of p_T in different multiplicity classes. Right panel: Ratio of ϵ_{rec} between different multiplicity classes and minimum bias events. Results are for pp collisions at $\sqrt{s}$ = 13 TeV. Errors are statistical only and calculated using Bayesian approach.

p_T for all multiplicity classes (see Appendix D.2). In minimum bias INEL pp collisions analysis is performed in small p_T bin compared to multiplicity dependent analysis. Therefore in minimum bias INEL pp collisions, correction due to re-weighting is negligible.

5.0.5 Corrected p_T spectra

Raw spectra are corrected for the efficiency and acceptance of the detector and branching ratio. The normalized corrected spectra is obtained using the following formula,

$$\frac{1}{N_{\text{INEL or INEL} > 0}} \frac{\mathrm{d}^2 n}{\mathrm{d}p_T \mathrm{d}y} = \frac{1}{N_{\text{accepted}}} \frac{\mathrm{d}^2 n^{\text{raw}}}{\mathrm{d}p_T \mathrm{d}y} \times \frac{1}{\text{BR} \times A \times \epsilon_{\text{rec}}} \times \epsilon_{\text{event}} \times \epsilon_{\text{signal}}.$$
(5.2)

Here N_{accepted}, n^{raw}, BR and $A \times \epsilon_{\text{rec}}$ correspond to the number of events, raw K^{*0} yield, branching ratio (0.666) and Acceptance $\times$ Efficiency of K^{*0}. The factor ϵ_{event} and ϵ_{signal} are the event loss and signal loss correction. ϵ_{event} embeds vertex reconstruction and event selection efficiencies and calculated using the Bayesian unfolding techniques with the MC data sample, as discussed in [32]. In case of K^{*0} measurement in INEL pp collisions vertex reconstruction efficiency and event selection efficiency are calculated separately and are discussed at the end of this section. ϵ_{event} is applied in order to normalize the measured yield to the true number of INEL>0 pp collisions in a given multiplicity bin. This is obtained by using Eq. 5.3

$$\epsilon_{\text{event}} = \frac{N_{\text{accepted}}}{N_{\text{INEL} > 0}}.$$
(5.3)

Here N_{accepted} is the number of accepted events after satisfying all event selection criteria and $N_{\text{INEL} > 0}$ is the number of events with a "true" production vertex located within $|z_{\text{vertex}}^{\text{true}}| < 10$ cm and at least one charged primary particle produced in $|\eta| < 1.0$. ϵ_{event} is calculated using PYTHIA event generator. In case of K^{*0} measurement

in INEL pp collisions, ϵ_{event} is used to get the total number of INEL events from the total number of accepted events, using the ratio of the ALICE V0 visible cross section [33, 34] to the total inelastic cross section. The value of ϵ_{event} in INEL pp collisions at $\sqrt{s} = 13$ TeV is 0.745 ± 0.019 [35]. Values of ϵ_{event} for various multiplicity classes in pp collisions at $\sqrt{s} = 13$ TeV are shown in Table 5.2.

Table 5.2: ϵ_{event} in pp collisions at $\sqrt{s} = 13$ TeV.

V0M multiplicity class (%)	ϵ_{event}
INEL > 0	0.892
I (0–1%)	0.998
II (1–5%)	0.999
III (5–10%)	0.998
IV (10–15%)	0.998
V (15–20%)	0.997
VI (20–30%)	0.994
VII (30–40%)	0.986
VIII (40–50%)	0.972
IX (50–70%)	0.935
X (70–100%)	0.757

K^{*0} measurements in INEL pp collisions are also corrected for the vertex reconstruction efficiency, calculated from data. The vertex reconstruction efficiency is the ratio of the number of triggered events with pileup rejection and the number of events for which a good vertex was found (i.e. it passes the vertex quality selections but without the selection criterion on the z-position of the vertex). The value of vertex reconstruction efficiency is 0.93.

The signal loss correction accounts the loss for K^{*0} signal in non-triggered events. ϵ_{signal} is calculated using the same simulation as used in the calculation for Acceptance × Efficiency. This correction factor is calculated by dividing the K^{*0} simulated

p_T spectrum before trigger and event selection criteria to the corresponding p_T spectrum after those selections. The left panel of Fig. 5.5 shows signal correction factor for K^{*0} as a function of p_T in INEL pp collisions at $\sqrt{s} = 13$ TeV and the right panel of Fig. 5.5 shows signal correction factor for K^{*0} in various V0M multiplicity classes of pp collisions at $\sqrt{s} =$13 TeV.
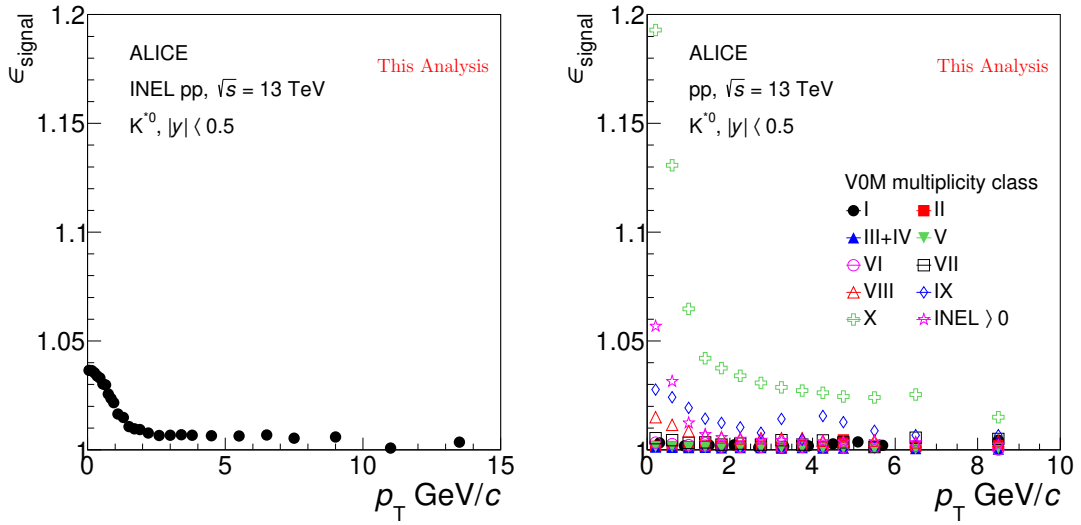
Figure 5.5: Signal loss correction factor ϵ_{signal} as a function of p_T for K^{*0} in INEL pp collisions (left panel) and in various V0M multiplicity classes of pp collisions (right panel) at $\sqrt{s} = 13$ TeV. ϵ_{signal} in INEL pp collisions (left panel) is not exactly same as ϵ_{signal} in INEL > 0 pp collisions (right panel) as the event selection criteria and p_T bining used for this two analyses are different.

Panel (a) of Fig. 5.6 shows p_T spectra of K^{*0} in INEL pp collisions at $\sqrt{s} = 13$ [37] and 7 TeV [38]. Measurement in pp collisions at $\sqrt{s} = 13$ TeV is compared with the p_T spectrum extracted from the PYTHIA 8 [1], PYTHIA 6 [36], and EPOS-LHC [2] models. Ratios of K^{*0} p_T spectra from model calculations to the experimentally measured p_T spectrum are shown in panel (b) of Fig. 5.6. All models describe the measured K^{*0} spectrum at intermediate p_T with reasonable accuracy but overestimate the measured K^{*0} spectrum at low p_T and high p_T. At low p_T (< 1 GeV/c), EPOS-LHC quantitatively describes the experimental measurement better compared
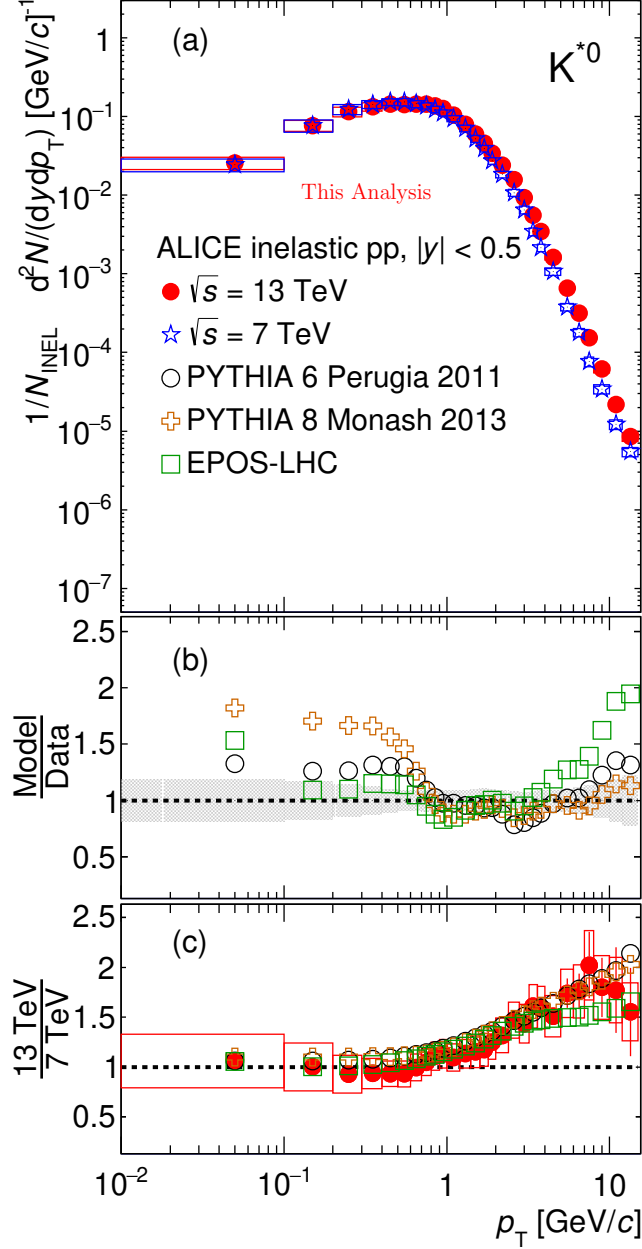
Figure 5.6: Panel (a): Transverse momentum spectra of K^{*0} measured at mid-rapidity ($|y| < 0.5$) in INEL pp collisions at $\sqrt{s} = 13$ TeV [37] (filled symbols) and 7 TeV [38] (open symbols). Statistical and systematic uncertainties are shown as vertical error bars and boxes, respectively. Panel (b): Ratios of K^{*0} p_T spectra from model calculations to the p_T spectra measured in the ALICE experiment in INEL pp collisions at $\sqrt{s} = 13$ TeV. The total fractional uncertainties of the data are shown in shaded band, i.e. the statistical and systematic uncertainties of the measurement have been summed in quadrature. Panel (c): Ratio of the p_T spectrum of K^{*0} in INEL pp collisions at $\sqrt{s} = 13$ TeV to $\sqrt{s} = 7$ TeV, along with the model calculations.

to PYTHIA 6 and PYTHIA 8, whereas at high p_T (> 4 GeV/c) PYTHIA 8 works better compared to other models. Panel (c) of Fig. 5.6 shows ratio of the p_T spectrum of K^{*0} between $\sqrt{s} = 13$ and 7 TeV. This ratio is consistent with unity at low p_T (< 1 GeV/c) and then exhibit a clear increase as a function of p_T. The p_T dependence of the ratio indicates that the hard processes or production of high p_T particle become dominant with the increase of collision energy. All studied MC models are in good agreement with the experimentally measured ratio of K^{*0} p_T spectrum in pp collisions at $\sqrt{s} = 13$ TeV and 7 TeV.

Figure 5.7 shows p_T spectra for K^{*0} in different multiplicity classes as well as ratios of these to the INEL > 0 spectrum [39]. The slope of the p_T spectrum increases from low to high multiplicity event classes. Change in the shape of the p_T spectrum is mainly dominant at low p_T (< 4 GeV/c), whereas at high p_T, spectra in various multiplicity classes have similar spectral shape, indicating that the processes that change the shape of p_T spectra in different multiplicity classes are dominant primarily at low p_T.

5.1   Sources of systematic uncertainties

For systematic study each of the event selection criteria, PID selection criteria, track selection criteria and signal extraction criteria are varied independently and contribution from each of the sources are added in quadrature to get the total systematic uncertainties, considering them uncorrelated to each other. Sources of systematic uncertainties are same as discussed in 3.5. In addition, systematic uncertainty due to the signal-loss correction factor is also evaluated. The correction factor is calculated using the two different simulation productions PYTHIA 8 Monash 2013 tune and PYTHIA 6, Perugia 2011 tune. The PYTHIA 8 correction is used as the default and
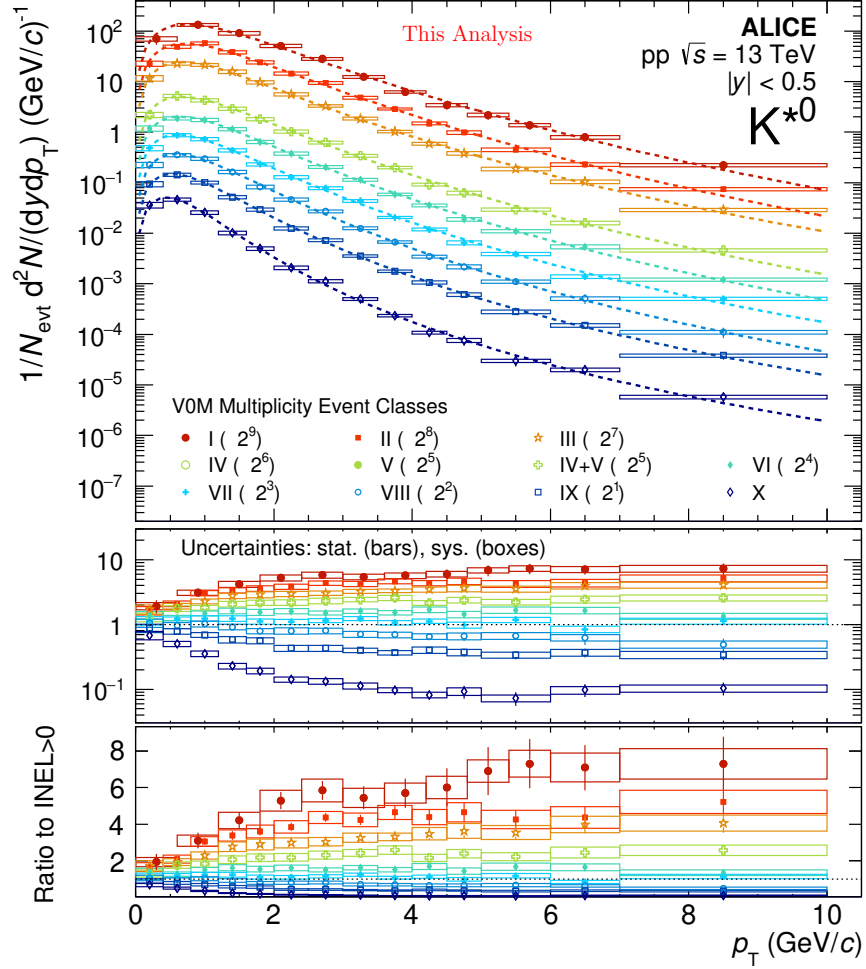
Figure 5.7: Upper panel: Transverse momentum spectra of K^{*0} pp collisions at $\sqrt{s} = 13$ TeV [39] for different multiplicity classes, scaled by factors as indicated in figure for better visibility. The Lower panels: The ratios of the multiplicity dependent p_T spectra to the INEL > 0 spectrum (both linear and logarithmic vertical scales have been shown). Dotted line corresponds to the Levy-Tsallis fit of the spectrum.

difference between PYTHIA 8 and PYTHIA 6 calculation is used as systematic uncertainty. This uncertainty is mainly contributes in 70-100% multiplicity class and for other multiplicity classes it is negligible. The left panel of Fig. 5.8 shows contribution of systematic uncertainties from various sources in multiplicity integrated pp collisions at $\sqrt{s} = 13$ TeV. The right panel of Fig. 5.8 shows systematic uncertainty due to signal loss correction in 70-100% multiplicity class. We do not observe significant multiplicity dependence on the estimated total systematic uncertainties in different multiplicity classes. Therefore, we have used % of total systematic uncertainty of minimum bias events for other multiplicity classes.
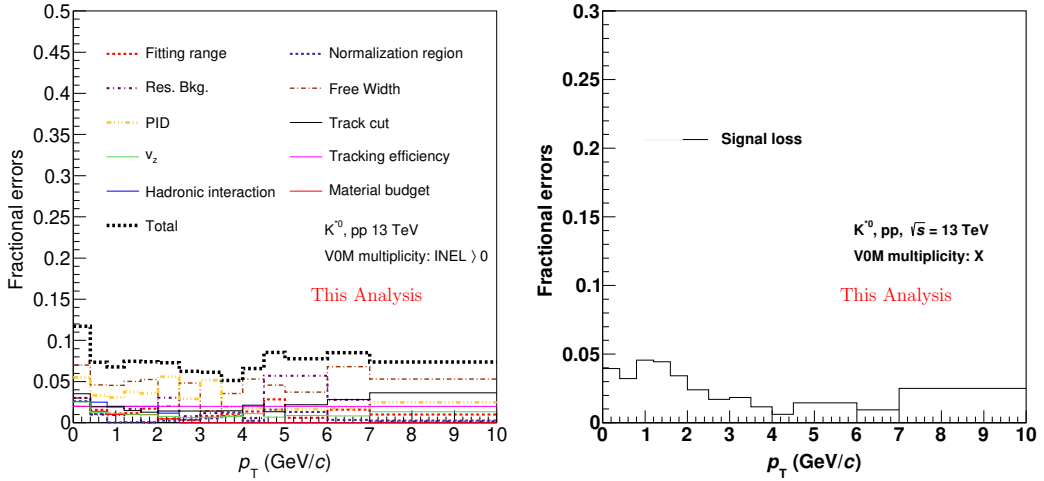
Figure 5.8: Left panel: Systematic uncertainties for K^{*0} in minimum bias pp collisions at $\sqrt{s} = 13$ TeV. Right panel: Uncertainty due to signal loss correction in 70-100% multiplicity class.

Systematic uncertainties are further smoothed to avoid fluctuations in systematic uncertainties. Barlow check has been performed for all the variations and if any source fails the Barlow check then only it contributes to the systematic uncertainties.

In addition, we have also estimated multiplicity uncorrelated systematic uncertainties. Systematic uncertainties across different multiplicity classes are largely cor-

related. Any type of correlated systematic variation will cause a similar amount of deviations from the default value across different multiplicity event classes. Uncorrelated systematic uncertainties are estimated by the "R" method which is also used in the K^{*0} analysis in p–Pb collision [8]. The uncorrelated systematic uncertainty is evaluated as,

$$\text{R} = 1 - \frac{\frac{Y^{\text{variation}}_{\text{multiplicity class: i}}}{Y^{\text{default}}_{\text{multiplicity class: i}}}}{\frac{Y^{\text{variation}}_{\text{INEL} > 0}}{Y^{\text{default}}_{\text{INEL} > 0}}}. \tag{5.4}$$

Here "Y" corresponds to the K^{*0} yield and "i" corresponds to the different multiplicity classes. Measurement with default selection criteria and systematic variations are denoted as "default" and "variation", respectively. The uncorrelated systematic uncertainties on $\mathrm{d}N/\mathrm{d}y$ and $\langle p_{\mathrm{T}} \rangle$ are given in Table 5.3.

5.2 Results

5.2.1 Transverse momentum integrated yield and mean transverse momentum

The p_{T} integrated yield and mean transverse momentum are calculated as discussed in 4.5.1. The K^{*0} is measured down to $p_{\mathrm{T}} = 0$ GeV/c. Therefore no low p_{T} extrapolation is needed to calculate $\mathrm{d}N/\mathrm{d}y$ and $\langle p_{\mathrm{T}} \rangle$. Measured $\mathrm{d}N/\mathrm{d}y$ and $\langle p_{\mathrm{T}} \rangle$ values in INEL pp collisions and for various multiplicity classes are shown in Table 5.3.

The left panel of Fig. 5.9 shows the $\mathrm{d}N/\mathrm{d}y$ of K^{*0} as a function of collision energy and the right panel of Fig. 5.9 shows the $\langle p_{\mathrm{T}} \rangle$ of K^{*0} as a function of collision energy in pp collisions. Both $\mathrm{d}N/\mathrm{d}y$ and $\langle p_{\mathrm{T}} \rangle$ of K^{*0} increases with collision energy.

Figure 5.10 shows the $\mathrm{d}N/\mathrm{d}y$ of K^{*0} and ϕ mesons as a function of $\langle \mathrm{d}N_{\mathrm{ch}}/\mathrm{d}\eta \rangle$ in pp collisions at $\sqrt{s} = 13$ TeV [39]. Measurements are compared with the results for pp collisions at $\sqrt{s} = 7$ TeV [40] and for p–Pb collisions at $\sqrt{s_{\mathrm{NN}}} = 5.02$ TeV [8]. $\mathrm{d}N/\mathrm{d}y$ increases linearly with increasing $\langle \mathrm{d}N_{\mathrm{ch}}/\mathrm{d}\eta \rangle$ for both the resonance particles.

Table 5.3: The dN/dy and $\langle p_T \rangle$ values for K^{*0} at mid-rapidity ($|y| < 0.5$) in various V0M multiplicity classes of pp collisions at $\sqrt{s} = 13$ TeV. The first, second and third uncertainty represents the statistical, total systematic and uncorrelated systematic uncertainties, respectively. Measurements for INEL pp collisions are also given.

V0M multiplicity classes	dN/dy	$\langle p_T \rangle$ (GeV/c)
I	$0.468 \pm 0.030 \pm 0.036 \pm 0.025$	$1.445 \pm 0.054 \pm 0.028 \pm 0.022$
II	$0.368 \pm 0.012 \pm 0.028 \pm 0.019$	$1.371 \pm 0.027 \pm 0.026 \pm 0.021$
III	$0.305 \pm 0.010 \pm 0.023 \pm 0.016$	$1.310 \pm 0.027 \pm 0.028 \pm 0.016$
IV + V	$0.244 \pm 0.006 \pm 0.019 \pm 0.010$	$1.253 \pm 0.018 \pm 0.026 \pm 0.013$
VI	$0.191 \pm 0.004 \pm 0.015 \pm 0.010$	$1.179 \pm 0.016 \pm 0.026 \pm 0.017$
VII	$0.157 \pm 0.004 \pm 0.012 \pm 0.007$	$1.117 \pm 0.018 \pm 0.020 \pm 0.013$
VIII	$0.125 \pm 0.003 \pm 0.009 \pm 0.006$	$1.042 \pm 0.016 \pm 0.023 \pm 0.011$
IX	$0.091 \pm 0.002 \pm 0.007 \pm 0.004$	$0.953 \pm 0.011 \pm 0.022 \pm 0.012$
X	$0.051 \pm 0.001 \pm 0.005 \pm 0.002$	$0.771 \pm 0.007 \pm 0.019 \pm 0.008$
INEL	$0.105 \pm 0.001 \pm 0.010$	$1.121 \pm 0.005 \pm 0.030$
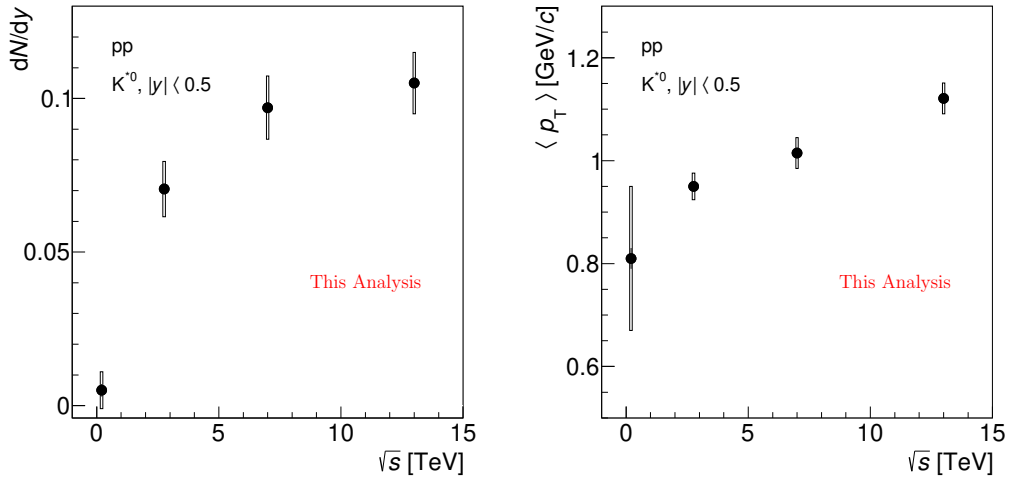
Figure 5.9: dN/dy and $\langle p_T \rangle$ as a function of $\sqrt{s}$ in pp collisions.

Measurements in pp collisions at $\sqrt{s} = 7$ TeV and for p–Pb collisions at $\sqrt{s_{\mathrm{NN}}} = 5.02$ TeV are consistent with measurements in pp collisions at $\sqrt{s} = 13$ TeV for similar values of $\langle \mathrm{d}N_{\mathrm{ch}}/\mathrm{d}\eta \rangle$. This indicates that the production rate of K^{*0} and ϕ do not depends on the collision system or energy and is driven by charge particle multiplicity in an event. Similar observation is also reported for other identified hadrons [41, 42]. Measured $\mathrm{d}N/\mathrm{d}y$ values for K^{*0} and ϕ mesons are also compared with the PYTHIA 6, PYTHIA 8, EPOS-LHC and DIPSY model calculations. EPOS–LHC and PYTHIA 8 without CR mechanism provide the best description for the K^{*0} $\mathrm{d}N/\mathrm{d}y$ values among all the model calculations presented here, whereas other PYTHIA calculations exhibit fair agreement with the measured data, and DIPSY tends to overestimate the K^{*0} yields. For the ϕ meson, EPOS–LHC gives a better description of the data, whereas other model calculation underestimate the yields.
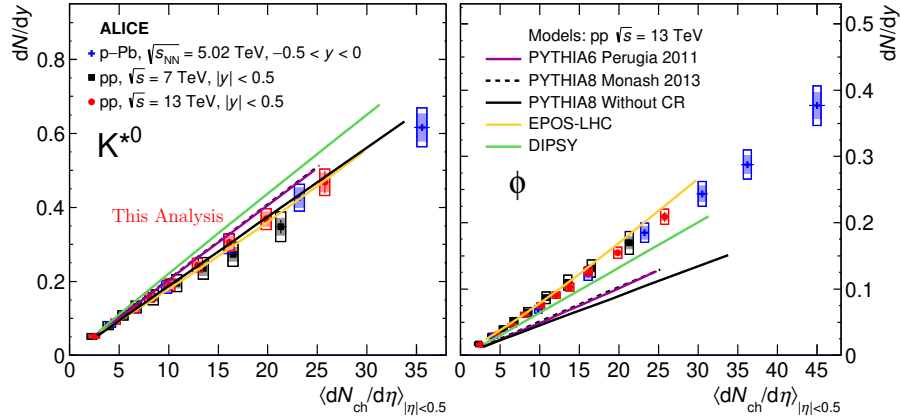
Figure 5.10: $\mathrm{d}N/\mathrm{d}y$ of K^{*0} and ϕ mesons as a function of $\langle \mathrm{d}N_{\mathrm{ch}}/\mathrm{d}\eta \rangle$ in pp collisions at $\sqrt{s} = 13$ TeV [39] along with the measurements from pp collisions at $\sqrt{s} = 7$ TeV [40] and p–Pb collisions at $\sqrt{s_{\mathrm{NN}}} = 5.02$ TeV [8]. The measurements in pp collisions at $\sqrt{s} = 13$ TeV are also compared with PYTHIA 6, PYTHIA 8, EPOS–LHC and DIPSY model calculations. Bars represent statistical uncertainties, open boxes represent total systematic uncertainties, and shaded boxes show the systematic uncertainties that are uncorrelated between multiplicity classes.

Figure 5.11 shows $\langle p_{\mathrm{T}} \rangle$ for K^{*0} and ϕ mesons as a function of $\langle \mathrm{d}N_{\mathrm{ch}}/\mathrm{d}\eta \rangle$ [39].
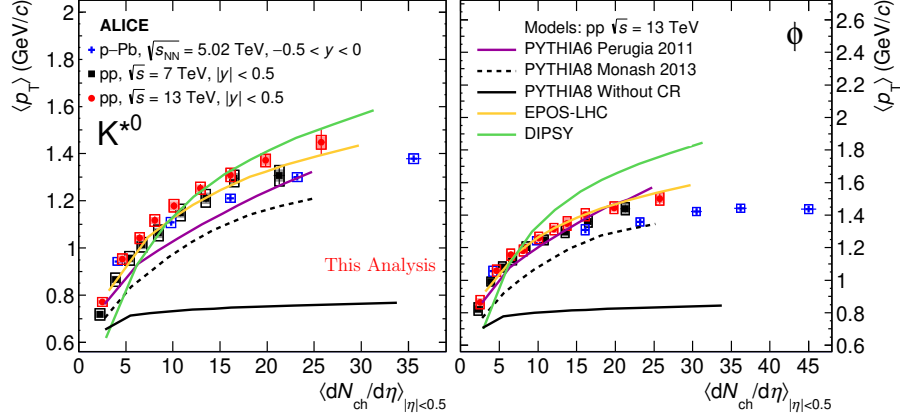
Figure 5.11: $\langle p_T \rangle$ of K^{*0} and ϕ mesons as a function of $\langle \mathrm{d}N_{\mathrm{ch}}/\mathrm{d}\eta \rangle$ in pp collisions at $\sqrt{s} = 13$ TeV [39] along with the measurements from pp collisions at $\sqrt{s} = 7$ TeV [40] and p–Pb collisions at $\sqrt{s_{\mathrm{NN}}} = 5.02$ TeV [8]. The measurements in pp collisions at $\sqrt{s} = 13$ TeV are also compared with PYTHIA 6, PYTHIA 8, EPOS–LHC and DIPSY model calculations. Bars represent statistical uncertainties, open boxes represent total systematic uncertainties, and shaded boxes show the systematic uncertainties that are uncorrelated between multiplicity classes.

Measurements are compared with the results from p–Pb and pp collisions at $\sqrt{s_{\mathrm{NN}}} = 5.02$ TeV [8] and $\sqrt{s} = 7$ TeV [40], respectively. $\langle p_T \rangle$ values increase with increasing $\langle \mathrm{d}N_{\mathrm{ch}}/\mathrm{d}\eta \rangle$, similar as observed for A–A collisions [43], where the rise of $\langle p_T \rangle$ with $\langle \mathrm{d}N_{\mathrm{ch}}/\mathrm{d}\eta \rangle$ is due to the increase of collective flow velocity with peripheral to central A–A collisions. The $\langle p_T \rangle$ values show a hint of energy dependence. For $\langle \mathrm{d}N_{\mathrm{ch}}/\mathrm{d}\eta \rangle >$ 5, the measured $\langle p_T \rangle$ values in pp collisions at 13 TeV are slightly higher compared to the measurements in pp collisions at 7 TeV and p–Pb collisions at 5.02 TeV for similar $\langle \mathrm{d}N_{\mathrm{ch}}/\mathrm{d}\eta \rangle$. Similar observation has been also reported for strange hadrons [42]. The measured $\langle p_T \rangle$ values are compared with five different model calculations: PYTHIA 6, PYTHIA 8 (both with and without CR), EPOS–LHC and DIPSY. Core–corona based EPOS model which has hydrodynamically expanding "core" part provides a good agreement with the measured $\langle p_T \rangle$ values as a function of $\langle \mathrm{d}N_{\mathrm{ch}}/\mathrm{d}\eta \rangle$. PYTHIA model without color reconnection provides an almost constant $\langle p_T \rangle$ with $\langle \mathrm{d}N_{\mathrm{ch}}/\mathrm{d}\eta \rangle$;

this is a very different behaviour with respect to the measurements. Inclusion of CR in models such as PYTHIA and DIPSY also give a qualitative agreement with the measurements. PYTHIA 8 calculations underestimate the $\langle p_{\mathrm{T}} \rangle$ values of K^{*0} and ϕ along with other strange hadrons (K_{S}^0, Λ, Ξ and Ω) [42]. Color reconnection introduces a flow-like effect, resulting in an increase in $\langle p_{\mathrm{T}} \rangle$ values with increasing multiplicity without assuming any hydrodynamic expansion [44]. PYTHIA 6 provides, a good description of the $\langle p_{\mathrm{T}} \rangle$ values for ϕ, but underestimate $\langle p_{\mathrm{T}} \rangle$ values of K^{*0}. The $\langle p_{\mathrm{T}} \rangle$ values obtained from EPOS–LHC calculations are consistent with the measured $\langle p_{\mathrm{T}} \rangle$ values for K^{*0} and ϕ. DIPSY gives a large increase in $\langle p_{\mathrm{T}} \rangle$ from low to high $\langle \mathrm{d}N_{\mathrm{ch}}/\mathrm{d}\eta \rangle$ than is actually observed; this discrepancy is greater for the ϕ and is also observed for other strange hadrons [42]. Among all the model results compared to the data, EPOS-LHC gives the best agreement. Increase of $\langle p_{\mathrm{T}} \rangle$ with $\langle \mathrm{d}N_{\mathrm{ch}}/\mathrm{d}\eta \rangle$ is explained by both hydrodynamical model and model that includes CR.

Figure 5.12 shows the values of $\langle p_{\mathrm{T}} \rangle$ for K^{*0} and ϕ mesons along with those for other hadrons. In central A–A collisions, a mass ordering of the $\langle p_{\mathrm{T}} \rangle$ values has been observed; particles with similar masses (e.g. K^{*0}, p and ϕ) have similar $\langle p_{\mathrm{T}} \rangle$ [45]. This behaviour has been attributed as a consequence of hydrodynamical radial flow. However, this mass ordering breaks down for small collision system. In pp collisions at $\sqrt{s} = 13$ TeV, the $\langle p_{\mathrm{T}} \rangle$ values for K^{*0} are greater than those for the more massive proton and Λ for the same multiplicity classes. The $\langle p_{\mathrm{T}} \rangle$ values for ϕ exceed those for Λ and even approach those for Ξ, despite the approximately 30% larger mass of the Ξ compared to ϕ. Violation of mass ordering of $\langle p_{\mathrm{T}} \rangle$ in small system supports the CR mechanism as an origin of the flow like behaviour observed in small collision systems. This could also be a manifestation of differences between the p_{T} spectra of mesons and baryons and have also been in the m_{T} spectra of hadrons in pp collisions, discussed later in this section.
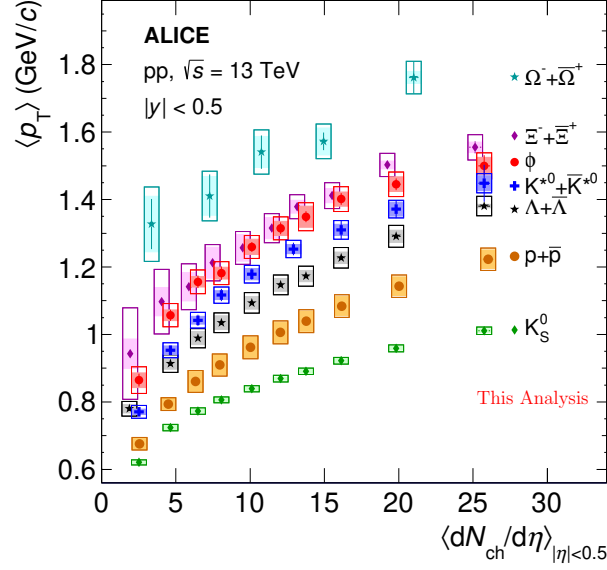
Figure 5.12: $\langle p_{\mathrm{T}} \rangle$ of K_S^0, p, K^{*0}, ϕ, Λ, Ξ and Ω as a function $\langle \mathrm{d}N_{\mathrm{ch}}/\mathrm{d}\eta \rangle$ in pp collisions at $\sqrt{s} = 13$ TeV [39]. Statistical uncertainties are represented by bars and total systematic uncertainties are represented by boxes. Shaded boxes show the systematic uncertainties that are uncorrelated between multiplicity classes.

5.2.2 Resonance to stable particle ratios

Figure 5.13 shows p_{T} integrated K^{*0}/K and ϕ/K ratio as a function of $\langle \mathrm{d}N_{\mathrm{ch}}/\mathrm{d}\eta \rangle$ [39]. Measurements in pp collisions at $\sqrt{s} = 13$ TeV are consistent with those obtained at pp collisions at $\sqrt{s} = 7$ TeV [40] and p–Pb collisions at $\sqrt{s_{\mathrm{NN}}} = 5.02$ TeV [8] for similar values of $\langle \mathrm{d}N_{\mathrm{ch}}/\mathrm{d}\eta \rangle$. K^{*0}/K ratio shows a decreasing trend with increasing $\langle \mathrm{d}N_{\mathrm{ch}}/\mathrm{d}\eta \rangle$ in all the collision systems. For pp collisions at $\sqrt{s} = 13$ TeV, the K^{*0}/K ratio in the highest multiplicity class is smaller compared to the lowest multiplicity class at a 2.3 σ level (considering only the multiplicity uncorrelated uncertainties). The decrease in K^{*0}/K ratio in central A–A collisions has been attributed to a re-scattering effect of K^{*0} decay daughters inside the hadronic medium [45]. Observed decreasing trend of K^{*0}/K ratio with increasing $\langle \mathrm{d}N_{\mathrm{ch}}/\mathrm{d}\eta \rangle$ indicates a possible presence of hadronic re-scattering in small collision system. The K^{*0}/K ratio in pp

collisions at $\sqrt{s}$ = 13 TeV is well described by EPOS–LHC model which includes hadronic re-scattering. PYTHIA and DIPSY overestimate the K^{*0}/K ratio at large multiplicities and do not reproduce the apparent decrease of K^{*0}/K ratio with increasing $\langle \mathrm{d}N_{\mathrm{ch}}/\mathrm{d}\eta \rangle$. The ϕ/K ratio in all collision systems is fairly constant as a function of $\langle \mathrm{d}N_{\mathrm{ch}}/\mathrm{d}\eta \rangle$. Due to large lifetime (10 times more than K^{*0}) of the ϕ meson, it decays outside the hadronic medium. Hence, decay daughters of ϕ meson do not re-scatter inside the hadronic phase. EPOS–LHC slightly overestimates the ϕ/K ratio, but is closer to the experimental measurements than PYTHIA and DIPSY model calculations which significantly underestimate the ϕ/K ratio.
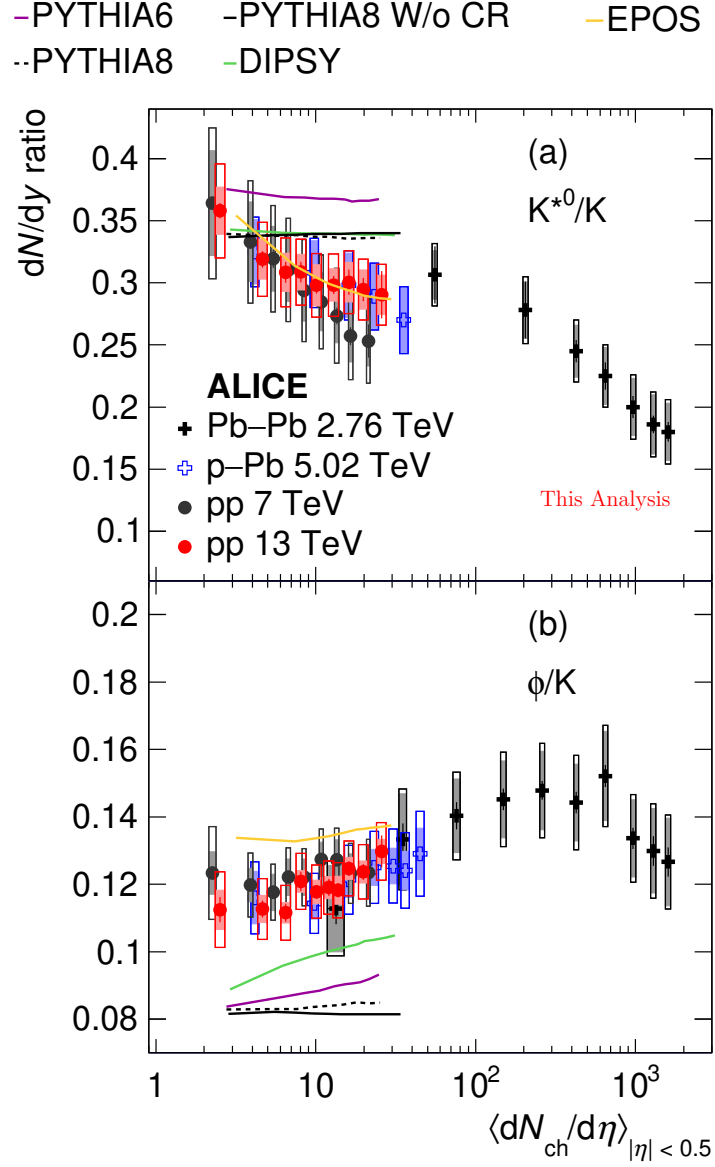
Figure 5.13: The K^{*0}/K (panel (a)) and ϕ/K (panel (b)) ratio as a function of $\langle dN_{ch}/d\eta \rangle$ in pp collisions at $\sqrt{s} = 13$ TeV [39] along with the measurements from pp collisions at $\sqrt{s} = 7$ TeV [40], p–Pb collisions at $\sqrt{s_{NN}} = 5.02$ TeV [8] and Pb–Pb collisions at $\sqrt{s_{NN}} = 2.76$ TeV [46]. The measurements in pp collisions at $\sqrt{s} = 13$ TeV are also compared with various model calculations. Bars represent statistical uncertainties, open boxes represent total systematic uncertainties, and shaded boxes show the systematic uncertainties that are uncorrelated between multiplicity classes.

5.2.3 Scaling properties of hadron production

Identified hadron production in high energy pp collisions exhibit two kinds of universal scaling: m_T scaling and x_T scaling. The m_T scaling is observed as low p_T, whereas the x_T scaling is observed at high p_T. Scaling properties of produced hadrons in pp collisions at $\sqrt{s} = 13$ TeV have been discussed below.

5.2.3.1 m_T scaling
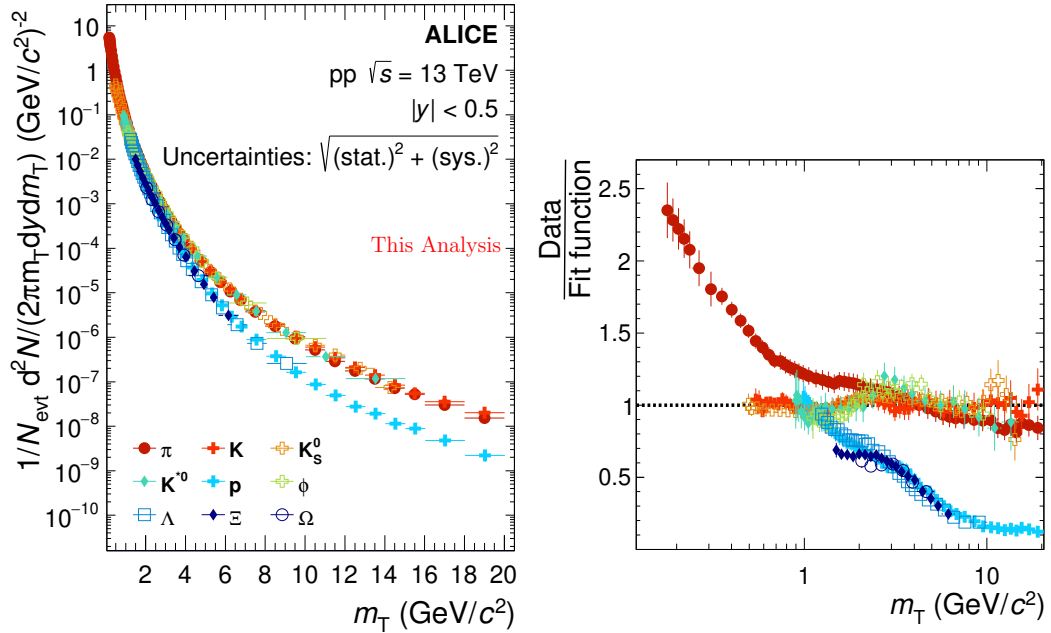
Figure 5.14: Left panel: Scaled m_T spectra for identified hadrons in pp collisions at $\sqrt{s} = 13$ TeV [37]. Right panel: Ratios of the scale m_T spectra to the function which fits the kaon m_T spectra.

The charged kaon and proton spectra are fitted separately with the modified Hagedorn function of the form, $a \times (e^{-bm_T} + m_T/c)^{-d}$, where a, b, c and d are fit parameters. The m_T spectra for other mesons are fitted in the measured m_T ranges ($m_T > 2$ GeV/c for the pion) with a parametrized fit function obtained from kaon spectra by leaving

the normalization parameter ("a") free. Then meson spectra are scaled with appropriate normalization factors so that their normalization parameters match with the normalization parameter of the kaon fit function. In a similar way m_{T} spectra for baryons are normalized to the proton m_{T} spectra by using parametrized proton fit function. The baryon spectra are further scaled so that all the m_{T} spectra have the same value at $m_{\mathrm{T}} = 1$ GeV/c^2. The left panel of Fig. 5.14 shows scaled m_{T} spectra of identified hadrons in pp collisions at $\sqrt{s} = 13$ TeV [37]. The right panel of Fig. 5.14 shows ratios of scaled m_{T} spectra of identified hadrons to the kaon fit function. We have observed two different universal scaling: one for mesons and another for baryons. A clear difference in the slope is observed between the baryon and meson spectra for $m_{\mathrm{T}} > 2$ GeV/c^2. The separation between the meson and baryon m_{T} spectra may be a reflection of the fact that, according to the Lund model of hadronization, meson formation via the fragmentation of strings requires the break up of only a quark and anti-quark pair, while baryon can be formed by the diquark and anti-diquark break up of the string. The separation between the baryon and meson m_{T} spectra becomes approximately constant for $m_{\mathrm{T}} > 10$ GeV/c^2. The pion m_{T} spectrum deviates at low m_{T} or low p_{T} from the universal m_{T} scaling of other mesons. This deviation of pion m_{T} spectrum at low m_{T} is likely due to feed-down from resonance decays.

5.2.3.2 x_{T} scaling

The empirical x_{T} scaling for identified hadrons are tested using the invariant cross sections in pp collisions at $\sqrt{s} = 13$, 7 and 2.76 TeV. The high p_{T} cross section of particle production can be expressed by Eq. 5.1. The exponent "n" in Eq. 5.1 is calculated from the ratio of the invariant cross sections at two different collision energies, scaled by the logarithm of the ratio of the two collision energy. Figure 5.15 shows n values of K^{*0} as a function of x_{T}, obtained by using the K^{*0} invariant
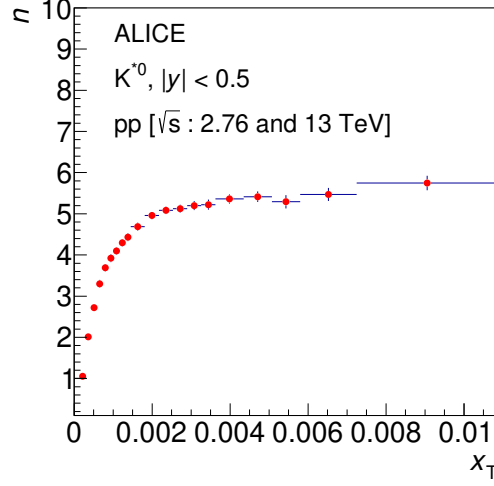
Figure 5.15: The x_T exponent "n" as a function of x_T for K^{*0} in pp collisions at 13 and 2.76 TeV.

cross section in pp collisions at 13 and 2.76 TeV. n depends on both x_T and $\sqrt{s}$. It increases with x_T in the low x_T region, where particle production is dominated by soft processes, and appears to saturate in the high x_T region. Exponent "n" is estimated for 3 different combination of collisions energies: (13 TeV, 7 TeV), (13 TeV, 2.76 TeV) and (7 TeV, 2.76 TeV). Obtained $n(x_\mathrm{T}, \sqrt{s})$ distributions are fitted with a constant in the range $2 \times 10^{-3} \leq x_\mathrm{T} \leq 6 \times 10^{-3}$ to get the respective n values for different energy combinations. These n values are then averaged to obtain the mean value ($\langle n \rangle$). In addition to K^{*0}, $\langle n \rangle$ values are also extracted for pion, kaon and proton to understand the hadron species dependency of x_T scaling. Each of the x_T spectrum for different hadrons in different energies is then scaled by $\sqrt{s}^{\langle n \rangle}$ to get the x_T scaling. The best scaling is achieved with the exponents $\langle n \rangle = 5.04 \pm 0.02$ for pion, $\langle n \rangle = 5.02^{+0.21}_{-0.25}$ for kaon, $\langle n \rangle = 5.83^{+0.13}_{-0.21}$ for proton, and $\langle n \rangle = 5.23 \pm 0.15$ for K^{*0}. The uncertainties on the $\langle n \rangle$ values are the maximum deviation of n values (obtained for 3 different combination of energies as discussed above) from the $\langle n \rangle$. The $\langle n \rangle$ values for all mesons are consistent with each other within uncertainties. Scaled x_T

179

spectra [37] for pion, kaon, proton and K^{*0} have been shown in Fig. 5.16. Identified
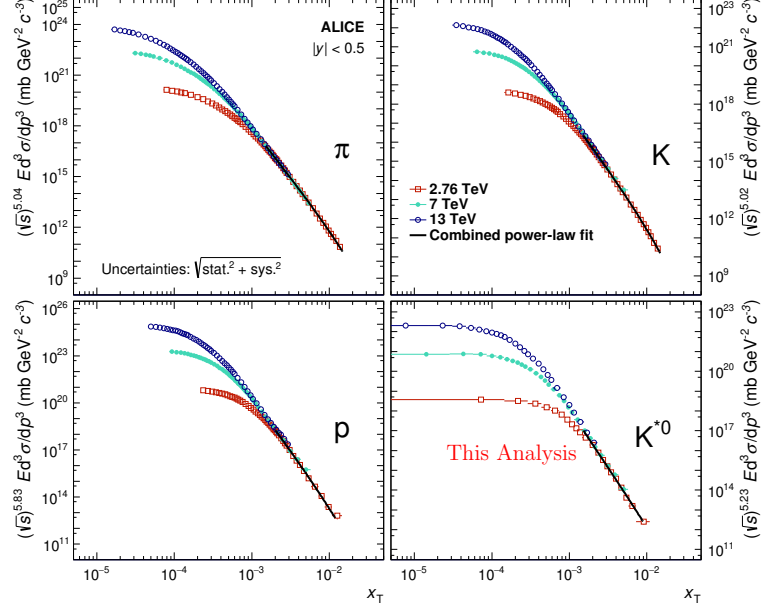

Figure 5.16: Scaled invariant yields of pion, kaon, K^{*0} and proton as a function of x_{T} in pp collisions at LHC energies [37]. Solid line represents a combined power-law fit in the high x_{T} region where the distributions show scaling behaviour.

hadrons at LHC energies follow the empirical x_{T} scaling behaviour at high p_{T} or x_{T}. The value of the exponent parameter $\langle n \rangle$ is found to be lower at LHC energies compared to RHIC energies [23]. It is also interesting to note that the value of $\langle n \rangle$ is higher for baryon compared to meson. The NLO pQCD including higher twist processes predict a larger value of the exponent for baryons compared to mesons [26] which is in contrast to the observations based on the leading twist processes, where the exponent $\langle n \rangle$ has only a weak dependence on hadron species.

5.3   Summary

In this chapter, we have reported K^{*0} production in INEL pp collisions and in various multiplicity classes of pp collisions at $\sqrt{s} = 13$ TeV. Measured K^{*0} spectrum in pp collisions at $\sqrt{s} = 13$ TeV has larger slope compared to the K^{*0} spectrum in

pp collisions at $\sqrt{s} = 7$ TeV. Ratio of K^{*0} $p_{\rm T}$ spectrum between 13 and 7 TeV is consistent with unity at low $p_{\rm T}$ and increases with increasing $p_{\rm T}$. This measurement indicates that the hard processes or production of high $p_{\rm T}$ particle become dominant with the increase of collision energy. We have observed a breaking between meson and baryon $m_{\rm T}$ spectra scaling for $p_{\rm T} > 2$ GeV/c. The pion $m_{\rm T}$ spectrum deviates at low $m_{\rm T}$ or low $p_{\rm T}$ from the universal $m_{\rm T}$ scaling of other mesons. This deviation is likely due to feed-down from resonance decays. $x_{\rm T}$ scaling holds fairly well for the identified hadrons produced at the LHC energies. The value of exponent parameter $\langle n \rangle$ is slightly higher for baryon compared to meson.

The slopes of K^{*0} $p_{\rm T}$ spectra increase with increasing charged particle multiplicity for $p_{\rm T} < 4$ GeV/c as a consequence $\langle p_{\rm T} \rangle$ also increases with increasing $\langle {\rm d}N_{\rm ch}/{\rm d}\eta \rangle$. Change in spectral shape with increasing $\langle {\rm d}N_{\rm ch}/{\rm d}\eta \rangle$ is qualitatively similar to the collective radial expansion observed in A–A collisions collisions, but can also be explained through color reconnection mechanism. The mass ordering of the $\langle p_{\rm T} \rangle$ observed in central Pb–Pb collisions is violated in the small collision system. $\langle p_{\rm T} \rangle$ as a function $\langle {\rm d}N_{\rm ch}/{\rm d}\eta \rangle$ shows a hint of increase with collision energy for similar $\langle {\rm d}N_{\rm ch}/{\rm d}\eta \rangle$. The $p_{\rm T}$ integrated K^{*0} yield increases linearly with increasing $\langle {\rm d}N_{\rm ch}/{\rm d}\eta \rangle$. ${\rm d}N/{\rm d}y$ values of K^{*0} in pp collisions at $\sqrt{s} = 13$ TeV are consistent with the results obtained from the pp collisions at $\sqrt{s} = 7$ TeV and p–Pb collisions at $\sqrt{s_{\rm NN}} = 5.02$ TeV for similar charged particle multiplicity. EPOS–LHC better describes the multiplicity dependence of ${\rm d}N/{\rm d}y$ and $\langle p_{\rm T} \rangle$ of K^{*0} compared to other MC event generators. We have found a decreasing trend of K^{*0}/K ratio with increasing charged particle multiplicity in pp collisions at $\sqrt{s} = 13$ TeV similar to that observed in the heavy-ion collisions [45]. This observation may indicates a possible presence of short lived hadron gas phase in small system like pp collisions.

References

[1] P. Z. Skands et al., Eur. Phys. J. C 74, 3024 (2014).

[2] K.Werner et al., Phys. Rev. C 89, 064903 (2014).

[3] V. Khachatryan et al. [CMS Collaboration], Phys. Rev. Lett. 116, 172302 (2016).

[4] S. Acharya et al.ALICE Collaboration], Phys. Rev. Lett. 123, 142301 (2019).

[5] J. Adam et al. [ALICE Collaboration], Nat. Phys. 13, 535 (2017).

[6] S. Acharya et al. [ALICE collaboration], Phys. Rev. C 99, 024906 (2019).

[7] S. Acharya et al. [ALICE collaboration], Eur. Phys. J. C 80, 167 (2020).

[8] J. Adam et al. [ALICE Collaboration], Eur. Phys. J. C 76, 245 (2016).

[9] B. Abelev et al. [ALICE collaboration], Phys. Rev. C 88, 044910 (2013).

[10] B. Abelev et al. [ALICE collaboration], Phys. Lett. B 736, 196 (2014).

[11] B. Abelev et al. [ALICE collaboration], Phys. Rev. Lett. 111, 222301 (2013).

[12] A. Ortiz Velasquez et al., Phys. Rev. Lett. 111 (4), 042001 (2013).

[13] T. Sj´ostrand et al., JHEP 0605, 026 (2006).

[14] C. Bierlichet al., J. High Energy Phys. 3, 148 (2015).

[15] T. S. Biro et al., Nucl. Phys. B 245, 449 (1984).

[16] N. Armesto et al., Phys. Lett. B 344, 301 (1995).

[17] R. Hagedorn, Nuovo Cimento, Suppl.3 no. CERN-TH-520, 147 (1965).

[18] B. Alper et al., Nucl. Phys. B 87, 19 (1975).

[19] B. I. Abelev et al. [STAR collaboration], Phys. Rev. C 75, 64901 (2007)

[20] T. Aaltonen et al. [CDF collaboration], Phys. Rev.D 79, 112005 (2009).

[21] F. Abe et al. [CDF collaboration], Phys. Rev. Lett. 61, 1819 (1988).

[22] C. Albajar et al. [UA1 collaboration], Nucl. Phys.B 335, 261(1990).

[23] J. Adams et al. [STAR collaboration], Phys. Lett. B 637, 161 (2006).

[24] S. Chatrchyan et al. [CMS collaboration], JHEP 08, 086(2011).

[25] J. F. Owens, Rev. Mod. Phys. 590, 465 (1987).

[26] F. Arleo et al., Phys. Rev. Lett. 105, 062002 (2010).

[27] S. Acharya et al. [ALICE Collaboration], Eur. Phys. J. C 80, 167 (2020).

[28] K.A. Olive et al. (Particle Data Group), Chin. Phys. C, 38, 090001 (2014).

[29] [ALICE Collaboration], https://alice-notes.web.cern.ch/node/563.

[30] [ALICE Collaboration], https://alice-notes.web.cern.ch/node/678.

[31] [ALICE Collaboration], https://alice-notes.web.cern.ch/node/219.

[32] [ALICE Collaboration], https://alice-notes.web.cern.ch/node/510.

[33] S. van der Meer, Tech. Rep. CERN-ISR-PO-68-31, CERN, 1968. https://cds.cern.ch/record/296752.

[34] [ALICE Collaboration], https://cds.cern.ch/record/2160174.

[35] [ALICE Collaboration], https://alice-notes.web.cern.ch/node/665.

[36] P. Z. Skands et al., Phys. Rev. D 82, 074018 (2010).

[37] S. Acharya et al. [ALICE Collaboration], arXiv:2005.11120.

[38] S. Acharya et al. [ALICE Collaboration], arXiv:1910.14410

[39] S. Acharya et al. [ALICE Collaboration], Phys. Lett. B 807, 135501 (2020).

[40] S. Acharya et al. [ALICE Collaboration], Phys. Rev. C 99, 024906 (2019).

[41] S. Acharya et al. [ALICE Collaboration], arXiv:2003.02394 [nucl-ex].

[42] S. Acharya et al. [ALICE Collaboration], Eur. Phys. J. C 80, 167 (2020).

[43] B. Abelev et al. [ALICE Collaboration], Phys. Rev. C 91, 024609 (2015).

[44] A. Ortiz Velasquez et al., Phys. Rev. Lett. 111, 042001 (2013).

[45] S. Acharya et al. [ALICE Collaboration], Phys. Lett. B 802, 135225 (2020).

[46] J. Adam et al. [ALICE Collaboration], Phys. Rev. C 95, 064606 (2017).

[47] [ALICE Collaboration], https://alice-notes.web.cern.ch/node/655.

Appendix A

A.1 Decay angular distribution of the vector meson

In this section, we discuss about the angular distribution of the vector meson decay products in vector meson's rest frame. Let us consider a vector meson (A) is at rest and it decays to two particles (B, C) having spin $\vec{S}_1$ and $\vec{S}_2$.

$$A \ \rightarrow \ B \ + \ C. \tag{A.1}$$

The total angular momentum $(\vec{J})$ of the vector meson is $\vec{J} = \vec{L} + \vec{S} = \vec{S} = 1$, where $\vec{L}$ is the orbital angular momentum and $\vec{S}$ is the spin angular momentum. Here, $\vec{L}$ = 0 as the vector meson is at rest. Let us consider the projection of $\vec{J}$ along any arbitrary quantization axis is M. Using the completeness relation of vector meson state $(|1, M\rangle)$, we can write

$$\sum_{M \ = \ -1, \ 0, \ 1} |1, \ M\rangle\langle 1, \ M| = 1. \tag{A.2}$$

In this study, we consider the quantization axis (z) along the perpendicular direction of the reaction plane, x axis along the impact parameter direction, and y axis along the beam direction. As the vector meson is at rest, therefore let consider the momentum of B is $\vec{p}(\theta^*, \ \phi^*)$ and the momentum of C is $-\vec{p}(\theta^*, \ \phi^*)$. Here θ^* and ϕ^* are the polar and the azimuthal angle, made by the decay daughters with z and x axes, respectively. In helicity basis the two particle final state can be express in terms of total angular momentum and helicities as,

$$|\theta^*, \ \phi^*, \ J, \ \lambda_1, \ \lambda_2\rangle \ = \ |\theta^*, \ \phi^*, \ J, \ \lambda\rangle, \tag{A.3}$$

194

where λ_1 and λ_2 are the helicities of particle B and particle C, and $\lambda = \lambda_1$ - λ_2 $= (\vec{S_1} - \vec{S_2}).\hat{p}$. As the total angular momentum is a conserved quantity, therefore the total angular momentum in final state is 1 same as for the vector meson and $|\theta^*, \phi^*, J, \lambda\rangle = |\theta^*, \phi^*, 1, \lambda\rangle$. In helicity basis, the final state physically corresponds to a state which have total angular momentum J (1 for this study) and its projection λ along the flight direction of any one of the decay daughter (direction is expressed in terms of θ^* and ϕ^*). As the both decay daughters are spin 0 particle, therefore in our study $\lambda = 0$ and the final state can be expressed as $|\theta^*, \phi^*, 1, 0\rangle$.

The decay angular distribution of the vector meson in its rest frame can be expressed as,

$$\frac{\mathrm{d}N}{\mathrm{d}cos\theta^*\mathrm{d}\phi^*} = \langle\theta^*, \phi^*, 1, 0|R\rho R^\dagger|\theta^*, \phi^*, 1, 0\rangle, \tag{A.4}$$

where R is the transition matrix and ρ is the spin density matrix. "$\dagger$" corresponds to the complex conjugate. Using Eq. A.2 and Eq. A.4, we can expressed decay angular distribution of the vector meson as,

$$\frac{\mathrm{d}N}{\mathrm{d}cos\theta^*\mathrm{d}\phi^*} = \sum_M\sum_{M'} \langle\theta^*, \phi^*, 1, 0|R|1, M\rangle$$
$$\langle1, M|\rho|1, M'\rangle\langle1, M'|R^\dagger|\theta^*, \phi^*, 1, 0\rangle, \tag{A.5}$$

where $\langle\theta^*, \phi^*, 1, 0|R|1, M\rangle$ corresponds to the amplitude of a transition from the state $|1, M\rangle$ to the state $|1, 0\rangle$. Using the Wigner D-matrix formalism [1], the amplitude can be expressed as,

$$\langle\theta^*, \phi^*, 1, 0|R|1, M\rangle = c\, D^{1\dagger}_{M, 0}\, (\phi^*, \theta^*, -\phi^*), \tag{A.6}$$

where c is a normalization constant and D corresponds to the Wigner D-matrix element. Using Eq. A.6, Eq. A.5 becomes

$$\frac{\mathrm{d}N}{\mathrm{d}cos\theta^*\mathrm{d}\phi^*} = \sum_M\sum_{M'} D^{1\dagger}_{M, 0}\, \rho_{M, M'}\, D^1_{M', 0}, \tag{A.7}$$

where $\rho_{M,M'} = \langle 1, M|\rho|1, M'\rangle$ corresponds to the density matrix elements. The Wigner D-matrix elements are given by,

$$D^1_{1,\,0} = -\frac{1}{2} \sin\theta^* \exp^{-i\phi^*}, \tag{A.8}$$

$$D^1_{0,\,0} = -\cos\theta^*, \tag{A.9}$$

$$D^1_{-1,\,0} = \frac{1}{2} \sin\theta^* \exp^{i\phi^*}. \tag{A.10}$$

Using the values of Wigner D-matrix elements, from Eq. A.7 we get,

$$
\begin{aligned}
\frac{\mathrm{d}N}{\mathrm{d}\cos\theta^*\mathrm{d}\phi^*} \propto\ & [\cos^2\theta^*\rho_{00} + \sin^2\theta^*(\rho_{11} + \rho_{-1-1})/2 \\
& + \sin 2\theta^* \cos\phi^*(\mathrm{Re}\rho_{-10} - \mathrm{Re}\rho_{01})/\sqrt{2} \\
& + \sin 2\theta^* \sin\phi^*(\mathrm{Im}\rho_{-10} - \mathrm{Im}\rho_{01})/\sqrt{2} \\
& - \sin^2\theta^*(\cos 2\phi^*\mathrm{Re}\rho_{1-1} + \sin 2\phi^*\mathrm{Im}\rho_{-11})].
\end{aligned} \tag{A.11}
$$

Integration over azimuthal angle and unit trace condition ($\rho_{-1-1} + \rho_{00} + \rho_{11} = 1$) leads Eq. A.11 to

$$\frac{\mathrm{d}N}{\mathrm{d}cos\theta^*} \propto [1 - \rho_{00} + (3\rho_{00} - 1)cos^2\theta^*]. \tag{A.12}$$

Appendix B

B.1 Event plane resolution correction

Let us consider a right handed coordinate system, where the beam direction is along z direction, the impact parameter direction is along x axis and the angular momentum direction is along y axis. The xz plane is known as the reaction plane. In the rest frame of vector meson, one of its decay daughter have momentum direction along $\hat{p}$. The unit vector $\hat{p}$ makes angle θ^* (polar angle) and ϕ^* (azimuthal angle) with the y and z axes, respectively. The coordinate system is shown in Fig: B.1.
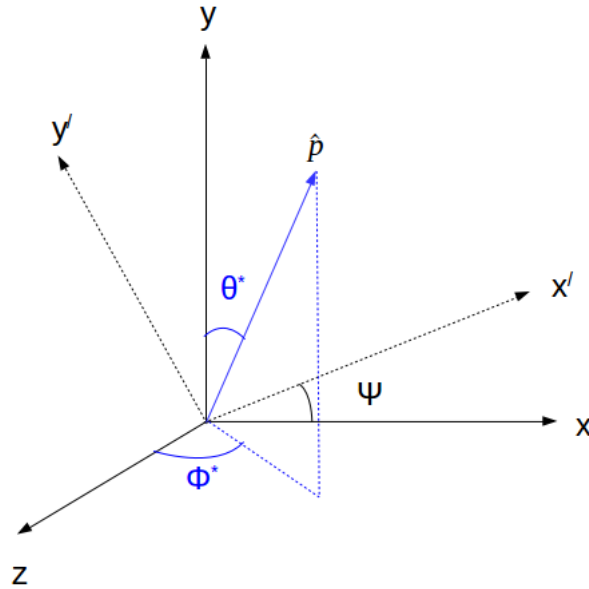
Figure B.1: The definitions of angles and coordinates. $\hat{p}$ is the momentum direction of vector meson decay daughter in vector meson rest frame.

The angular distribution of vector meson's decay daughters in the rest frame of vector meson can be expressed as,

$$
\begin{aligned}
\frac{\mathrm{d}N}{\mathrm{d}\cos\theta^*\mathrm{d}\phi^*} \quad \propto \quad & [\cos^2\theta^*\rho_{00}^{\mathrm{RP}} + \sin^2\theta^*(\rho_{11}^{\mathrm{RP}} + \rho_{-1-1})/2 \\
& + \sin 2\theta^*\cos\phi^*(\mathrm{Re}\rho_{-10}^{\mathrm{RP}} - \mathrm{Re}\rho_{01}^{\mathrm{RP}})/\sqrt{2} \\
& + \sin 2\theta^*\sin\phi^*(\mathrm{Im}\rho_{-10}^{\mathrm{RP}} - \mathrm{Im}\rho_{01}^{\mathrm{RP}})/\sqrt{2} \\
& - \sin^2\theta^*(\cos 2\phi^*\mathrm{Re}\rho_{1-1}^{\mathrm{RP}} + \sin 2\phi^*\mathrm{Im}\rho_{-11}^{\mathrm{RP}})].
\end{aligned} \quad (\mathrm{B.1})
$$

In experiment, the impact parameter direction can not be measured. Therefore we use the event plane as a proxy of reaction plane. Let us consider the event plane vector is along x′ and can be obtained by a rotation of the x and y axes by angle ψ about the z axis. The estimated event plane has finite resolution which can be estimated by averaging over a large number of events. The distribution of the event plane vector is centered around the true reaction plane (here x axis) with finite width. The distribution of ψ over many events is an even function centered at zero. Thus, the event plane resolution (R) can be defined as,

$$
R \; = \; \langle\,\cos(2\psi)\,\rangle, \text{ and } \langle\,\sin(2\psi)\,\rangle \; = \; 0. \quad (\mathrm{B.2})
$$

The unit vectors in the reaction plane frame and in the event plane frame are related by,

$$
\hat{\mathrm{x}} \; = \; \cos(\psi)\hat{\mathrm{x}}' \; - \; \sin(\psi)\hat{\mathrm{y}}', \quad (\mathrm{B.3})
$$

$$
\hat{\mathrm{y}} \; = \; \sin(\psi)\hat{\mathrm{x}}' \; + \; \cos(\psi)\hat{\mathrm{y}}', \quad (\mathrm{B.4})
$$

and

$$
\hat{\mathrm{z}} \; = \; \hat{\mathrm{z}}'. \quad (\mathrm{B.5})
$$

Let us consider in rotating frame (event plane frame) the polar and azimuthal angles are θ' and ϕ'. The momentum direction of vector meson's decay daughter in two different frames can be expressed as,

$$\hat{p} \;=\; \sin\theta^* \cos\phi^* \; \hat{z} \;+\; \sin\theta^* \sin\phi^* \; \hat{x} \;+\; \cos\theta^* \; \hat{y} \tag{B.6}$$

and

$$\hat{p} \;=\; \sin\theta^{*\prime} \cos\phi^{*\prime} \; \hat{z}' \;+\; \sin\theta^{*\prime} \sin\phi^{*\prime} \; \hat{x}' \;+\; \cos\theta^{*\prime} \; \hat{y}'. \tag{B.7}$$

Using Eq. B.11, B.12, B.13, B.14 and B.15 we get,

$$\hat{p}.\hat{z} \;=\; \sin\theta^* \cos\phi^* \;=\; \sin\theta^{*\prime} \cos\phi^{*\prime}. \tag{B.8}$$

$$\hat{p}.\hat{x} \;=\; \sin\theta^* \sin\phi^* \;=\; \sin\theta^{*\prime} \sin\phi^{*\prime} \cos\psi \;-\; \cos\theta^{*\prime} \sin\psi. \tag{B.9}$$

$$\hat{p}.\hat{y} \;=\; \cos\theta^* \;=\; \sin\theta^{*\prime} \sin\phi^{*\prime} \sin\psi \;+\; \cos\theta^{*\prime} \cos\psi. \tag{B.10}$$

By substituting Eq. B.8, Eq. B.9 and Eq. B.10 in Eq. B.1 and after integrating over $\phi^{*\prime}$ we get,

$$\begin{aligned}
\frac{\mathrm{d}N}{\mathrm{d}\cos\theta^{*\prime}} \;\propto\; & \left[1 \;-\; \{\rho_{00}^{\mathrm{RP}} \;-\; \frac{1}{2}\sin^2\psi(3\rho_{00}^{\mathrm{RP}} \;-\; 1)\} \right] \\
& + \left[3\{\rho_{00}^{\mathrm{RP}} \;-\; \frac{1}{2}\sin^2\psi(3\rho_{00}^{\mathrm{RP}} \;-\; 1)\} \;-\; 1 \right] \cos^2\theta^{*\prime} \\
\propto\; & (1 \;-\; \rho_{00}^{EP}) \;+\; (3\rho_{00}^{EP} \;-\; 1)\cos^2\theta^{*\prime}.
\end{aligned} \tag{B.11}$$

Using Eq. B.11, the relation between ρ_{00}^{RP} and ρ_{00}^{EP} can be written as,

$$\rho_{00}^{\mathrm{EP}} \;=\; \rho_{00}^{\mathrm{RP}} \;-\; \frac{1}{2}\sin^2\psi(3\rho_{00}^{\mathrm{RP}} \;-\; 1). \tag{B.12}$$

Averaging over many events will lead to $\langle\sin^2(\psi)\rangle = (1 - R)/2$ and by substituting it in Eq. B.12 we get,

$$\rho_{00}^{\mathrm{EP}} \;=\; \rho_{00}^{\mathrm{RP}} \;-\; \frac{1}{2}(1 \;-\; R)(3\rho_{00}^{\mathrm{RP}} \;-\; 1). \tag{B.13}$$

Equation B.13 can be further simplified as,

$$\rho_{00}^{\mathrm{EP}} - \frac{1}{3} = \left(\rho_{00}^{\mathrm{RP}} - \frac{1}{3} \right) \frac{1 + 3R}{4}. \tag{B.14}$$

Therefore, ρ_{00}^{EP} is related to ρ_{00}^{RP} by

$$\rho_{00}^{\mathrm{RP}} - \frac{1}{3} = \left(\rho_{00}^{\mathrm{EP}} - \frac{1}{3} \right) \frac{4}{1 + 3R}. \tag{B.15}$$

B.2 PID selection criteria

Figure B.2 and B.3 show PID selection criteria, used for this analysis.
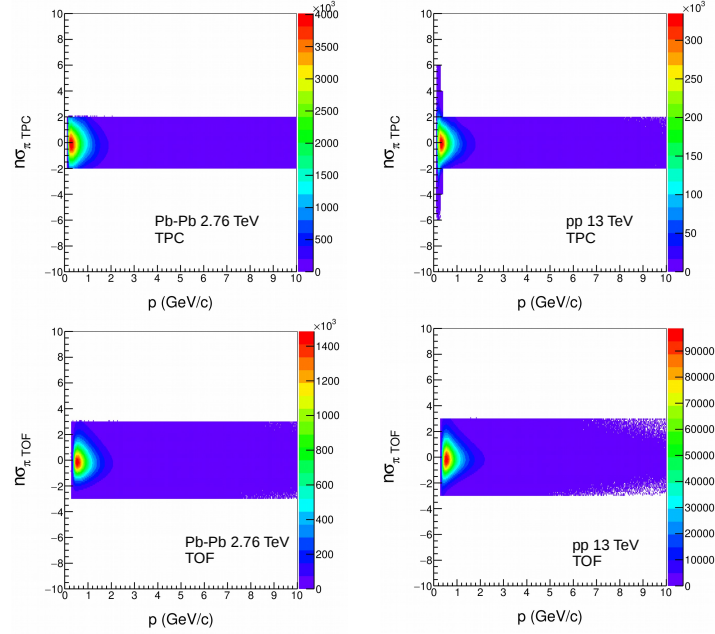
Figure B.2: $|n\sigma_{TPC}|$ and $|n\sigma_{\mathrm{TOF}}|$ distributions as a function of momentum for selected pion candidates in Pb–Pb collisions at $\sqrt{s_{\mathrm{NN}}} = 2.76$ TeV and in pp collisions at $\sqrt{s} = 13$ TeV.

B.3 Event plane distribution

Figure B.4 and B.5 show the event plane angle distribution for various centrality classes, obtained from V0A and V0C detectors, respectively.
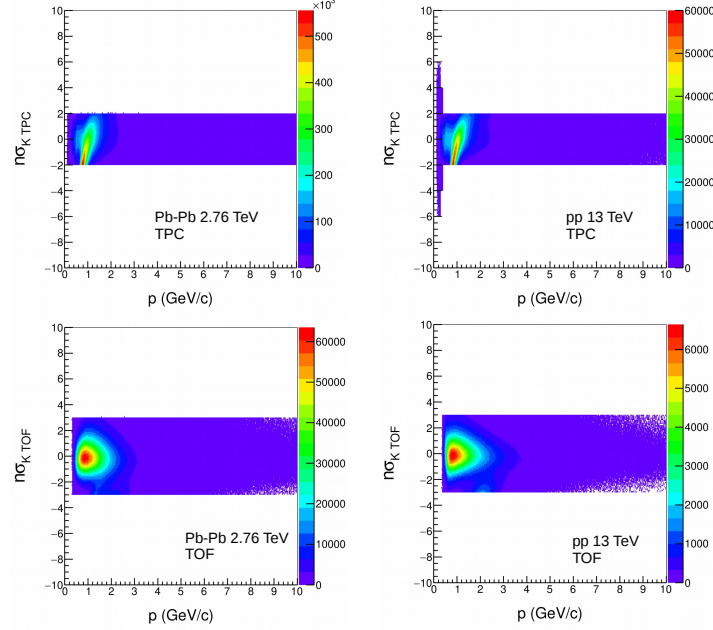
Figure B.3: $|n\sigma_{\mathrm{TPC}}|$ and $|n\sigma_{\mathrm{TOF}}|$ distributions as a function of momentum for selected kaon candidates in Pb–Pb collisions at $\sqrt{s_{\mathrm{NN}}} = 2.76$ TeV and in pp collisions at $\sqrt{s} = 13$ TeV.

B.4 Resonance mass position, width and mass resolution

K^{*0} mass in different $\cos\theta^*$ bins are extracted from the Breit-Wigner fit function. The left panel of Fig. B.6 shows extracted K^{*0} mass as a function of p_{T} for different $\cos\theta^*$ bins in 10–50% centrality class of Pb–Pb collisions. Extracted K^{*0} masses at low p_{T} are seem to be lower than PDG value and this is also observed in K^{*0} spectra analysis [2]. ϕ mass and width as a function of p_{T} in different $\cos\theta^*$ bins are extracted from the Voigitian fit function. The right panel of Fig. B.6 shows extracted ϕ mass as a function of p_{T} for different $\cos\theta^*$ bins in 10–50% Pb–Pb collisions at $\sqrt{s_{NN}} = 2.76$ TeV.

The left panel of Fig. B.7 shows ϕ meson mass resolution extracted from MC, as a function of p_{T} in different $\cos\theta^*$ bin in Pb–Pb collisions at 2.76 TeV. The right panel of Fig. B.7 shows extracted ϕ width as a function of p_{T} for different $\cos\theta^*$ bins in
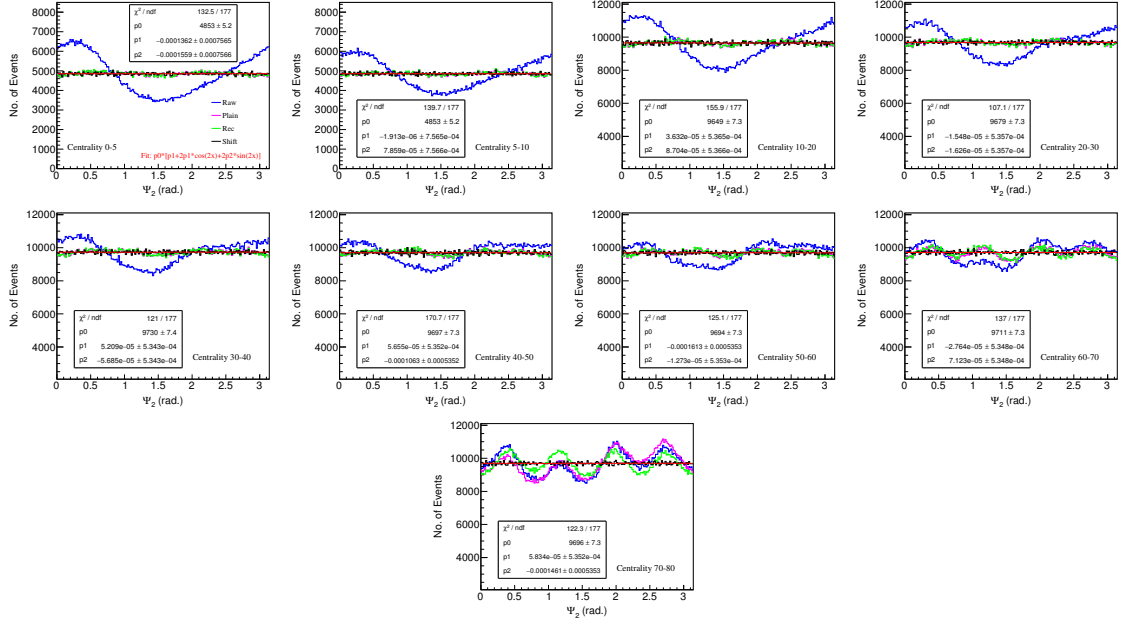
Figure B.4: The event plane angle (Ψ_2) distribution from V0A in various centralities before correction (blue line), after gain equalization (magenta line), recentering (green line) and shift correction (black line) in Pb–Pb collisions at $\sqrt{s_{\mathrm{NN}}} = 2.76$ TeV. The red line shows the fit (Eq. 3.11) to Ψ_2 distribution after shift correction.
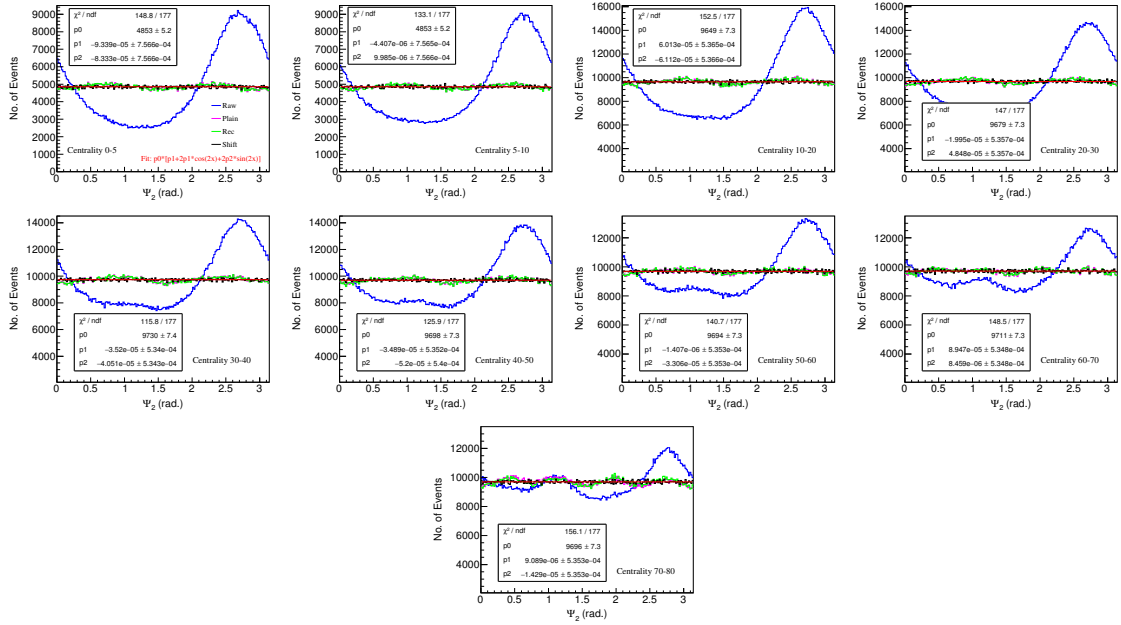
Figure B.5: The event plane angle (Ψ_2) distribution from V0C in various centralities before correction (blue line), after gain equalization (magenta line), recentering (green line) and shift correction (black line) in Pb–Pb collisions at $\sqrt{s_{\mathrm{NN}}} = 2.76$ TeV. The red line shows the fit (Eq. 3.11) to Ψ_2 distribution after shift correction.
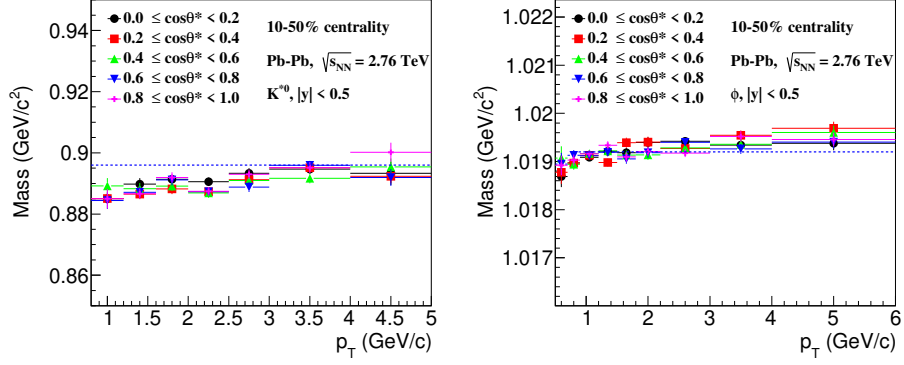
Figure B.6: Left panel: K^{*0} mass as a function of $\cos\theta^*$ in 10–50% Pb–Pb collisions at $\sqrt{s_{NN}} = 2.76$ TeV. Right panel: ϕ mass as a function of p_T for different $\cos\theta^*$ bins in 10–50% central Pb–Pb collisions at $\sqrt{s_{NN}} = 2.76$ TeV. Errors are statistical only.

10–50% Pb–Pb collisions at $\sqrt{s_{NN}} = 2.76$ TeV.
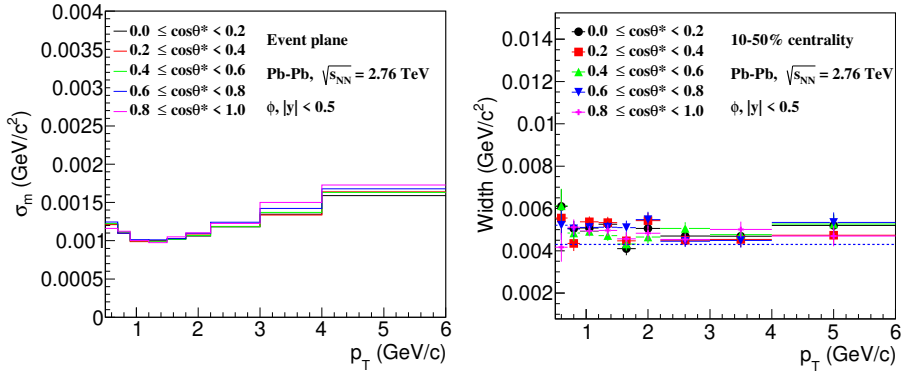
Figure B.7: Left panel: ϕ meson mass resolution as a function of p_T in different $\cos\theta^*$ bin in Pb–Pb collisions at 2.76 TeV. Results are from MC simulation. Right panel: ϕ width as a function of p_T for different $\cos\theta^*$ bins in 10–50% central Pb–Pb collisions at $\sqrt{s_{NN}} = 2.76$ TeV. Errors are statistical only.

B.5 Invariant mass distributions
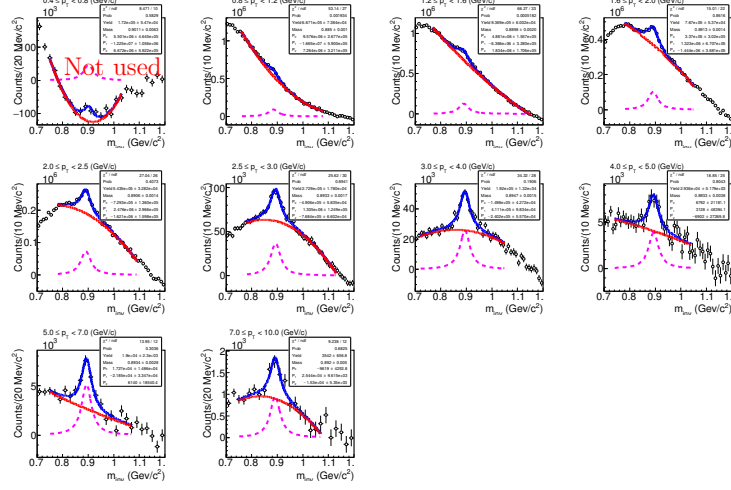
Figure B.8: Invariant mass distribution $M_{\pi K}$ after mixed event background subtraction and fitted with Breit-Wigner + residual background function in centrality class 10–50% for various p_{T} bins in $\cos\theta^*$ bin $0.0 < \cos\theta^* < 0.2$. Quantization axis is perpendicular to the EP.
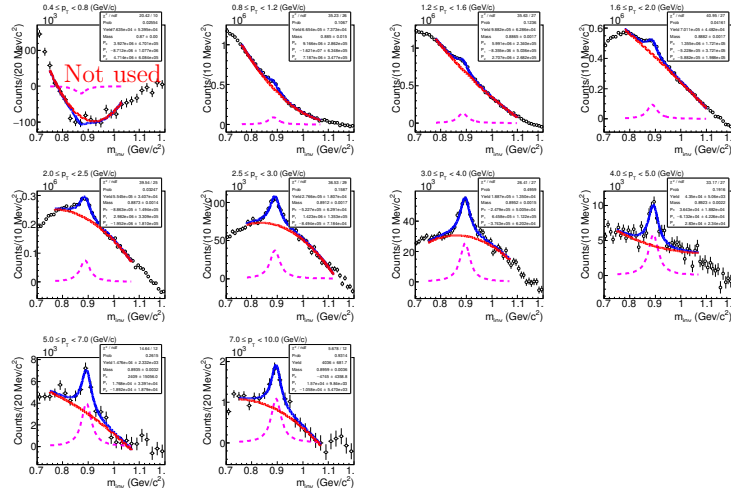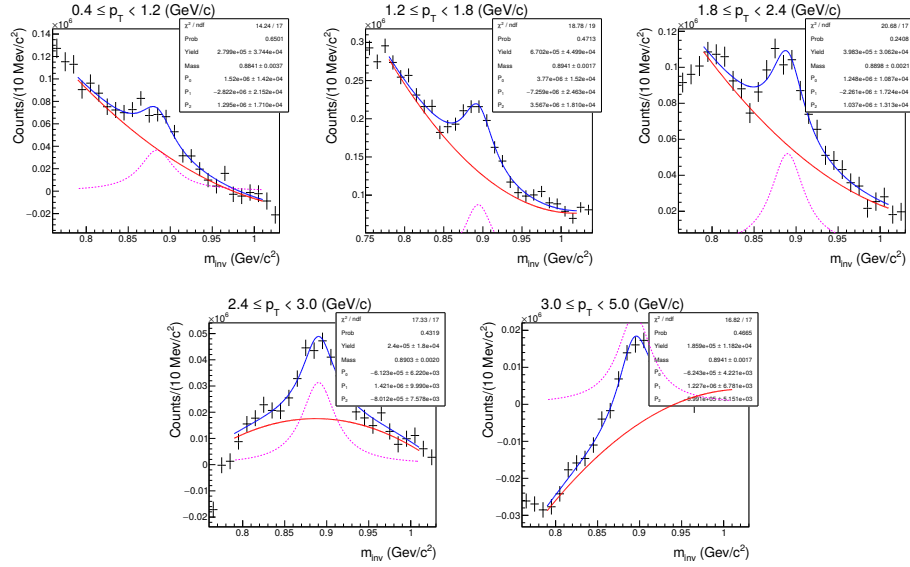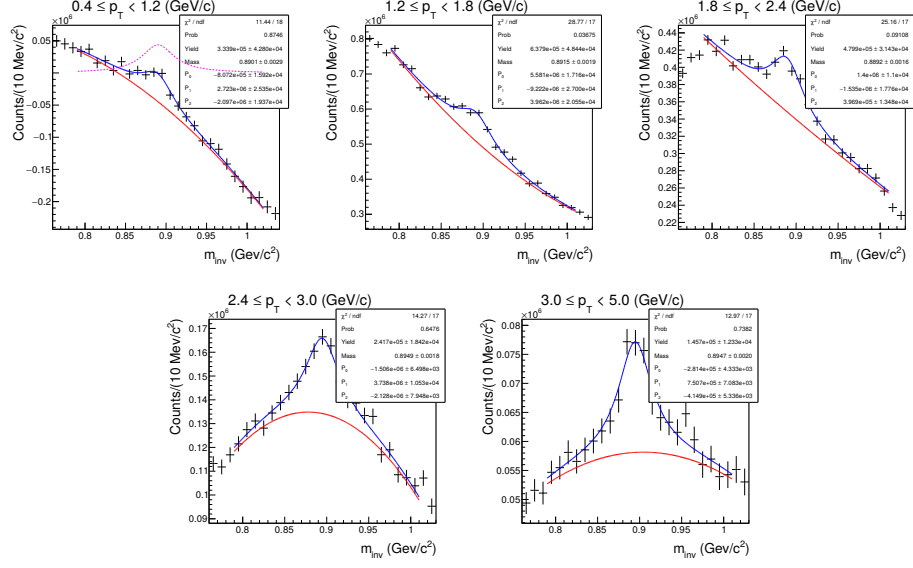

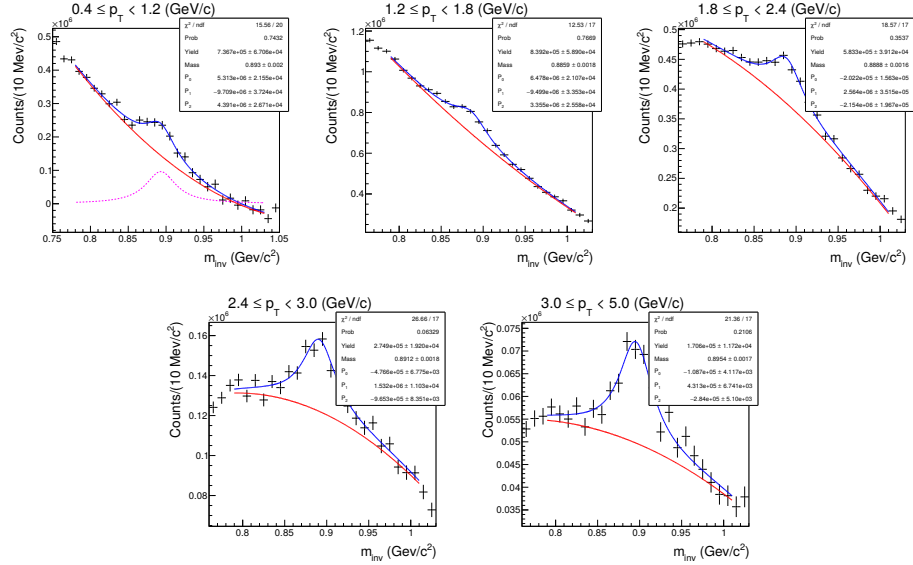Figure B.9: Invariant mass distribution $M_{\pi K}$ after mixed event background subtraction and fitted with Breit-Wigner + residual background function in centrality class 10–50% for various p_{T} bins in $\cos\theta^*$ bin $0.2 < \cos\theta^* < 0.4$. Quantization axis is perpendicular to the EP.
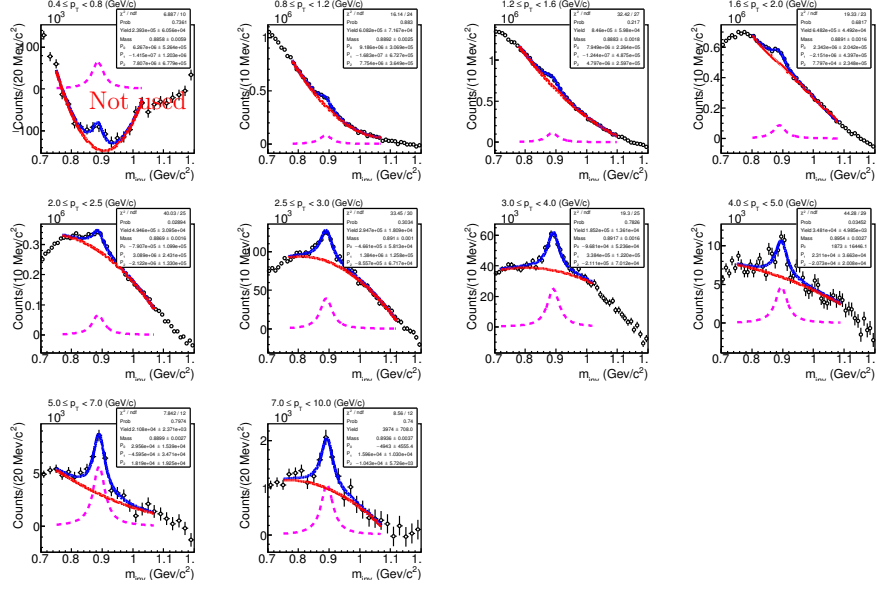
Figure B.10: Invariant mass distribution $M_{\pi K}$ after mixed event background subtraction and fitted with Breit-Wigner + residual background function in centrality class 10–50% for various p_T bins in $\cos\theta^*$ bin $0.4 < \cos\theta^* < 0.6$. Quantization axis is perpendicular to the EP.
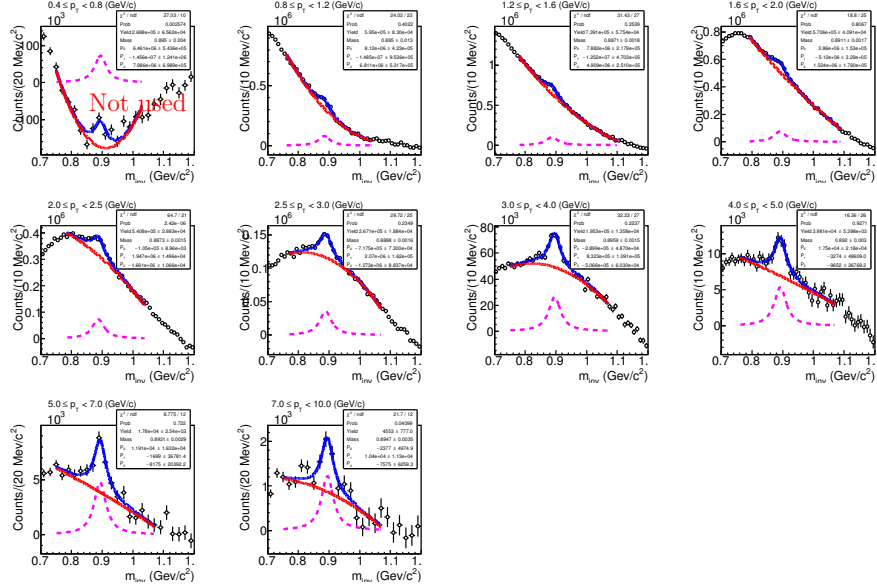
Figure B.11: Invariant mass distribution $M_{\pi K}$ after mixed event background subtraction and fitted with Breit-Wigner + residual background function in centrality class 10–50% for various p_T bins in $\cos\theta^*$ bin $0.6 < \cos\theta^* < 0.8$. Quantization axis is perpendicular to the EP.
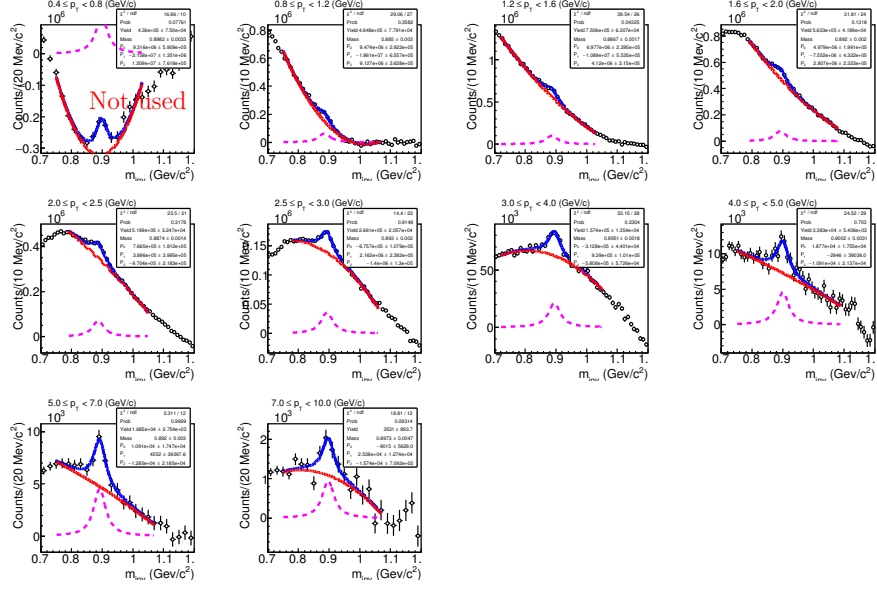
Figure B.12: Invariant mass distribution $M_{\pi K}$ after mixed event background subtraction and fitted with Breit-Wigner + residual background function in centrality class 10–50% for various p_T bins in $\cos\theta^*$ bin $0.8 < \cos\theta^* < 1.0$. Quantization axis is perpendicular to the EP.
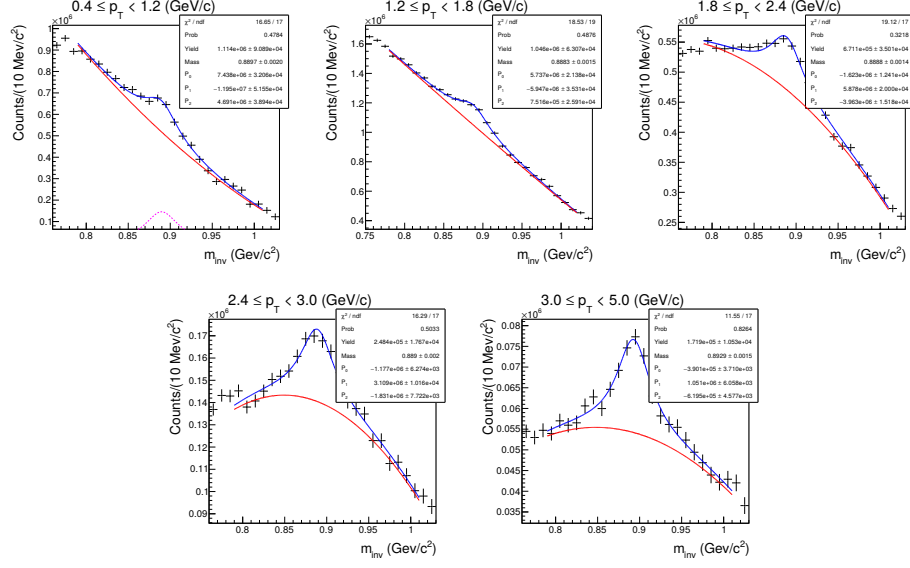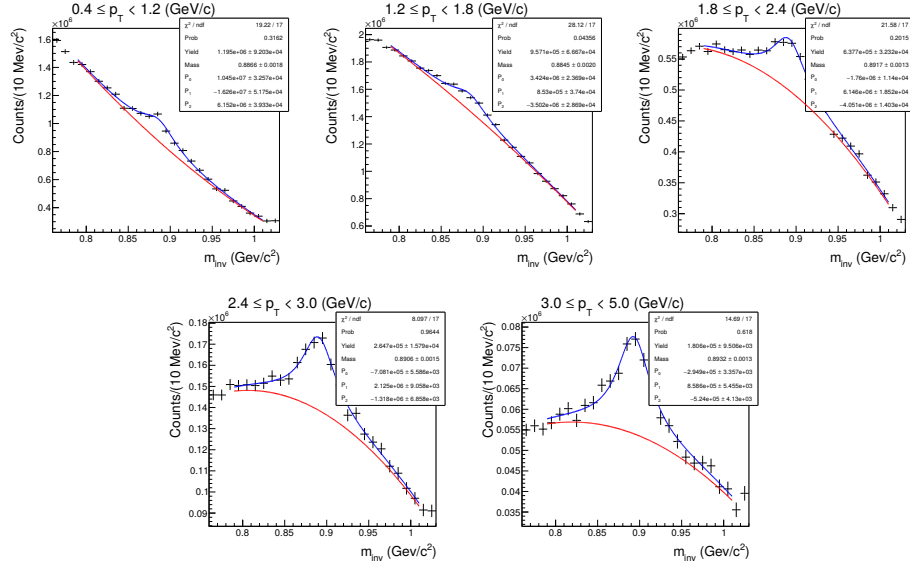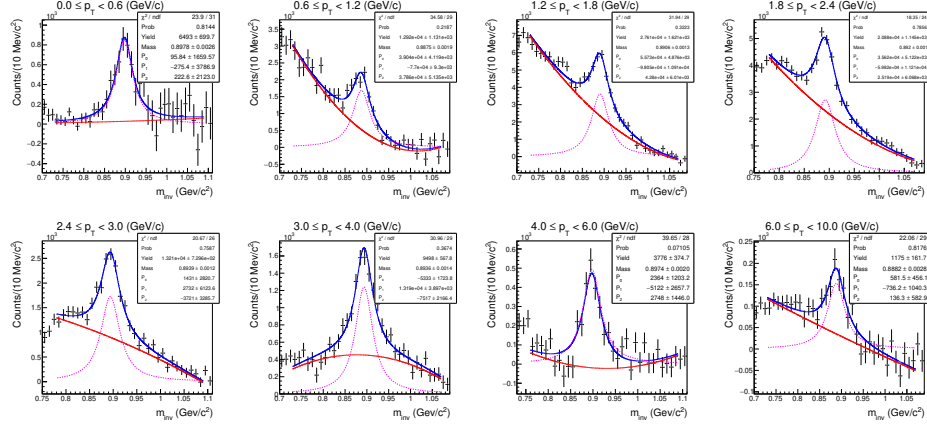

Figure B.13: Invariant mass distribution of same event πK pairs after normalized mixed event background subtraction and fitted with Breit-Wigner + residual background function in various p_T intervals for $0.0 < \cos\theta^* < 0.2$ in 10–50% Pb–Pb collisions at $\sqrt{s_{\mathrm{NN}}} = 2.76$ TeV. Quantization axis is perpendicular to the PP.
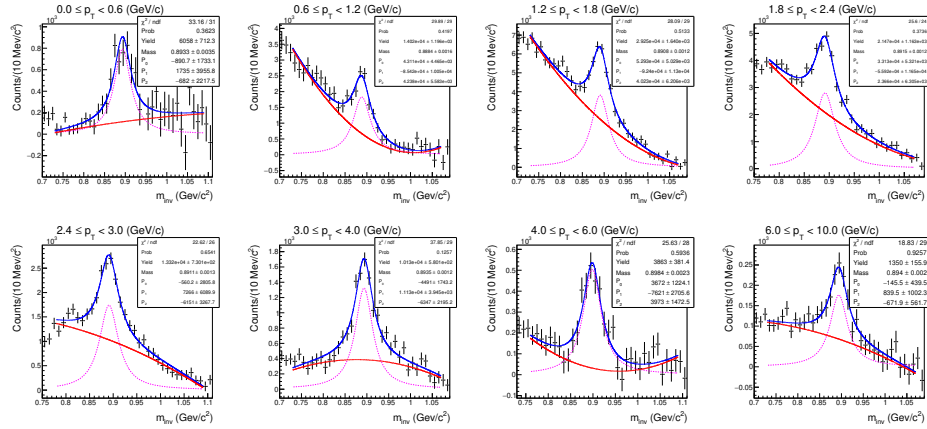
Figure B.14: Invariant mass distribution of same event πK pairs after normalized mixed event background subtraction and fitted with Breit-Wigner + residual background function in various p_{T} intervals for $0.2 < \cos\theta^* < 0.4$ in 10–50% Pb–Pb collisions at $\sqrt{s_{\mathrm{NN}}} = 2.76$ TeV. Quantization axis is perpendicular to the PP.
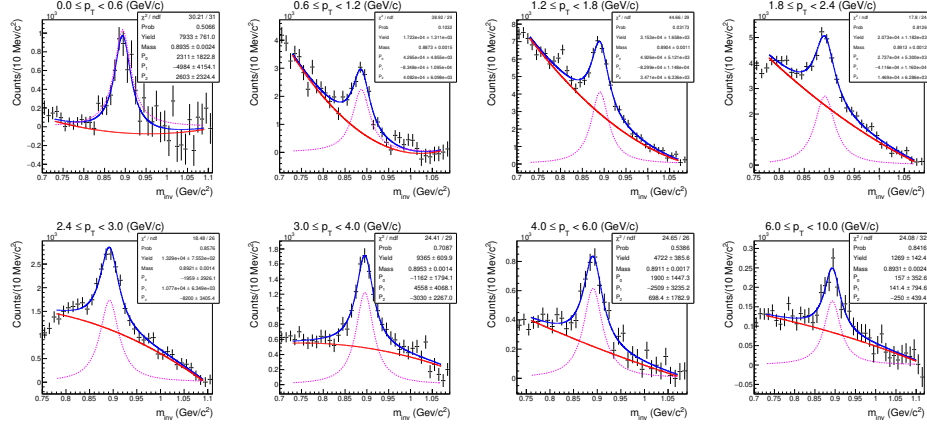

Figure B.15: Invariant mass distribution of same event πK pairs after normalized mixed event background subtraction and fitted with Breit-Wigner + residual background function in various p_{T} intervals for $0.4 < \cos\theta^* < 0.6$ in 10–50% Pb–Pb collisions at $\sqrt{s_{\mathrm{NN}}} = 2.76$ TeV. Quantization axis is perpendicular to the PP.
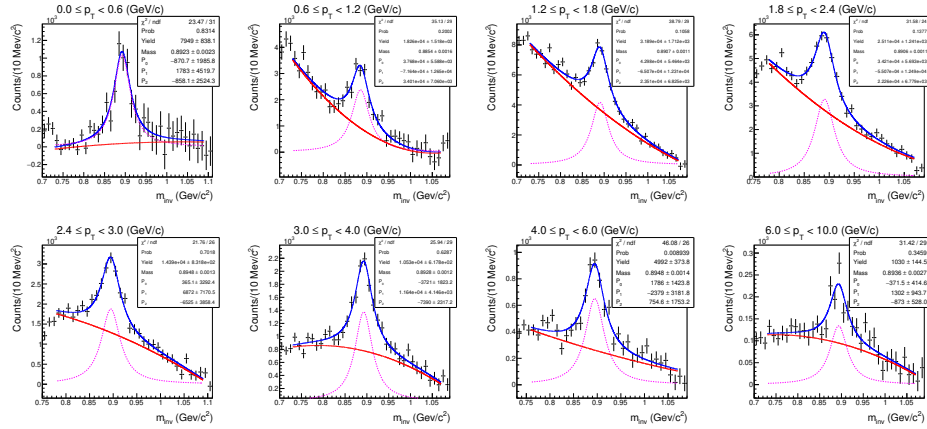
Figure B.16: Invariant mass distribution of same event πK pairs after normalized mixed event background subtraction and fitted with Breit-Wigner + residual background function in various p_T intervals for $0.6 < \cos\theta^* < 0.8$ in 10–50% Pb–Pb collisions at $\sqrt{s_{NN}} = 2.76$ TeV. Quantization axis is perpendicular to the PP.

Figure B.17: Invariant mass distribution of same event πK pairs after normalized mixed event background subtraction and fitted with Breit-Wigner + residual background function in various p_T intervals for $0.8 < \cos\theta^* < 1.0$ in 10–50% Pb–Pb collisions at $\sqrt{s_{NN}} = 2.76$ TeV. Quantization axis is perpendicular to the PP.
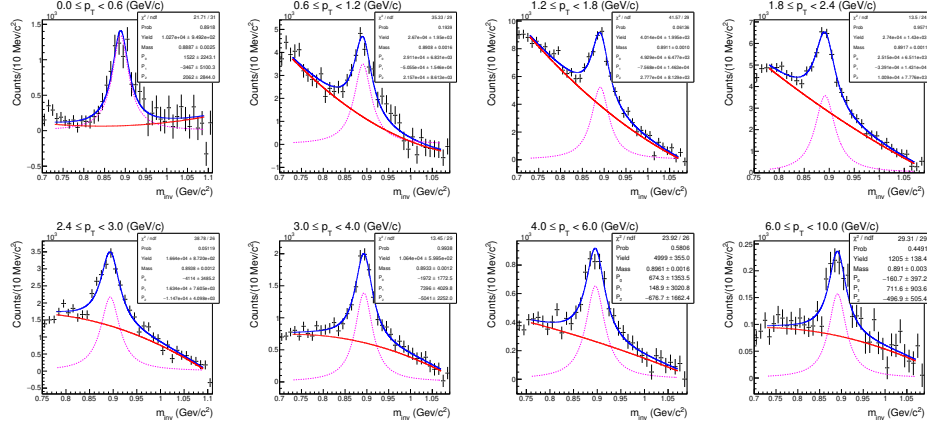
Figure B.18: Invariant mass distribution of same event πK pairs after normalized mixed event background subtraction and fitted with Breit-Wigner + residual background function in various p_{T} bins for $0.0 < \cos\theta^* < 0.1$ in pp collisions at $\sqrt{s} = 13$ TeV. Quantization axis is perpendicular to the PP.

Figure B.19: Invariant mass distribution of same event πK pairs after normalized mixed event background subtraction and fitted with Breit-Wigner + residual background function in various p_{T} bins for $0.1 < \cos\theta^* < 0.2$ in pp collisions at $\sqrt{s} = 13$ TeV. Quantization axis is perpendicular to the PP.

Figure B.20: Invariant mass distribution of same event πK pairs after normalized mixed event background subtraction and fitted with Breit-Wigner + residual background function in various p_T bins for $0.2 < \cos\theta^* < 0.3$ in pp collisions at $\sqrt{s} = 13$ TeV. Quantization axis is perpendicular to the PP.
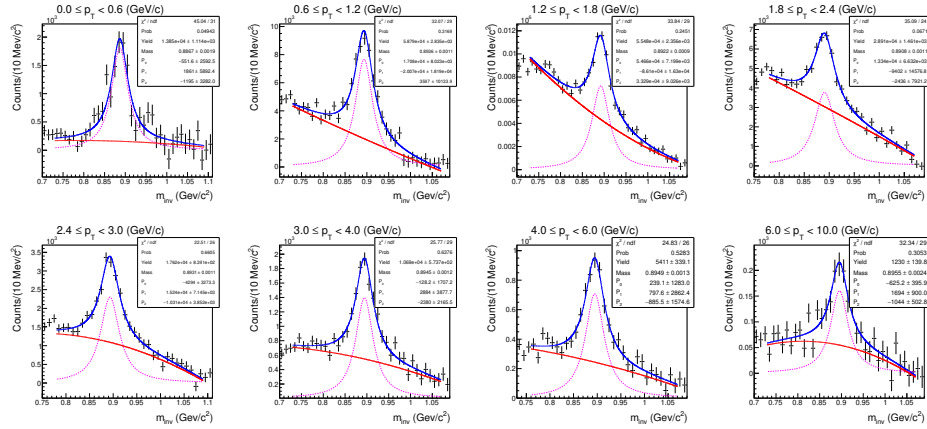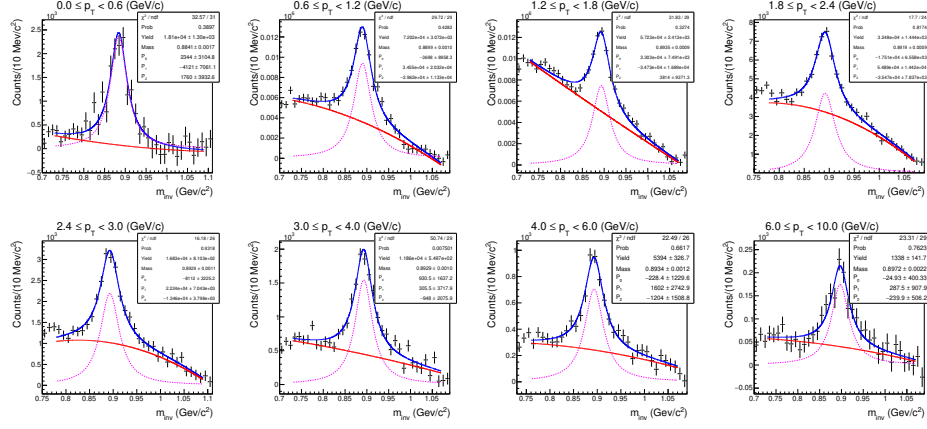

Figure B.21: Invariant mass distribution of same event πK pairs after normalized mixed event background subtraction and fitted with Breit-Wigner + residual background function in various p_T bins for $0.3 < \cos\theta^* < 0.4$ in pp collisions at $\sqrt{s} = 13$ TeV. Quantization axis is perpendicular to the PP.
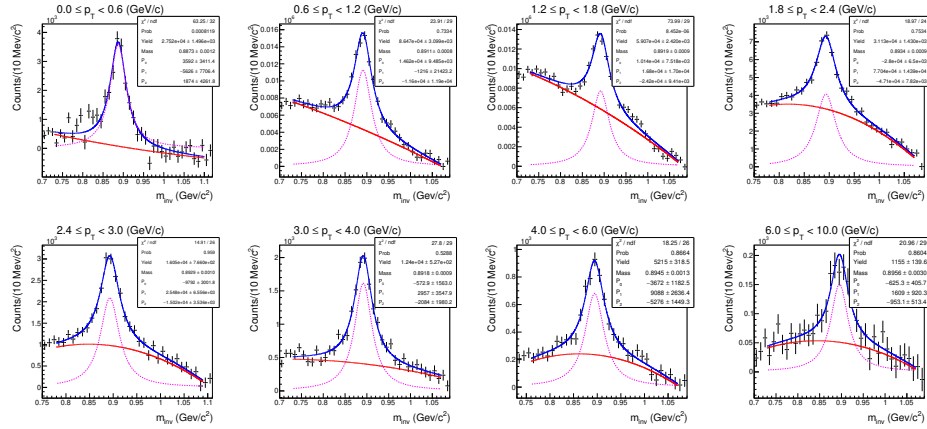
Figure B.22: Invariant mass distribution of same event πK pairs after normalized mixed event background subtraction and fitted with Breit-Wigner + residual background function in various p_T bins for $0.4 < \cos\theta^* < 0.5$ in pp collisions at $\sqrt{s} = 13$ TeV. Quantization axis is perpendicular to the PP.
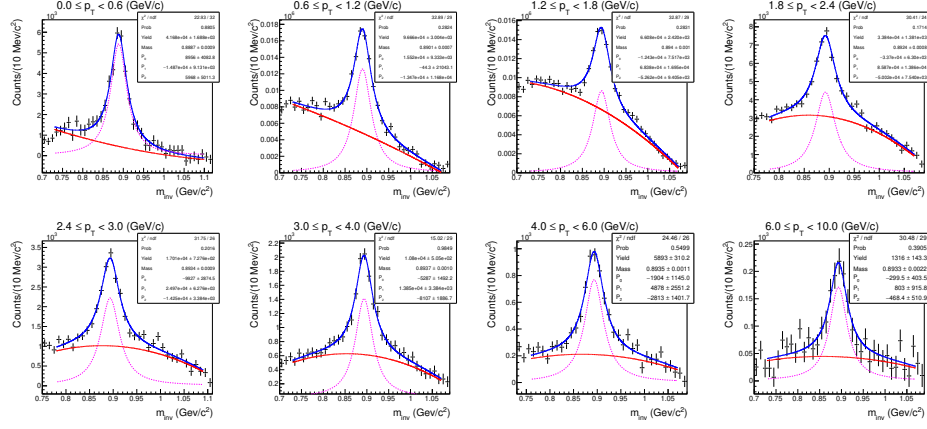

Figure B.23: Invariant mass distribution of same event πK pairs after normalized mixed event background subtraction and fitted with Breit-Wigner + residual background function in various p_T bins for $0.5 < \cos\theta^* < 0.6$ in pp collisions at $\sqrt{s} = 13$ TeV. Quantization axis is perpendicular to the PP.
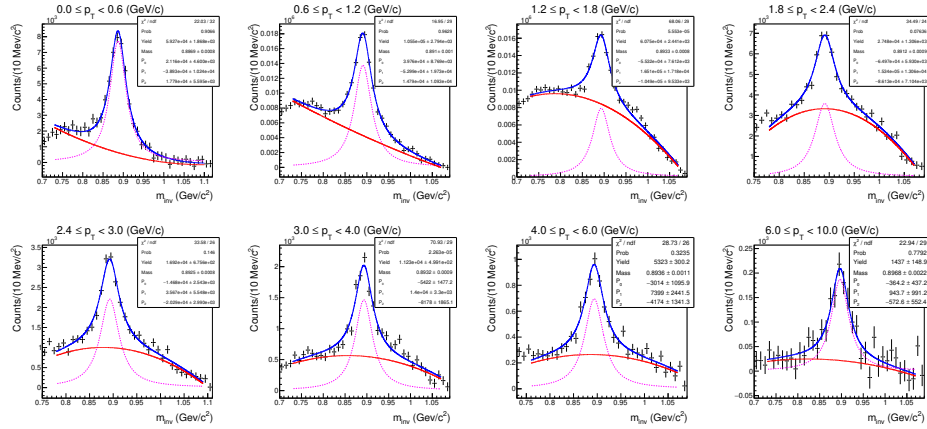
Figure B.24: Invariant mass distribution of same event πK pairs after normalized mixed event background subtraction and fitted with Breit-Wigner + residual background function in various p_T bins for $0.6 < \cos\theta^* < 0.7$ in pp collisions at $\sqrt{s} = 13$ TeV. Quantization axis is perpendicular to the PP.
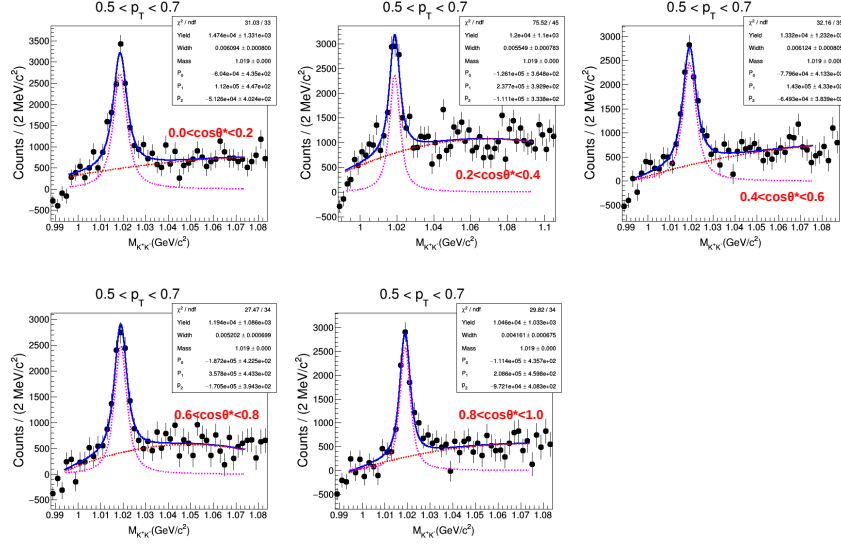

Figure B.25: Invariant mass distribution of same event πK pairs after normalized mixed event background subtraction and fitted with Breit-Wigner + residual background function in various p_T bins for $0.7 < \cos\theta^* < 0.8$ in pp collisions at $\sqrt{s} = 13$ TeV. Quantization axis is perpendicular to the PP.

Figure B.26: Invariant mass distribution of same event πK pairs after normalized mixed event background subtraction and fitted with Breit-Wigner + residual background function in various p_T bins for $0.8 < \cos\theta^* < 0.9$ in pp collisions at $\sqrt{s} = 13$ TeV. Quantization axis is perpendicular to the PP.

Figure B.27: Invariant mass distribution of same event πK pairs after normalized mixed event background subtraction and fitted with Breit-Wigner + residual background function in various p_T bins for $0.9 < \cos\theta^* < 1.0$ in pp collisions at $\sqrt{s} = 13$ TeV. Quantization axis is perpendicular to the PP.
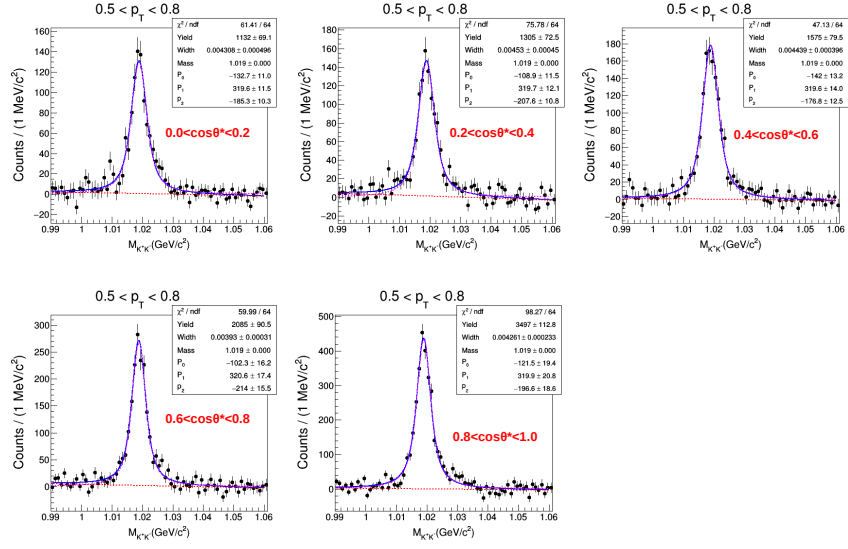
Figure B.28: Invariant mass distribution of unlike charged KK pairs after mixed event background subtraction in different $\cos\theta^*$ bins for $0.5 < p_\mathrm{T} < 0.7$ GeV/c in 10–50% Pb–Pb collisions at 2.76 TeV, fitted with voigitian+Polynomial 2 function. Quantization axis is perpendicular to the EP.
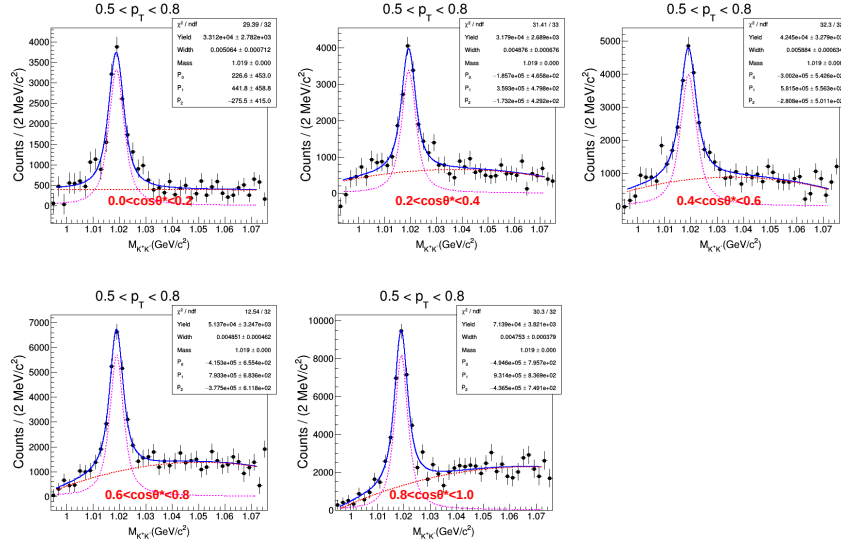
Figure B.29: Invariant mass distribution of unlike charged KK pairs after mixed event background subtraction in different $\cos\theta^*$ bins for $0.5 < p_\mathrm{T} < 0.8$ GeV/c in 10–50% Pb–Pb collisions at 2.76 TeV, fitted with voigitian+Polynomial 2 function. Quantization axis is perpendicular to the PP.

Figure B.30: Invariant mass distribution of unlike charged KK pairs after mixed event background subtraction in different $\cos\theta^*$ bins for $0.5 < p_{\mathrm{T}} < 0.8$ GeV/c in pp collisions at 13 TeV, fitted with voigitian+Polynomial 2 function. Quantization axis is perpendicular to the PP.

B.6 Spin alignment measurements for K_S^0 in Pb–Pb collisions

The K_S^0 is reconstructed using their decay topology. The reconstruction method and yield extraction for this analysis are the same as that of the Pb–Pb collisions described in Ref. [3]. The raw yield is calculated by subtracting a fit to the background from the total number of V0 candidates in the peak region. A bin counting method is used to count the number of K_S^0 in the invariant mass range 0.42 - 0.57 GeV/c^2 (say N_T). The number of K_S^0 counted in this way also includes some background. A 2$^{\text{nd}}$ order polynomial function is used to fit the background excluding the peak region. Then the 2$^{\text{nd}}$ order polynomial is integrated in the signal range (0.42 - 0.57 GeV/c^2 say N_{bkg}) to estimate the background contribution to the K_S^0 signal. Then the raw K_S^0 (N^{raw}) candidate are measured by subtracting N_{bkg} from N_T. Figure B.31 showsto Fig. B.35 are the invariant mass distribution of unlike charged $M_{\pi\pi}$ distributions in selected p_T and $cos\theta*$ intervals with respect to the production plane. Figure B.36 to Fig. B.40 are the invariant mass distribution of unlike charged $M_{\pi\pi}$ distributions in selected p_T and $cos\theta*$ intervals with respect to the event plane.

The signal is extracted in eight p_T bins for particular $\cos\theta^*$ and centrality bin. The p_T spectra are measured in five $\cos\theta^*$ intervals starting from -1.0 to 1.0 (-1 to -0.7, -0.7 to - 0.3, -0.3 to 0.3, 0.3 to 0.7 and 0.7 to 1.0) for 20–40 centrality bins in Pb–Pb collisions at 2.76 TeV. The raw p_T spectra for different $\cos\theta^*$ bins in 20–40% centrality class at $\sqrt{s_{\text{NN}}} = 2.76$ TeV are shown in Fig. B.41. Left panel of Fig.B.41 shows raw p_T spectra for the production plane analysis and right panel of Fig. B.41 shows raw p_T spectra for the event plane analysis.

To get the final yields, the obtained K_S^0 raw yields were corrected for the Acceptance × Efficiency ($A \times \epsilon$) extracted from MC simulations. Minimum bias Pb–Pb
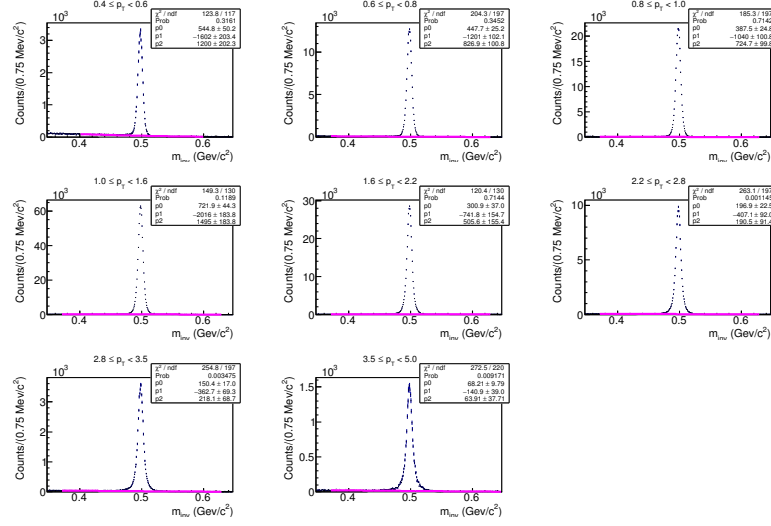
Figure B.31: Signal extraction for K^0_S in different p_T bins for $-1 \leq \cos\theta^* < -0.7$ and 20–40% centrality class in Pb–Pb collisions at $\sqrt{s_{NN}} = 2.76$ TeV and $|y| < 0.5$. Quantization axis is normal to the production plane.
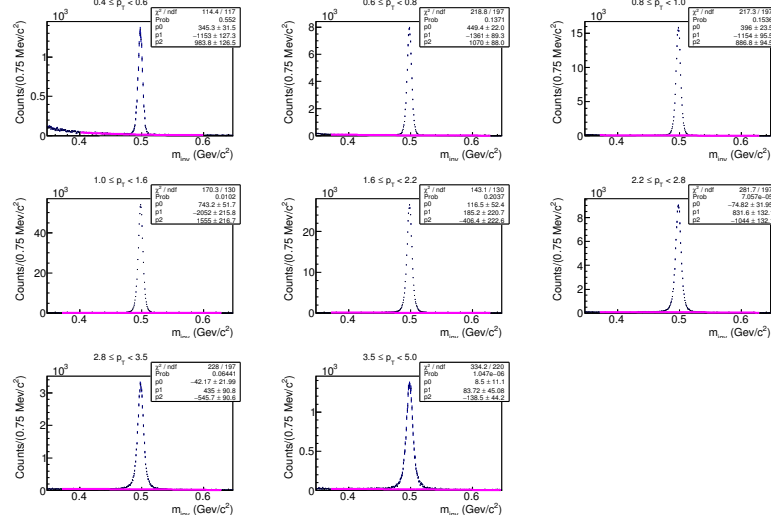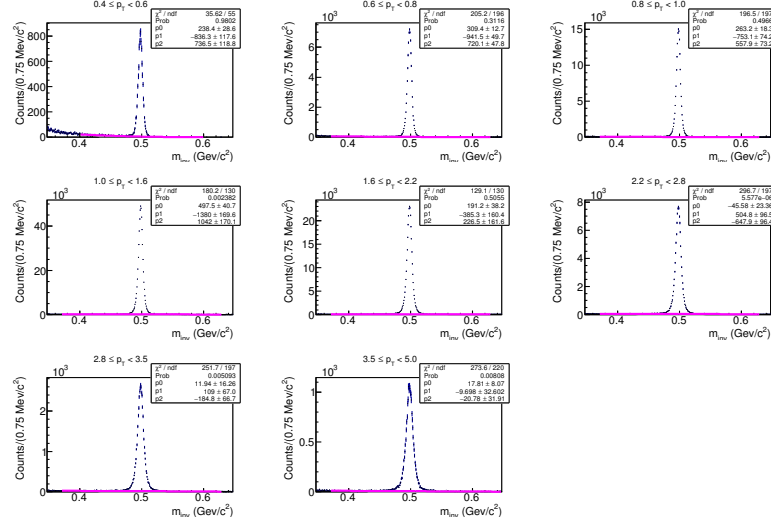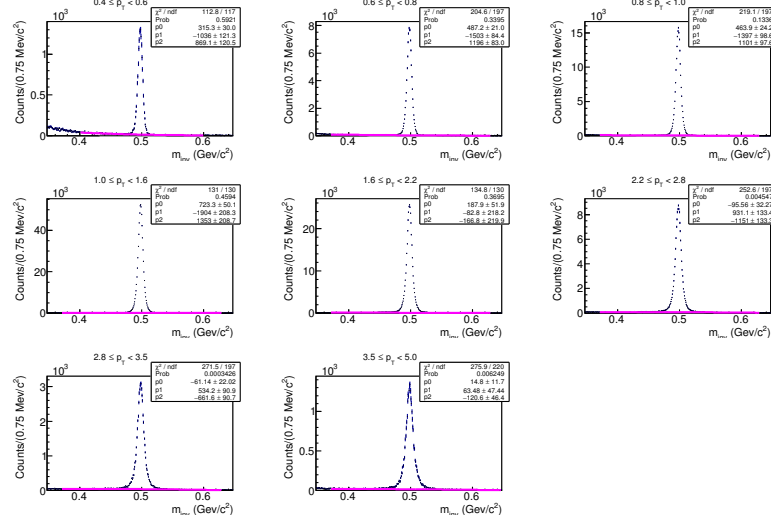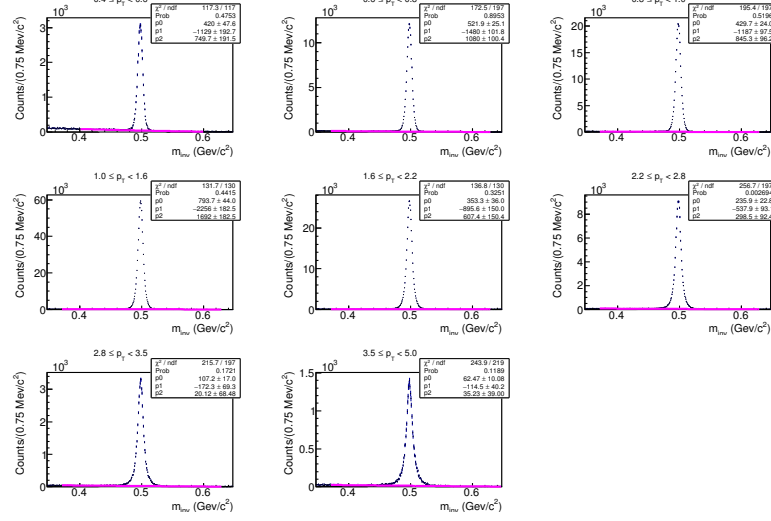

Figure B.32: Signal extraction for K^0_S in different p_T bins for -0.7$\leq \cos\theta^* <$-0.3 and 20–40% centrality class in Pb–Pb collisions at $\sqrt{s_{NN}} = 2.76$ TeV and $|y| < 0.5$. Quantization axis is normal to the production plane.

Figure B.33: Signal extraction for K_S^0 in different p_T bins for -0.3≤cos θ* <0.3 and 20–40% centrality class in Pb–Pb collisions at $\sqrt{s_{NN}}$ = 2.76 TeV and $|y| < 0.5$. Quantization axis is normal to the production plane.
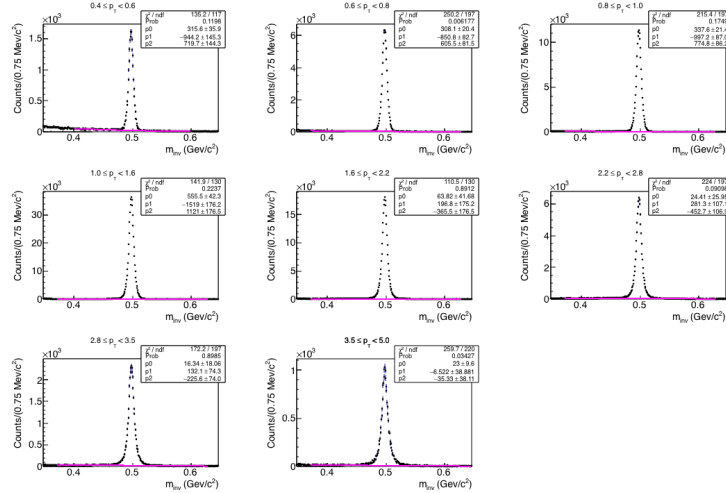

Figure B.34: Signal extraction for K_S^0 in different p_T bins for 0.3≤cos θ* <0.7 and 20–40% centrality class in Pb–Pb collisions at $\sqrt{s_{NN}}$ = 2.76 TeV and $|y| < 0.5$. Quantization axis is normal to the production plane.
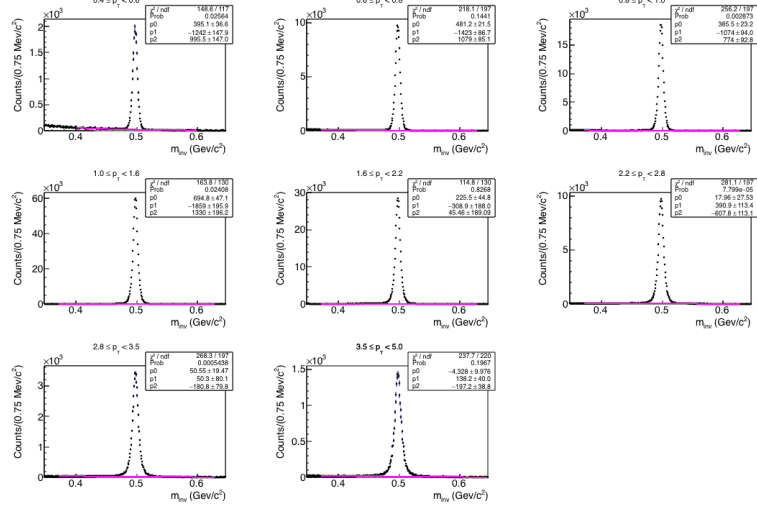
Figure B.35: Signal extraction for K_S^0 in different p_T bins for $0.7 \leq \cos\theta^* < 1.0$ and 20–40% centrality class in Pb–Pb collisions at $\sqrt{s_{NN}} = 2.76$ TeV and $|y| < 0.5$. Quantization axis is normal to the production plane.

Figure B.36: Signal extraction for K_S^0 in different p_T bins for $-1 \leq \cos\theta^* < -0.7$ and 20–40% centrality class in Pb–Pb collisions at $\sqrt{s_{NN}} = 2.76$ TeV and $|y| < 0.5$. Quantization axis is normal to the event plane.
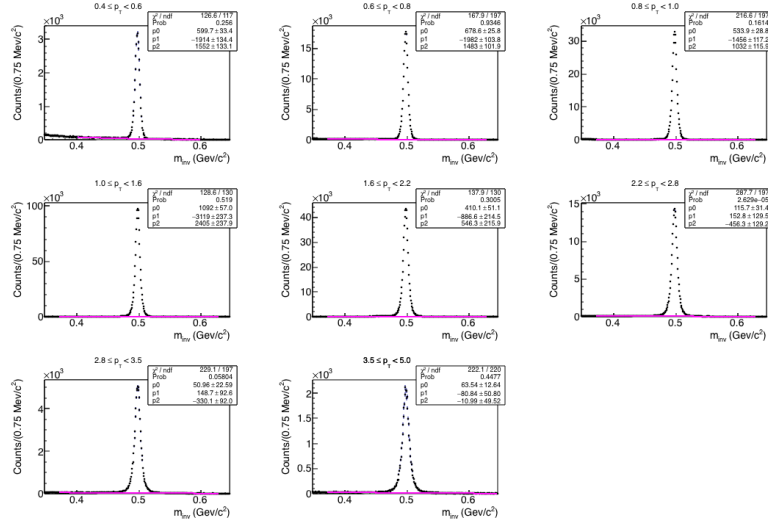
Figure B.37: Signal extraction for K_S^0 in different p_T bins for $-0.7 \leq \cos\theta^* < -0.3$ and 20–40% centrality class in Pb–Pb collisions at $\sqrt{s_{NN}}$ = 2.76 TeV and $|y| < 0.5$. Quantization axis is normal to the event plane.
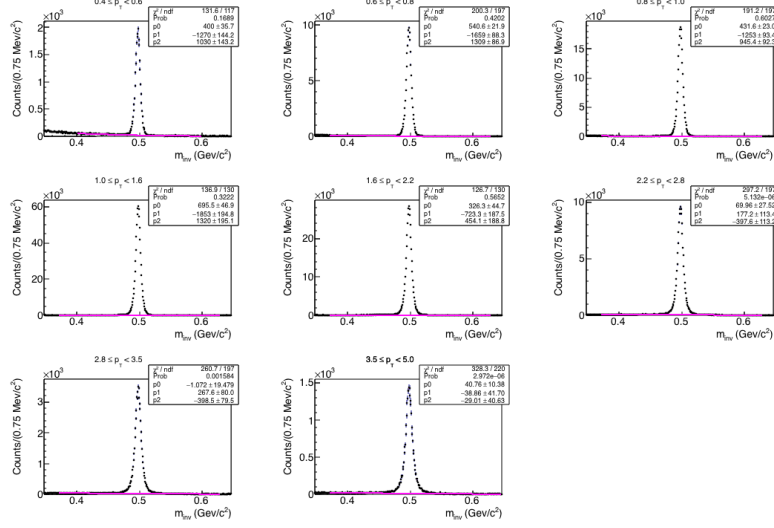

Figure B.38: Signal extraction for K_S^0 in different p_T bins for $-0.3 \leq \cos\theta^* < 0.3$ and 20–40% centrality class in Pb–Pb collisions at $\sqrt{s_{NN}}$ = 2.76 TeV and $|y| < 0.5$. Quantization axis is normal to the event plane.
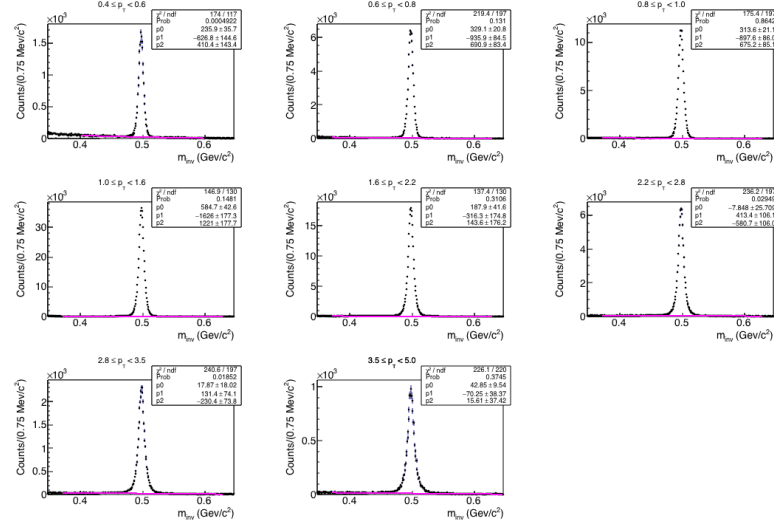
Figure B.39: Signal extraction for K_S^0 in different p_T bins for $0.3 \leq \cos \theta^* < 0.7$ and 20–40% centrality class in Pb–Pb collisions at $\sqrt{s_{NN}} = 2.76$ TeV and $|y| < 0.5$. Quantization axis is normal to the event plane.

Figure B.40: Signal extraction for K_S^0 in different p_T bins for $0.7 \leq \cos \theta^* < 1.0$ and 20–40% centrality class in Pb–Pb collisions at $\sqrt{s_{NN}} = 2.76$ TeV and $|y| < 0.5$. Quantization axis is normal to the event plane.
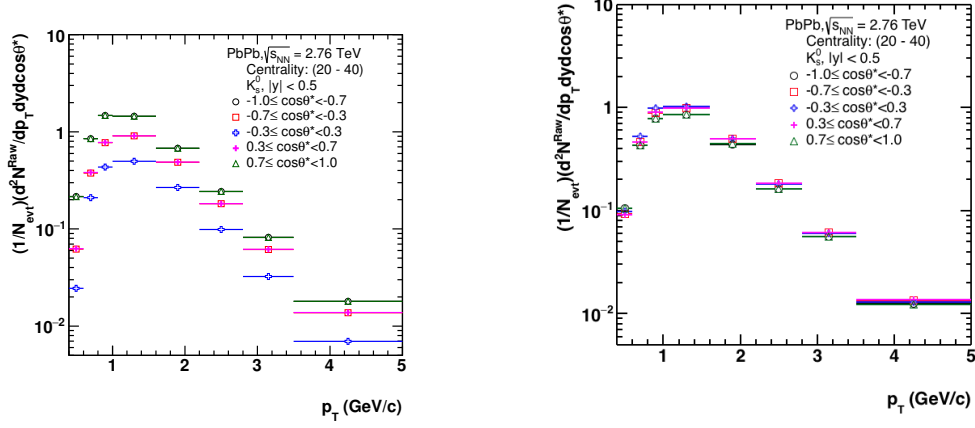
Figure B.41: Raw spectra for K_S^0 in 20–40 % centrality class in Pb–Pb collisions at $\sqrt{s_{NN}} = 2.76$ TeV and $|y| < 0.5$ for different $\cos\theta^*$ bins. Left panel shows raw p_T spectra for the production plane analysis and right panel shows raw p_T spectra for the event plane analysis.
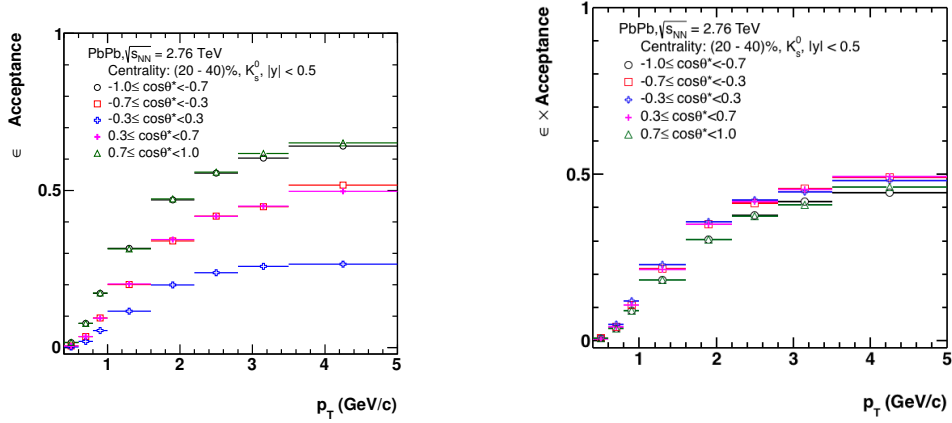

Figure B.42: Efficiency × Acceptance as a function of p_T for different $\cos\theta^*$ for K_S^0 in 20–40% centrality class in Pb–Pb collisions at $|y| < 0.5$. Left panel shows Efficiency × Acceptance for the production plane analysis and right panel shows Efficiency × Acceptance for the event plane analysis

events were simulated using the HIJING event generator. Figure B.42 shows the variation of $A \times \epsilon$ as a function of p_T for different $\cos\theta^*$ bins in 20–40% centrality class at $\sqrt{s_{NN}} = 2.76$ TeV. The raw p_T spectrum in each $\cos\theta^*$ bin is corrected with corresponding $A \times \epsilon$ distributions.
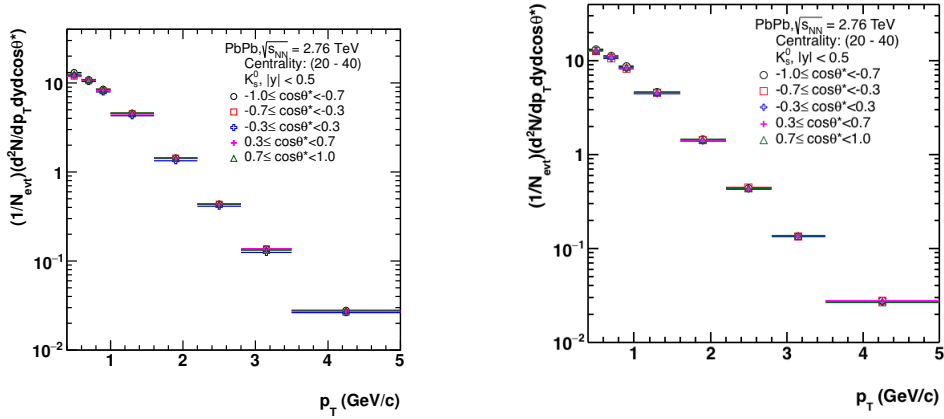

Figure B.43: The efficiency and acceptance corrected p_T spectra of K_S^0 in 20–40 % centrality class in Pb–Pb collisions at $\sqrt{s_{NN}} = 2.76$ TeV and $|y| < 0.5$ for different $\cos\theta^*$ bins. Left panel shows corrected p_T spectra for the production plane analysis and right panel shows corrected p_T spectra for the event plane analysis.

The acceptance, efficiency and branching ratio corrected p_T spectra for different $\cos\theta^*$ bins in 20–40% centrality class at $\sqrt{s_{NN}} = 2.76$ TeV are shown in Fig. B.43. After correcting the p_T spectrum in each $\cos\theta^*$ bin, we plot yield vs $\cos\theta^*$ for each p_T bin. The $\cos\theta^*$ distributions are fitted with the Eq. 3.1. Figure B.45 and Fig. B.46 shows corrected $\cos\theta^*$ distributions in different p_T bins for the production plane and event plane analysis, respectively. Also the distributions are fitted with Eq. 3.1 to get the ρ_{00} in each p_T bin. The p_T spectrum from this analysis is compared with the published p_T spectrum for 20–40% centrality class shown in Fig. B.44. The bottom plot shows the ratio between the p_T spectrum from this analysis and the published data [3]. The two spectra are in good agreement within 3%.
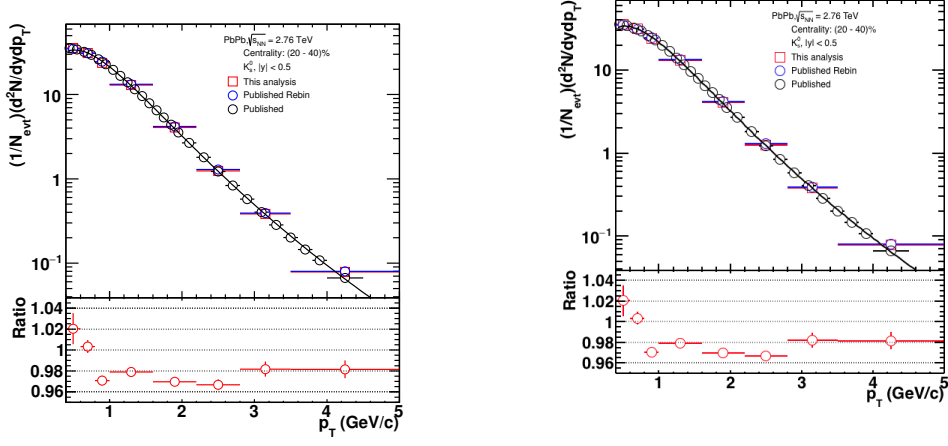
Figure B.44: The efficiency and acceptance corrected p_T spectra of K_S^0 in 20–40% centrality class in Pb–Pb collisions at $\sqrt{s_{NN}} = 2.76$ TeV compared with the published result. The ratio is between the p_T spectrum of this analysis to the published data [3]. Left panel figure is for the production plane and right panel figure is for the event plane.
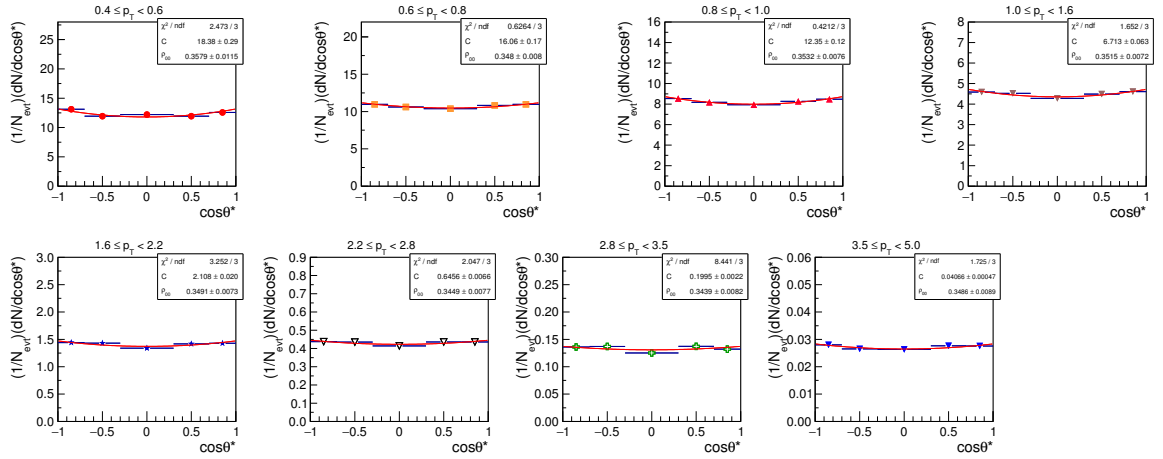

Figure B.45: The efficiency and acceptance corrected $\cos\theta^*$ distributions of K_S^0 decay daughter for different p_T bins. The results are for 20–40% Pb–Pb collisions at $\sqrt{s_{NN}}$ = 2.76 TeV in $|y| <$0.5. Distributions are fitted with the Eq. 3.1. Quantization axis is perpendiculat to the production plane.
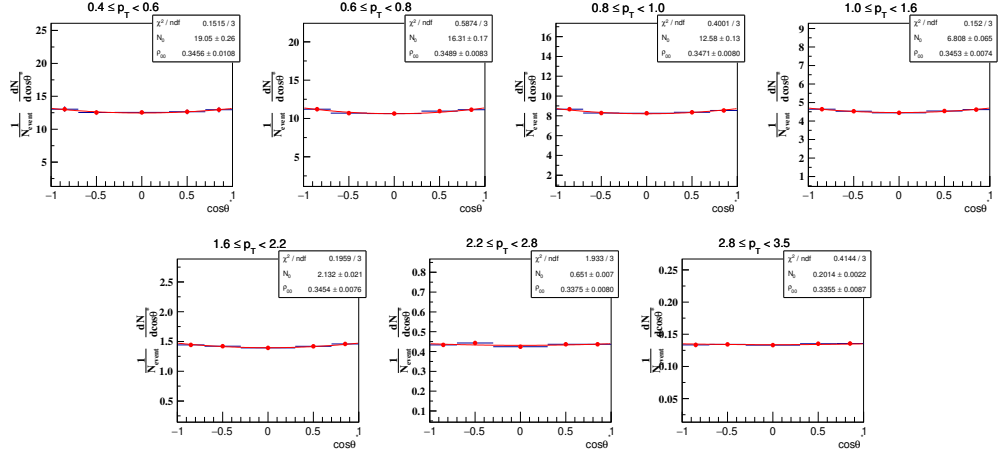
Figure B.46: The efficiency and acceptance corrected $\cos\theta^*$ distributions of K_S^0 decay daughter for different p_T bins. The results are for 20–40% Pb–Pb collisions at $\sqrt{s_{NN}}$ = 2.76 TeV in $|y|$ <0.5. Distributions are fitted with the Eq. 3.1. Quantization axis is perpendicular to the event plane.
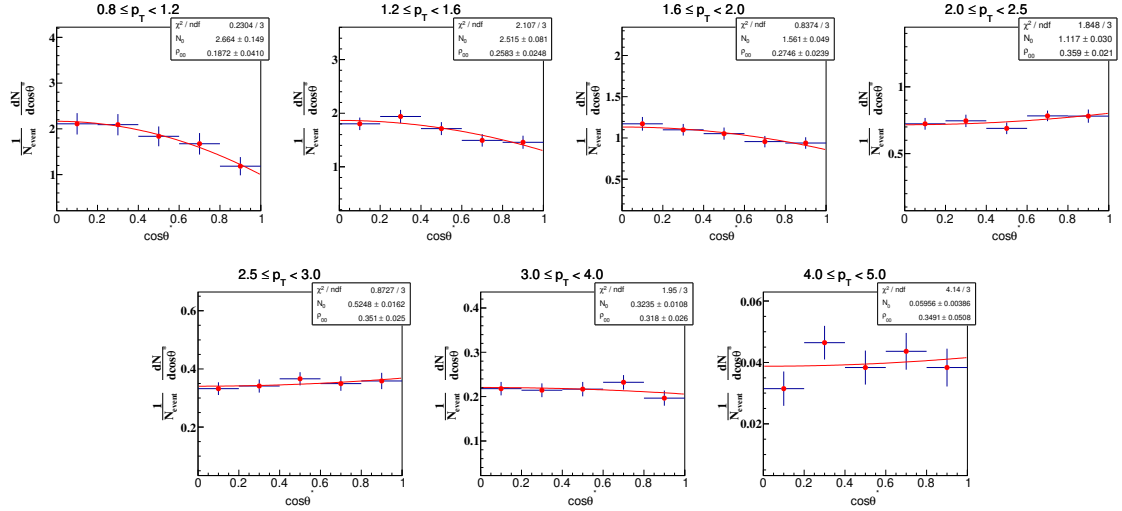
B.7   Corrected $\cos\theta^*$ distributions

Figure B.47: The efficiency and acceptance corrected $\cos\theta^*$ distributions of K^{*0} decay daughter for different p_T bins. The results are for 10–50% Pb–Pb collisions at $\sqrt{s_{NN}}$ = 2.76 TeV in $|y|$ <0.5. Distributions are fitted with the function, mentioned in Eq. 3.1. Quantization axis is perpendicular to the EP.
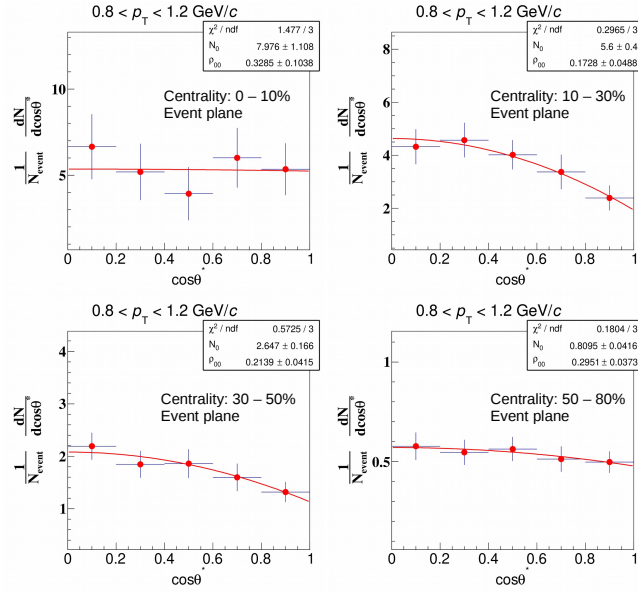
Figure B.48: The efficiency and acceptance corrected $\cos\theta^*$ distribution of K^{*0} decay daughter for $0.8 < p_\mathrm{T} < 1.2$ GeV/c in different centrality classes of Pb–Pb collisions at $\sqrt{s_\mathrm{NN}} = 2.76$ TeV. Measurements are done with respect to normal to the event plane in mid-rapidity.

Figure B.49: The efficiency and acceptance corrected $\cos\theta^*$ distribution of K^{*0} decay daughter for $3.0 < p_\mathrm{T} < 5.0$ GeV/c in different centrality classes of Pb–Pb collisions at $\sqrt{s_\mathrm{NN}} = 2.76$ TeV. Measurements are done with respect to normal to the event plane in mid-rapidity.
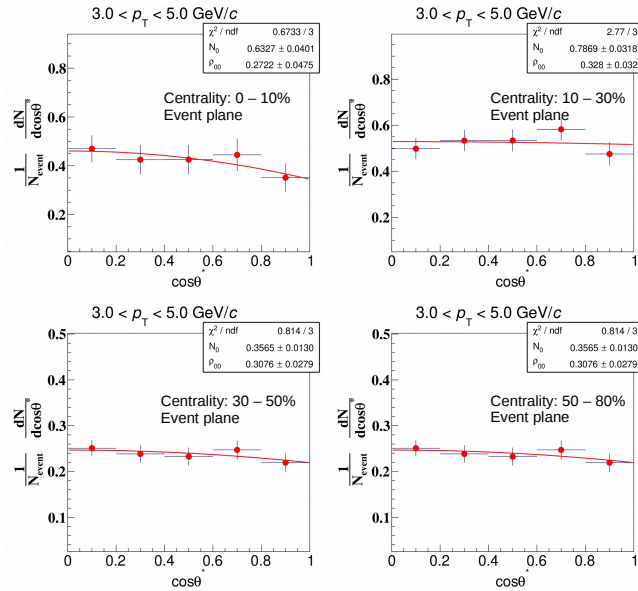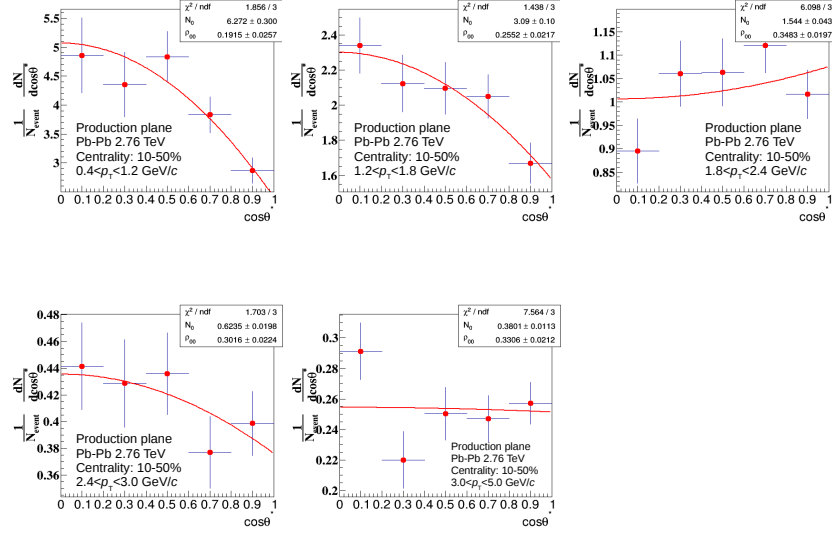
Figure B.50: The efficiency and acceptance corrected $\cos\theta^*$ distributions of K^{*0} for different p_T bins are shown. Distributions are fitted with the function, mentioned in Eq. 3.1. The results are for 10–50% Pb–Pb collisions at $\sqrt{s_{NN}} = 2.76$ TeV in $|y| < 0.5$. Measurements are done with respect to normal to the production plane.
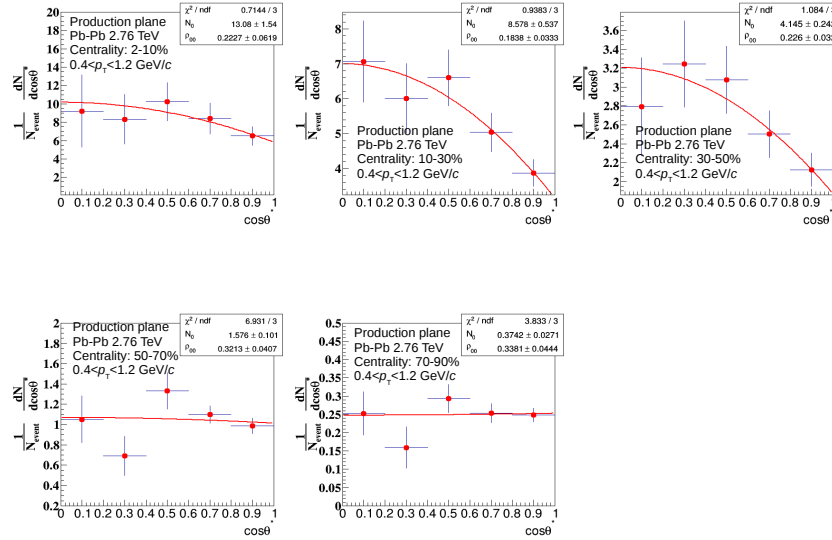

Figure B.51: The efficiency and acceptance corrected $\cos\theta^*$ distribution of K^{*0} decay daughter for $0.4 < p_T < 1.2$ GeV/c in different centrality classes of Pb–Pb collisions at $\sqrt{s_{NN}} = 2.76$ TeV. Measurements are done with respect to normal to the production plane in mid-rapidity.
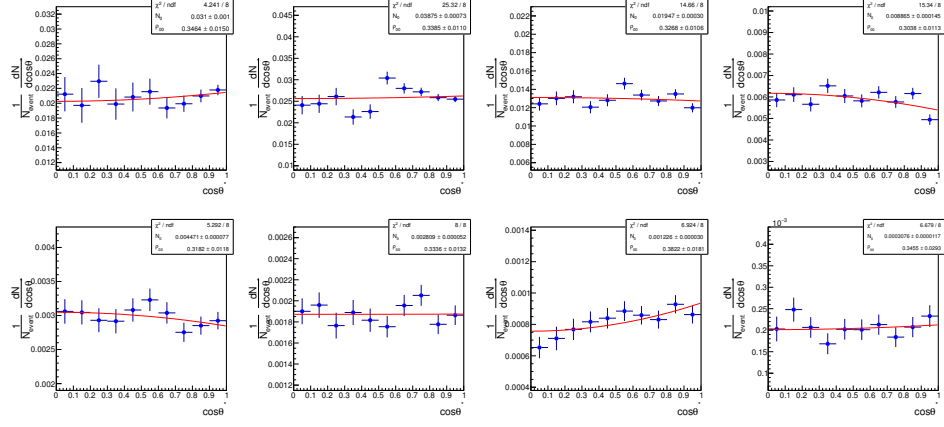
Figure B.52: The efficiency and acceptance corrected $\cos\theta^*$ distributions of K^{*0} decay daughter for different p_T bins are shown. Distributions are fitted with the function, mention in Eq. 3.1. Results are for pp collisions at $\sqrt{s} = 13$ TeV and $|y| < 0.5$. Quantization axis is perpendicular to the PP.
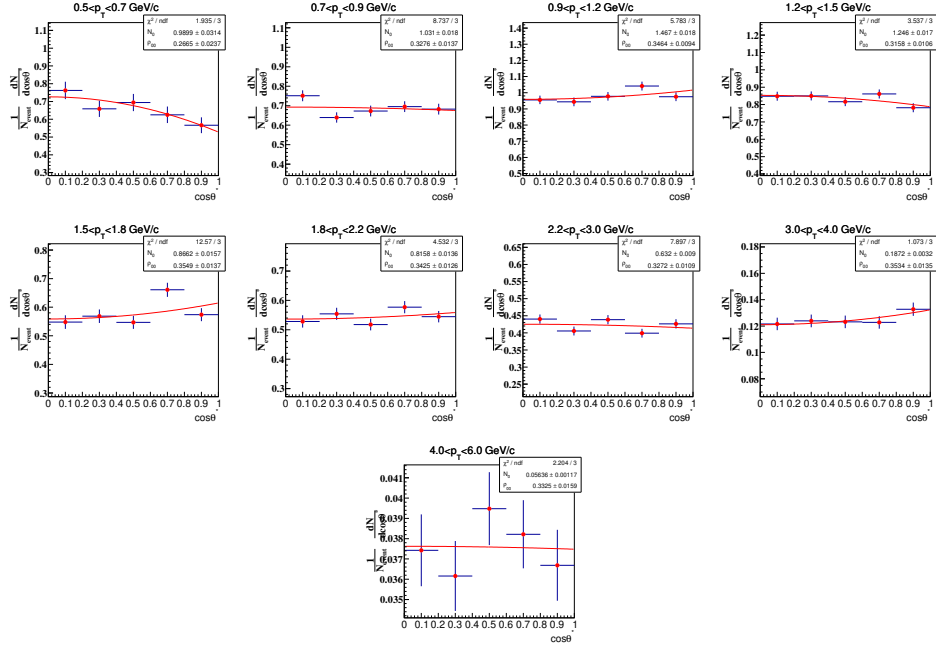

Figure B.53: The efficiency and acceptance corrected $\cos\theta^*$ distributions of ϕ meson decay daughter in 10–50% Pb–Pb collisions at 2.76 TeV in $|y| < 0.5$ for different p_T bins are shown. Distributions are fitted with the function, mentioned in Eq. 3.1. Quantization axis is perpendicular to the EP.
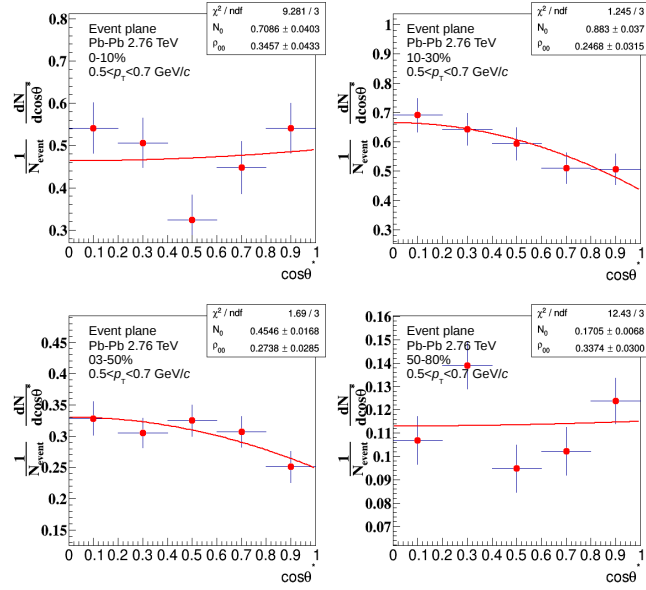
Figure B.54: The efficiency and acceptance corrected $\cos\theta^*$ distribution of ϕ meson decay daughter at mid-rapidity for different centrality classes in $0.5 < p_T < 0.7$ GeV/c in Pb–Pb collisions at $\sqrt{s_{NN}} = 2.76$ TeV. Quantization axis is perpendicular to the EP.

Figure B.55: The efficiency and acceptance corrected $\cos\theta^*$ distribution of ϕ meson decay daughter at mid-rapidity for different centrality classes in $3.0 < p_T < 5.0$ GeV/c in Pb–Pb collisions at $\sqrt{s_{NN}} = 2.76$ TeV. Quantization axis is perpendicular to the EP.
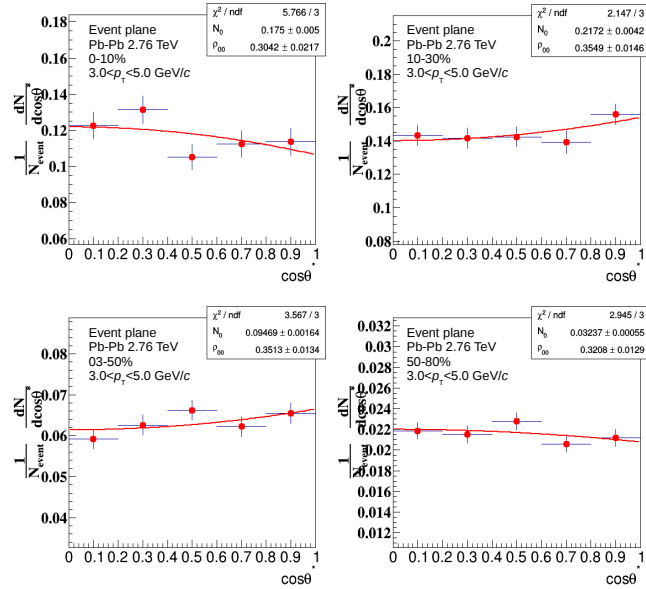
Figure B.56: The efficiency and acceptance corrected $\cos\theta^*$ distributions of ϕ meson decay daughter for various p_T bins in Pb–Pb collisions at 2.76 TeV. Distributions are fitted with the function, mentioned in Eq. 3.1. Quantization axis is perpendicular to the PP.
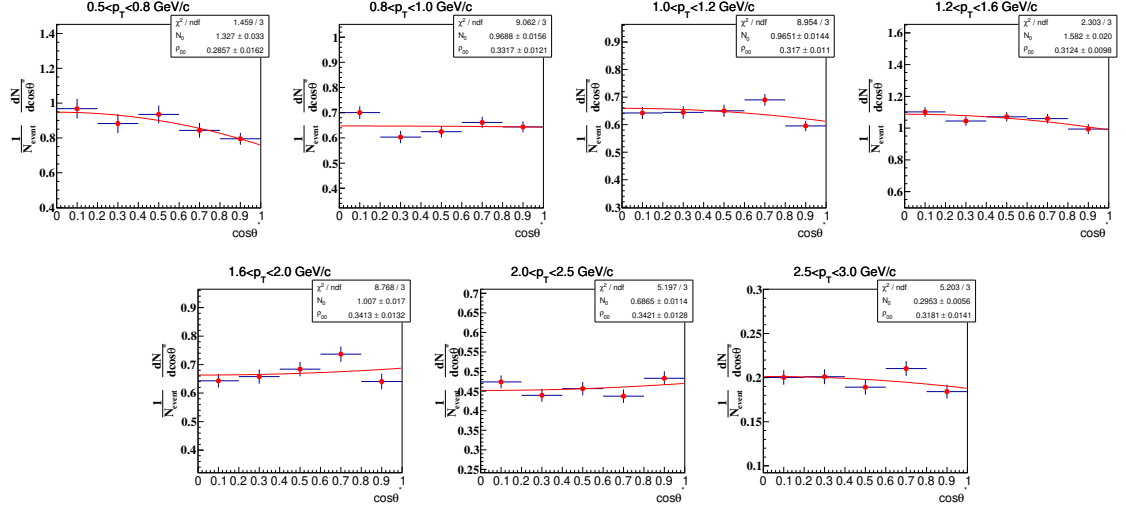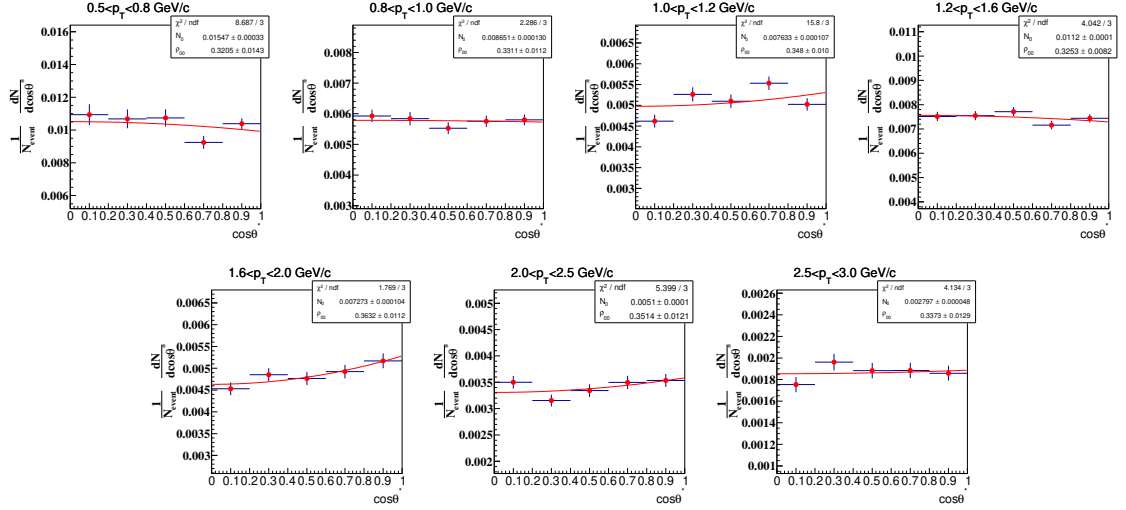

Figure B.57: The efficiency and acceptance corrected $\cos\theta^*$ distributions of ϕ meson decay daughter for various p_T bins in pp collisions at 13 TeV. Distributions are fitted with the function, mentioned in Eq. 3.1. Quantization axis is perpendicular to the PP.
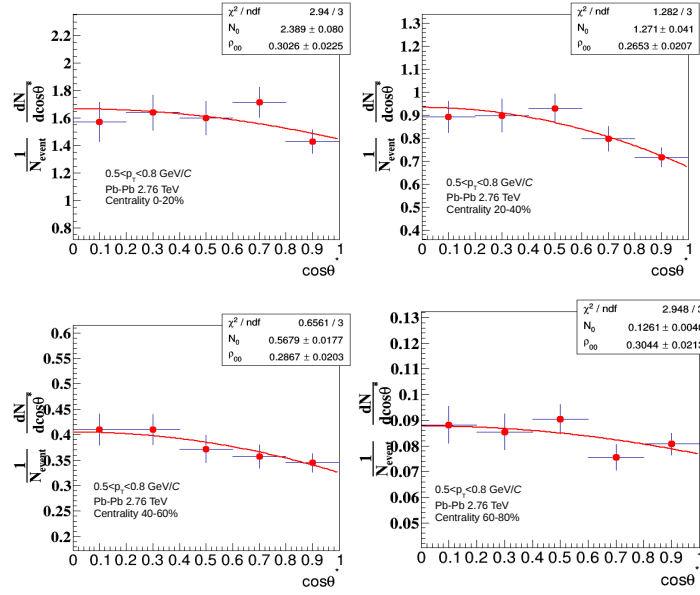
Figure B.58: The efficiency and acceptance corrected cosθ* distributions of φ meson decay daughter for $0.5 < p_{\rm T} < 0.8$ GeV/c in different centrality classes of Pb–Pb collisions at 2.76 TeV. Distributions are fitted with the function, mentioned in Eq. 3.1. Quantization axis is perpendicular to the PP.

Figure B.59: The efficiency and acceptance corrected cosθ* distributions of φ meson decay daughter for $3.0 < p_{\rm T} < 5.0$ GeV/c in different centrality classes of Pb–Pb collisions at 2.76 TeV. Distributions are fitted with the function, mentioned in Eq. 3.1. Quantization axis is perpendicular to the PP.
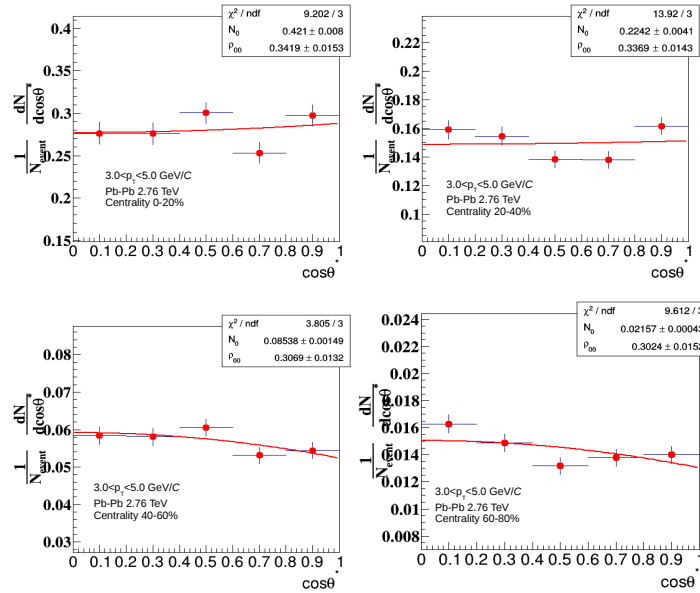
B.8 K^{*0} spin alignment using random event plane

A test has been performed by measuring the ρ_{00} of K^{*0} with respect to normal to the random event plane. The event plane angle is generated using uniform random numbers between 0 to π as shown in Fig. B.60. In order to increase statistics, we have generated 10 random event planes in each event by using 10 different random seeds. Figure B.61 shows invariant mass distribution in p_T bin 0.8-1.2 GeV/c. FigureB.62 shows raw spectra, Acceptance $\times$ Efficiency ($A \times \epsilon_{\rm rec}$), re-weighting factor, and $A \times \epsilon_{\rm rec}$ and branching ratio corrected spectra in various $\cos\theta^*$ bins. Figure B.63 shows corrected $\cos\theta^*$ distributions for K^{*0} in different p_T bins. Measurements for the random event plane are consistent with 1/3 except lowest p_T bin. In lowest p_T bin ρ_{00} is slightly lower compared to 1/3 but higher compared to measurements in the event plane. The measurements for the random event plane at lowest p_T bin is lower than 1/3 as the quantization axis is always perpendicular to the z axis, resulting in a residual effect.
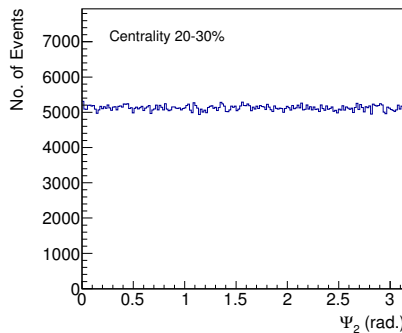
Figure B.60: The event plane angle distribution generated using uniform random numbers between 0 to π.

The left panel of Fig. B.64 shows ρ_{00} vs. p_T for the random event plane measurements. The right panel of Fig. B.64 shows comparison between the random event and random production plane. The random production plane is calculated by randomiz-
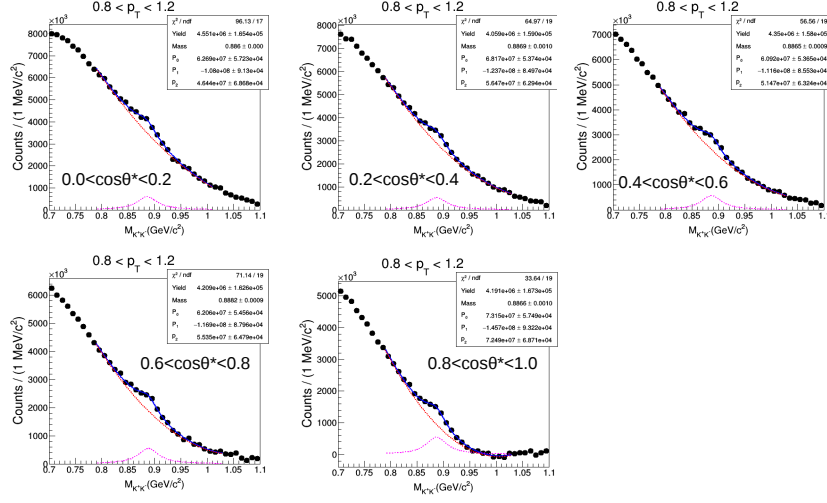
Figure B.61: Invariant mass distribution $M_{\pi K}$ after mixed event background subtraction and fitted with Breit-Wigner + residual background function in centrality class 10–50% for p_T bin 0.8-1.2 GeV/c in various $\cos\theta^*$ bins. Quantization axis is perpendicular with respect to the random event plane.

ing the momentum direction of each track. Measurements for the random event plane and random production plane are consistent with each other.

B.9 K^{*0} spin alignment using quantization axis random in 3-dimension

Figure B.65 shows the invariant mass distributions, Acceptance $\times$ Efficiency and corrected $\cos\theta^*$ distributions in p_T bin 0.8–1.2 GeV/c and 10–50% Pb–Pb collisions for K^{*0} with respect to the quantization axis which is random in 3-dimension. We can see that if the quantization axis is random in 3 dimension, then the residual effect observed in RndEP analysis is not present and the ρ_{00} value is consistent with 1/3.
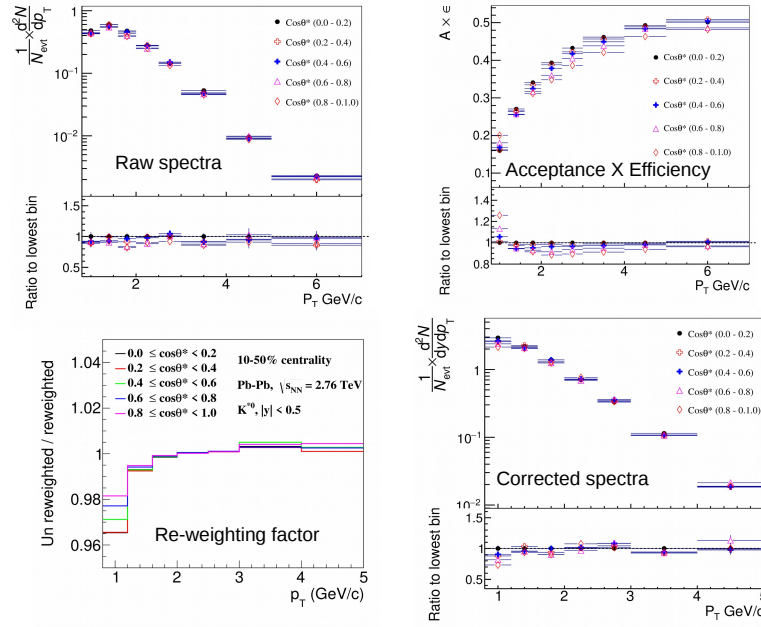
Figure B.62: Raw spectra, $A \times \epsilon_{\text{rec}}$, re-weighting factor, and $A \times \epsilon_{\text{rec}}$ and branching ratio corrected spectra in various $\cos\theta^*$ bins. Quantization axis is perpendicular with respect to the random plane.
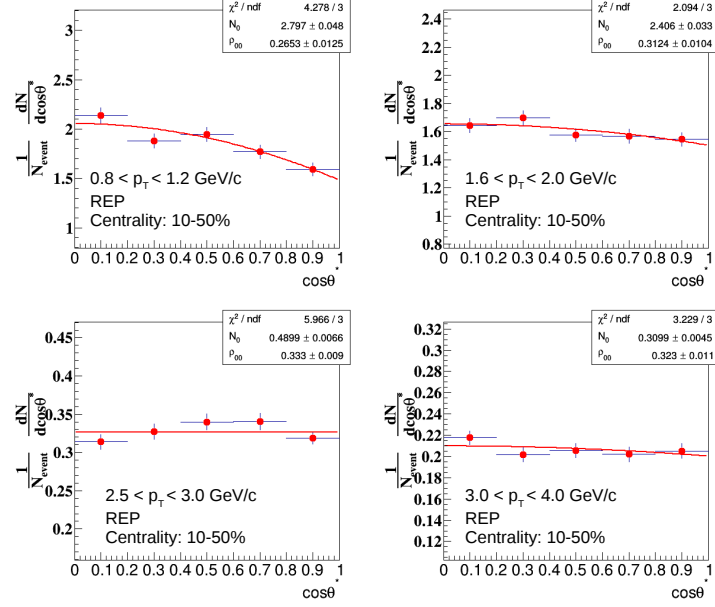
Figure B.63: The efficiency and acceptance corrected $\cos\theta^*$ distribution in different p_{T} bins. Errors are statistical error. Quantization axis is perpendicular with respect to the random plane.
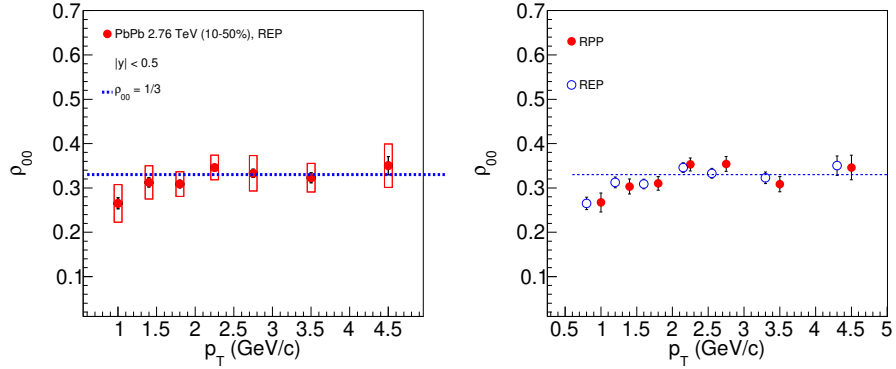
Figure B.64: Left panel: ρ_{00} vs. p_{T} in Pb–Pb collisions at $\sqrt{s_{\mathrm{NN}}} = 2.76$ TeV. Statistical uncertainties on data points are represented by bars and systematic uncertainties on data points are represented by boxes. Quantization axis is perpendicular to the random event plane. Right panel: Comparison between the random production and random event plane measurements.

Figure B.65: Invariant mass distributions, Acceptance × Efficiency and the efficiency and acceptance corrected $\cos\theta^*$ distributions in p_T bin 0.8–1.2 GeV/c and 10–50% Pb–Pb collisions for K^{*0} with respect to the quantization axis which is random in 3-dimension.
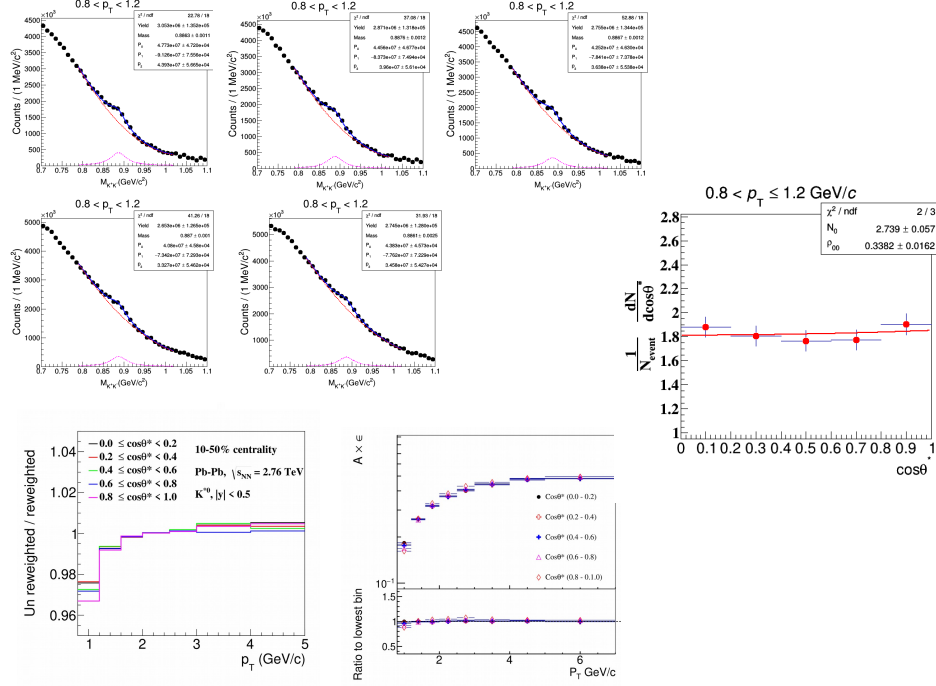
B.10 Checks related to efficiency calculation

B.10.1 Effect of acceptance on the production plane analysis

We used a toy model to study the acceptance effect on $\cos\theta^*$ distribution of K^{*0} decay daughter. We used following steps to generate K^{*0}.

1. K^{*0} mass is generated by using gRandom→BreitWigner(resonanceMass, resonanceWidth).

2. K^{*0} p_T is generated by using gRandom→Exp(0.8).

3. K^{*0} rapidity is generated by using gRandom→Uniform(-0.5, 0.5).

4. K^{*0} azimuthal angle is generated by using gRandom→Uniform($-\pi$, $+\pi$).

Total no of generated K^{*0} is 500000. "TGenPhaseSpace" class of root is used to decay the generated K^{*0}. To study the acceptance effect we used two acceptance
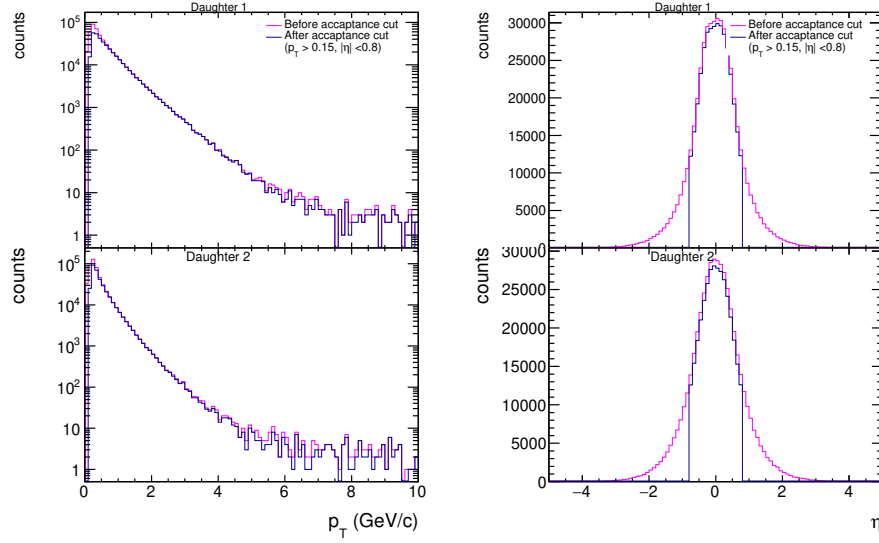
Figure B.66: Left panel shows p_T distribution of both decay daughters, before and after acceptance criteria. Right panel shows η distribution of both decay daughters, before and after acceptance criteria. Here daughter1 corresponds to kaon and daughter2 corresponds to pion.

criteria, 1) $p_T > 0.15$ and 2) $|\eta| < 0.8$ to select decay daughters. Figure B.66 shows the p_T and η distributions of kaon and pion before and after applying the acceptance criteria. Figure B.67 shows the $\cos\theta^*$ distribution of kaon, before and after applying the acceptance criteria.

B.10.2 MC closure test

We have performed a MC closure test to verify our analysis method. Resonance signals are extracted by subtracting the mixed event background from unlike charged invariant mass distribution of their decay daughters, similarly as data. Extracted raw yields are compared to the "true" MC reconstructed K^{*0} yield ("true" MC reconstructed K^{*0} are those which are used in efficiency correction). Then the extracted signals are corrected with acceptance $\times$ efficiency to get the corrected yield and corrected $\cos\theta*$ distribution. Results are compared with the MC generated yield. Extracted yields are found to be consistent with the MC generated yields. Figure B.68 shows
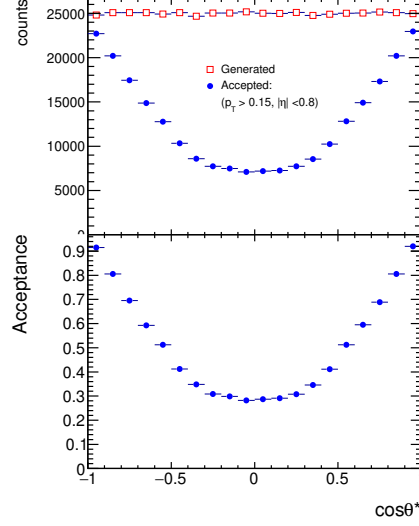
Figure B.67: Cosθ^* distribution of kaon, before and after acceptance criteria.

an example for MC closure test. Figure B.68 also shows Acceptance $\times$ Efficiency as a function of $\cos\theta^*$.

B.10.3 2D efficiency: cos$\theta*$ vs. ϕ-ψ_{rp} for K^{*0} in p_{T} bin 0.8 - 1.2 GeV/c w.r.t. the event plane(EP)

Figure B.69 shows 2D maping of $A \times \epsilon_{\mathrm{rec}}$ for K^{*0} in p_{T} bin 0.8 - 1.2 GeV/c w.r.t. EP, obtained from HIJING. In our measurements we have taken $\phi - \psi_{rp}$ integrated efficiency ($[A \times \epsilon_{\mathrm{rec}}]_{case1}$) which are consistent with the efficiency ($[A \times \epsilon_{\mathrm{rec}}]_{case2}$) obtained by averaging over the $A \times \epsilon_{\mathrm{rec}}$ of each $\phi - \psi_{rp}$ bins. Table B.1 shows comparison between $[A \times \epsilon_{\mathrm{rec}}]_{case1}$ and $[A \times \epsilon_{\mathrm{rec}}]_{case2}$.

B.10.4 Effect of event plane estimation on Acceptance $\times$ Efficiency correction

Event plane estimation in HIJING is done from MC generated tracks within the η acceptance of V0C detector. The event plane vector is estimated by using following
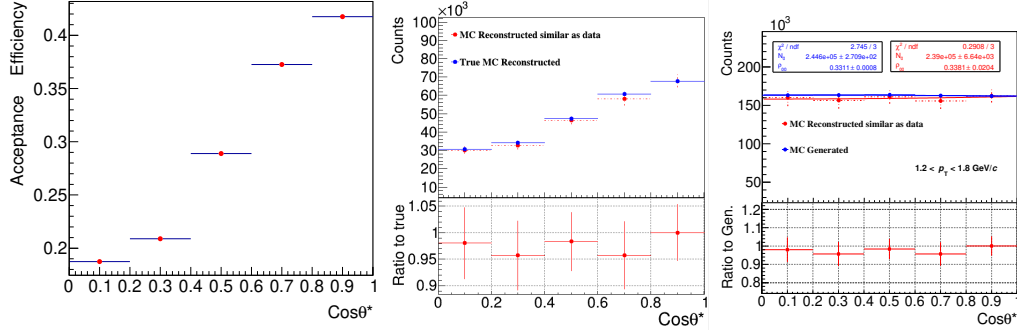
Figure B.68: Acceptance × Efficiency vs. $\cos\theta^*$, raw yield and comparison of corrected $\cos\theta*$ distribution, calculated from the MC reconstruction data using data driven method to those obtained from the MC generated data.

Table B.1: Comparison of $A \times \epsilon_{\rm rec}$ for K^{*0} in $p_{\rm T}$ bin 0.8 - 1.2 GeV/c w.r.t. EP, obtained from HIJING

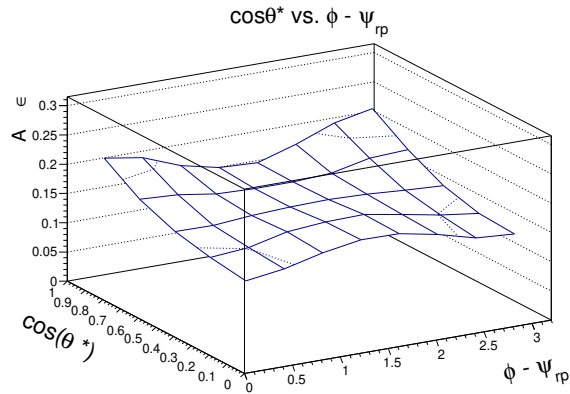| $\cos\theta^*$ bin	$[A \times \epsilon_{\rm rec}]_{case1}$	$[A \times \epsilon_{\rm rec}]_{case2}$
0.0–0.2	0.154	0.149
0.2–0.4	0.157	0.154
0.4–0.6	0.162	0.160
0.6–0.8	0.175	0.177
0.8–1.0	0.197	0.204

Figure B.69: 2D maping of acceptance × efficiency for K^{*0} in $p_{\rm T}$ bin 0.8 - 1.2 GeV/c w.r.t. EP
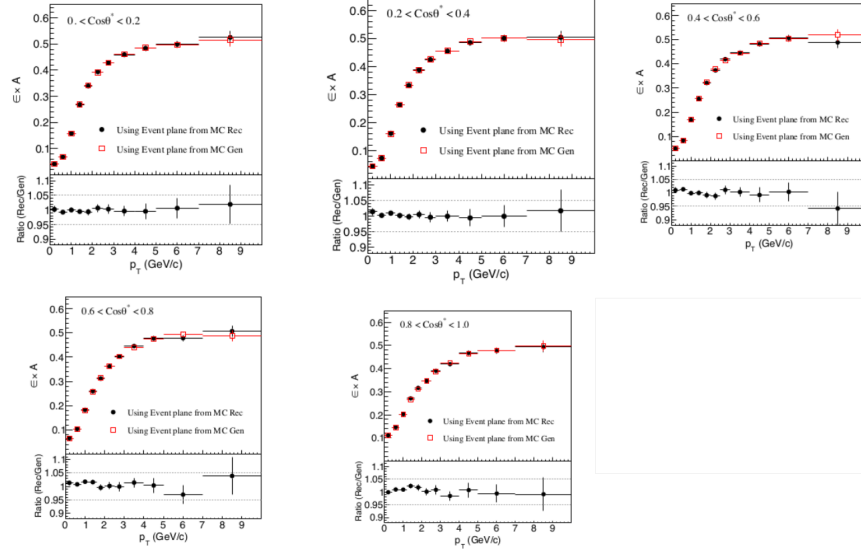
Figure B.70: Acceptance × Efficiency vs. p_{T} for different $\cos\theta*$ bins for two diffrent way of EP estimation: 1)EP is estimated by MC generated tracks 2)EP is estimated by MC reconstructed tracks.

equations

$$Q_{n,x} = \sum_{n=i} w_i cos(n\phi_i) = Q_n cos(n\Psi_n); \quad Q_{n,y} = \sum_{n=i} w_i sin(n\phi_i) = Q_n sin(n\Psi_n).$$
(B.16)

We have also estimated the event plane vector by using the MC reconstructed tracks. Comparison between efficiencies using MC generated tracks and MC reconstructed tracks to calculate EP vector are given in Fig. B.70.

B.10.5 Correction of Pb–Pb result with the efficiency from PYTHIA

Figure B.71 shows comparison of ρ_{00} vs. p_{T} in 10–50% Pb–Pb collisions w.r.t. the production plane for two different efficiency correction: 1) efficiency is calculated by using HIJING production 2) efficiency is calculated by using PYTHIA production.
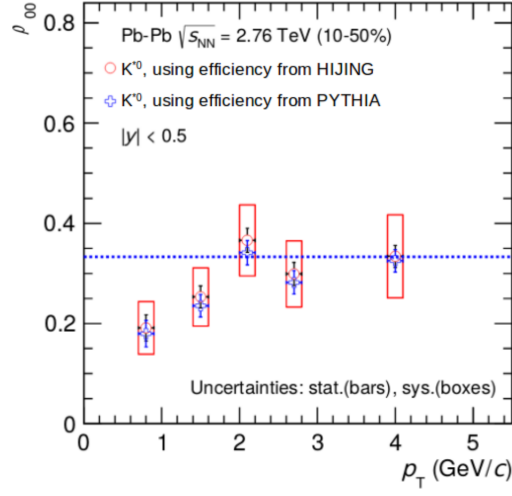
Figure B.71: ρ_{00} vs. p_T in 10–50% Pb–Pb collisions w.r.t. the production plane for two different efficiency correction, one is from HIJING and another is from PYTHIA.

B.10.6 Efficiency calculation by using momentum information of generated tracks and reconstructed tracks to calculate cos$\theta*$

Efficiency is calculated by using momentum information of generated tracks and reconstructed tracks to calculate cos$\theta*$. Comparison for this two cases are given in Fig. B.72. Calculated efficiencies in different cos$\theta*$ bin as a function of p_T are consistent for this two cases. Two cases are

case1: $\cos\theta^*$ in both generated and reconstructed level are calculated using the momentum information from generated level.

case2: $\cos\theta^*$ in reconstructed level are calculated using the momentum information of reconstructed track.
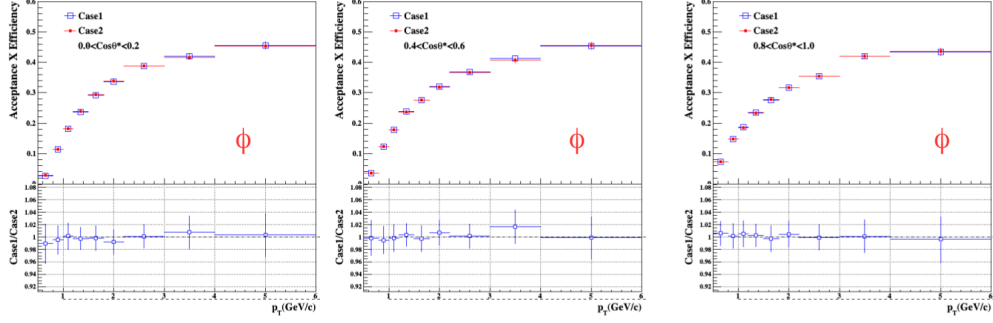
Figure B.72: Acceptance x efficiency vs. p_T in 10–50% Pb–Pb collisions w.r.t. the production plane for ϕ meson in different $\cos\theta*$ bins for two diffrent cases. In one case momentum information from generated tracks are used and in another case momentum information from reconstructed tracks are used.

B.11 MC generated and reconstructed spectra in pp analysis

Figure B.73 shows MC generated and reconstructed p_T distributions for K^{*0} different $\cos\theta^*$ bins. A dip near $p_\mathrm{T} = 0.7$ GeV/C is observed in the MC reconstructed p_T distribution. This effect is mainly coming because of the analysis acceptance. K^{*0} analysis with respect to the production plane in Pb–Pb collisions is also performed in $0.8 < p_\mathrm{T} < 1.2$ GeV/C to avoid the p_T region near 0.6 GeV/C, where a sudden drop in yield is observed from MC simulation. In small p_T bin, signal stays and ρ_{00} is lower than 1/3, following the observed p_T dependency as shown in Fig. B.74.

B.12 Estimation of systematic uncertainty

Method1:

Default method of systematic uncertainty estimation on ρ_{00}, used for this analysis is described in Sec. 3.5. In order to extract the systematic uncertainty on ρ_{00}, we fitted the acceptance and efficiency corrected $\cos\theta^*$ distribution from each of the
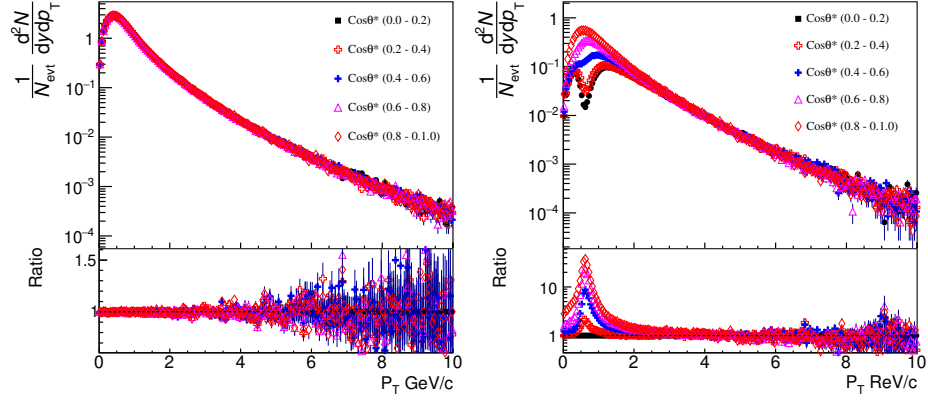
Figure B.73: MC generated and reconstructed p_T distributions for K^{*0} different $\cos\theta^*$ bins with respect to PP in 10–50% Pb–Pb collisions are shown respectively in the left and right panel of the figure. Lower panel of each figure shows ratio to minimum $\cos\theta^*$ bin.

systematic source to get ρ_{00} for those sources. Let for a given source we have k number of variations. Then the systematic uncertainty on ρ_{00} due to this source is $\sqrt{\frac{1}{k}\sum_{i=1}^{k}\left(\rho_{00}^{def} - \rho_{00}^{i}\right)^2}$. Finally we add the contribution from each of the sources in quadrature to obtain total systematic uncertainty on ρ_{00}.

Method2:

We have also performed an alternative way to extract systematic uncertainty. In this method, systematic uncertainty on the measured vector meson yield in each $\cos\theta^*$ bin is used during the fitting of $\cos\theta^*$ distribution to get the ρ_{00} value and the error on ρ_{00} corresponds the systematic uncertainty on ρ_{00}. This method is a crude method as the correlation between systematic uncertainties on yield in each $\cos\theta^*$ bins does not remove by this method. Let consider a systematic source for which yields in each $\cos\theta^*$ bins are increased by 5%. As a result this source will contribute 5% systematic uncertainty on yields, hence on the ρ_{00}. But in reality this source does not change the shape of the $\cos\theta^*$ distribution so the systematic uncertainties due to this source should be zero, which can be obtained by method1.
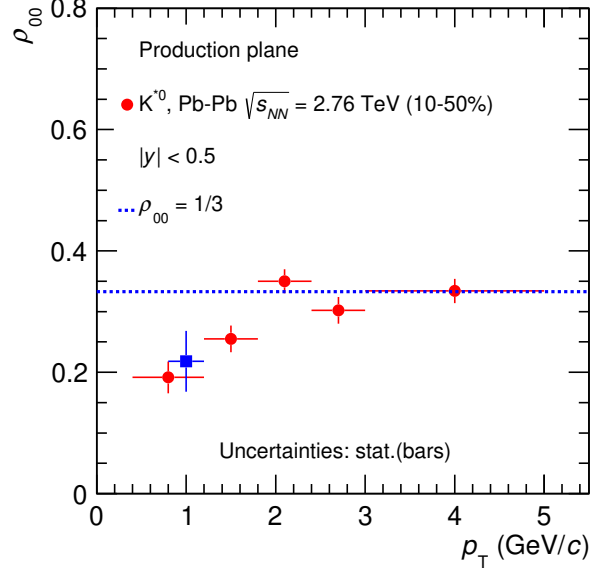
Figure B.74: ρ_{00} vs. p_T for K^{*0} in 10–50% Pb–Pb collisions at $\sqrt{s_{NN}} = 2.76$ TeV with respect to the production plane.

We cave compared the systematic uncertainties obtained from both these methods and found the systematic uncertainties on ρ_{00} from two different methods are compatible. For the comparison we have taken the $\cos\theta^*$ distribution of K^{*0} decay daughter w.r.t. PP for $0.4 < p_T < 1.2$ GeV/c in 10–50% Pb–Pb collisions at $\sqrt{s_{NN}} = 2.76$ TeV. Figure B.75 shows the acceptance and efficiency corrected $\cos\theta^*$ distribution of of K^{*0} decay daughter and the uncertainties on data points are systematic uncertainties on measured K^{*0} yields. We have found that the total systematic uncertainty on ρ_{00}, obtained from method2 is 23%, whereas the total systematic uncertainty on ρ_{00}, obtained from method1 (shown in Fig 3.18) is 18%.

B.13   Comparison between K^{*0} and $\bar{K}^{*0}$

Figure B.76 shows comparison between ρ_{00} vs. p_T for K^{*0} and $\bar{K}^{*0}$ in 10–50% Pb–Pb collisions w.r.t. the production plane. Results for particle and anti particles are
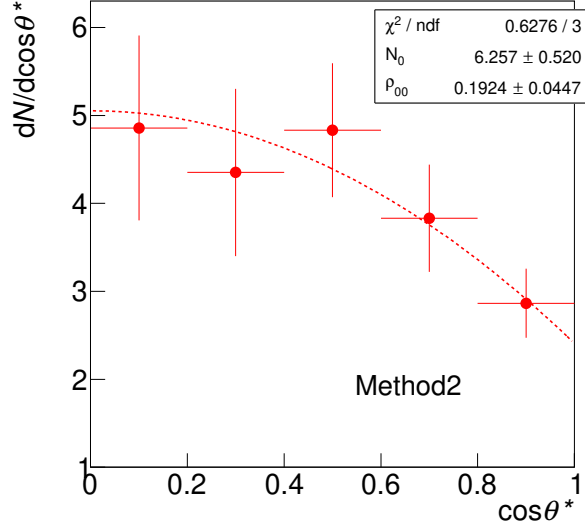
Figure B.75: The acceptance and efficiency corrected $\cos\theta^*$ distribution of of K^{*0} decay daughter w.r.t. PP for $0.4 < p_{\mathrm{T}} < 1.2$ GeV/c in 10–50% Pb–Pb collisions at $\sqrt{s_{\mathrm{NN}}} = 2.76$ TeV. Uncertainties on data points correspond the systematic uncertainties on yields. Distribution is fitted with the function, mentioned in Eq. 3.1 to obtain systematic uncertainties on ρ_{00}.

consistent with each other within statistical error.

B.14   Analysis with high statistics Pb–Pb 5.02 TeV data

The ρ_{00} values for K^{*0} with respect to the production plane are extracted for high statistics (run 2015: 30 M event, run 2018: 100 M event) Pb–Pb collisions data at $\sqrt{s_{\mathrm{NN}}} = 5.02$ TeV. Figure B.77 shows the extracted ρ_{00} values as a function of p_{T}.
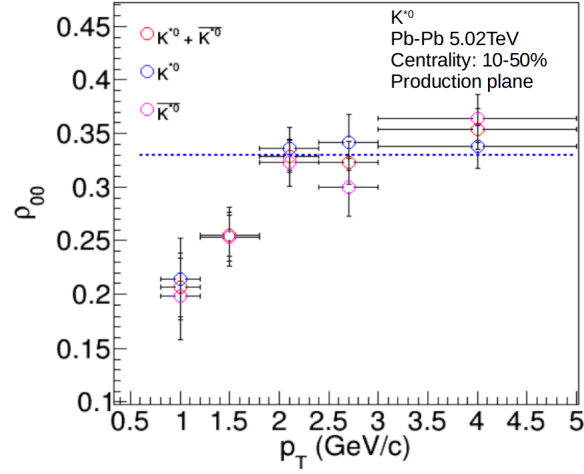
Figure B.76: ρ_{00} vs. p_{T} for K^{*0} and $\bar{K}^{*0}$ in 10–50% Pb–Pb collisions w.r.t. the production plane.
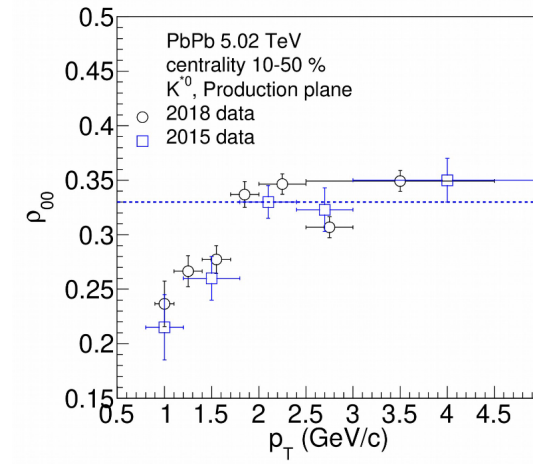

Figure B.77: ρ_{00} vs. p_{T} for K^{*0} in 10–50% Pb–Pb collisions at $\sqrt{s_{\mathrm{NN}}} = 5.02$ TeV with respect to the production plane.

Appendix C

Invariant mass distributions of unlike charged πK pairs for various p_{T} intervals in 0–30% and 70–90% Xe–Xe collisions at $\sqrt{s_{\mathrm{NN}}} = 5.44$ TeV are shown in Fig. C.1 and Fig. C.2, respectively.

Figure C.1: Mixed event background subtracted πK invariant mass distribution in 0–30% Xe–Xe collisions, fitted with a Breit-Wigner + 2nd order polynomial of $M_{K\pi}$ function. The Breit-Wigner function describes the K^{*0} signal and the residual background is described by the 2nd order polynomial function. Uncertainties on data points are statistical only.
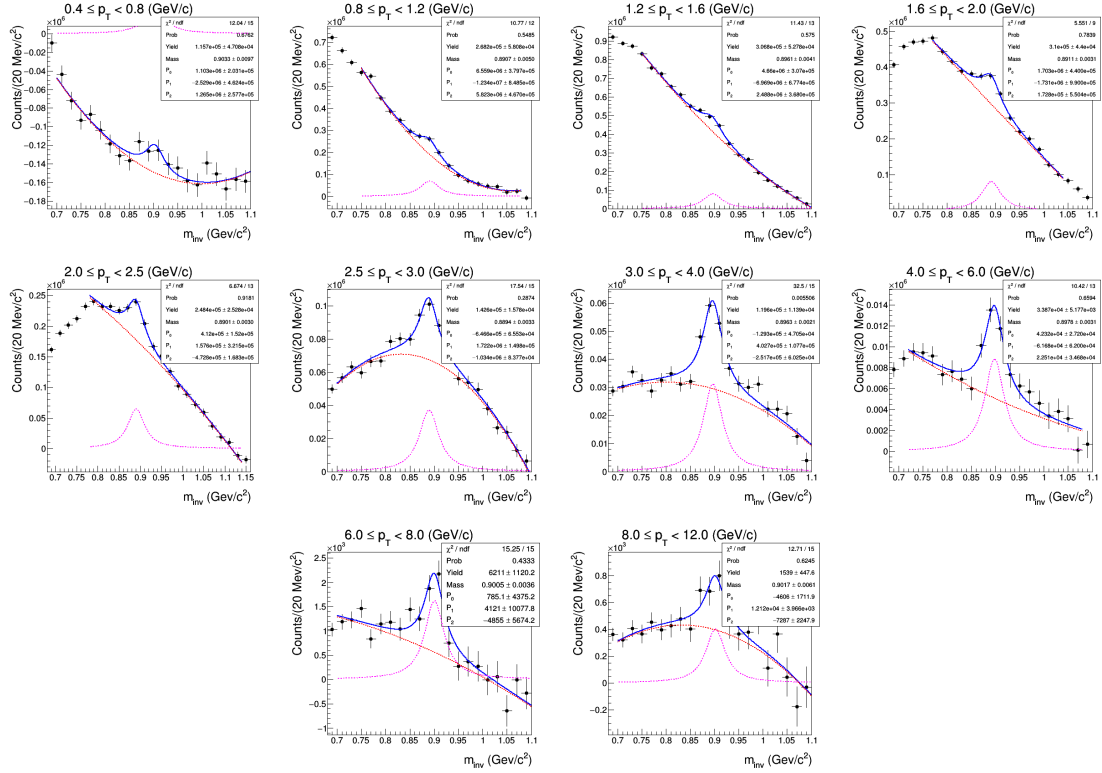
Figure C.2: Mixed event background subtracted πK invariant mass distribution in 70–90% Xe–Xe collisions, fitted with a Breit-Wigner + 2nd order polynomial of $M_{K\pi}$ function. The Breit-Wigner function describes the K^{*0} signal and the residual background is described by the 2nd order polynomial function. Uncertainties on data points are statistical only.
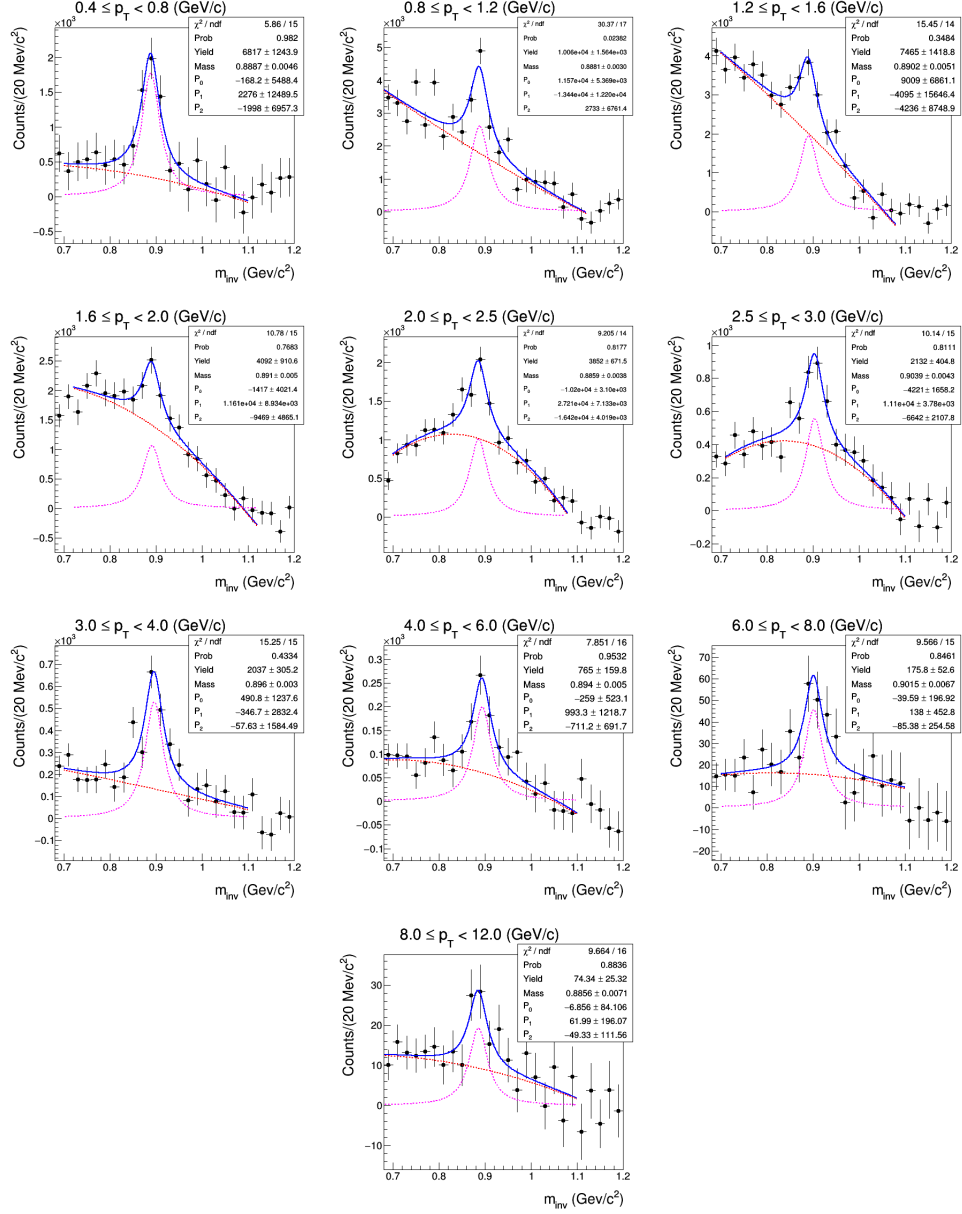
Appendix D

D.1 Invariant mass distributions

Figure D.1 and D.2 shows πK invariant mass distribution after mixed event background subtraction for different p_T ranges for 1–5% and minimum bias pp collisions at $\sqrt{s} = 13$ TeV in $|y| <0.5$, respectively. Invariant mass distributions for other multiplicity classes can be found in [4].
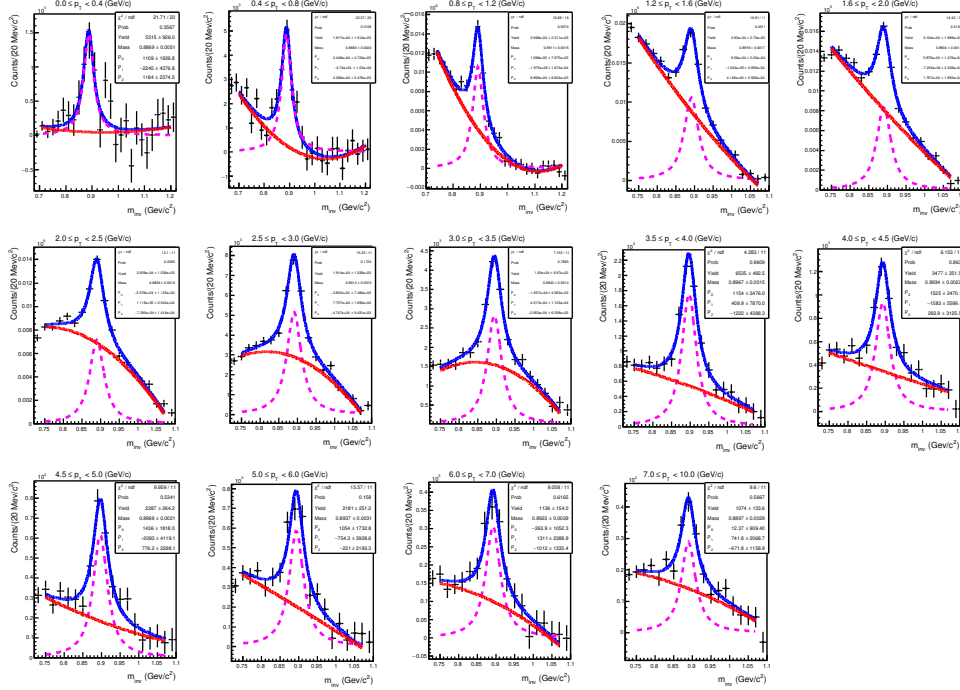

Figure D.1: πK invariant mass distribution after mixed event background subtraction for different p_T ranges in multiplicity bin 1-5% are shown. Distributions are fitted with Breit-Wigner + 2nd order polynomial function, where blue, magenta and red lines describe the signal + residual background, signal and residual background respectively. The results are from pp collisions at $\sqrt{s} = 13$ TeV in $|y| <0.5$.

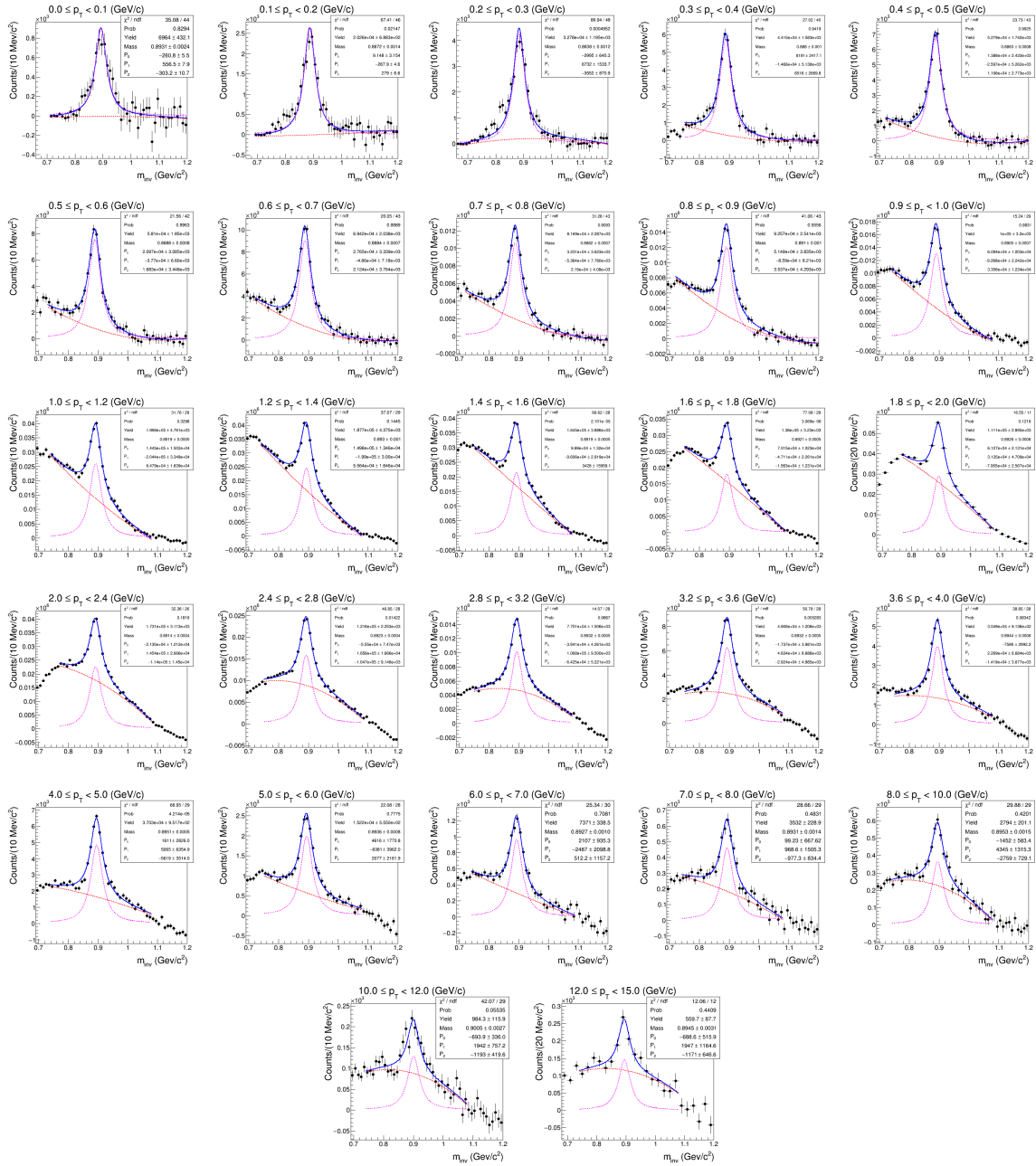Figure D.2: πK invariant mass distribution after mixed event background subtraction for different p_{T} ranges in INEL pp collisions at $\sqrt{s} = 13$ TeV in $|y| <$0.5. Distributions are fitted with Breit-Wigner $+$ 2$^{\mathrm{nd}}$ order polynomial function, where blue, magenta and red lines describe the signal $+$ residual background, signal and residual background, respectively.

D.2   Re-weighting factor

Re-weighting factors as a function of p_T in different multiplicity classes are shown in Fig D.3.
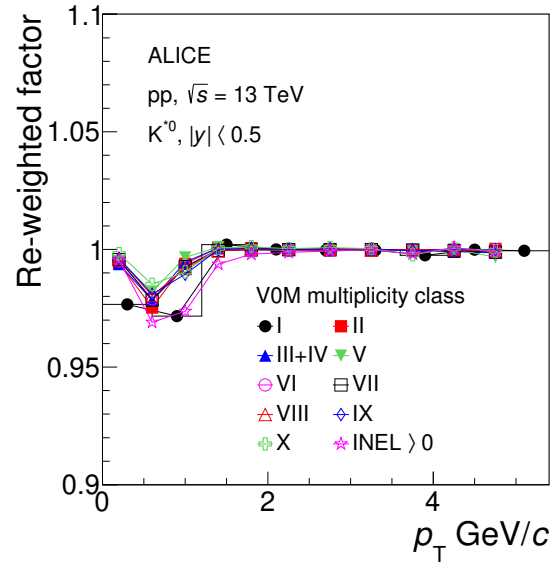

Figure D.3: Re-weighting factor as a function of p_T for K^{*0} in different multiplicity classes of pp collisions at $\sqrt{s} = 13$ TeV in $|y| < 0.5$.

References

[1] M. E. Rose, Elementary theory of angular momentum [John Wiley & Sons, Inc.], 1957.

[2] B. Abelev et al. [ALICE Collaboration], Phys. Rev. C 91, 024609 (2015).

[3] B. B. Abelev et al. [ALICE Collaboration], Phys. Rev. Lett. 111, 222301 (2013).

[4] A. K. Dash et al. [ALICE Collaboration], https://alice-notes.web.cern.ch/node/655.

Thesis Highlight

Name of the Student: Sourav Kundu
Name of the CI/OCC: NISER   Enrolment No.: PHYS11201504005
Thesis Title: Angular and momentum distribution of vector mesons produced in proton-proton and heavy-ion collisions at LHC energies
Discipline: Physical Sciences
Sub-Area of Discipline: High-energy heavy-ion collision experiment
Date of viva voce: 23/12/2020

A large angular momentum ($O(10^7)\ \bar{h}$) is expected to be created in ultra-relativistic heavy-ion collision, when two heavy-ion nuclei collide with non-zero impact parameter. In presence of such large angular momentum, produced quarks can be polarized due to spin-orbital angular momentum interaction of QCD. Polarization of quarks can be further transferred to the polarization of produced hadrons during the process of hadronization.

The spin-oribital angular momentum interactions are one of the most important effect in several branches of physics causing fine structure in atomic physics and shell structure in nuclear physics, and is a key ingredient in the field of spintronics in materials sciences. In this thesis I studied the spin alignment of produced vector mesons in heavy-ion collisions, in order to search the effect of spin-orbital angular momentum interaction in ultra-relativistic heavy-ion collisions. Spin alignment is quantified by measuring the spin density matrix element ρ_{00} which is the probability of finding a vector meson in spin state 0 out of 3 possible spin states (-1, 0, 1). In the absence of spin alignment all 3 spin states are equally probable, hence $\rho_{00} = 1/3$. The ρ_{00} values will deviate from 1/3 in presence of spin alignment or preferential orientation of vector meson's spin. presence of spin-orbital angular momentum interactions. The $\rho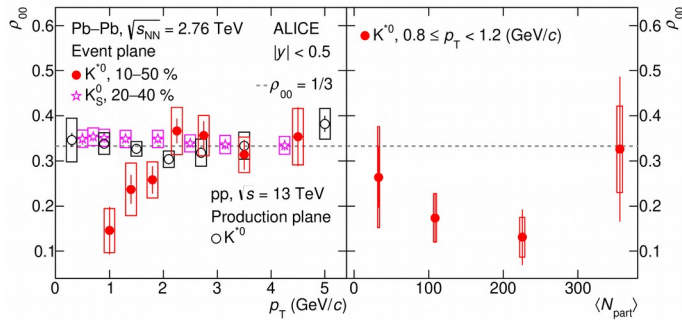_{00}$ values for vector mesons can be measured experimentally by studying the angular distribution of the decay daughter of vector meson with respect to the direction of angular momentum which is perpendicular to the reaction plane (subtended by the beam axis and impact parameter direction).

Figure 1: Left panel: ρ_{00} as a function of transverse momentum for K^{*0} in Pb–Pb and pp collisions, and for K_s^0 in Pb–Pb collisions. Right panel: Centrality dependence of ρ_{00} for K^{*0} mesons in Pb–Pb collisions.

We report for the first time a significant spin alignment effect (3σ level for K^{*0} and 2σ level for φ) for vector mesons in heavy-ion collisions. A deviation of ρ_{00} from 1/3 at low transverse momentum and in mid-central Pb–Pb collisions, supports the presence of a large initial angular momentum in non-central heavy-ion collisions, which leads to quark polarization via spin-orbit coupling, subsequently transferred to hadronic degrees of freedom by hadronization via recombination. Obtained centrality dependence of spin alignment effect of vector mesons is similar to the impact parameter dependence of initial angular momentum created in heavy-ion collisions. The initial angular momentum due to the extended size of the nuclei and the finite impact parameter in non-central heavy-ion collisions is missing in proton-proton collisions. Determination of ρ_{00} for vector mesons produced in pp collisions and for spin zero K_s^0 produced in heavy-ion collisions provide a null test for spin alignment of vector mesons measured in the present work.